Doctoral Dissertation
Doctoral Program in Energy Engineering (35^{th}cycle)

Thermal Energy Storage Technologies

Fast modelling, realisation and experimental characterisation of innovative latent heat storage units for system integration

By

Alessandro Colangelo

******

Supervisor(s):
Prof. Verda Vittorio, Supervisor
Prof. Lanzini Andrea, Co-Supervisor
Guelpa Elisa, Co-Supervisor

Doctoral Examination Committee:
Prof. Oronzio Manca, Referee, Università degli Studi della Campania
Prof. Testi Daniele, Referee, Università di Pisa
Prof. Piacentino Antonio, Università degli Studi di Palermo
Prof. Santarelli Massimo, Politecnico di Torino
Prof. Fasano Matteo, Politecnico di Torino

Politecnico di Torino
2023

Declaration

I hereby declare that, the contents and organization of this dissertation constitute my own original work and does not compromise in any way the rights of third parties, including those relating to the security of personal data.

Alessandro Colangelo
2023

* This dissertation is presented in partial fulfillment of the requirements for **Ph.D. degree** in the Graduate School of Politecnico di Torino (ScuDo).

Tutti corrono, ma verso dove? Perché?
Molti sentono che questo correre non ci si addice
e che ci fa perdere tanti vecchi piaceri.
Ma chi ha ormai il coraggio di dire:
"Fermi! Cambiamo strada"?

Tiziano Terzani, Un indovino mi disse

Acknowledgements

I see this thesis as the conclusion of a long journey that started 11 years ago, when I attended the first lessons in the Energy Engineering bachelor's course at Politecnico di Torino. Those first years instilled in me great curiosity and an interest for research. That's why I consider the PhD a natural conclusion of this process. Unfortunately, I would be lying if I said that I particularly enjoyed these last years passed as a PhD candidate. Nevertheless, I don't want to come to harsh conclusions at the time of this writing. I'm sure I'll be able to judge this period under a different light in future.

Yet, I managed to conclude this work. And this would not have been possible without some people that deserve acknowledgement. I want to start with my office mates Francesco, Riccardo (with whom I also shared great memories during the Masters's course!), Daniele, Azad, Francesco and all the other guys at the Energy Center Lab. Also thanks to Martina and Giulia on the other side of the campus for the sincere discussions. Remaining in PoliTO, I would also like to thank Andrea and Marta, for giving me the possibility to do a few hours of teaching in front of a class full of students. I always had a certain fascination for teaching and I am thankful for this experience. Also thanks to my supervisors Vittorio and Elisa.

Then, I would like to thank my lovely group of friends: Federico, Ilaria, Davide, Miriana, Emanuele, Elisa, Matteo, Sarah, Mirko e Martina. The joy I have in spending the time with you all helps overcoming all the difficulties.

Then, of course, my family deserves a special thank. My parents, Antonio e Claudia, for the encouragement in starting this long journey and their endless support. My little sister, Giulia, for the open-hearted confessions (and the lunches together!). My grandparents, for the past sacrifices that created favourable conditions for such a journey.

Finally, I must say a huge thank to my beloved Chiara. For pushing me forward through the difficulties. For making my life better with your simple presence. For the

patience you had when I was writing this manuscript (especially in the weekends!) and for countless other reasons.

Abstract

The building sector alone is responsible for roughly 1/3 of the global final energy consumption and almost half of this energy demand is destined to space and water heating. Although low-carbon heating technologies are growing, such an energy demand is mostly met by fossil fuels. Hence, thermal energy storage (TES) technologies are a pivotal element for supporting high shares of renewable energy and increased demand flexibility in the heating sector. Among the available energy storage options, Latent Heat Thermal Storage (LHTS) has gained increasing attention because it offers considerably higher energy density at a nearly constant temperature level if compared to sensible storage systems. Such features are particularly attractive for applications in urban contexts, which are generally characterised by a limited installation space for TES units. Despite this great potential, only a limited number of commercial devices has reached market deployment. This may be ascribed to two existing conditions: the lack of fast and accurate models facilitating the integration of LHTS units in energy systems and the limited knowledge on how full-scale LHTS devices interact with the heating systems in which they are incorporated.

In an attempt to overcome these gaps, this thesis provides some contributions both from a methodological and an application point of view. The method-related advances concern the presentation of a fast, accurate and experimentally validated dynamic model for system-level simulations of shell-and-tube latent heat storage units. Such a model is entirely based on a-priori known physical and geometrical parameters and does not require any experimental parameter calibration. Moreover, this modelling approach is rather general and has the potential to support both LHTS optimal sizing and LHTS system level performance investigation. On the other hand, the application-oriented advances regard the documentation of the realization process and the experimental measurements of two 40-kWh shell-and-tube LHTS prototypes characterised by a different inner heat exchanger design. These storage units are studied and analyzed from two perspectives. On the one hand, the experimental

facility is used to validate the aforementioned dynamic model comparing the numerical outcomes against the experimentally measured quantities for both the LHTS prototypes. On the other hand, a comparative analysis centred on the performance of the two LHTS tanks is performed. To conclude, the role of latent heat thermal storage is assessed in the framework of the EU research project RE-cognition, which aims at an intelligent integration of multiple energy and storage technologies in buildings.

Contents

List of Figures

List of Tables

Nomenclature

Roman Symbols

A	Matrix for the 1D discretized pure advection problem
A_{lat}	Lateral surface of each pipe discretized volume [m^2]
A_{pipe}	Pipe external surface [m^2]
b	Right-end side vector for the 1D discretized pure advection problem
c_p	Specific heat capacity [J/(kg°C)]
d_i	Pipe inner diameter
E	Energy [J]
G	Flow rate [l/h or kg/s]
h	Enthalpy [J/kg]
h_{conv}	Convective heat transfer coefficient [W/(m^2K)]
k	Thermal conductivity [W/(m°C)]
$L \ or \ \Delta h_{lat}$	Latent heat specific content [J/kg]
l_c	PCM characteristic length around each pipe [m]
M	Mass [kg]
q	Heat rate [W or W/m]
q'''	Volumetric heat generation [W/m^3]

SOC State of charge [-]

T Temperature [°C]

u Fluid velocity [m/s]

V Volume [m^3]

z Longitudinal axis

Greek Symbols

β Shape factor [-]

Δ Difference

ρ Density [kg/m^3]

τ_0 Time scale factor [s]

Superscripts

n n-th timestep

Subscripts

0 initial condition

avg average

dis discharge

in inlet

j j-th discretized element

l liquid

ls solid-liquid interface

n normalized

out outlet

pc phase change point

ref arbitrary reference condition

s solid

tot total

$wall$ contact wall between HTF pipe and PCM-HCM assembly

Acronyms / Abbreviations

$ACEME$ Automated Cognitive Energy Management Engine

$BIPV$ Building Integrated Photovoltaics

DH District Heating

HCM High Conducting Material

HP Heat Pump

HSC Hybrid Solar Cooling

HTF Heat Transfer Fluid

ICT Information and Communication Technology

$LHTS$ Latent Heat Thermal Storage

Nu Nusselt non-dimensional number

PCM Phase Change Material

Pr Prandtl non-dimensional number

Re Reynolds non-dimensional number

RET Renewable Energy Technology

$RMSE$ Root Mean Square Error

TES Thermal Energy Storage

$TopOpt$ Topological Optimization

$VAWT$ Vertical Axis Wind Turbine

Chapter 1

Introduction

1.1 Context

The increasing energy demand pushed by the unprecedented worldwide population growth rate, the rising climate concerns and the actual geopolitical situation require a radical change of paradigm in the way we produce and consume energy. Despite the efforts and pledges of numerous countries, our economy and society are still largely relying on fossil-fuels, as demonstrated by the yearly reports of the International Energy Agency [1]. To address this vital challenge, renewable energy technologies alone are not sufficient due to the intrinsic unpredictability of renewable energy sources. In this context, energy storage solutions constitute the pivotal element for sustaining the transition from a fossil fuel-based society (which can access energy whenever needed) to a renewable-based society (which would like to access energy whenever needed).

A relevant contribution might come from the building sector, which is responsible for 30% of total global final energy consumption [2]. As a mtter of fact, almost half of the energy demand for buildings was used for space and water heating in 2021, leading to 2450 Mt of direct CO_2 emissions [3]. Although low-carbon heating technologies are growing, fossil fuels still meet over 60% of the buildings heating energy demand [3]. Hence, thermal energy storage (TES) technologies can help to integrate high shares of renewable energy, increase demand flexibility and abate the dependency on fossil fuels [4]. Among the available options for TES, those based on latent heat have gained much attention in the recent years [5] and a few

companies have started investing on this type of technology. Such storage systems rely on interesting materials known as Phase Change Materials (PCMs), which are characterised by high energy density and allow charge/discharge cycles at a nearly constant temperature when transforming their state from liquid to solid and vice versa [6]. The former feature is particularly relevant for applications in the residential sector, which is generally characterised by a limited installation space for TES devices. In this context, an in-depth knowledge on how such Latent Heat Thermal Storage (LHTS) units interact with the surrounding heating system is essential.

1.2 Aims and objectives

The literature on Latent Heat Thermal Storage (LHTS) technologies is rather rich and extensive: the properties of PCMs are widely known and tested and numerous guidelines for realising efficient LHTS devices have been provided. However, the Technology Readiness Level (TRL) of these systems has hardly reached the first step of the deployment phase (level 7) [7]. Despite the great potential, only a limited number of commercial devices can be considered proven in an operational environment. This suggests that improvements to well-identified solutions could fully exploit the potential of LHTS technologies and overcome the present barriers.

Most of the research in the field addressed only two specific problems: the enhancement of the heat transfer inside LHTS units and the optimization of PCM properties. However, in these investigative approaches a crucial element is missing: the integration of LHTS devices in heating systems. This is missing both from the point of view of the optimal sizing and the optimal operation. Such a gap may be ascribed to several engineering challenges. Among these, one evidently arises: the lack of computationally fast and accurate mathematical models facilitating the incorporation of latent heat storage units into energy system simulation environments. Furthermore, a second barrier is often represented by the little knowledge on how full-scale LHTS technologies interact with the heating systems in which they are integrated. In an attempt to overcome these gaps, the following research questions are addressed in this thesis:

Q1: *Is it possible to develop a dynamic LHTS model that is fast, accurate and experimentally validated for system level simulations?*

Q2: *Can the parameters of such a model be independent on experimental calibration?*

Q3: *How can the inner heat exchanger design affect the performance of shell-and-tube LHTS units?*

Q4: *How shell-and-tube LHTS units interact with a real heating system in terms of the most relevant operational parameters (i.e. heat rate, state of charge and heating system temperatures)?*

1.3 Outline of the dissertation

Fig. 1.1 presents the outline of the present dissertation.

Chapter 2 summarises the state of the art on Latent Heat Thermal Storage (LHTS) technologies. This chapter sets the context around the research field on LHTS systems. First, a detailed background concerning the PCM thermo-physical properties and the LHTS design approaches is presented. Then, the most common modelling approaches are discussed, spanning from detailed to simplified representations. Finally, a few LHTS prototype installations are listed.

Chapter 3 thoroughly describes the design choices that led to the realization of two shell-and-tube Latent Heat Thermal Storage (LHTS) units and their relative testing system. The content of this chapter spans from theoretical and evidenced-based notions to extremely practical considerations. Both of these elements were necessary for realizing two full-scale shell-and-tube LHTS devices and install them inside a complex testing rig emulating a residential heating system. In few words, this chapter constitutes the basis to answer the research questions **Q2**, **Q3** and **Q4**.

Chapter 4 carefully presents a newly developed 1-dimensional dynamic model to simulate the behaviour of shell-and-tube LHTS units from a system perspective with a low computational effort. Particular attention is devoted to the underlying hypothesis and the model boundary conditions. In few words, the proposed modelling approach couples a 1D pure advection problem for the LHTS pipes with a mathematical description of the time-dependent heat rate released by the inner components of the LHTS during discharge (i.e. the ensemble of PCM and fins). This mathematical representation is referred as thermal power characteristic curve, allowing to map

the LHTS performance under different boundary conditions. Hence, this chapter partially answer to the research question **Q1**.

Chapter 5 completes the answers to the research questions **Q1**, **Q2** and **Q3** by presenting an experimental analysis related to the two realized LHTS units. More specifically, the 1D dynamic model is here validated and the performance of the two LHTS tanks (characterized by a diverse inner heat exchanger design) is assessed.

Chapter 6 answers to the research question **Q4** by reporting the outcomes of a EU research project known as RE-cognition. A consistent part of the PhD activities presented in this thesis were developed within this project framework, with the aim of integrating the aforementioned LHTS prototypes in one of the project pilot sites (i.e., the Energy Center, a building owned by Politecnico di Torino).

Finally, Chapter 7 draws the conclusions by discussing the achievements and limitations of this work and identifying future research opportunities.

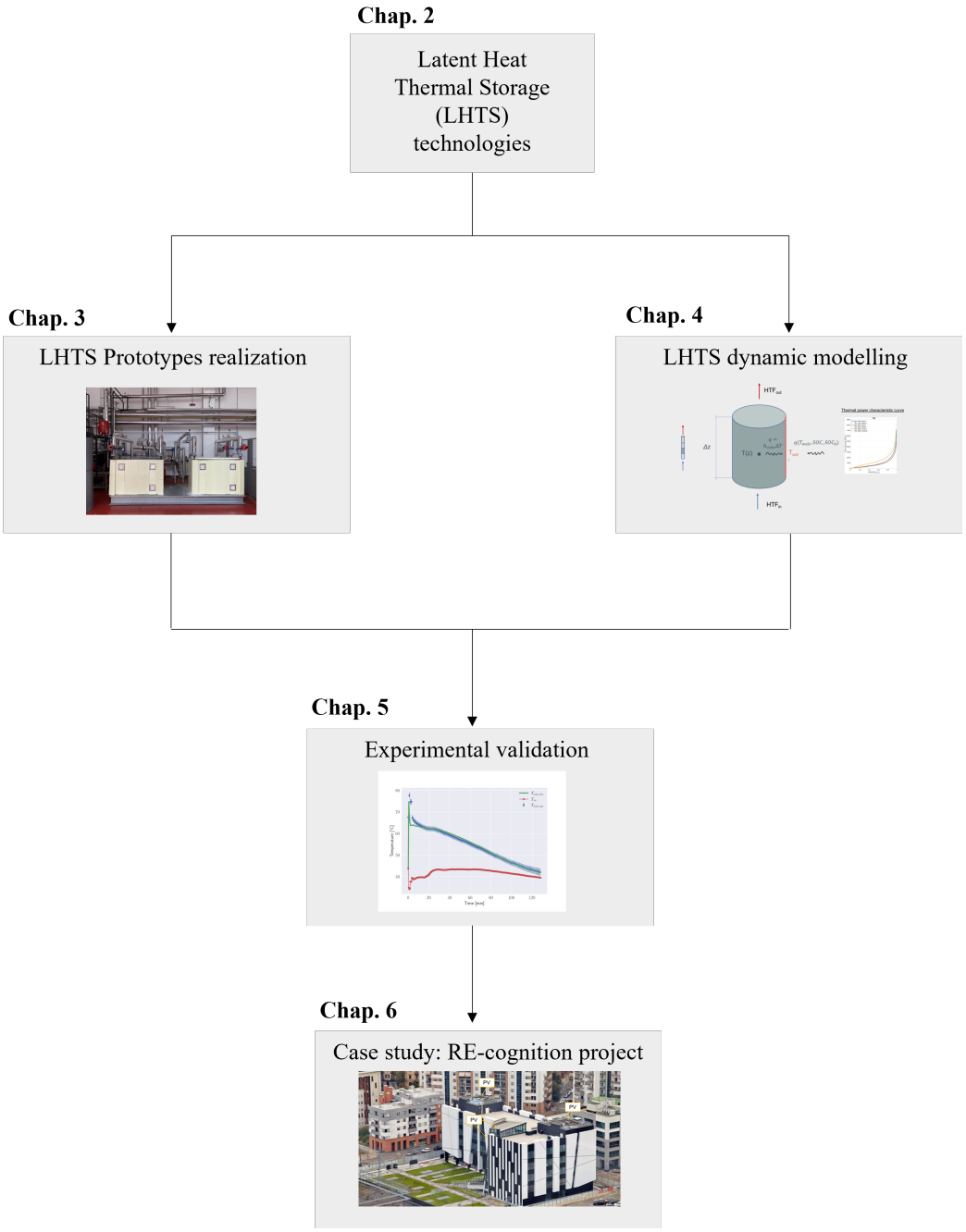

Fig. 1.1 Thesis outline

Chapter 2

State of the art on Latent Heat Thermal Storage

The present chapter aims at summarising the findings available in the scientific literature concerning the most relevant aspects of thermal energy storage by means of technologies based on latent heat. The upcoming sections are detailed as follows.

Section 2.1 sets the framework in which Latent Heat Thermal Storage (LHTS) technologies should be contextualised.

Section 2.2 provides an overview on the thermo-physical properties of the materials on which LHTS technologies are based, i.e. Phase Change Materials (PCMs). A classification for PCMs is provided and their advantages and drawbacks are outlined.

Section 2.3 contextualises the ways in which storage mediums (i.e. PCMs) and heat transfer mediums can be arranged in order to realise LHTS systems.

Section 2.4 focuses on the techniques for enhancing the heat transfer mechanism in a specific category of LHTS systems, i.e. those based on shell-and-tube heat exchangers.

Section 2.5 provides an overview on the modelling approaches for representing the thermal behaviour of LHTS systems. Both detailed and simplified modelling approaches are here discussed with examples.

Eventually, section 2.6 presents a few LHTS prototypes realizations that have been reported in the literature so far.

2.1 Overview on thermal energy storage

Space and water heating accounted for almost half of the energy demand in buildings in 2021, leading to 2450 Mt of direct CO_2 emissions worldwide [3]. As far as Europe in concerned, more than 60% of the energy for space and water heating in buildings derives from fossil fuels [3], despite the ambitious climate targets set by the European Commission. The advantage of a widespread use of boilers fuelled by fossil fuels is undeniable: end users can meet their heating needs at any time. In contrast, renewable energy sources are characterised by varying degrees of intermittency and are therefore less reliable. Even when considering urban district heating systems, the sharp increase in heating demand in the first hours of the morning leads to greater greenhouse gas emissions at the facility level [8]. In this context, the path towards decarbonisation of the heating sector needs a crucial supporting element: thermal energy storage (TES).

Before delving into the description of TES systems, it is worth mentioning the general forms of energy storage systems (ESS) documented in literature. Four main types of ESS can be identified [9, 10]: mechanical, electrochemical, chemical and thermal. Mechanical energy storage is generally used at large scale for grid applications, as they convert electrical energy into potential or kinetic energy during off-peak hours and revert this process when the electricity demand is higher. The major technologies for this application are represented by pumped hydro energy storage, compressed air energy storage and flywheel energy storage. On the contrary, electrochemical energy storage can be deployed at different scales, from small residential applications to utility scale. Such storage systems are essentially constituted by numerous types of batteries, such as lead acid, lithium based (Li metal, Li-ion, Lithium polymer), metal air, nickel based and flow batteries. A vast literature on this topic is available and the interested reader is referred for example to [11, 12]. Finally, chemical energy storage mainly concerns the production of hydrogen and biofuels whose chemical energy is subsequently released on-demand through various types of fuel cells [10].

As far as thermal energy storage is concerned, the literature [13] identifies three main options depending on the storage medium:

1. **Sensible** thermal energy storage (TES or STES);
2. **Latent** heat thermal energy storage (LHTS or LHTES);

3. **Thermo-chemical** heat storage (TCS)

Sensible thermal storage uses the energy content related to the temperature difference in solids or liquids. In this case, the amount of thermal energy stored depends on three parameters: the specific heat capacity of the medium, its temperature change and the amount of storage material. Water is often used for sensible heat storage systems due to its high availability and high heat capacity. However, when operating temperatures are above 100°C, oils, molten salts or liquid metals are preferred. For air heating applications, rock beds are often used instead. In contrast, latent heat storage utilises the large amount of energy absorbed or released by a material that undergoes a phase change from solid to liquid and vice versa. These materials are generally referred to as phase change materials (PCM). The storage capacity thus depends on the enthalpy of fusion and the amount of the chosen PCM. A wide range of materials are suitable for this purpose, as explained in more detail in the following section. Finally, thermochemical systems are based on the breaking and reformation of molecular bonds in reversible chemical reactions. In this case, the relevant parameters are the endothermic heat of reaction and the extent of transformation. Latent and thermochemical storage systems are characterised by a much greater energy density compared to sensible storage systems. Latent and thermochemical systems can store up to 4-10 times [14] more energy than sensible storage systems for the same volume (with thermochemical systems having the highest energy density). Therefore, both represent a promising technology when installation space is limited, as is often the case in urban contexts. However, thermochemical systems are still in the early development phase, while knowledge of latent storage technologies is more advanced and their Technology Readiness Level (TRL) is closer to market maturity.

2.2 Phase Change Materials

Phase change materials (PCMs) are industrial products that undergo a phase transition, generally between a solid and a liquid state. One of the characteristic features of PCMs is their ability to store and release significant amounts of thermal energy at a near constant temperature through the latent heat of fusion/solidification of the material. As depicted in Fig. 2.1, PCMs serve as a near-isothermal heat reservoir. However, the phase transition temperature is specific to each type of PCM. Therefore, the choice of PCM depends heavily on the requirements of the specific

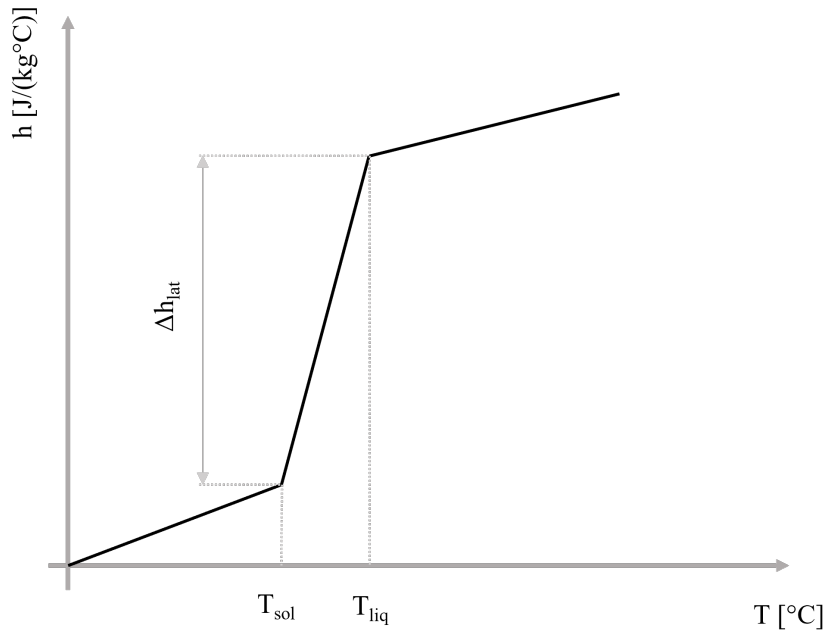

Fig. 2.1 Schematics of the enthaply-temperature relation in PCMs

application for which the PCM is intended. Thanks to these properties, the use of PCMs has often been proposed as a means of utilising excess energy and balancing the discrepancy between energy demand and supply when they do not coincide in time [15, 16]. These properties make PCMs ideal for a wide range of industrial and domestic applications.

Several characteristics should be considered when evaluating the performance of a selected PCM, including thermophysical, chemical, kinetic, environmental and economic properties [17–20]. To maximise heat storage capacity, the following properties should be carefully evaluated:

- the latent heat of fusion/solidification;
- the specific sensible heat capacity;
- the density.

As far as the latter parameter is concerned, the PCM volume change between solid and liquid phase should be kept as low as possible. Indeed, the PCM container is often oversized to accommodate the maximum volume during the liquid phase

and avoid stresses [15]. In addition, PCMs should have long-term stability. Their thermophysical properties should remain constant regardless of the number of melting/solidification cycles. When considering industrial or residential applications, safety is a priority. The materials used should be non-toxic, non-flammable and chemically compatible with their container to avoid corrosion or leakage.

From a broader perspective, the environmental impact of PCMs can be assessed through a life cycle analysis (LCA) of all phases of the product's life cycle. Several LCA studies have shown that PCM applications in buildings generally have positive environmental impacts [21–23]. In addition to the environmental impacts of PCMs, several authors have also investigated the economic feasibility of their applications in buildings. Depending on material costs and energy prices, they arrived at contrasting results [24]. Some analyses found reasonable payback periods (between two and ten years) [25–27], while others concluded that PCMs are not economically beneficial [28, 29]. As a result, PCMs are currently mainly used in research-related applications and their prices are still relatively high for broad market penetration. In general, PCMs are also characterised by some disadvantages that should be considered when selecting this type of material for a specific application. The main disadvantages can be summarised as follows:

- Low thermal diffusivity;
- Phase segregation;
- Phase separation;
- Hysteresis;
- Subcooling.

These negative properties can affect the ability of PCM to store thermal energy, as they are a source of poor stability [15, 30].

Thermal diffusivity is an important aspect to consider when evaluating the performance of phase change materials (PCMs). The homogeneity of the temperature distribution within the material is highly influenced by the thermal diffusivity, which in turn affects the use of the material's heat storage capacity. The thermal diffusivity of PCMs is generally mediocre, due to the combination of low thermal conductivity (often between 0.2 and 0.5 W/(mK)) and high specific latent heat capacity. To

address this problem, various solutions have been proposed, such as blending PCMs with additives or using extended highly conductive surfaces to improve heat transfer across the PCM layer.

Phase segregation is a consequence of non-equilibrium solidification during rapid cooling in incongruent transformations. Under such circumstances, the process of diffusion heat exchange - which is a gradual process in the solid state of the material - is not sufficient to ensure homogenisation of the composition, resulting in the formation of layered grains with an average composition that varies from the core to the edge. As a result, the solidification process is completed at a lower temperature. Unfortunately, in some cases it is not possible to change the speed of the heat transfer process and the only way to mitigate this effect is to choose other materials.

As far as phase separation is concerned, this phenomenon refers to the transformation of a single-phase system into a multi-phase system. The main cause is the gravitational effect resulting from differences in density. For example, in the case of salt hydrates in liquid form, the salt component may settle at the bottom of the mixture due to its higher density compared to water. Similarly, some mixtures of microencapsulated PCMs and water may exhibit a creaming effect, where the lighter PCM floats on the denser water matrix. These phenomena result in a two-phase system with local component concentrations that deviate from the original design, causing the overall properties of the mixture to vary and become inhomogeneous. To counteract phase separation, the most common solutions involve either mechanical mixing or the addition of surfactants and suitable additives.

Hysteresis occurs when PCMs show different behaviour during heating and cooling processes. More precisely, this phenomenon leads to different transition temperatures and latent heat capacities between the melting and solidification processes. The hysteresis is generally caused by slow crystal formation during solidification. Solutions to overcome this drawback are similar to those discussed for mitigating the phase segregation phenomenon, as both problems are related to the heat transfer rate.

Finally, subcooling occurs when a phase change material has a liquid form, even if its current temperature is lower than the solidification temperature of the material (Fig. 2.2). In fact, the solidification process begins with the formation of the first solid crystals (also called nuclei). If this process does not take place or the nucleation rate is too low, the PCM will remain liquid even at lower temperatures. As a result, the latent heat content is not released properly. However, as soon as the phase change

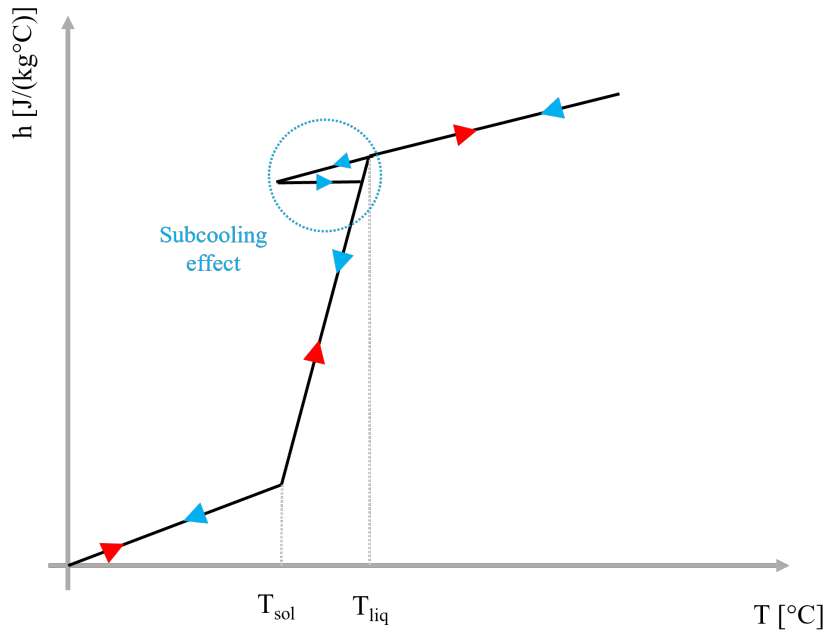

Fig. 2.2 Schematics of the enthaply-temperature relation in PCMs with subcooling effect

is activated, the temperature rises abruptly to the solidification temperature and remains almost constant until the process is completed. If the selected PCM has this disadvantage, the addition of nucleators can support the activation of the phase change process.

2.2.1 Classification of PCMs

As already anticipated, when choosing a suitable PCM for a specific application, several physical, technical, and economic requirements should be considered [15]. The physical aspects are the primary selection criteria and the ideal PCM should have a phase change temperature that matches the application, a high phase change enthalpy per unit volume, high thermal conductivity to allow the unit to be charged and discharged in a timely manner, no phase separation to maintain reversible cycles without performance degradation, and little subcooling for charge/discharge cycles over a small temperature range. The technical requirements relate to the chemical properties of the PCM [31], which should be chemically stable, non-toxic, non-flammable and compatible with the construction material to avoid corrosion. The economic requirements concern the availability of low-cost storage materials. No sin-

gle storage material satisfies all of these requirements, but PCMs can be categorized according to their physical and technical properties [32, 19, 33, 34]. Organic PCMs can be subdivided into paraffins, fatty acids, alcohols, and glycols, while inorganic PCMs are divided into salts, salt hydrates, and metallic alloys. Eutectic mixtures consist of different constituents and can be organic-organic, organic-inorganic, or inorganic-inorganic. Fig. 2.3 depicts a possible classification strategy based on chemical properties.

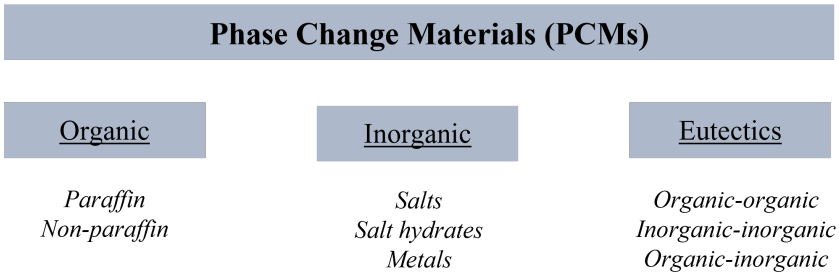

Fig. 2.3 Classification of Phase Change Materials, adapted from [34]

The melting temperature and the phase transformation enthalpy are not independent [15]. Fig. 2.4 shows that there is a rough correlation between the melting temperature and the specific enthalpy of phase transformation. Storage materials with a high melting temperature, such as salts, have a high energy density, while PCMs with a low melting temperature can only store a limited amount of latent heat during the phase transition. Table 2.1 contains typical energy density ranges of PCMs together with popular useful TES alternatives. In general, exploiting phase change can reduce the size of a water tank storage at a reference temperature difference of 20°C by at least a factor of 2.

Table 2.1 Reference energy densities of different storage materials (adapted from [36])

Material	Energy density [MJ/m^3]
Sensible storage	
Water	84 (ΔT = 20 °C)
Rocks	50 (ΔT = 20 °C)
Organic oils	30-33 (ΔT = 20 °C)
Salts	39-75 (ΔT = 20 °C)
Latent heat storage	
Paraffins	169-204
Salt hydrates	263-548
Salts	631-1584

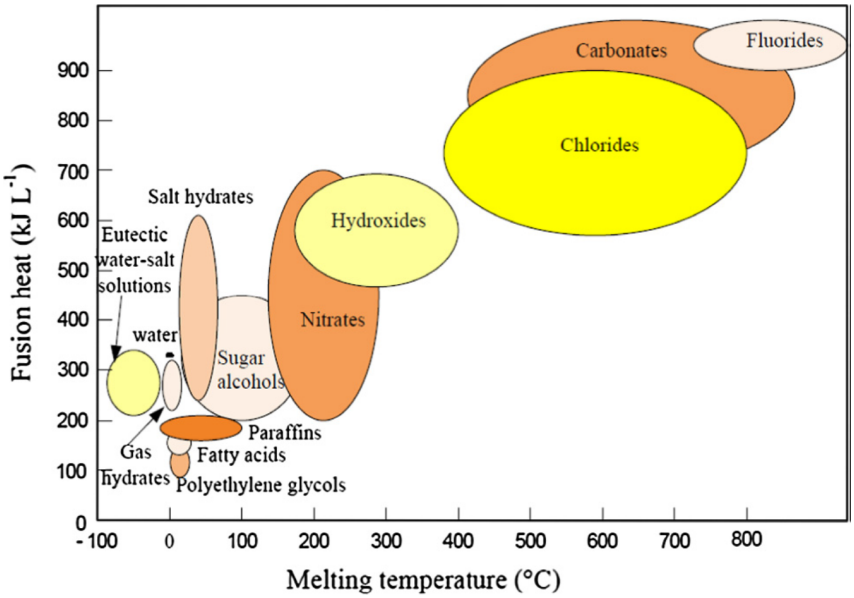

Fig. 2.4 Overview of PCMs melting temperature and enthalpy of fusion for different classes of materials [35]

Organic PCMs

The classification of organic PCMs into paraffin and non-paraffin materials has been reported multiple times in literature [15, 18, 30, 34]. Paraffin PCMs are also known as alkanes. Generally, they exhibit no phase segregation, possess high specific latent heat capacity of fusion/solidification, and have chemical stability. For these reasons

they are the most used PCMs in commercial applications. However, they have lower density than inorganic PCMs and are flammable (above 200°C). Furthermore, they are characterised by low thermal conductivity ($\simeq$ 0.2 W/(mK)), leading to reduced heat diffusion and storage capability. Additionally, paraffin materials have high volume variations during phase transition, which may not be compatible with plastic containers. In general, and the alkanes melting temperature increases with an increase in the number of carbon atoms in their molecular chain. Therefore, controlling the number of carbon atoms during the preparation process is crucial to meet the intended application requirements.

On the other hand, non-paraffin PCMs, such as fatty acids, esters, glycols, and alcohols are less commonly used due to their higher cost and corrosiveness [33]. Fatty acids have thermo-physical properties similar to those of paraffins [15]. Eutectic mixtures of fatty acids can lower the phase change temperature of pure acids without significantly affecting the enthalpy of phase change, while esters derived from stearic acid and palmitic acid have low melting temperatures and high enthalpies of phase change [37]. Some studies [38–40] reported that fatty acids and their esters have moderate thermal stability after repeated cycling, but the thermal stability of these PCMs can be impacted by impurities, as noted in [37]. Polyethylene glycol (PEG) is the most commonly used glycol PCM [15]. This is a polymer available in various grades and it is characterised by higher melting temperatures and enthalpies as its molecular weight grows. PEGs are chemically and thermally stable, as demonstrated in several experimental studies [41, 42]. Finally, sugar alcohols have not received much attention from researchers so far [43]. They have melting temperatures ranging from 90°C to 200°C and can provide high latent heat per unit volume due to their high density and specific enthalpy of phase change. However, some sugar alcohols showed poor stability to thermal cycling [44], indicating the need for further research.

Inorganic PCMs

Inorganic PCMs have some advantages compared to organic materials [32], such as lower cost, non-flammability and relatively high specific latent heat capacity of fusion/solidification and thermal conductivity ($\simeq$ 0.5 W/(mK)). Additionally, salt hydrates have lower embodied energy compared to other materials, making them a preferred choice in a Life Cycle Assessment perspective. The literature indicates that inorganic PCMs include various types such as salt hydrates, salts and metals, which

possess different properties and limitations [15, 33]. Salt hydrates refer to inorganic salts that retain a specific number of water molecules within their crystal structure. The phase change process of salt hydrates involves the hydration or dehydration reaction of the salt, either partially or totally. However, some negative properties of salt hydrates include critical supercooling effect, high volume change during phase transition, phase separation and corrosiveness towards metals [45, 46, 41, 15]. Salts, on the other hand, are considered suitable for high- temperature applications due to their high melting temperatures [47]. However, their thermo-physical properties vary substantially depending on the type of salt and compatibility problems with some common heat transfer fluids have been reported [47, 48]. Finally, while metal and metal alloys have a high density, which can complicate the design of containers, they have a melting enthalpy per unit volume comparable to that of salts [49] and exhibit a high thermal conductivity, allowing for fast charge and discharge kinetics without the need for heat transfer enhancement systems [34]. However, the lack of a comprehensive database of thermo-physical data for metallic materials complicates their selection for thermal energy storage purposes [34].

Eutectic mixtures

As reported in the literature [18], eutectic PCMs are a combination of two or more components in a wide range of proportions that typically do not interact with each other from a chemical point of view. This mixture forms a new compound that undergoes a congruent melting with the formation of two separate solid phases at a lower temperature than that of each individual component. Eutectic mixtures possess a sharp melting point similar to pure substances. However, their application in building systems is very limited and there are only a few studies available in the literature that report their thermo-physical properties.

2.2.2 Phase change temperature selection

According to various review papers such as those by Agyenim and Hewitt [50], Rathgeber et al. [51], Zhao and Wang [52], Cunha and Eames [53], Salunkhe and Jaya Krishna [54], and Huang et al. [55], phase change materials (PCMs) used in heat storage applications must possess certain properties such as thermo-physical, kinetic, chemical and economic properties. However, the selection of suitable PCMs

for a specific application should primarily consider the phase-change temperature range to ensure adequate phase transition during thermal cycling. As a matter of fact, Agyenim [56] proposed a classification of PCMs based on their melting temperature, arguing that this criterion is directly linked to the applications. In general, storage materials with low melting temperatures (Tm < 65°C), such as water, water-salt solutions and all organic PCMs, are suitable for domestic heating and cooling, storage of off-peak electricity and integration in building materials. Indeed, this temperature range is the most extensively investigated [56]. Materials melting at intermediate temperatures (80°C < Tm < 120°C), such as some paraffins, sugar alcohols, and some salt hydrates, are used for storage on the evaporator side of LiBr-H_2O absorption cooling systems or for storage in large district heating networks [57]. Storage materials with high melting temperatures (Tm > 150°C), such as salts, salt eutectics and metals, can be used in storage units connected to CSP plants or industrial waste-heat recovery systems [49].

As far as space heating systems are concerned, their operating temperature depends on various factors such as the heat transfer media, the heating terminal devices, the heat generation devices and also the thermophysical characteristics of the building envelope. The temperature required at the demand side is determined by the comfort requirements, while the temperature at the source side depends on the heating source in the system. As a general trend, when fossil fuels constitute the heat source, the temperature difference between the source and the thermal comfort range is extremely high. Hence, the group of suitable PCMs is broad but also the competition with hot water storage systems increases [15]. When considering solar heating, instead, the choice is restricted due to the fact that the higher the selected phase change temperature, the higher is also the temperature at the collector outlet. This might have a detrimental effect on the solar collector's efficiency [15]. Several recommendations concerning PCMs transition temperatures can be found in the literature for different residential heating systems. For instance, Agyenim and Hewitt [50] suggest PCMs with a melting point in the range of 50°C to 60°C for coupling with the hot side of a domestic heat pump (HP). Similarly, Rathgeber et al. [51] recommend a melting point of at least 45°C for integrating heat pumps in space heating systems. For solar heating systems, instead, Salunkhe and Jaya Krishna [54] propose PCMs with a melting point of 25°C to 35°C. Further examples are also collected in Table 2.2, which shows how different PCMs were selected according to the intended application. This table shows how the choice is extremely

case-sensitive. The combination between heat pumps and LHTS systems appear particularly flexible thanks to a plethora of refrigerant fluids available for HPs. Hence, these two technologies can be adapted to a wide range of operative temperatures. On the contrary, the use of LHTS units in residential solar systems is generally restricted to medium-to-low temperatures (45°C – 55°C). Similarly, the deployment of LHTS units in combination with micro-CHP or DH systems is shifted towards higher operative temperatures (> 65 °C).

Table 2.2 Examples of phase change temperature selection (T_{pc}) according to the intended application (adapted from [58])

PCM	T_{pc} **[°C]**	Δh_{lat} **[kJ/kg]**	**Application**	**Ref.**
Inorganic	29	191	HP	[59]
Organic	40	220	HP	[60]
Inorganic	46	210	HP	[61]
Inorganic	46	210	HP, solar	[62]
Organic	47	142	HP	[63]
Inorganic	48	210	HP	[64]
Inorganic	48	201	HP	[65]
Organic	49	180	HP	[66]
Organic	50	200	HP, solar	[67]
Organic	52	168	solar	[68]
Inorganic	52.4	220	solar	[55]
Inorganic	53	224	HP	[69]
Organic	54	200	HP, solar	[53]
Inorganic	58	266	HP	[70]
Organic	58	172	HP	[50]
Inorganic	58	266	HP	[69]
Organic	61	222	HP	[69]
Organic	64.5	208	micro-CHP	[71]
Organic	70	260	DH	[72]

2.3 Types of Latent Heat Thermal Storage systems

The general problem of heat transfer from source to storage and from storage to sink can be addressed in three basic ways according to Mehling and Cabeza [15] (Fig. 2.5):

- exchanging heat at the surface of the storage;
- exchanging heat on large surfaces within the storage;
- exchanging heat by exchanging the storage medium.

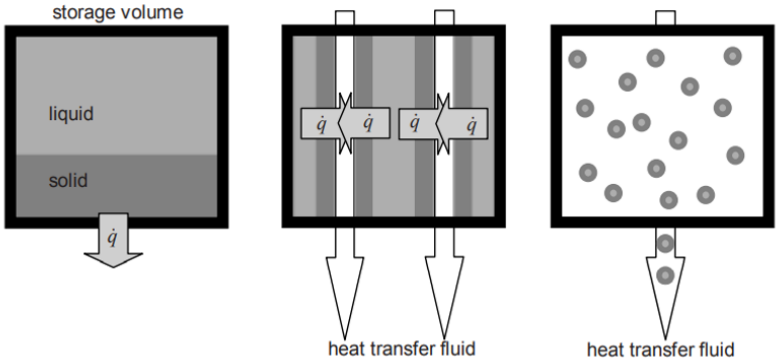

Fig. 2.5 Schematics of the heat transfer process for different LHTS concepts [15]

The former strategy is generally adopted in well-insulated transport box for temperature-sensitive goods, ice packs for cooling injuries, pocket heaters, or to prevent the overheating of an electronic component. For this reason, these types of storage are not further treated in this chapter. The second type of heat transfer solution mostly involves heat exchangers and module type storage units using macro-encapsulated PCMs. The difference between these two concepts is graphically represented in Fig. 2.6. Finally, the latter type of solution mostly concerns slurry type storage systems.

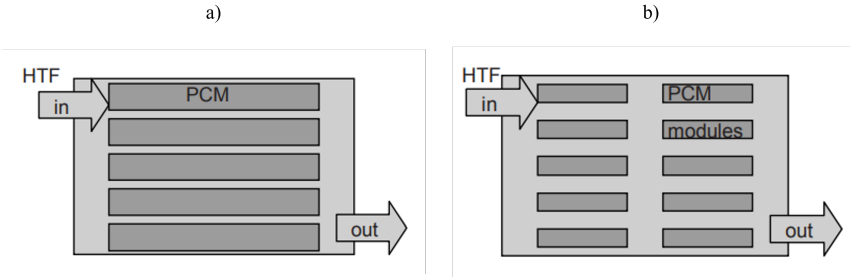

Fig. 2.6 Schematics of the concept behind the LHTS heat exchanger type (a) vs PCM module type (b) [15]

The module type storage is based on macro-encapsulated PCM modules for heat storage. As demonstrated by Mehling and Cabeza [15], the utilization of macro-encapsulated PCM modules offers significant advantages in both manufacturing and marketing. This is because the PCM operating problems, such as volume change and heat exchange, can be addressed through the module geometry. As a result, the macro-encapsulated PCM module can be considered a stand-alone product with its own warranty. Moreover, the storage design highly versatile. These PCM modules often take the form of macroencapsulated bags, flat plates, dimple sheets, or spherical capsules, with the latter being the most popular option due to their ability to self-arrange when filled into a tank (thus achieving a maximum package density of 74 vol.%). This type of storage can combine latent heat with a significant fraction of sensible when the heat transfer fluid is constituted by water, water-salt, or water-glycol mixtures (over 25 vol.%). Instead, when air is the heat transfer fluid, however, flat plates, bags, or dimple sheets are preferred because of their larger surface-to-volume ratios. However, it should be noticed that varied geometries and sizes of modules, HTF flow rates, and application-specific boundary conditions can complicate the storage operation.

A storage system using a heat exchanger consists of a storage vessel containing the storage medium (the PCM) and an internal heat exchanger. The heat transfer fluid, such as water, flows through the heat exchanger and exchanges heat with the phase change material (PCM) in the storage vessel. The heat exchanger typically comprises several pipes evenly distributed throughout the storage volume (shell-and-tube type). This type of storage has several distinguishing characteristics. For instance, the storage density is generally high considering that up to 95% of the volume can be occupied by the PCM. The pipes of the heat exchanger are filled with a flowing

HTF, leading to very high power at the beginning. The time evolution of the thermal power then depends mainly on the design of the heat exchanger. The heating or cooling power of the storage is proportional to the HTF's heat capacity, volume flow rate, and temperature difference between inlet and outlet. If we assume that the volume flow rate and heat capacity remain constant, the power is proportional to the temperature difference between inlet and outlet. At the beginning of the discharging phase, cold heat transfer fluid enters at the inlet section leading to a peak in the outlet temperature. Once the sensible heat stored above the phase change temperature is extracted from the storage material, the outlet temperature falls below the phase change temperature. The release of the latent heat slows down the temperature drop. Two main thermal resistances come into play: the constant thermal resistance in the heat transfer fluid and heat exchanger wall and the increasing thermal resistance in the PCM. If the thermal resistance in the PCM, which increases with time, is small, the constant thermal resistance in the heat transfer fluid and heat exchanger wall is dominant and leads to a transient plateau in in the outlet temperature and thermal power. Usually, the thermal resistance within the PCM has a significant contribution, causing the power and outlet temperature to decrease gradually.

To conclude this general overview on LHTS typologies, the main features of slurry storage systems are here summarized. This novel concept involves the creation of a two-phase fluid by mixing a carrier fluid with a dispersed PCM. Typically, water is used as the carrier fluid due to its high thermal conductivity, high specific heat capacity, good compatibility with PCMs, ease of handling, low cost, and environmental safety [73]. This two-phase fluid is referred to as a PCM slurry and has the benefit of preserving the high thermal inertia of PCMs while increasing the thermal diffusivity through convection in the carrier fluid. Additionally, the slurry reduces phase segregation and subcooling phenomena, making it a suitable choice for various applications, including active systems like latent heat thermal energy storage, heat exchangers, and thermal control systems. The literature identifies five types of PCM slurries [74]. These include ice slurries, where ice particles are dispersed in a water carrier fluid; PCM micro-emulsions, where the PCM is homogeneously mixed with the carrier fluid using an emulsifying agent; mPCM slurries, where mPCM capsules are dispersed into a carrier fluid (usually water); clathrate hydrate PCM slurries, which are composed of a host molecule of water molecules forming a woven structure that accommodates molecules of another substance (guest molecule); and shape-stabilized PCM slurries, which are mixtures based on shape-stabilized PCM.

There are several in-depth and comprehensive reviews available in the literature that discuss PCM slurries. These reviews cover a wide range of topics related to these materials, including the methods used for preparing them, as well as the definition of their thermal and rheological properties [73–77]. However, since this work deals with heat exchanger type latent heat thermal storage systems, PCM slurries are not assessed further.

2.4 Shell-and-tube LHTS fins design approaches

Among the various LHTS alternatives presented in 2.3, the two most suitable LHTS solutions for space heating applications are arguably the heat exchanger and the module type storage units. The shell-and-tube heat exchanger type of LHTS is a well-studied configuration, as evidenced by the literature [78]. In general, this configuration is favored due to its many advantages, including its straightforward design, cost-effectiveness, low pressure drop [79, 80], large heat transfer area, high discharging power, and overall high effectiveness [81]. As a result, the shell-and-tube type of LHTS is widely employed and considered to be the most commonly used configuration [82]. Indeed, this thesis is focused on the modelling, realisation and experimental characterisation of two shell-and-tube LHTS units. For this reason, this section provides an overview on the design approaches suitable for such a configuration.

The design of shell-and-tube LHTS is a complicated process encompassing a wide range of issues [83]. However, the geometric design is generally the most crucial aspect. As already anticipated, most of the PCMs possessing a practical interest have low thermal conductivity. This limits the amount of energy that can be transferred between the HTF flowing in the pipes and the PCM in a useful time span. Consequently, the optimal design of extended high conducting surfaces around the HTF pipes is essential to reduce the average diffusion distance between the HTF and the PCM. As a result, the optimization of fins' shape has been a subject of great interest in the heat transfer community for several decades. Numerous comprehensive reviews of this topic, ranging from material preparation methods to thermal and rheological properties, can be found in the literature. As a general trend, recent studies focused on five fin layouts [36]:

- Longitudinal
- Circular
- Y-shaped or tree
- Pins
- Helical

Longitudinal fins are the most used extended surface geometry in LHTS, accounting for over 60% of installations [84]. According to Khan et al. [85], an accurate design of longitudinal fins is crucial for performance in shell-and-tube systems. In particular, they found that it is more advantageous to increase the fin length rather than thickness. However, longitudinal fins tend to inhibit natural convection in liquid PCM, resulting in slower charging rates [86]. Fins occupying 60% of the annular distance were recommended for free cooling by Solomon [86]. Darzi et al. [87] found that longitudinal fins are highly effective for solidification but yield negligible contribution for melting, while Beck et al. [88] recommended designs that guarantee unrestricted natural convection for improved melting rates. Research by Yuan et al. [89] and Kazemy et al. [90] identified an optimal tilt angle of longitudinal fins that enhances convective transport. Experiments conducted by Liu and Groulx [91] showed that four diagonal fins yield reduced melting time compared to two horizontal and two vertical fins, with negligible differences in performance for solidification.

Circular fins were not as widely studied as longitudinal fins for LHTS. However, the simple layout and ease of manufacturing of circular fins has motivated the development of this concept, as evidenced by the large number of recent studies [92]. Wang et al. [93] investigated the effect of fin pitch, height, and thickness and found that small inter-fin distances yielded a larger effect of fin height than thickness. The authors of [94] recommended a specific fin number, thickness, and inter-fin distance based on a parametric study of natural convection in vertical units that minimized melting time. Jmal and Baccar [95] noticed a similar trend for solidification in air-PCM units. Kuboth et al. [96] showed numerically that varying the fin density distribution along the HTF pipe is beneficial for performance and recommended increasing the fin density linearly from the inlet to the outlet using a growth factor of 10.

Pin fin geometries were first used as heat transfer enhancers in PCM for electronics cooling applications. In a recent review [84] on heat transfer enhancement in LHTS, this layout is only listed as a suitable alternative to plate fins for maximum heat dissipation in heat sinks, and no reference to studies in the field of LHTS is given. However, there are two examples of applications to thermal storage units. Bruno et al. [97] were the first research group to consider external pins attached to the HTF pipes, and their work reported reduced performance compared to circular fins. A similar conclusion was drawn by the authors of [98], where the pin fin effectiveness was calculated to be lower than that of annular fins. However, it is essential to keep the amount of HCM constant when comparing alternative configurations [97, 98], and natural convection must be considered since pins allow nearly unrestricted motion of buoyant eddies [97].

The development of Y-shaped or tree fins was motivated by the need for performance improvement of longitudinal fins. Sciacovelli et al. [99] used a response surface optimization method to optimize the fin length and bifurcation angle and found that the discharge efficiency can be increased by 24% if optimal fins with two bifurcations are chosen. In a recent development [100], the authors obtained an optimized tilt angle along the longitudinal direction such that the solidification time is reduced. Lohrasbi et al. [101] also adopted the same optimization approach to optimize V-shaped geometries where the bifurcation of the Y geometry is in contact with the HTF pipe. Recently, researchers have started to consider more unconventional geometries, such as the snowflake-shaped fin geometry parametrized by the authors of [102], which reported significant performance improvements compared to conventional longitudinal fins. Similar structures were obtained by a group of authors at the Institute of Engineering Thermodynamics (DLR Germany) [103], who later analysed also the effect of different fins design and axial distance through a thorough numerical investigation [104].

Another option that researchers have recently started to consider is represented by helical fins. Rozenfeld et al. [105] proposed a helical fin layout that yielded an increased melting rate with respect to conventional alternatives. Furthermore, it demonstrated practical advantages such as the prevention of voids in solidification, prevention of large pressures in melting, and ease of maintenance. The same geometry was previously considered by the authors of [88], whose numerical results suggested that the helical configuration is responsible for a small performance reduction compared to simple longitudinal fins.

The fin design guidelines mentioned above rely on a pre-defined fin shape and, thus, may not lead to the best overall performance achievable with a given amount of PCM and HCM. In this regard, topology optimization has emerged as a promising approach for innovative LHTS design, enabling the optimal distribution of material to enhance performance [106, 107]. Topology optimization provides design freedom, and various methods can be used to achieve optimal dissipative HCM structure. For example, sizing optimization involves optimizing the number and thickness of bar connections, while shape optimization involves drilling "holes" in an HCM block to determine the optimal shape and size of each hole. However, both methods rely on a fixed number of holes determined a priori. In contrast, topology optimization identifies the optimal shape without prior assumptions. With such a modelling approach, the simulation begins with a computational domain made of artificial material with average properties of the PCM and HCM. As the optimization process proceeds, some areas of the domain evolve towards PCM, while others evolve towards HCM.

To conclude this section, it should be mentioned that when realizing a shell-and-tube LHTS unit several practical aspects must be considered. More specifically, the ideal fins design might be adapted to real-world constraints and cost-performance trade-off. These practical aspects are deepened in Chapter 3.

2.5 State of the art on LHTS modelling

The phase change process involves a moving boundary (∂D_{ls}) that separates the liquid domain (D_l) from the solid domain (D_s). A simplified sketch of this process is presented in Fig. 2.7.

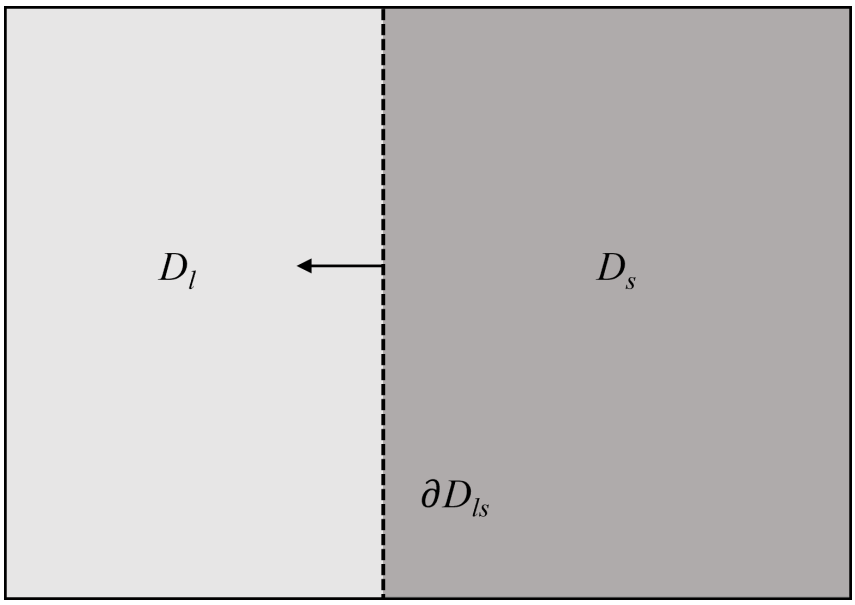

Fig. 2.7 Schematics of the solid-liquid interface during the PCM phase change process (adapted from [36])

The full modelling of this process is rather complicated, however assuming negligible advective transport, constant density, constant specific heat, and a precise melting temperature, the thermal response of this phenomenon can be described through the following equations:

$$\rho_s c_{p,s} \frac{\partial T}{\partial t} = \nabla \cdot (k_s \nabla T) \qquad in \;\; D_s, \tag{2.1}$$

$$\rho_l c_{p,l} \frac{\partial T}{\partial t} = \nabla \cdot (k_l \nabla T) \qquad in \;\; D_l, \tag{2.2}$$

$$T = T_{pc} \qquad on \;\; \partial D_{ls}, \tag{2.3}$$

$$k_s \nabla T - k_l \nabla T = \rho_s \Delta h_{lat} u_{\partial D_{ls}} \qquad on \;\; \partial D_{ls} \tag{2.4}$$

where T is the temperature, ρ_s and ρ_l are respectively the solid and liquid densities, $c_{p,s}$ and $c_{p,l}$ are the solid and liquid specific heat capacities, k_s and k_l are the conductivity tensors of the solid and of the liquid phases, Δh_{lat} is the latent heat per unit mass, $u_{\partial D_{ls}}$ is the normal propagation velocity of the solid-liquid interface

and T_{pc} is the average phase change temperature. The heat diffusion in the solid and liquid domains is respectively described by equations Eq. 2.1 and Eq. 2.2. The phase change front is identified by Eq. 2.3. Finally, Eq. 2.4 is generally known as the Stefan condition [108], representing the heat balance at the moving interface.

During the late 19th century, Stefan developed an analytical solution for diffusive isothermal melting in a semi-infinite 1D medium with constant thermo-physical properties under the assumption of a single phase [109]. This solution only applies when only one phase is present, which is the case when the initial temperature of the medium corresponds to the melting temperature [109]. In dimensionless units, the velocity of the interface is determined by the Stefan number ($Ste = (c_p \Delta T_{pc})/\Delta h_{lat}$). Neumann later extended Stefan's work to include two-phase melting problems when the initial temperature field is below the melting temperature [109]. Unfortunately, the analytical solutions for the Stefan problem only apply to semi-infinite problems with constant thermo-physical properties and homogeneous initial conditions. To increase the flexibility of the problem formulation, approximate analytical methods have been developed. One such method is the heat balance method proposed by Godman et al. [110], which involves selecting an approximating function for the temperature that satisfies the boundary conditions (e.g., polynomial or trigonometric series), integrating in space to obtain an Ordinary Differential Equation (ODE), and solving the ODE in time. The authors adopted a thermal layer approach, similar to the boundary layer in fluid mechanics, which allowed the integration domain to be restricted. This assumption is based on the fact that a sudden temperature change at a boundary is not immediately felt throughout the medium [110]. While approximate analytical methods can handle more complex boundary conditions, choosing an appropriate approximating function is challenging and may be prohibitive in multi-dimensional problems.

To solve phase change problems of practical interest, numerical methods have been developed, which can be classified into two broad categories: fixed grid and deforming grid methods. Fixed grid methods enable the solution of the Stefan problem on a (structured) spatial grid that does not conform to the solid-liquid interface. Examples of such methods include enthalpy-based and immersed boundary techniques [109]. In contrast, deforming grid methods dynamically adapt the spatial or temporal grid to conform with the regions occupied by the two phases. Gupta et al. [111] proposed a variable time-stepping strategy to keep a fixed spatial mesh and move the boundary of one mesh element during each time-step, but this approach is

not suitable for multi-dimensional problems with complicated domains. The dynamic adaptation of the space grid is typically used in the Finite Element Method (FEM) community [108], with examples including [112–115]. Although deforming grid methods are more accurate, they are computationally expensive [108], and the choice of the deformation direction is critical for the method's accuracy and stability, as grid distortions and highly skewed elements must be avoided. Additionally, variable-grid methods may be challenging to use in problems with non-smooth solid-liquid interfaces or without a sharp phase change temperature [116]. In the following subsections, the three most common fixed grid approaches are summarized. These are: the enthalpy method, the apparent heat capacity method, and the source method.

2.5.1 The enthalpy method

The governing equation on which the enthalpy method is based is the following:

$$\frac{\partial h}{\partial t} = \nabla \cdot (k \nabla T) \tag{2.5}$$

In Eq. 2.5 the total enthalpy per unit volume is defined according to Eq. 2.6, where T_{ref} is the reference temperature adopted for the enthalpy calculation and f is the PCM liquid fraction (whose value is always comprised between 0 and 1).

$$h = (1-f)\int_{T_{ref}}^{T} \rho c_{p,s} d\tau + f\left(\int_{T_{ref}}^{T} \rho c_{p,l} d\tau + \rho \Delta h_{lat}\right) \tag{2.6}$$

This method was originally developed by Voller et al. [117]. In this study, the authors noted that, in cases where subcooling and phase separation are negligible, the liquid fraction can be expressed as a function of the temperature alone. The authors also demonstrated that Eq. 2.5 can be derived from the Stefan problem. This formulation provides several advantages over the original Stefan problem. It reduces a two-region problem to a single-region problem with a single governing equation, which does not require the tracking of the melting front and satisfies the interface condition (Eq. 2.4) implicitly. The interface location can be calculated as a post-processing step. This formulation can also handle phase change phenomena that do not result in a sharp interface. To solve Eq. 2.5, an energy-enthalpy relation needs to be defined, and a popular approach is to use the enthalpy as the primary

state variable. In this case, the temperature can be updated at each time step based on the current enthalpy field, and the enthalpy field can be computed based on the diffusive term assembled in the previous step. The enthalpy-based approach has an advantage over temperature-based methods, as the temperature-enthalpy relation is continuous even in the case of isothermal phase change.

2.5.2 Apparent heat capacity method

The technique of modeling phase change using the apparent heat capacity involves increasing the specific heat of the PCM. In the absence of convective transport, the governing equation becomes a nonlinear Fourier equation (Eq. 2.7), with the term c_a representing the apparent heat capacity. This term preserves the nonlinearity resulting from the liquid fraction, f, in the enthalpy-temperature relation [11].

$$c_a \frac{\partial T}{\partial t} = \nabla \cdot (k \nabla T) \tag{2.7}$$

Dividing equation Eq. 2.5 by Eq. 2.7 gives equation Eq. 2.8, which does not require auxiliary variables and is formulated as a function of a single state field, i.e. temperature [118].

$$c_a = \frac{\partial h}{\partial T} \tag{2.8}$$

This method is widely used in literature and can be easily incorporated into existing numerical codes. However, obtaining the apparent heat capacity through analytical differentiation of the enthalpy-temperature relation may lead to numerical problems, especially in cases where $h(T)$ contains jump discontinuities, as in isothermal phase change. To overcome this issue, a common approach is to smear the discontinuity to allow for differentiability, for example, by considering a constant specific heat in each phase. It is crucial to take special care in selecting the time-marching scheme to avoid inaccuracies, as a small timestep value can lead to large nonlinearities that may affect the convergence of the iterative solution procedure. Moreover, a steep c_a spike may cause the latent heat effect to be lost completely in the time-marching process [118].

2.5.3 Source method

The technique known as the source method is used to model the latent heat nonlinearity through a source term [117]. This method is based on the idea that a melting or solidification body acts as a thermostat that absorbs or releases energy from the system. When convective transport is negligible, the governing equation can be simplified to Eq. 2.9.

$$\rho c_p \frac{\partial T}{\partial t} = \nabla \cdot (k \nabla T) - \rho \Delta h_{lat} \frac{\partial f}{\partial t} \tag{2.9}$$

Unlike the apparent heat capacity technique, the source method does not require the use of artificial smearing to deal with the melting temperature range. However, the liquid fraction field f must be computed at each time step. Iterative methods similar to those used for the enthalpy method have been developed to solve the source method, with the earliest methods having robust but slow convergence [117]. Voller and Swaminathan [119] presented an improved iteration method that has faster convergence.

2.5.4 Simplified modelling approaches

As demonstrated by De Gracia and Cabeza [120], the use of enthalpy method is a widely used approach for predicting the thermal performance of LHTS units. However, this approach requires detailed numerical models able to capture the intrinsic physical complexity of the phase change phenomenon [121]. Moreover, most of the numerical models available in literature are focused on LHTS design optimization with the aim of enhancing the heat transfer between the PCM and the heat transfer fluid (HTF). For instance, Niyas et al. [122] performed a numerical study of a shell-and-tube LHTS prototype filled with PCM salts with a full 3D model. Using commercial software based on a finite element scheme, they determined the optimal number of HTF tubes and longitudinal fins per tube that minimizes the overall discharging time. They also monitored a few performance parameters of the identified configuration, such as the melting fraction, charging/discharging times, outlet HTF temperature, and energy stored. Then, results were validated with experiments [123] showing good agreement. Esapour et al. [124] developed a detailed 3D in-house code to study the performance of an annular LHTS with

multiple tubes. They determined the effect of the arrangement and number of pipes on the liquid fraction and melting time. Successively, the same model [125] was also adopted to investigate the influence of variable operational parameters such as HTF inlet temperature and flow rate on the LHTS performance. Similarly, Saddegh et al. [126] compared the thermal behavior of a shell-and-tube LHTS using a 2D conduction–convection heat transfer model for two different LHTS orientations (vertical and horizontal). Also Sciacovelli et al. [99, 127, 128] often relied on a two-dimensional LHTS cross-section model for fins optimization, solving the underlying equations with a commercial finite volume code. A comprehensive review on the numerical modelling approaches available in literature can be found at the following reference [129].

However, when addressing dynamic heating system simulation, simplified but accurate models are necessary to reduce computational time [130] through an approximation of the temperature gradients in the PCM domain [131, 132]. For instance, Parry et al. [133] adopted the following simplification approach: a 3D computational model for a shell-and-tube LHTS was calibrated with experimental results. This was successively reduced to a one-dimensional radial model by employing an effective diffusivity technique. According to the authors, this model is suited to predict performance over long-time spans. Neumann et al. [134] coupled a 1D model for the heat exchanger tubes and a reduced 3D model for the PCM and fins. This model can be used to improve the geometric and operational parameters of fin-and-tubes LHTSs with a limited computational effort, although the PCM parameters should be carefully calibrated. An original simple model was proposed by Tay et al. [135]. This is based on the effectiveness-number of transfer units, and it was calibrated on a tube-in-tank salt-based PCM system with radial circular fins. The correlation proposed by the authors is semi-empirical, and it can be used for sizing and optimizing LHTS systems. A further interesting simplification methodology was suggested by Johnson et al. [136]. First, they analyzed the heat transfer properties of a tube assembly cross-section through a 2D finite volume model. Then, they produced a 1D radial model in Dymola for the ensemble of PCM and fins able to yield comparable results. Finally, they coupled this latter model with a 1D axial model for the HTF again in Dymola and studied the time evolution of the thermal heat flux for different configurations. Although these studies present fast and simplified models, they still address the challenge of optimal LHTS design. Only recently, a few studies produced one-dimensional models with the aim of simulating the LHTS performance in the

broader context of energy systems. For instance, Waser et al. [137] proposed a mathematical modelling approach to be implemented in commercial software packages such as TRNSYS or Simulink for system level performance investigation. A few other dynamic simulations can be found in literature [61, 70, 138], although these mostly concern LHTS units with encapsulated PCM.

2.6 LHTS prototypes and system integration

Several reports have assessed the Technology Readiness Level (TRL) of PCM and LHTS systems for heating and cooling applications. For instance, IEA Annex 33 Task 58's final report published in 2020 suggests that the TRL of several lab based LHTS varies from 5 to 7, while only a few commercial solutions can be considered proven in an operational environment [7]. In 2017, the European Association for Storage of Energy (EASE) and European Energy Research Alliance (EERA) defined the TRL of salt hydrate and paraffin-based systems comprised between 6 and 8 since some solutions had already reached partial commercialization in real applications at the time [139]. However, the report also noted that active LHTS systems with controllable heat transfer power were still absent from the market.

Recent studies have reported on the actual operation of commercial LHTS installations, but studies for space heating applications are limited, with only a few papers in the literature. For example, a case study on a commercial building in China analysed peak-load shifting patterns in a heating system integrated with a 2-MWh LHTS unit for a continuous operational period of 22 days [140]. The presence of such an important LHTS system allowed to cut the operating costs for heating by 45% exploiting the lower electricity prices during off-peak hours to activate the electric boiler supplying the heating system. Despite an actual loss in the effective storage capacity due to insufficient charging, this study claims that such an installation can be paid back within 2 years.

Another realization example was proposed by Bentivoglio et al. [72], who presented the thermal performance of a LHTS unit integrated into a novel urban heating network. The authors showed the charging/discharging operation of a 180-kWh demonstrative LHTS system installed in a substation of a residential district heating network in France. The HTF inlet flowrate was controlled to maintain constant charging/discharging power at different levels ranging between 25 kW

and 100 kW. Nevertheless, incomplete solidification and lower-than-designed peak discharge power were observed because of the real HTF inlet temperature, which was higher that expected. More specifically, the return temperature in the heat distribution system exceeded by 10°C the design level, thus significantly reducing the temperature difference driver the discharging process.

A further large-scale example was realized by Laing et al. [141], although this was integrated in a 1 MW pilot direct steam generation power plant in Spain. The prototypal 700 kWh PCM storage module was intended for evaporating water both in constant and sliding pressure mode. The authors successfully tested this component under three different operational modes: once-through, natural circulation and forced circulation. All these modes were feasible and showed great potential for future cost reductions assuming an upscaling of the whole storage system. In particular, the presence of such a large LHTS unit could allow the elimination of either only the recirculation pump or even the complete circulation cycle including the steam drum.

Finally, an interesting lab-scale LHTS prototypal realization was presented by Xu et al. [142]. This study focuses on the performance of numerous ellipsoid-shaped macro-encapsulated PCM components filling a water tank with a total volume of 0.382 m^3. Different HTF inlet flow rates were tested and the HTF temperature increase across the tank was reported. Furthermore, this lab-scale prototype was used to validate a one-dimensional packed bed model that was later used for analysing the LHTS-HP interaction in a residential heating system [143].

Chapter 3

Design and realization of two shell-and-tube LHTS prototypes

This chapter is dedicated to the description of the design choices that led to the realization of two shell-and-tube Latent Heat Thermal Storage (LHTS) units and their relative testing system.

Section 3.1 explains the rationale behind the storage units conceiving and design. The features of their constituting materials are thoroughly presented and discussed in light of their intended application. Moreover, a detailed subsection is dedicated to the process that led to the definition of the extended surfaces for the heat exchanger pipes.

Section 3.2 reflects on several practical considerations that had to be made in order to realize the two storage prototypes. First, the pipes arrangement and distribution are analysed. Then, the filling procedure is summarised. Finally, the overall geometrical storage specifications are provided.

Section 3.3 punctually describes the laboratory experimental facility used to test the two LHTS tanks. All the features of the system mechanical and digital components are presented and contextualized.

Eventually, section 3.4 summarises the key findings of this chapter.

Some portions of this chapter were already presented at the following conference:

- *35th International Conference on Efficiency, Cost, Optimization, Simulation and Environmental Impact of Energy Systems (ECOS 2022)*, held in Copenhagen from 3rd to 7th July 2022.

Moreover, part of this chapter was also used to produce the following deliverables of the European project RE-cognition (grant number 815301):

- *D2.4: Optimized Latent-Heat based Thermal Energy Storage technology*
- *D2.9: Optimized Latent-Heat based Thermal Energy Storage technology (v2)*

3.1 Rationale behind LHTS prototype design and realization

When considering the LHTS for supporting users' peak thermal demands in district heating networks, a highly desirable feature is represented by a fast-discharging process (< 1h – 1.5h). The previous literature review showed how several design concepts (micro and macro encapsulated, shell-and-tube, etc.) can be adopted in the realization of a latent heat thermal storage unit. Among these alternatives, the shell-and-tube proved to guarantee such a performance if well designed. For this reason, this type of design was selected to realize two LHTS prototypes characterised by a different disposition of the fins around the pipes. Furthermore, a shell-and-tube LHTS is more easily manufacturable thanks to a large presence of suppliers experienced in the realization of traditional shell-and-tube heat exchangers.

The aim of this work is twofold. On the one hand, it aims at studying the integration of these two LHTS units from a system perspective thanks to the experimental testing loop that is available in the laboratory of the Energy Center (a building owned by the Politecnico di Torino). On the other hand, a second objective consists in analysing the performance of two different fast-discharging fins derived from numerical studies available in literature. The former type of heat transfer enhancement is obtained with longitudinal fins along the axis of each pipe. The latter, instead, was inspired by a topological optimization of the high conductive material around the storage tubes. These two types of fins are predicted to strongly enhance the heat

transfer between the PCM and the water circulating in the building heating system if compared to common industrial solutions. More details are provided in section 3.1.2.

Once the general framework was defined, four essential questions had to be addressed in order to shape and characterize the envisioned LHTS prototypes. These are:

- *What should be the size of the LHTS units?*
- *Which should be the phase change temperature of the PCM considering its application? What desirable thermophysical features should this material possess?*
- *How should the ideal fins design be adapted to real world constraints?*
- *Which thermophysical features should the fins high conductive material have?*

All these questions are thoroughly answered in the upcoming sections.

3.1.1 Prototypes size and PCM choice

The choice regarding the size of the LHTS prototypes is related to two aspects: the application for which these storage units are ideally intended for and the physical constraints posed by the installation site (which is represented by the Energy Center lab environment in this case). Indeed, the "size" of each storage unit can be better expressed by the following three variables: the energy content, the occupied volume, and the total weight. All these quantities are not independent from one another because they all depend on the thermophysical properties of the chosen storage material (i.e., the PCM). Hence, the first step coincided with the selection of the most suitable type and quantity of Phase Change Material for the intended application. Subsequently, the limits on the overall storage weight and volume were verified.

Having in mind the secondary side of a district heating network, the choice of a suitable PCM was restricted to those with a medium melting temperature (60-80°C). Indeed, the first driving parameter is the PCM melting temperature, which needs to be compatible with the temperature level of the interfacing heating system. A second important requirement regards the PCM energy density. In this regard,

higher values are desired to reduce the overall occupied volume and increase their competitiveness with traditional sensible storage units. However, PCMs with the highest energy density often present a few drawbacks as described in section 2.2. A further aspect to consider regards the PCM compatibility with the high conductive material of the pipes and fins and the environment after disposal. Moreover, an additional desirable feature is represented by cycle stability (i.e., the PCM should have a minimal degradation rate throughout the charging and discharging cycles). Finally, also safety issues (mainly absence of flammability and toxicity) should be considered.

Taking all the above-mentioned parameters into account, a PCM developed by *CRODA* was chosen for the filling of the LHTS tanks. This is a bio-based paraffin that melts and solidifies in the range of 70-74 °C. Thanks to its organic nature, it is not toxic nor flammable in its operative range. Furthermore, it guarantees an excellent chemical compatibility with the most common high conductive materials used for the LHTS fins and pipes. A detailed summary of its thermophysical properties is reported in 3.1.

Table 3.1 Thermophysical properties of *Phase change material 74* [144]

Property	**Units**	**Value**
Peak melting temperature	°C	75
Latent heat, melting	kJ/kg	226
Peak crystallisation temperature	°C	71
Latent heat, crystallisation	kJ/kg	-224
Density (solid)	kg/m^3	939
Density (liquid)	kg/m^3	858
Flash point	°C	288
Specific heat capacity (liquid)	kJ/kg°C	2
Specific heat capacity (solid)	kJ/kg°C	1.8
Thermal cycles without change in properties	-	10000

Once the type of PCM was set, the energy content of each storage unit was determined considering a typical residential condominium with 8-10 users (roughly 2500 m^3) connected to the Turin district heating network that aims at reducing its morning peak heat demand. For such a condominium, the availability of a 40-

kWh thermal energy storage would remarkably reduce its morning peak demand depending on the season. Hence, a target energy content of 40 kWh was set.

Finally, the overall volume and weight constraints were verified. There was no volume constraint for this particular laboratory installation, although a compact solution is more attractive if compared with traditional sensible storage units. On the contrary, a limit on the total LHTS weight was present due to maximum resistance of the lab floor (2500 kg/m^2).

Considering all the above-mentioned desirable features and constraints, each LHTS unit was filled with 492 kg of PCM. As a result, each storage tank is able to store around 31 kWh of thermal energy in the form of latent heat. Then, the sensible energy content should also be accounted depending on the water supply and return temperature difference (Eq. 3.1).

$$E_{stored} = M_{PCM}L + M_{PCM}c_{p,s}(T_{pc} - T_{min}) + M_{PCM}c_{p,l}(T_{max} - T_{pc}) \tag{3.1}$$

Where: M_{PCM} is the mass of the PCM contained in the storage unit (492 kg), L is the average PCM latent heat content (225 kJ/kg), $c_{p,s}$ is the PCM specific heat capacity when solid (1.8 kJ/kg°C), $c_{p,l}$ is the PCM specific heat capacity when liquid (2 kJ/kg°C), T_{pc} is the PCM average phase change temperature (73 °C), T_{min} is the design minimum temperature of the heating system, T_{max} is the design maximum temperature of the heating system.

3.1.2 Fins design

The design of efficient fins enhancing the heat transfer in LHTS units constitutes a difficult task. First of all, there are two main criteria that can be followed when looking for an optimal fins design. On the one hand, one might be interested in minimizing the overall time necessary to store or release a specific amount of energy. Hence, this route aims at maximising the LHTS speed of charge or discharge. On the other hand, one might be interested in guaranteeing a steady heat rate when the storage is discharged [107]. As a matter of fact, sensible storage systems such as domestic hot water tanks can deliver a constant thermal power for most of their discharging process. Instead, in shell-and-tube LHTS systems, heat travels by diffusion from the internal pipe to the PCM. Consequently, the

average temperature difference and, accordingly, the thermal power output present a decreasing exponential trend in time. Moreover, optimal fins design strongly depends on whether it is intended for melting or solidification [106]. This difference is mainly due to the fact that the PCM melting process (i.e., the storage charging phase) can take advantage of the convective heat transfer mechanism as the PCM liquid fraction increases. On the contrary, the PCM solidification process (i.e., the storage discharging phase) is largely dominated by heat diffusion as soon as a solid PCM layer is formed around the LHTS pipes and fins [145].

As already anticipated, the two LHTS prototypes realized for this study were originally intended for reducing users' peak thermal demands in district heating networks. In this view, their predominant feature should be a fast-discharging process (<1h – 1.5h). Hence, the fins design was oriented towards optimal solidification performance. In addition, a further LHTS desirable feature when considering DH integration is represented by the possibility of having separate hydraulic loops (one used for charging and one used for discharging). As proved by Pizzolato et al. [146], the application of a fin topological optimization approach to such a configuration yields a peculiar fins design suggestion. Hence, considering all the aforementioned aspects, two different types of fins were chosen for the two LHTS tanks realised for this study:

- Standard **longitudinal fins** around each pipe
- **Rods** connecting "hot" pipes (i.e., those intended for charge) and "cold" pipes (i.e., those intended for discharge)

The choice of the former type of fin, i.e. the longitudinal one, was supported by several studies in literature [85, 87]. Moreover, Pizzolato et al. [106] demonstrated that simple longitudinal fins fairly approximate the ideal fins design for fast PCM solidification obtained with a topological optimization approach. In addition, they also proved that this type of fins guarantees good charging performance for at least the 80% of the LHTS charging process. Thus, aluminium matrices fitting the profile of the copper pipes were realized after several discussions about the practical feasibility of these fins with a few manufacturers (Fig. 3.1a). This aluminium matrix is made of 12 equally spaced longitudinal fins (1 mm thick) following a hexagonal perimeter (Fig. 3.1b). This determines an alternation between longer (30 mm) and shorter fins (25 mm). The hexagonal shape of the matrix perimeter derives from the choice

for the pipe arrangement inside the LHTS tank (see section 3.2 for details). The length of the fins is maximized to reach the furthest regions of the PCM, avoiding the contact with the surrounding pipes at the same time.

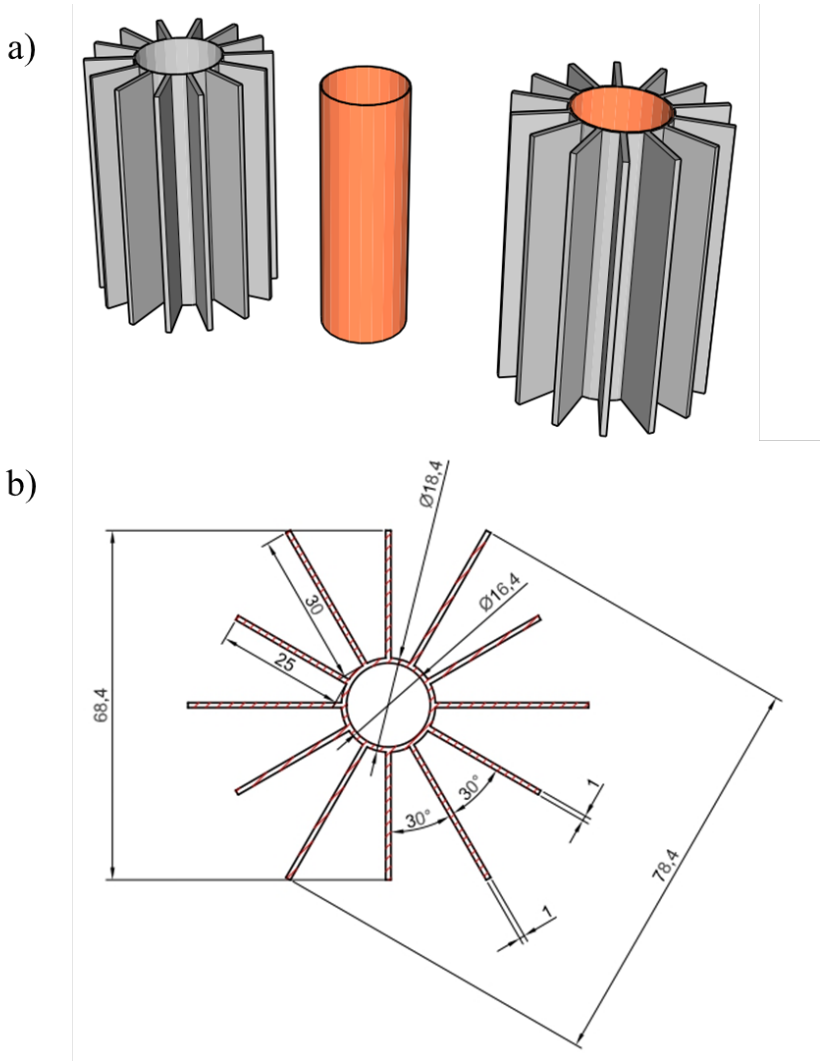

Fig. 3.1 (a): Longitudinal fins matrix; (b): Longitudinal fins geometry

The latter type of HCM extended surface, instead, was directly derived from the fins topological optimization study performed by Pizzolato et al. [146]. For this reason, in the following it will be also referred as “TopOpt” configuration. As anticipated, this concept consists in connecting the LHTS pipes intended for charge (“hot” pipes) with those intended for discharge (“cold” pipes) with thick HCM pins (Fig. 3.2).

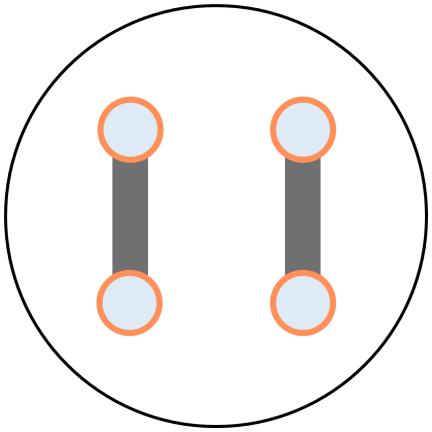

Fig. 3.2 Concept behind "TopOpt" configuration, adapted from [146]

As a matter of fact, their optimization approach was applied to a LHTS system with two separate hydraulic loops characterized by a horizontal pipes disposition. The results of their study demonstrate how connecting “hot” and “cold” pipes in such a configuration minimises the total charge-discharge duty cycle time. More specifically, the LHTS discharging process should benefit from this configuration because these HCM pins connected to an inactive “hot” pipe favour the heat transfer towards the region where the PCM is still liquid (which otherwise would be only triggered by the small PCM thermal conductivity). However, translating this concept into a feasible design was not a trivial task. After several discussions with possible manufactures, the best trade-off was found in perforated aluminium sheets. The manufacturing process of this type of fins is summarised as follows. First, a single rectangular aluminium sheet was coupled with all the LHTS pipes (Fig. 3.3a). Then, the excessive aluminium quantity was removed through a laser cut. Consequently, a configuration where “hot” and “cold” pipes are connected with only aluminium rods was achieved (Fig. 3.3b). This procedure was repeated for several parallel layers of aluminium sheets in such a way that the overall weight of the “TopOpt” fins was equal to the total weight of the longitudinal fins. In this way, the two LHTS configurations are comparable. As a result, 87 parallel layers were obtained, yielding to 160 HCM pins. The distance between each layer is 10 mm, while the pin thickness is 5 mm. Ideally, this value should have been smaller in order to increase the total number of parallel HCM layers and maximise the fins performance. However, aluminium sheets thinner than 5 mm are not stiff enough to sustain the cutting procedure. Hence, this was the best trade-off identified with the manufacturers.

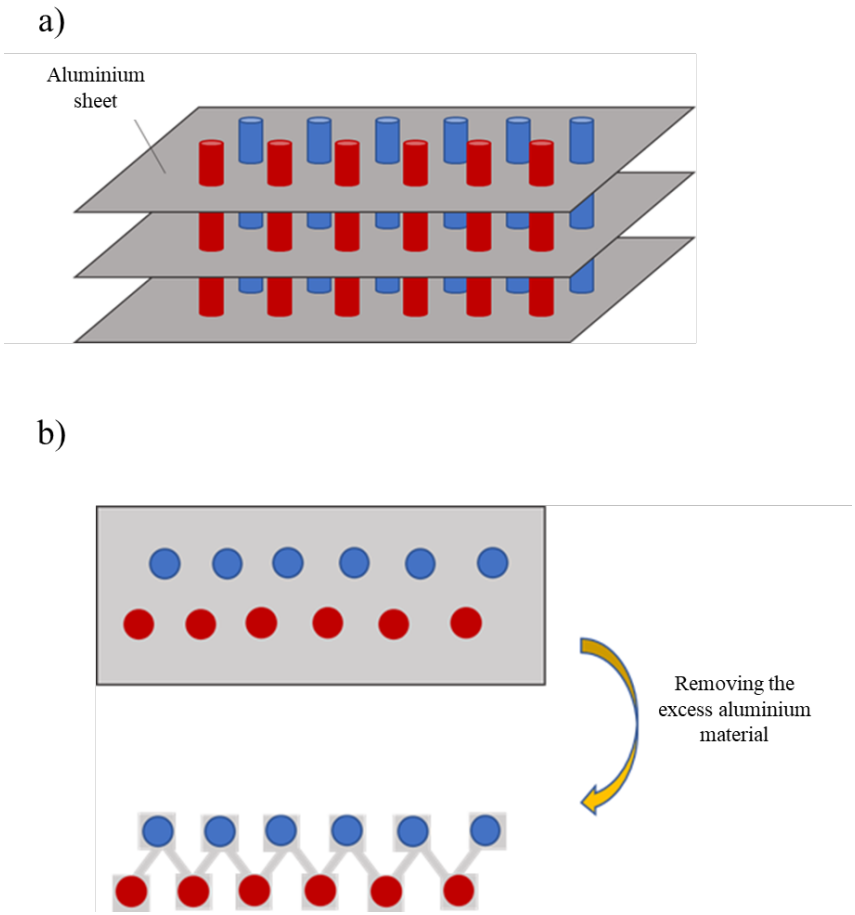

Fig. 3.3 (a): Original Aluminium sheets; (b): Final cuts trough aluminium sheets

3.1.3 Fins high conducting material

As far as the choice of the high conducting material (HCM) for pipes and fins is concerned, the three most common options (aluminium, copper and steel) were all considered. General selection criteria are thermal conductivity, density, corrosion potential and cost [15]. In general, steel is often disregarded in the LHTS community because of its low thermal conductivity and high density. However, industrial standard components for heat transfer enhancement are frequently made of steel. Thus, this material represented a practical option. Copper, instead, is the most effective enhancer material considering its extremely high thermal conductivity. However, installations relying on copper are bulky and expensive due to the very large density of this material. Instead, aluminium is characterized by a high conductivity

and a low density. In addition, several studies proved the absence of corrosion in different conditions. For these reasons, aluminium is often the preferred choice for HTF pipes and fins. A summary of the thermo-physical properties of these materials is reported in Table 3.2.

Table 3.2 Thermophysical properties of typical high conducting materials

Property	Steel	Copper	Aluminium
Thermal conductivity [W/(mK)]	30-50	350	200
Specific heat capacity [kJ/(kgK)]	0.5	0.4	0.9
Density [kg/m^3]	7800	8900	2700

Considering both practical and performance constraints, a combination of copper and aluminium was selected. More specifically, the pipes are made of copper, while an external matrix made of aluminium adheres to the pipes in both LHTS configurations. Concerning the unit with longitudinal fins, an important feature to guarantee is represented by the perfect contact between the pipe and the aluminium matrix (which is developed all along the pipe axis). This was achieved through an expanding process inside the pipes when the two parts were assembled together. Finally, it should be remarked that the manufacturing process of these two types of fins represented an ad-hoc procedure. As a result, the cost of these components is high compared to other options on the market. More specifically, the realization of the pipes with longitudinal fins had a cost of roughly 9.5 €/m, while the cost for the other fin configuration was around 12 €/m.

3.2 LHTS prototypes realization

Once the fins design was defined for both the storage tanks, several practical considerations had to be made in order to realize these units. These considerations were generated by the following questions:

- *How many pipes should constitute the internal heat exchanger? With what diameter?*
- *How should the pipes disposition be arranged inside the storage tank?*

- *What should be the pipes orientation? Vertical or horizontal?*
- *How should the active heat exchanger be enclosed?*

First of all, as already anticipated the two LHTS tanks were designed targeting a DH application. In this view, having two separate pipe loops (one for the LHTS charge, one for the LHTS discharge) constitutes a useful feature. This concept (Fig. 3.4) yields to several benefits:

- Simple mechanical system design
- Possibility to work with two different HTFs for charge and discharge without contact or contamination
- Possibility of simultaneous charge and discharge
- Possibility to work with different operating pressures (e.g., in DH the pressure of the primary circuit is above 10 bar, while the pressure in the secondary circuit is around 3 bar)

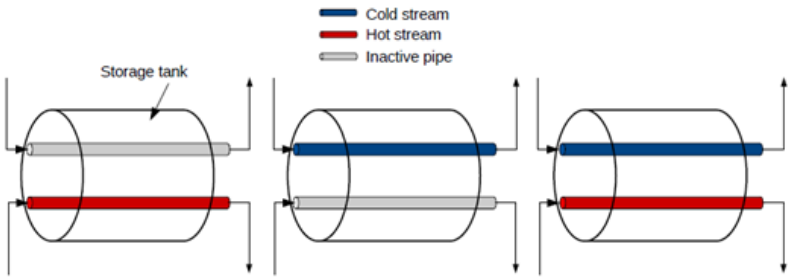

Fig. 3.4 Schematics of LHTS with separate hydraulic loops: charging phase (left), discharging phase (middle), possible combination of the two (right) [146]

Moreover, the "TopOpt" fins were derived considering decoupled charging and discharging loops. Hence, both the LHTS tanks were designed having this operational possibility in mind. Nevertheless, thanks to the characteristics of the lab testing system, they can be operated either as a single hydraulic loop (i.e., all the tubes are simultaneously crossed by the HTF) or as two separate hydraulic loops. Further details regarding the testing system are reported in 3.3.

Overall, the LHTS internal heat exchanger is constituted by 96 pipes, each with an internal diameter of 14.9 mm. Half of these are intended for the charging phase (i.e., "hot pipes"), while the remainder is intended for the discharging phase (i.e., "cold pipes"). The number of tubes and their diameter affects the geometrical characteristics of the LHTS tanks. Hence, the combination of these two variables was selected based on the following criteria:

- Market availability;
- Good proportion among storage external dimensions (i.e., LHTS not excessively long, short, or high);
- Reasonable quantity of PCM around each pipe.

The pipes arrangement inside the LHTS tank is also a crucial parameter as it influences the average heat diffusion distance in the PCM (together with the fin type). Indeed, two main constraints were considered for the definition of the tubes disposition:

1. The need to minimise the quantity of PCM far from the HCM of the pipes and fins to avoid the presence of regions where the PCM does not melt or solidify in a reasonable time;
2. The need to realize pipes collectors for the practical connection of the heat exchanger tubes with the hydraulic loop of the testing facility.

Regarding the former consideration, a trade-off had to be found between the design of a compact LHTS and the need to avoid overlapping tubes and fins. The overall LHTS volume is fixed because the total amount of PCM is determined by the quantity of the stored energy (see section 3.1.1). Hence, any modification of the inter-pipe distance affects the dimensions of the LHTS tank. More specifically, a short inter-pipe distance yields to a small LHTS cross section area but also to a large LHTS maximum length. Although a compact cross section area positively affects the time for charging and discharging, an excessively long storage cannot fit in the space available for its installation. Furthermore, as pipes get closer, their fins might overlap and bend due to thermal expansion. As far as the pipes collectors are concerned, these constitute a second relevant constraint affecting the arrangement of the tubes.

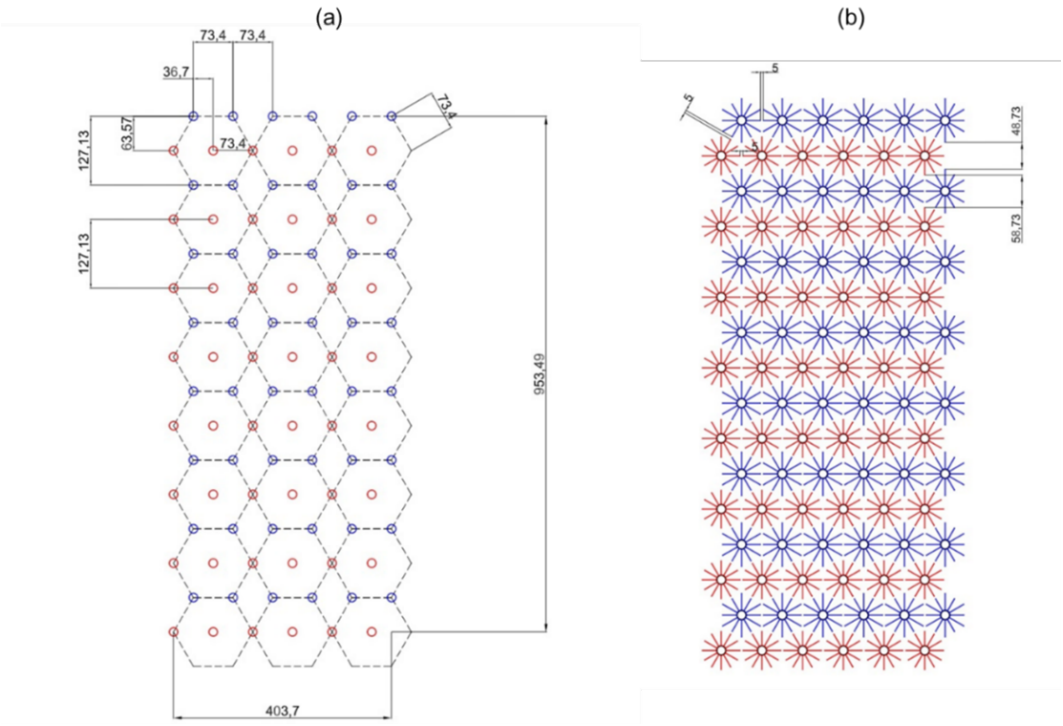

Fig. 3.5 Charge (red) and discharge (blue) pipes arrangement: (a) without fins; (b) with fins

Collectors are essential for a balanced HTF flow distribution inside each pipe of the storage heat exchanger. Hence, since collectors are straight tubes, they influence the arrangement of the pipes to which they are connected. A further practical question to be addressed concerned the pipes orientation, which can be vertical or horizontal. As a matter of fact, the need to realize pipe headers for each storage tank was the main reason behind the selection of the horizontal orientation. Indeed, a vertical orientation would have required a much more complicated solution for the pipe collectors located at the bottom of the storage. Moreover, the heat transfer inside the LHTS tank with longitudinal fins is dominated by diffusion because this type of fin blocks the PCM natural convection [104]. Hence, the performance of this storage is almost insensible to the tank inclination. On the contrary, the heat transfer inside the LHTS tank with the "TopOpt" fins aims at exploiting the PCM natural convection inside a horizontal storage (see section 3.1.2).

Summarising, the final layout is presented in Fig. 3.5. As can be seen, the pipes are arranged in uniform cold and hot rows to facilitate the successive connection with the collectors (Fig. 3.6). A homogeneous distribution of these pipes (with alternate hot and cold pipes in each row) was initially considered, but then discarded due

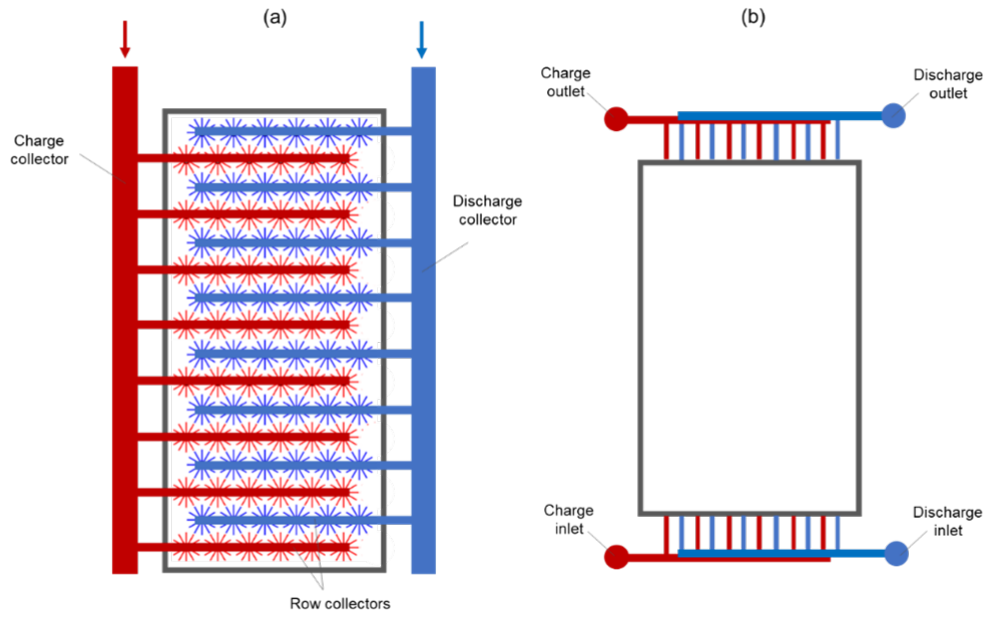

Fig. 3.6 Pipe collectors for charge and discharge loops: (a) frontal view; (b) top view

to the increased difficulty in the connection with the pipes headers. The choice of placing "hot pipes" below the "cold pipes" is expected to favour the overall heat transfer in the PCM thanks to natural convection (see section 3.1.2). Indeed, the solid PCM (usually around the "cold pipes") has a larger density with respect to the liquid PCM (usually around the "hot pipes"). Thus, buoyancy forces are expected to move the solid PCM downwards and the liquid PCM upwards, enhancing the PCM mixing.

Finally, the active heat exchanger in Fig. 3.6 was enclosed in a stainless-steel external case. This is characterized by three windows to inspect the PCM status during charge and discharge. Moreover, a transparent plexiglass cover was placed on the top, thus allowing a thorough PCM visual analysis during tests. The whole external case was then insulated with 4-cm thick polystyrene panels.

3.2.1 LHTS assembly and PCM filling procedure

After the manufacturing of the two internal heat exchangers as previously detailed, the whole LHTS units were assembled. First of all, the internal heat exchanger was inserted inside the protective external case with the aid of a crane (Fig. 3.7).

Fig. 3.7 Assembly of LHTS inner heat exchanger and external case

Subsequently, the LHTS tanks were positioned over an ad-hoc designed plate which redistributes the weight of the storage units over the lab floor. After that, the LHTS tanks were filled with the PCM contained in 10 cylindrical barrels (Fig. 3.8). These barrels contained the selected PCM in the form of small pellets. The filling procedure of the LHTS unit with the "TopOpt" fins was rather smooth, since these PCM pellets could be poured in their solid state over the hot pipes and percolate towards the bottom thanks to the fins geometry. On the contrary, the filling operation of the LHTS unit with the longitudinal fins was rather long. Indeed, the axial development of the fins blocked the movement of the solid PCM pellets. As a result, the PCM in the barrels had to be melted through flexible electrical resistances and then poured inside the storage tank through a specific pump.

Fig. 3.8 PCM barrels

3.2.2 LHTS rendering and technical specifications

This section presents a graphical representation of the two LHTS units and summarises their main technical specifications. Fig. 3.9 presents a 3D rendering of the assembly with "TopOpt" fins, while Fig. 3.10 for the assembly with longitudinal fins.

The overall geometrical specifications of the storage units are instead available in Table 3.3. As already stated, the main difference between the two LHTS configurations resides in the way in which the high conductive fins are arranged around each pipe. Issues regarding the actual manufacturing of these types of fins have already been discussed in section 3.1.3. The performance of these two units is assessed in section 5.4.

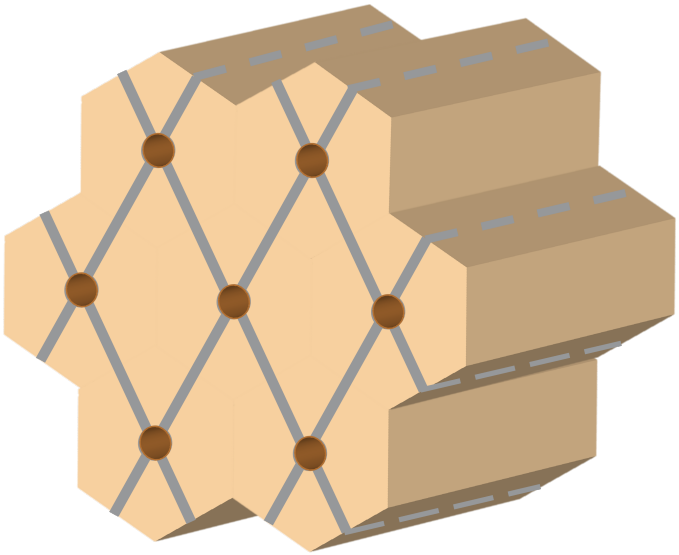

Fig. 3.9 3D rendering of TopOpt LHTS internal assembly

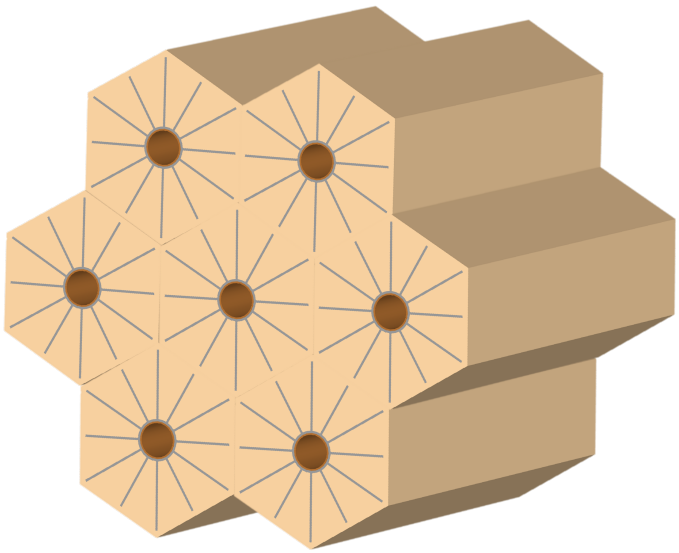

Fig. 3.10 3D rendering of Longitudinal LHTS internal assembly

Table 3.3 LHTS prototypes technical specifications

Feature	TopOpt LHTS	Longitudinal LHTS
Pipes inner diameter [mm]	14.9	14.9
Pipes length [m]	1.29	1.29
Volume of active PCM [m^3]	0.573	0.573
Mass of active PCM [kg]	492	492
Mass of high conducting material (Al + Cu) [kg]	119.8	119.8
Total heat exchange area [m^2]	25.8	82.5

3.3 Description of the experimental testing rig

From an energy system point of view, the operation of a LHTS unit can be divided into three different phases:

- The **discharging phase**, when the total or partial user heat demand is satisfied through the LHTS;
- The **charging phase**, when an amount of thermal energy is stored in the LHTS (for example when there is a mismatch between heat demand and heat production or when it is economically convenient);
- The **idle phase**, when the LHTS is not operated.

A high-level representation of these three operational phases is reported below. During the discharging phase (Fig. 3.11), the LHTS contributes to the satisfaction of the user heat demand (Q_{user}). In this phase the system controller acts on three main components: a pump for the discharge hydraulic loop (P_{dis}) and two valves for the connection with the existing heating system (V_{d1} and V_{d2}). If an automatic regulation system is present, the mass flow rate ($G_{circuit}$) can be controlled, thus the thermal power to the user is modulated. However, it should be noticed that mass flow regulation range is limited by the features of the heating system. On the contrary, the hot water supply temperature (T_{sup}) cannot be directly controlled because it depends on the LHTS characteristics (unless a recirculation of cold water is implemented

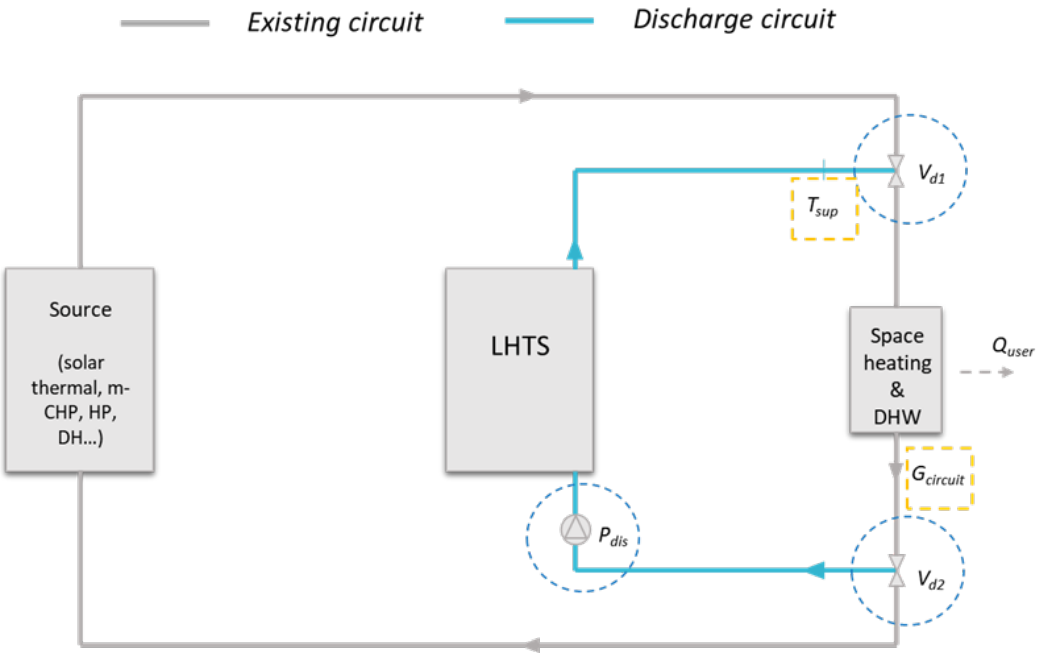

Fig. 3.11 Schematics of LHTS system integration (discharging phase)

to reduce the outlet temperature). Instead, during the charging phase (Fig. 3.12), the LHTS receives an amount of thermal energy that is not immediately delivered to the user. As in the previous case, the system controller generally acts on three components in order to deviate the hot water flow towards the LHTS: a pump (P_{ch}) and two valves (V_{c1} and V_{c2}). Again, if a regulation system is present, the mass flow rate (G_{charge}) can be controlled to adjust the thermal power delivered to the LHTS. The hot water charging temperature (T_{charge}) depends on the features of the heating technology that is coupled to the storage. In general, particular attention has to be paid regarding the PCM melting temperature to ensure an effective coupling with the heating system.

Finally, during the idle phase (Fig. 3.13) the LHTS is excluded from the heating system acting on the necessary valves (in this case V_{c1}, V_{c2} and V_{d1}, V_{d2}). Under these circumstances the storage does not receive nor release thermal energy from/to the heating system.

With these operational configurations in mind, an experimental set up was designed and realized in the laboratory of the Energy Center, a building owned by the Polytechnic University of Turin (Fig. 3.14).

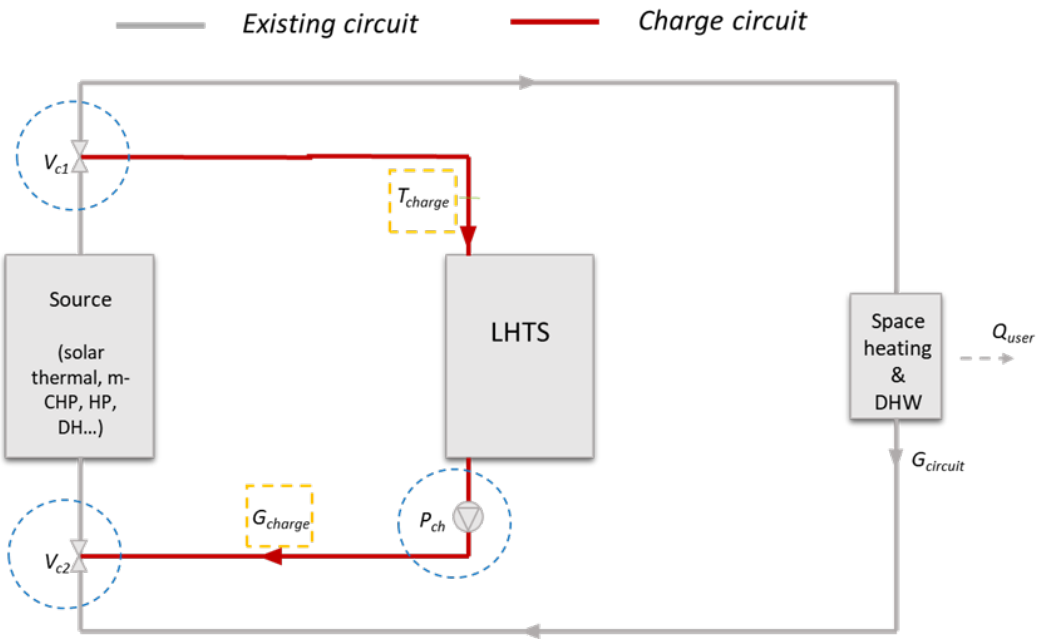

Fig. 3.12 Schematics of LHTS system integration (charging phase)

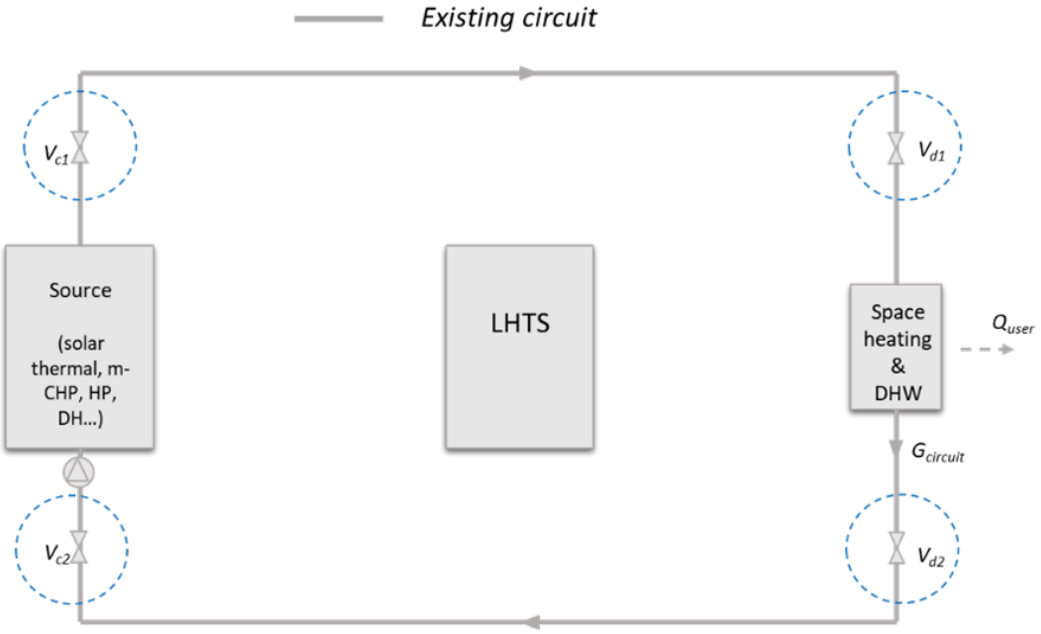

Fig. 3.13 Schematics of LHTS system integration (idle phase)

Fig. 3.14 "TopOpt" (left) and "Longitudinal" (right) LHTS units in the laboratory environment

A detailed sketch of the entire hydraulic circuit is reported in Fig. 3.15. The main components are:

- The **heat source**, represented by the district heating substation and the electric resistance;
- The **heat sink**, represented by the dry cooler;
- Three groups of **mechanical valves** (V1, V2 and V3);
- The circulating **pump**;
- The two **LHTS tanks**.

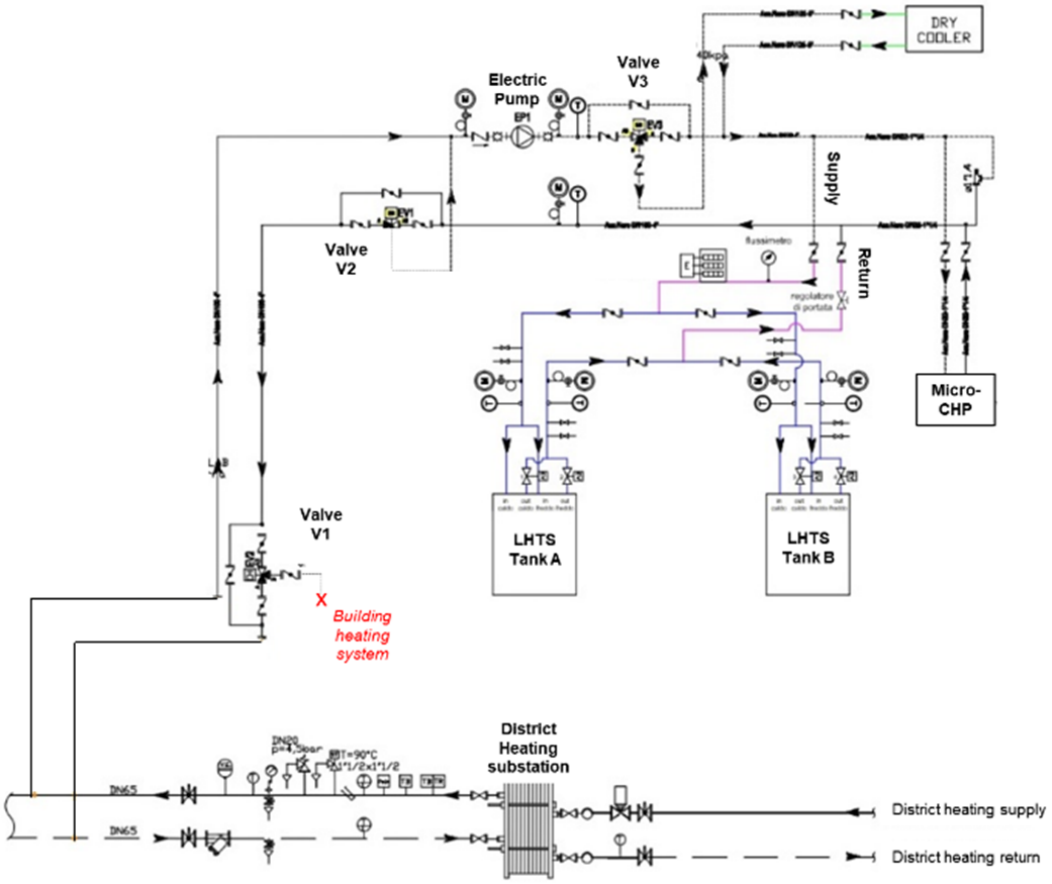

Fig. 3.15 Schematics of the experimental testing rig for the LHTS tanks

The heat source was initially intended to be the DH substation alone. However, an electrical resistance was added to sustain the charging process and serve as a backup. The DH substation is a plate heat exchanger (Fig. 3.16) located in the building technical room and dedicated to the heat demand of the experimental technologies present in the building (currently an absorption chiller and the LHTS units). According to the manufacturer, the nameplate size of this substation is 200 kW. Nevertheless, a constant stream of hot water with a temperature higher or equal to 80°C should be supplied in order to melt the PCM contained in the LHTS tanks. Unfortunately, such a performance on the secondary side of a district heating network strongly depends on the season and the building location. As a result, during the LHTS testing campaigns it was not possible to use the DH substation as a source for the experimental system. Such an inconvenient was overcome through the continuous use of the electrical resistance (Fig. 3.17) during the LHTS charging phase. This

component is installed on the common supply branch, just before the derivation of the two hydraulic subsystems dedicated to each LHTS unit. Its nameplate electrical power is 17 kW. Even though the heat rate is lower compared to the DH substation, during the experimental tests the PCM melting of a single LHTS tank was always completed within 4-5 hours depending on its starting temperature.

Fig. 3.16 District heating substation (heat source dedicated to the experimental testing rig)

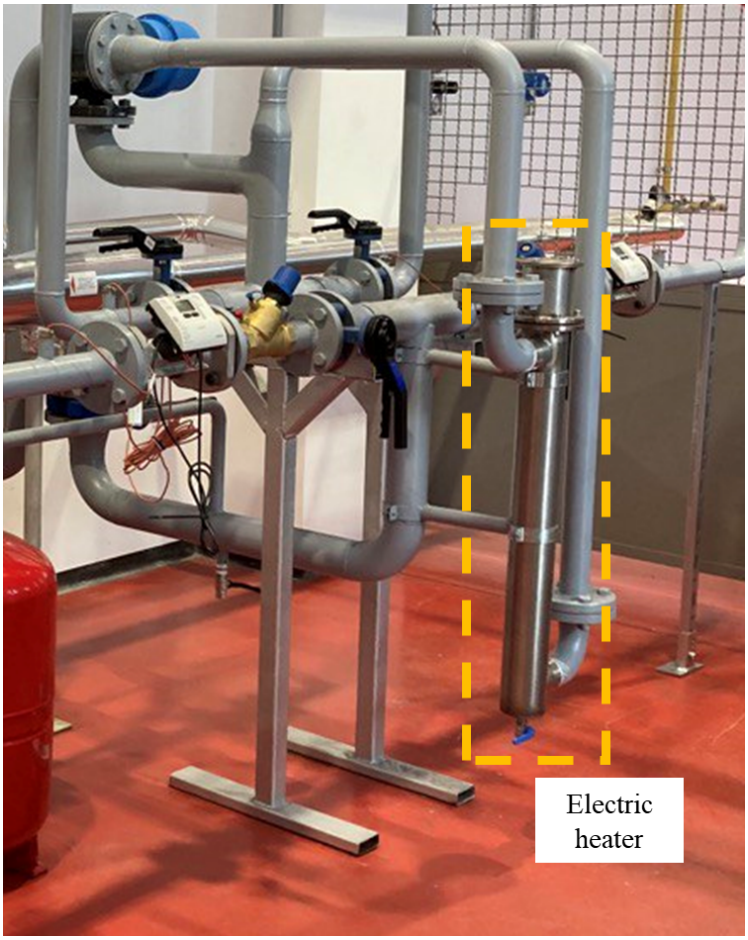

Fig. 3.17 Electric heater (heat source dedicated to the experimental testing rig)

Instead, when the LHTS needs to be discharged, the generated thermal power is dissipated through a dry cooler placed on the building rooftop (Fig. 3.18). This works as the only heat sink within the experimental loop. As a matter of fact, the connection between the experimental hydraulic loop represented in (Fig. 3.15) and the rest of the building heating system has still to be implemented. In this context, the presence of the dry cooler allows to test the discharging phase of the LHTS tanks even when the released thermal energy cannot be supplied to the rest of building. The selected dry cooler model is *SCIROCCO – L W 63-3 B 4 D*, manufactured by *Stefani*. This component is characterised by a rated cooling power of 112.4 kW and a maximum water mass flow rate of 21.6 m^3/h. This size was selected with the aim of preserving two functions: the possibility to discharge both the LHTS units simultaneously and the possibility to add a micro-CHP within the same experimental

circuit. Moreover, to increase the operational flexibility, this dry cooler is driven by an inverter which can regulate the fan speed from 10% to 100%.

Fig. 3.18 Dry cooler (heat sink dedicated to the experimental testing rig)

Although the charging and discharging phases of the LHTS tanks are two separate processes, some parts of the system ducts are used in both phases, as can be seen from Fig. 3.15. In this context, the operation of two three-way mechanical valves (V1 and V2) is essential. These valves are characterised by an inlet flow and two outlet flows. Depending on the supply tension of these valves (continuously adjustable between 0 V and 24 V), the two outlet flows can be regulated. As already anticipated, during the charging phase the storage tanks are heated by the electrical resistance. During this period, V1 and V2 close the paths towards the DH substation and the dry cooler, thus allowing the heat exchange only between the LHTS tanks and the

electric heater. It should be noticed that if the DH substation could be properly adopted as a heat source, V1 would allow the use of this component together with the electric heater (in series) or exclusively (if the electric heater was switched off). Similarly, during the discharging phase V1 avoids the water flow towards the DH substation, while V2 deviates the water flow towards the dry cooler. Furthermore, it should be noticed that this experimental loop is already predisposed to divert the LHTS discharged heat towards the rest of the building heating system (through V3). However, as already anticipated, the heat recovery from the experimental facility is not yet implemented and V3 is currently switched off.

As far as the pumping system is concerned, an adjustable electric pump equipped with an inverter was already present (Fig. 3.19). As a matter of fact, the central core of the whole experimental loop for thermal applications had already been realised in the Energy Center laboratory, while the peripheral components (dry cooler and LHTS subsystems) were designed for this doctoral project. The model of the pump is *Grundfos TPE2 D 100-150*. Thanks to the fine regulation through its electric inverter a wide range of water mass flow rate values can be tested during the discharging phase, as can be seen from the pump characteristic curve in Fig. 3.19. Like the dry cooler, it should be noticed that also this pump is slightly oversized for the current needs of the experimental loop. However, this size fits with the intention of expanding the hydraulic circuit in future. Moreover, each LHTS branch is endowed with a manual flow controller which allows to vary the hydraulic circuit resistance, thus extending the operating field of the pump.

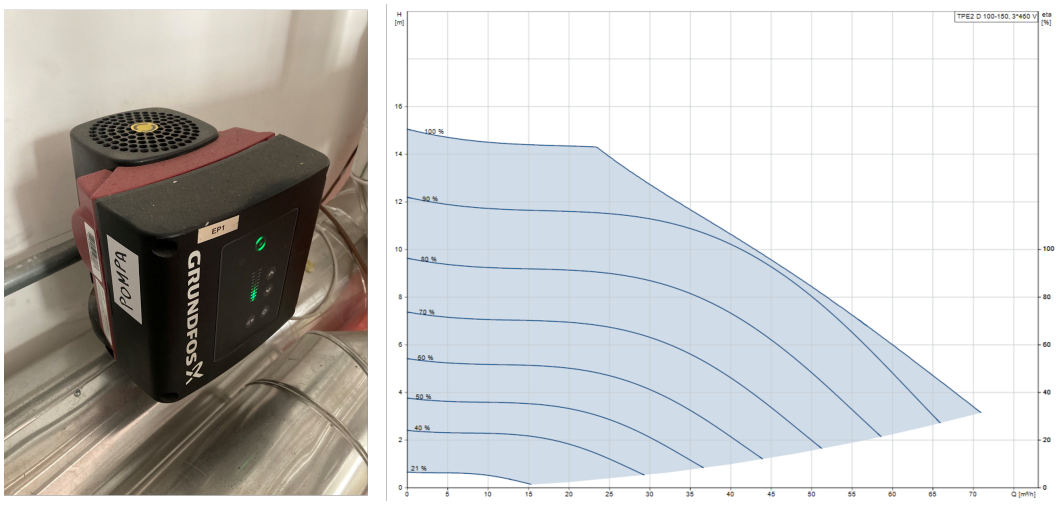

Fig. 3.19 Electric pump with characteristic curve

Finally, the portion of the hydraulic circuit dedicated to the two LHTS tanks is here presented. The components involved during the charging and discharging phases are reported in detail in Fig. 3.20. Two electric valves (EV) at the outlet of each storage tank manage two separate water pipe circuits. This connection scheme allows operating the LHTS units in two ways. Depending on the position of the electric valves, the charging and discharging process of each LHTS tank can be performed through two different groups of pipes (the pipes rows are dedicated alternatively to charge and discharge). In this case, only one EV is open at the LHTS outlet. On the contrary, when both the EVs are open at the LHTS outlet, the charging and discharging processes share the same pipes (i.e. all the 96 tubes are used). The possibility of managing independently two different pipe circuits determines great flexibility in the testing conditions. Considerations regarding the convenience of these two configurations have already been addressed in 3.2.

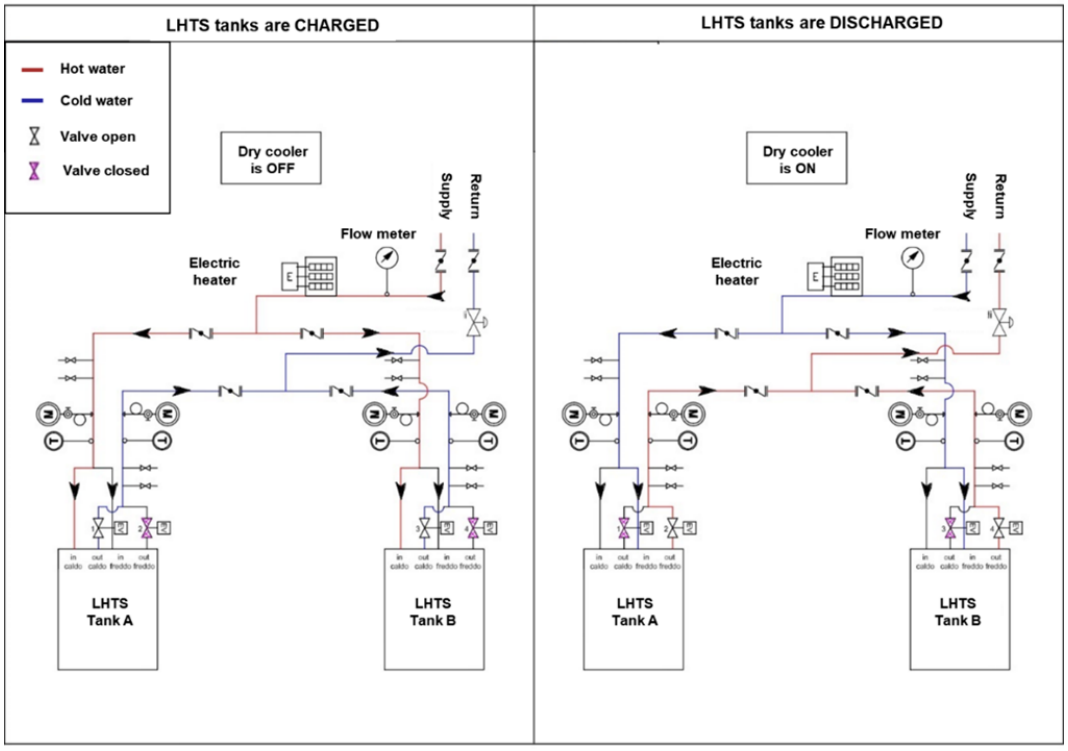

Fig. 3.20 Schematics of the active components during LHTS charging and discharging phases

3.3.1 Field sensors

The energy performance of the two LHTS tanks is monitored through two dedicated heat meters (*Kamstrup MULTICAL 403*). These allow to register and measure the following quantities: water inlet temperature, water outlet temperature, water mass flow rate and thermal power. The main features of this type of heat meter are reported in Table 3.4, while its accuracy is reported in Table 3.5. The overall heat meter accuracy is determined by the sum of the errors of three components: the flow sensor error (E_F), the calculator error (E_c) and the sensor pair error (E_t). Moreover, it also depends on the nominal flow rate (q_p) and the measured temperature difference ($\Delta\Theta$) [147].

Table 3.4 Main specifications of heat meters (*Kamstrup MULTICAL 403*)

Feature	**Quantity**
Temperature range [°C]	2-180
Differential temperature [°C]	3-178
Flow range [m^3/h]	0.6-15
Temperature sensor	2-wire, Pt500

Table 3.5 Accuracy of heat meters (*Kamstrup MULTICAL 403*) [147]

Heat meter component	**Accuracy**
Flow sensor	$E_f = \pm(1+0.01q_p/q)$ %
Calculator	$E_c = \pm(0.15+2/\Delta\Theta)$ %
Sensor pair	$E_t = \pm(0.4+4/\Delta\Theta)$ %

The internal status of each LHTS unit is monitored through 16 thermocouples. As depicted in Fig. 3.21, four main locations were selected: one at the bottom of the tank, one at the top of the tank, one at the centre and one on the side. For each of these positions, four thermocouples were laid at a regular interval distance (0.4 m) in the water flow direction. The location of these sensors was chosen to verify the thermal behaviour of the PCM. The vertical disposition (from top to bottom) was selected to analyse possible thermal gradients, since the liquid PCM has a lower density with respect to its solid phase, thus higher temperatures are in general expected on the top.

Similarly, the lateral point was chosen to analyse possible side effects. In this case, however, one single location was deemed sufficient considering the symmetry of the storage unit. Instead, the location of thermocouples in the direction of the water flow was an obvious choice to verify the PCM axial thermal gradients.

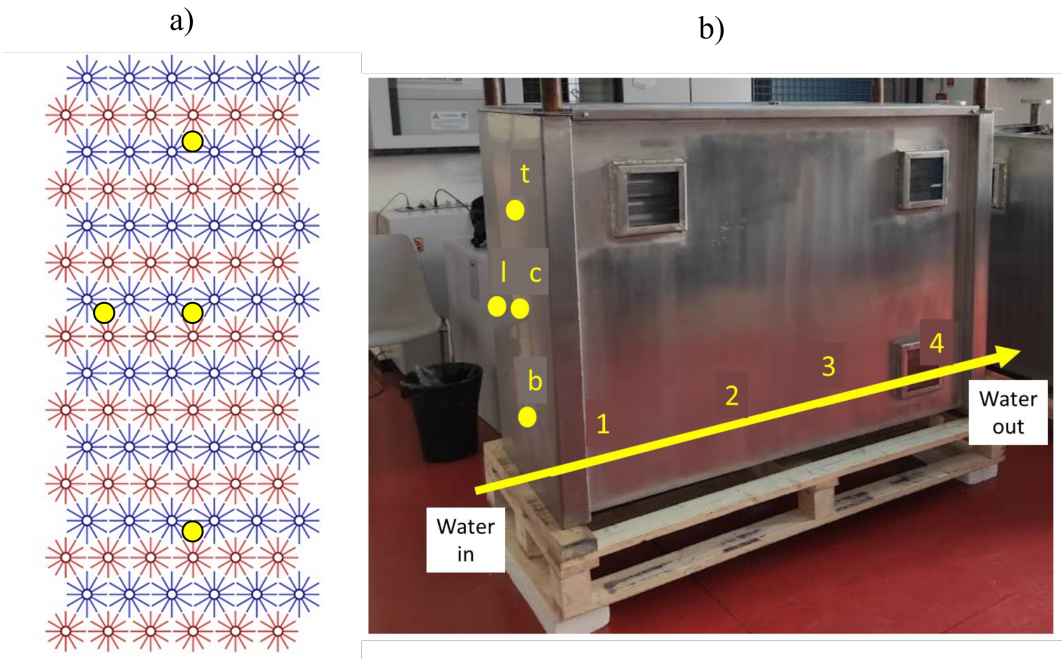

Fig. 3.21 Disposition of LHTS internal thermocouples

These thermocouples where manually inserted in the LHTS units inside four empty pipes. These were specifically conceived in order to avoid the thermocouples excessive displacement induced by the PCM buoyancy forces. Regarding their specifications, these thermocouples are classified as *Pt100 class B*, thus they have an absolute accuracy of ± 1°C.

3.3.2 Controlling and monitoring platform

The entire experimental test bench is monitored and controlled through a dedicated Programmable Logic Controller (*MECT TP1070*), which exploits the *Modbus TCP/IP* protocol to collect the physical quantities of interest from the field sensors and to control the main components of the hydraulic circuit (valves, dry cooler and electric heater). A view of this PLC is reported in Fig. 3.22. All the monitored

quantities are recorded every 30 seconds and stored on a local .dat file. This can be accessed remotely using the internal building network. The data acquisition and interpretation processes were carried out through an ad-hoc *Python* script.

Fig. 3.22 Programmable Logic Controller (PLC) dedicated to the experimental testing rig

3.4 Key findings of the present chapter

The present chapter thoroughly reported the steps for the realization of two large-scale shell-and-tube LHTS units together with their testing facility. Starting from the initial concept and scope, all the practical design choices were motivated and justified. Particular attention was devoted to the fins design, which constitutes the core of the LHTS units. More specifically, two high-performance concepts derived from the available literature were carefully studied and, subsequently, realised taking into account numerous real-world constraints. Moreover, these storage units were conceived targeting a typical problem in district heating applications: the reduction of morning peak demands. Nevertheless, the LHTS design is rather general and it is expected to be suitable for several other applications if a PCM with a different transition temperature is considered. In conclusion, the work presented in this chapter gives useful practical insights and might be helpful for those attempting to realize similar devices.

Chapter 4

1-dimensional dynamic LHTS model

The goal of this chapter is the description of a newly developed 1-dimensional dynamic model to simulate the behaviour of shell-and-tube LHTS units from a system perspective with a low computational effort. The proposed model formulation is rather general and entirely based on a-priori known physical parameters. Thus, the modelling approach proposed hereafter has the potential to enable the following activities:

- The determination of an LHTS optimal size tailored on the specific needs of the examined heating system (**design phase**);
- The simulation of LHTS control strategies and relative effects on residential heating systems (**operational phase**).

Section 4.1 provides an overview of the adopted methodology. The scope and the modelling strategies are here clarified. A visual representation of the modelling approach is introduced to underline the fact that the HTF pipe domain and the PCM-HCM assembly domain are modelled separately.

Section 4.2 presents the features of the 1-dimensional pure advection model for the HTF pipe. The underlying hypotheses and the model boundary conditions are here explained.

Section 4.3 punctually describes the analytical modelling approach adopted to represent the dynamic behaviour of the remaining PCM-HCM assembly. All the assumptions regarding the physical parameters are introduced and discussed. In few words, analytical thermal power characteristic curves are identified.

Section 4.4 details the solution algorithm adopted for the coupling of the HTF and PCM-HCM models. The combination of these two results in the overall dynamic performance of the modelled LHTS heat exchanger.

Section 4.5 provides an initial benchmark for performance of the developed model. As a matter of fact, this section compares its output with the results achieved through a much more detailed 3D LHTS numerical model.

Eventually, section 4.6 summarises the key findings of this chapter.

Some portions of this chapter were published in the following article and presented at the following conference:

- Colangelo, A.; Guelpa, E.; Lanzini, A.; Mancò, G.; Verda, V. *Compact Model of Latent Heat Thermal Storage for Its Integration in Multi-Energy Systems*. Appl. Sci. 2020, 10, 8970.
- *34th International Conference on Efficiency, Cost, Optimization, Simulation and Environmental Impact of Energy Systems (ECOS 2021)*, held in Taormina from 27th June to 2nd July 2021.

4.1 Overview on the adopted methodology

To facilitate the integration of LHTS units in thermal or multi-energy systems, this study proposes a compact modelling approach for rapidly simulating the dynamic behaviour of shell-and-tube LHTS units. As already underlined in Chapter 2, most of the works available in literature focus their attention on the detailed simulation of the PCM melting/solidification process to also compute the thermal output of LHTS heat exchangers. Therefore, resource-intensive models are generally presented. However, from a system perspective the essential quantities to predict are: 1) the heat transfer fluid (HTF) outlet temperature, 2) the LHTS state of charge and 3) the heat transfer rate given the HTF inlet mass flow rate and temperature. In this context, the thorough modelling of the PCM transformations is superfluous. Simple predictive models for steady state heat exchangers are very well known and largely available in literature, such as the effectiveness number of transfer units and the logarithmic mean temperature difference method. Their results accurately predict the output of the modelled heat exchangers, allowing both simulations of operative working

conditions and design comparisons. Unfortunately, these methods cannot be directly applied to LHTS heat exchangers because of their intrinsic transient operation.

The methodology proposed in this thesis addresses the abovementioned limitations by modelling separately the two constituent sub-domains of shell-and-tube LHTS heat exchangers, i.e. the HTF domain and the assembly of PCM and high conducting material (HCM). The HTF is the fluid flowing inside the LHTS pipes and generally coincides with the fluid circulating inside the hydronic heating system to which the LHTS is connected. The HCM and PCM assembly, instead, constitutes the remaining part of the heat exchanger, i.e. it is the ensemble of the storage material, the pipes material and the pipe fins. By modelling these two domains separately, the heat flux exchanged at the contact wall is decoupled. More specifically, the two domains are modelled according to the following approaches:

- The HTF domain is reduced to a 1-dimensional pure advection numerical model along the axial pipe direction (see section 4.2);
- The complexity of the PCM-HCM assembly is represented only through its transient thermal behaviour. This is modelled using analytical thermal power characteristic curves based on the considered LHTS thermo-physical and geometrical parameters (see section 4.3).

A visual representation of the proposed methodology is presented in Fig. 4.1. In few words, at any time instant of the storage discharging phase, the heat flux transferred from the PCM-HCM assembly towards the HTF mainly depends on three parameters: the equilibrium temperature at the contact wall (T_{wall}), the current storage state of charge and the conditions at the beginning of the discharging phase. Therefore, at any time instant of the storage discharging phase, the heat source in the HTF advection-conduction numerical model can be computed.

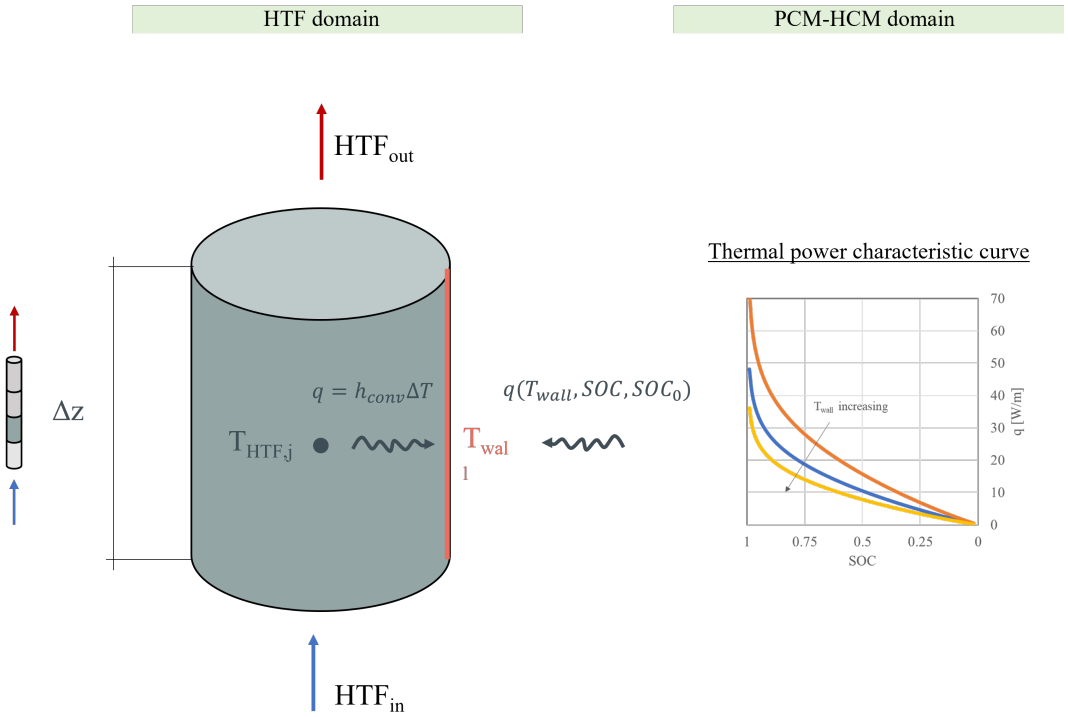

Fig. 4.1 Graphical representation of the adopted methodology

As a result, this dynamic modelling approach allows to predict the time evolution of the quantities of interest from a storage system integration perspective (the HTF outlet temperature, the LHTS state of charge and the energy transfer rate). The presented two sub-models were developed taking the LHTS discharging phase as a reference. The reason for the major interest in modelling this LHTS operational phase resides in the intended application of the LHTS storage units developed for this thesis, i.e. peak demand reduction in DH networks. Nevertheless, the proposed modelling approach is rather general and it is expected to provide reliable results also for the LHTS charging phase. The upcoming sections clarify the hypotheses at the base of the two sub-models, detail their coupling algorithm and quantify the large savings in the computational time compared to a full LHTS thermo-fluid dynamic model.

4.2 Model for the Heat Transfer Fluid (HTF) domain

The thermal model for the HTF flowing inside the LHTS pipes is here presented. Considering that the relevant direction is the axial one, a 1D model along the z axis is adopted (Fig. 4.2).

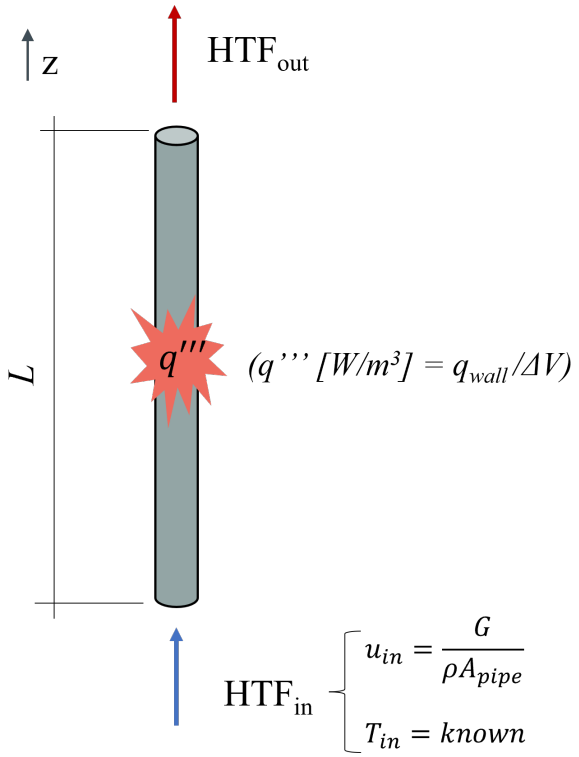

Fig. 4.2 Graphical representation of the model for the Heat Transfer Fluid (HTF) domain

Moreover, taking into account the thermal properties of the HTF fluid (which is generally water in hydronic heating systems), heat conduction in the axial direction is negligible with respect to mass transport. Indeed, for the most common operating conditions, the velocity of the HTF (u) is such that $uL/\alpha_{HTF} >> 1$ (where α_{HTF} is the thermal diffusivity of water and L is the length of the pipe). Hence, the temperature of the HTF along the axis of the pipe at each time instant is modelled though a 1D pure advection problem, as shown in Eq. 4.1.

$$\frac{\partial T(z,t)}{\partial t} + u\frac{\partial T(z,t)}{\partial z} = \frac{1}{\rho_{HTF} c_{p,HTF}} q'''(z,t) \tag{4.1}$$

Where ρ_{HTF} is the HTF density [kg/m^3]; $c_{p,HTF}$ is the HTF specific heat capacity [J/(kgK)] and $q'''(z,t)$ is the volumetric heat generation rate [W/m^3]. To simplify the problem, ρ_{HTF} and $c_{p,HTF}$ can be considered independent on the HTF temperature.

As far as the boundary conditions are concerned, temperature and velocity at the tube inlet are fixed at each time instant. This is due to the fact that in hydronic heating systems the LHTS inlet conditions are fully known in terms of temperature and mass flow rate because they derive from the radiators return line (during the storage discharging phase) or from the boiler supply line. At the pipe outlet, instead, an adiabatic Robin boundary condition is imposed ($\partial T/\partial z|_{z=L} = 0$). This is a rather general condition when modelling such problems.Regarding the numerical scheme, Eq. 4.1 is discretized with a finite volume approach. This guarantees that the energy is conserved in each section of the pipe. Consequently, the volumetric heat generation (q''') can be computed from the thermal power generated by the corresponding axial section of the PCM-HCM assembly when a specific wall temperature (T_{wall}) is reached at the contact wall (see Eq. 4.2).

$$q'''(z,t) = \frac{q_{PCM-HCM}(T_{wall}(z,t),\, SOC(z,t),\, SOC_0)}{A_{pipe}\Delta z} \tag{4.2}$$

Where: $q_{PCM-HCM}(z,t)$ is the thermal power incoming from the PCM-HCM assembly [W]; $T_{wall}(z,t)$ is the temperature at the contact wall between the HTF domain and PCM-HCM assembly domain; $SOC(z,t)$ is the state of charge of each axial volume of PCM-HCM assembly; SOC_0 is the initial state of charge.

The wall temperature at each time step is the crucial parameter that guarantees the same heat transfer rate from the PCM-HCM assembly to the wall and from the wall to the axial HTF temperature ($T_{HTF}(z,t)$). More details regarding the heat rate generated by the PCM-HCM assembly, the solution algorithm, and the coupling of the HTF and PCM-HCM domains are provided in sections 4.3 and 4.4. Finally, the advective heat flux between two consecutive cells is calculated with an upwind differencing scheme, while the time formulation is implicit. The space discretization interval Δz is set to 0.01 m, while the adopted time-step is 1 s. Both of them proved to yield results that are independent on the spatial and temporal discretization schemes.

4.3 Thermal power characteristic curves for LHTS heat rate

The previous section introduced the partial differential equation describing the heating (and possibly cooling) of the HTF flowing inside the LHTS heat exchanger pipes (Eq. 4.1). As already mentioned, the term related to the heat source for this domain (q''') depends on the heat rate ($q_{PCM-HCM}$) that the quantity of PCM-HCM allocated to each pipe is able to release (during the storage discharge) or absorb (during the storage charge). Hence, the following non-trivial questions arise:

- *Is it possible to identify an analytical expression for* $q_{PCM-HCM}$?
- *If yes, which is the most suitable analytical function for* $q_{PCM-HCM}$?

Since LHTS units rely on the change of phase of PCM materials to store thermal energy, their performance is not constant in time. As a matter of fact, the rate at which energy is released or absorbed by these storage units decreases in time. This phenomenon is attributed to the resistive solid or liquid PCM layer that is gradually formed around the HTF pipe and fins as the discharging or charging process advances. In other words, as the solidification or melting front moves away from the surface where heat is removed from or introduced in the PCM domain, the heat rate (between the PCM-HCM assembly and the HTF) decreases. Hence, the energy content of the PCM domain is saturated as time advances (see Fig. 4.3). It should be noticed that this saturation process is intrinsic in the nature of any storage device. Thus, the potentiality of the proposed modelling approach is expected to be rather wide and far-reaching.

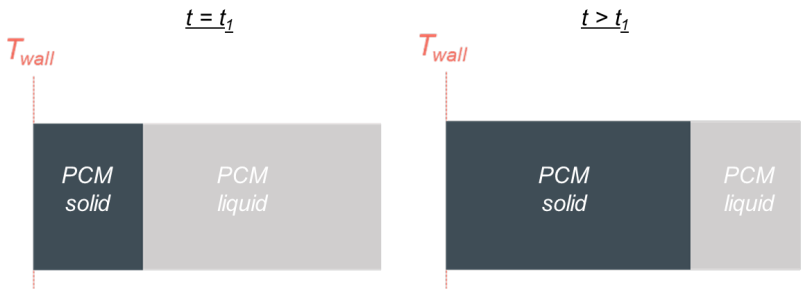

Fig. 4.3 Graphical representation of PCM transition inside LHTS systems

In the attempt to find a mathematical formulation that suits the abovementioned needs, it was observed that the PCM energy saturation process can be described through a suitable cumulative distribution function (CDF). Considering the discharging phase, the energy that a LHTS unit releases in time ($E_d(t)$) varies between zero and a maximum value. This quantity coincides with the amount of energy stored inside the LHTS at the beginning of the discharging process (ΔE_{tot}). If the discharged energy is normalized with respect to the LHTS energy content ($E_{d,n}(t)$), this quantity becomes a monotonically increasing function between 0 and 1 whose slope decreases in time, as shown in Fig. 4.4.

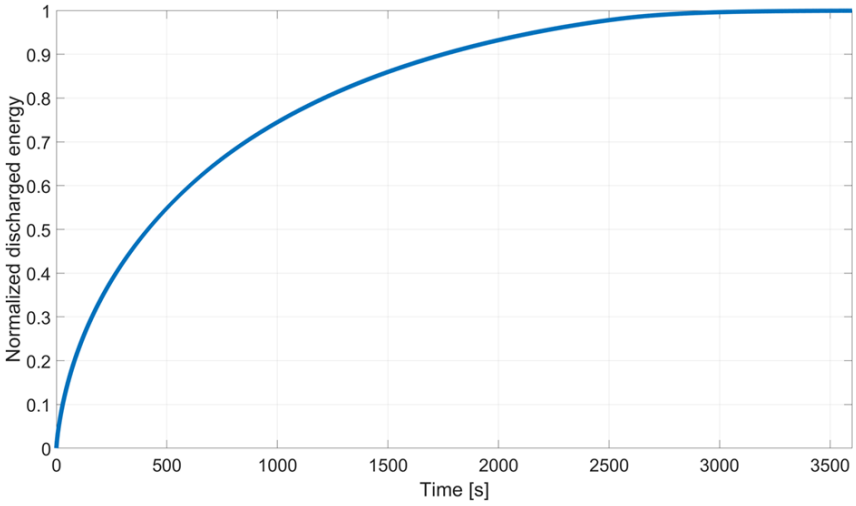

Fig. 4.4 Example of normalized discharged energy evolution in time

The slope of the curve (and consequently the time interval for reaching a full discharge condition) generally depends on three factors: the LHTS design, the operating boundary conditions, and the initial storage conditions. Considering the necessity to account for these variables, a general expression for a monotonically increasing CDF was identified in Eq. 4.3.

$$E_{d,n}(t) = \frac{E_d(t)}{\Delta E_{tot}} = 1 - exp\left[-\left(\frac{t}{\tau_0}\right)^{\beta}\right] \tag{4.3}$$

This expression is also known as the cumulative function for the Weibull distribution. One of the main advantages of this formulation consists in the necessity of defining only two parameters: the scale factor (τ_0) and the shape factor (β). Both of them strongly affect the slope of the curve. The following subsections (4.3.1 and

4.3.2) thoroughly describe their derivation based only on LHTS thermo-physical and geometrical variables, which are known a-priori. Incidentally, this aspect constitutes one of the most attractive features of the modelling approach proposed in this thesis because it is completely independent on experimental coefficients.

In order to link the models for the two subdomains (HTF and PCM-HCM assembly), an expression for the heat rate should be evaluated in Eq. 4.1. The thermal power released by the PCM-HCM assembly at each time instant corresponds to the time derivative of Eq. 4.3. As a result, also the temporal evolution of the LHTS thermal power $q_{LHTS}(t)$ depends on τ_0 and β, as shown by Eq. 4.4.

$$q_{LHTS}(t) = \Delta E_{tot} \frac{dE_{d,n}(t)}{dt} = \Delta E_{tot} \frac{\beta}{\tau_0} \left(\frac{t}{\tau_0}\right)^{\beta-1} exp\left[-\left(\frac{t}{\tau_0}\right)^{\beta}\right] \tag{4.4}$$

However, Eq. 4.4 may not be convenient for the calculation of the heat rate released by the PCM-HCM assembly towards the HTF. This is due to the fact that the independent variable in this equation is the time. The expression with the time variable is deemed to be reasonable only as far as the LHTS is constantly operated under the same boundary conditions (i.e., constant HTF inlet mass flow rate and temperature). In practice, however, operating boundary conditions might change during the storage discharging (or charging) process. Consequently, a more general formulation relating the available thermal power to the LHTS current state of charge (SOC) is preferred. To achieve this goal, a change of variable is performed. First of all, the mathematical expression for SOC is defined (Eq. 4.5). This is actually derived from Eq. 4.3. Then, as shown in Eq. 4.6, the time variable is made explicit from Eq. 4.5. Finally, substituting Eq. 4.6 into Eq. 4.4, a new expression for the thermal power is obtained (Eq. 4.7).

$$SOC(t) = exp\left[-\left(\frac{t}{\tau_0}\right)^{\beta}\right] \tag{4.5}$$

$$t = \tau_0 \left[ln\left(\frac{1}{SOC}\right)\right]^{\frac{1}{\beta}} \tag{4.6}$$

$$q_{LHTS} = \Delta E_{tot} \frac{\beta SOC}{\tau_0(T_{wall}, SOC_0)} \left[ln\left(\frac{1}{SOC}\right)\right]^{\frac{\beta-1}{\beta}} \tag{4.7}$$

It should be noticed that this expression has a meaning only for $0 < SOC \leq 1$. Even though the state of charge could be null in theory, this condition is extremely difficult to reach in practice. Hence, the constraint prescribing strictly positive SOC values is not supposed to have any practical implication. Indeed, as demonstrated by the experimental tests (see Chapter 5), the last 10-15% of the LHTS total energy content either requires a very long timespan to be recovered or it is released at low temperature. Thus, its practical value is rather questionable. Moreover, it should be remarked that the expression in Eq. 4.7 actually corresponds to a family of functions that can be referred as **thermal power characteristic curves**. This is due to the fact that the parameter τ_0 is actually dependent on the temperature at the contact wall (T_{wall}) and the initial state of charge (SOC_0), as demonstrated in section 4.3.1. In few words, these thermal characteristic power curves are able to describe the behaviour of a LHTS heat exchanger characterised by a specific design and operated under specific boundary conditions. As a result, the LHTS heat exchanger performance can be mapped through these curves after the definition of the scale factor τ_0 and the shape factor β.

4.3.1 Derivation of the time constant (τ_0)

In the framework introduced in the previous section, the scale factor τ_0 represents a time constant. By definition, this instant indicates the time needed by the PCM-HCM assembly to release 63.2% of its total energy content (see Eq. 4.8).

$$E_{d,n}(\tau_0) = \frac{E_d(\tau_0)}{\Delta E_{tot}} = 0.632 \tag{4.8}$$

Consequently, this parameter is an index for the LHTS speed of discharge: the lower the value of τ_0, the faster the discharging process. Several studies proved that the LHTS speed of discharge is largely influenced by the boundary conditions at which the LHTS unit is operated [148–150] and the heat exchanger design [106, 104]. Hence, the scale factor τ_0 can be expected to be correlated to these factors. For instance, assuming that the inner wall of the HTF pipe is kept at a constant temperature T_{wall} for the whole discharging process, the speed of discharge increases as T_{wall} decreases because of the higher temperature difference between the wall and the PCM phase change temperature (T_{pc}). Therefore, the two terms composing

Eq. 4.8, i.e. the total energy content ΔE_{tot} and the energy released after τ_0 seconds ($E_{d,n}(\tau_0)$), are expressed as a function of the abovementioned influential factors.

The total energy stored in the LHTS (ΔE_{tot}) is the sum of the initial PCM and HCM energy content (Eq. 4.9). Both the HCM sensible energy content and the PCM sensible and latent energy content are evaluated between the initial homogeneous temperature ($T_{PCM,0}$) and the minimum temperature at which the PCM-HCM assembly could be theoretically cooled down (i.e., T_{wall}). All the terms in Eq. 4.9 can be easily retrieved from the thermo-physical characteristics of the employed materials, except for the value of the LHTS initial state of charge (SOC_0). Although this term can obviously vary between 0 and 1 depending on the duration of the preceding charging process, most of the application cases of interest begin the LHTS discharging process only after a full charge of the storage. As a result, SOC_0 is often equal to 0.95÷1 at the beginning of a new storage discharge, even though the methodology proposed in this thesis does not exclude other cases a-priori.

$$\Delta E_{tot} = \rho_{PCM} V_{PCM} SOC_0 \left[\int_{T_{wall}}^{T_{PCM,0}} c_p dT + \Delta h_{lat} \right] \tag{4.9}$$

On the contrary, the energy discharged after the time interval τ_0 ($E_d(\tau_0)$) is estimated through an average thermal power (q_{avg}) released by the PCM-HCM assembly towards the HTF within that time span (Eq. 4.10).

$$E_d(\tau_0) = q_{avg}\tau_0 \tag{4.10}$$

However, the subsequent estimation of q_{avg} requires some approximations and dimensional analyses to be expressed. In the LHTS discharging phase, heat is mainly transferred by conduction [151, 15, 104], apart from a brief initial transitory where natural convection is also appreciable. Moreover, the relevance of the conductive mechanism is evident when the LHTS heat exchanger design is particularly compact, such as the longitudinal configuration presented in Chapter 3. Furthermore, the PCM thermal resistance is predominant compared to the one of the HCM. Hence, the average heat flux during the time interval represented by τ_0 is assumed to be approximated by the conductive heat flux across a PCM layer of thickness l_c (see Eq. 4.11), where l_c is an estimate for the average PCM thickness around the HTF pipe and fins. Thus, l_c represents a characteristic length that depends on the LHTS

heat exchanger design. From a dimensional point of view, l_c is a length that can be expressed as $l_c = V_{PCM}/A_{contact}$ (where $A_contact$ is the total contact area between the HCM fins and the PCM). As far as the driving temperature difference is concerned, the meaningful quantities in the first half of the discharging process are deemed to be the wall temperature (T_{wall}) and the initial PCM temperature (T_0).

$$q_{avg} = \frac{k_{PCM}}{l_c} A_{contact}(T_0 - T_{wall}) \tag{4.11}$$

As a result, substituting Eq. 4.11 into Eq. 4.10 and then substituting this result together with Eq. 4.9 into Eq. 4.8, Eq. 4.12 is obtained. As can be seen, the time constant τ_0 can be expressed as a function of:

- The geometrical features of the LHTS heat exchanger (l_c)
- The initial condition of the PCM (SOC_0 and $T_{PCM,0}$)
- One of the most relevant parameters driving the heat exchange between the HTF and the PCM (i.e., T_{wall})

Therefore, considering that the LHTS geometrical features and initial conditions are known before performing the LHTS dynamic simulation, such an expression for τ_0 allows to estimate the thermal power released by the PCM-HCM assembly towards the HTF (see Eq. 4.12) at each time step only as a function of the equilibrium contact wall temperature T_{wall} (the SOC, which represents the other independent variable, is actually known at the beginning of each simulation time step).

$$\tau_0 = \frac{\rho_{PCM}\, l_c^2\, SOC_0 \left[\int_{T_{wall}}^{T_{PCM,0}} c_p dT + \Delta h_{lat}\right]}{k_{PCM}(T_{PCM,0} - T_{wall})} \tag{4.12}$$

To conclude this section, it should be mentioned that this modelling approach for τ_0 is deemed to be valid when the initial PCM condition is homogeneous. However, in few cases this might not be the actual initial condition. For example, when a LHTS unit is partially charged and then immediately discharged, only a smaller layer of PCM is liquid around the LHTS fins. Regions that are far from the fins instead remain solid. In such a case, the initial state of charge (SOC_0) will certainly be lower than 1 and the time constant τ_0 will be reduced. However, to be consistent with the presented modelling approach also the PCM characteristic length is deemed to be

reduced because the active PCM quantity allocated to each pipe is actually lower compared to the case in which the LHTS is fully charged and the PCM condition is homogeneous. Therefore, an additional factor multiplying l_c in Eq. 4.12 could be introduced to account for non-homogeneous PCM initial conditions. Unfortunately, it was not possible to verify this conjecture during the experimental campaign, thus the introduction of such an additional coefficient is here only mentioned for possible further model improvement.

4.3.2 Derivation of the shape factor (β)

As far as the shape factor β is concerned, a value lower than or equal to 1 is expected because it guarantees a monotonic decreasing behaviour in time for the discharged thermal power curve (Eq. 4.4). As a matter of fact, if β is set larger than 1 the mathematical curve describing the thermal power would present an inflection point, which is not realistic. The effect of this parameter is mostly visible in the second half of the discharging process (see Fig. 4.5). The shape factor affects the final time at which the LHTS energy content is completely released (i.e., the end of the discharging process).

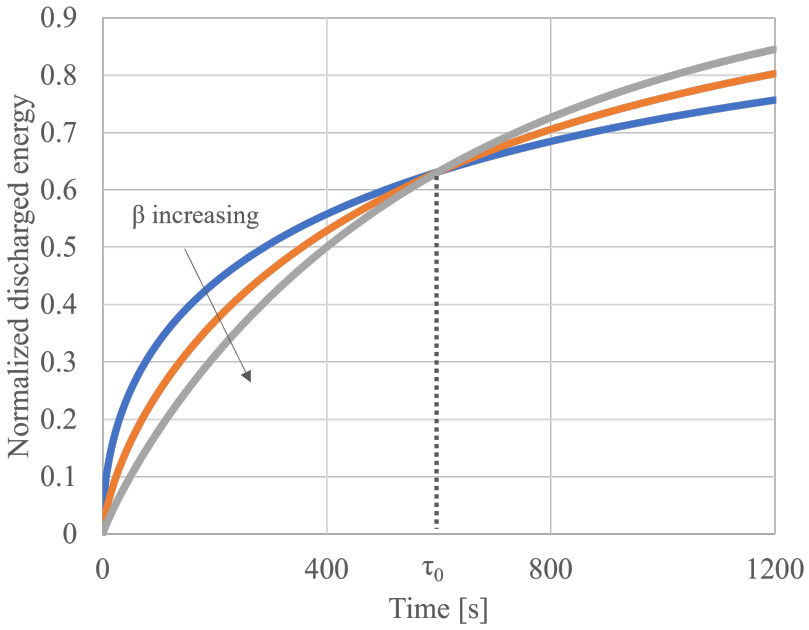

Fig. 4.5 Effect of different shape factor values on the normalized discharged energy evolution

Our intuition is that the value of the shape factor depends on the proportion between the PCM and HCM mass contained in the LHTS heat exchanger. Indeed, the HCM mass (M_{HCM}) speeds up the discharging process due to its high thermal conductivity. On the contrary, the PCM mass (M_{PCM}) slows down this process because its thermal conductivity is several orders of magnitudes lower than the one of the HCM. Moreover, this latter effect is expected to be increasingly relevant as the LHTS discharging phase proceeds. In fact, it is increasingly difficult to extract energy from the PCM mass as a solid PCM layer thickens between the pipe and furthest PCM regions. Therefore, the shape factor β is set to be the "weight" that the PCM mass has over the total LHTS heat exchanger mass, as shown in Eq. 4.13.

$$\beta = \frac{M_{PCM}}{M_{PCM} + M_{HCM}} \tag{4.13}$$

Differently from the characteristic time τ_0, β is always constant because it only depends on the LHTS composition. Indeed, for the two LHTS prototypes described in Chapter 3 β is equal to 0.8 because they have the same values of M_{PCM} and M_{HCM}, even though these two quantities are differently distributed. To conclude, it should be remarked that an alternative path to express this value would be through an experimental calibration. As a matter of fact, this constituted the author's initial intention because the absence of a dimensional meaning of β did not provide any hint for this parameter estimation. However, this approach would have undermined the initial idea of providing a dynamic LHTS model completely independent on experimental calibrations. The intuition described in this section proved to be accurate enough, as demonstrated by the comparison between the numerical and experimental results in Chapter 5. Consequently, a further experimental calibration of the shape factor was not deemed necessary.

4.4 Model solution algorithm

This section describes how the model for the HTF pipe domain (section 4.2) and the model for PCM-HCM assembly (section 4.3) are coupled in order to achieve the ultimate goal of simulating the behaviour of a shell-and-tube LHTS from a system perspective. The problem stated by Eq. 4.1 is solved numerically by means of a *Python* script. The adopted solution algorithm is represented in Fig. 4.6.

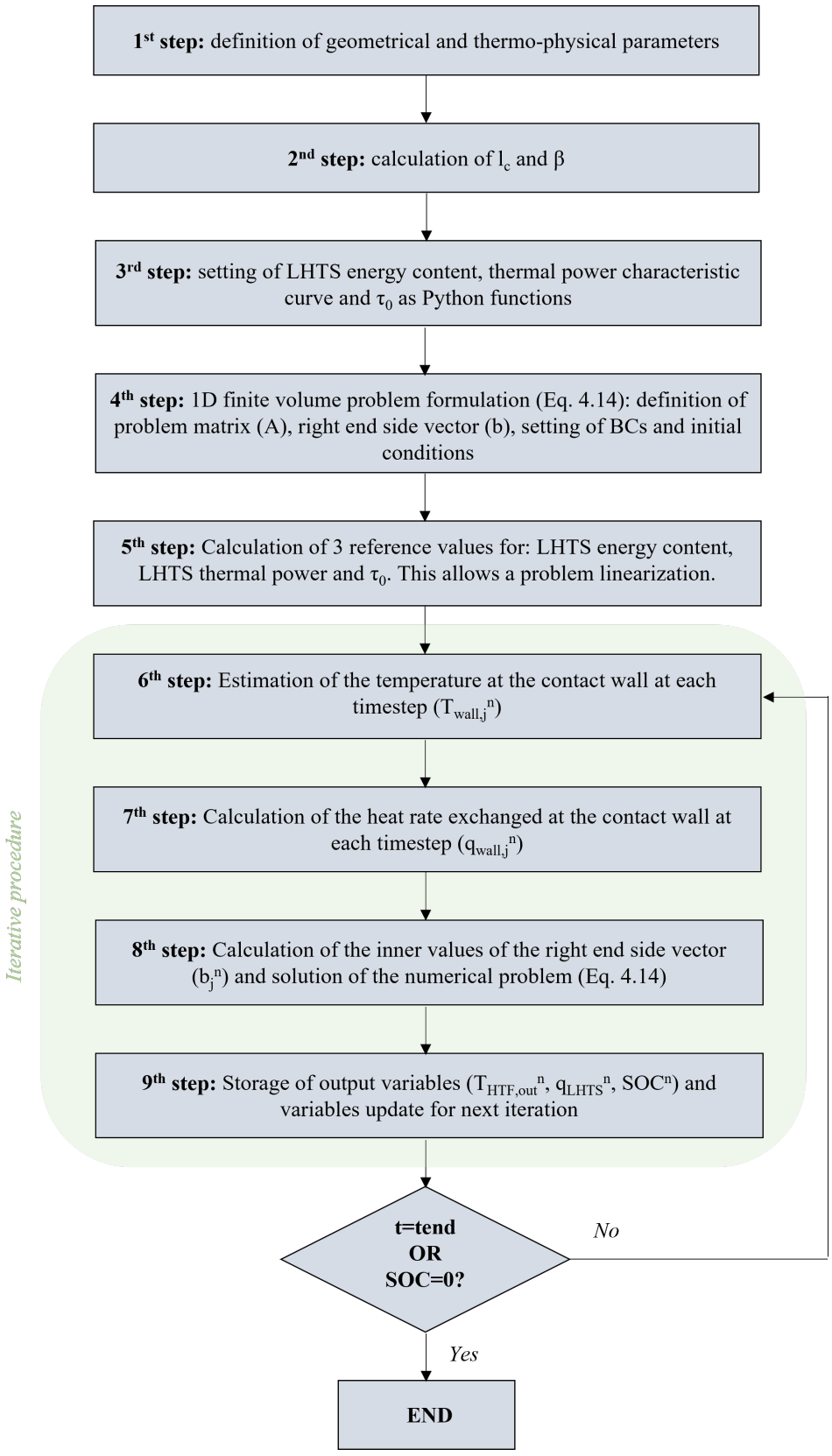

Fig. 4.6 Flow chart of the solution algorithm

The first step of the proposed methodology is constituted by the definition of the geometrical features of the LHTS unit and the thermophysical properties of the employed materials (both the PCM and the HCM). After that, two invariable key parameters are calculated: the PCM characteristic length (l_c) and the shape factor β (Eq. 4.13). Successively, three crucial quantities are defined as *Python* functions. These are:

- The LHTS energy content (see Eq. 4.9);
- The LHTS thermal power characteristic curve (see Eq. 4.7);
- The time constant τ_0 (see Eq. 4.12).

It is particularly important to define the LHTS energy content as a function because this allows to set an ideal discharge ending condition at each timestep. As a matter of fact, the total amount of energy that can be released by the LHTS unit depends on the inlet HTF temperature due to the PCM sensible energy content. Ideally, a LHTS unit is completely discharged when the PCM temperature is in equilibrium with the entering HTF temperature.

The fourth step coincides with the classical one-dimensional finite volume problem formulation (Eq. 4.14) to be solved at each simulation timestep. Consequently, the HTF pipe domain is discretized in smaller intervals. In this case the selected discretization interval Δz is set equal to 0.01 m. Then, the problem matrix A and the right end side vector b are built including the inlet and outlet boundary conditions. The quantities of interest are also initialized. It should be mentioned that the discretized version of the problem represented by Eq. 4.1 yields a sparse matrix. Hence, a suitable *Python* library is used to optimise the memory allocation and speed up the calculations in such a sparse problem.

$$A^n \cdot T^n_{HTF} = b^n \tag{4.14}$$

The fifth step consists in the definition of ΔE_{ref}, $\tau_{0,ref}$ and q_{ref}, which are three general reference values allowing to linearize the problem solution in the successive steps. These quantities are evaluated according to Eq. 4.9, Eq. 4.12 and Eq. 4.7 by setting T_{wall} to a reference temperature of 20°C (T_{ref}). This value does not influence the results and it can be freely chosen by the user as long as it is much lower than the PCM solidification temperature.

At this point of the solution algorithm, it is possible to calculate the HTF temperature distribution along the pipe ($T^n_{HTF,j}$) at each time step (n) though a cyclic procedure. In few words, the aim of this cyclic loop is to find a solution for Eq. 4.14 at each time step. To do that, the inner terms of the right-end side vector b must be evaluated at each time step because they depend on the thermal power that is exchanged between the HTF domain and the PCM-HCM domain. First of all, the temperature at the contact wall $T^n_{wall,j}$ is estimated considering that the dependence between $q^n_{wall,j}$ and $T^n_{wall,j}$ (expressed by Eq. 4.7) is linear when the SOC value is fixed, i.e. at each time step (see Fig. 4.7).

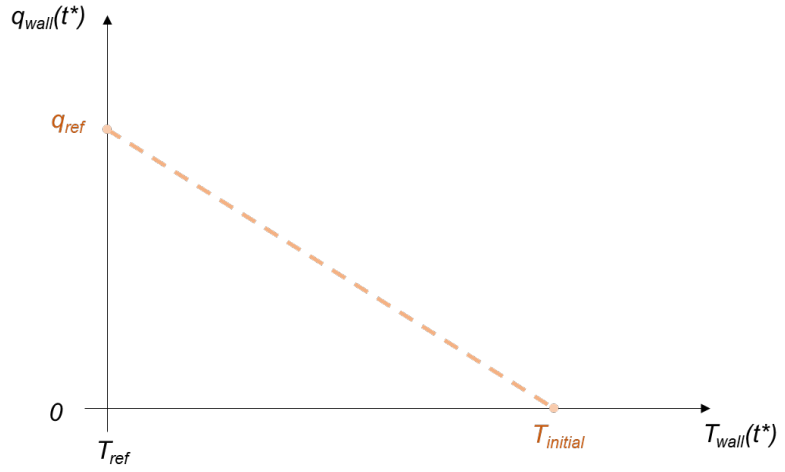

Fig. 4.7 Linearization of the heat rate exchanged at the contact wall between the HTF domain and the PCM-HCM domain

The thermal power exchanged at the contact wall ($q^n_{wall,j}$) can be thus expressed through the following linear relation (Eq. 4.15) imposing an a priori reference value (q_{ref}):

$$q^n_{wall,j} = q_{ref} - q_{ref}\frac{T^n_{wall,j} - T_{ref}}{T_{PCM,0} - T_{ref}} \tag{4.15}$$

However, $q^n_{wall,j}$ can be also expressed considering the HTF pipe domain through Eq. 4.16. Here the driving temperature difference is evaluated as a function of the HTF axial temperature at the previous time step ($T^{n-1}_{HTF,j}$) in order to avoid an implicit iterative procedure that could lead to possible instabilities in the solution algorithm.

The other parameters in this equation are the heat transfer coefficient h_{conv} and the lateral external surface of each HTF pipe discretized volume ($A_{lat,j}$).

$$q^n_{wall,j} = h_{conv} A_{lat,j} (T^n_{wall,j} - T^{n-1}_{HTF,j}) \tag{4.16}$$

As a result, combining Eq. 4.15 and Eq. 4.16, $T^n_{wall,j}$ can be calculated at the beginning of each time step through the following formula (Eq. 4.17):

$$T^n_{wall,j} = \frac{q_{ref} - \frac{T_{ref} q_{ref}}{T_{ref} - T_{PCM,0}} + h_{conv} A_{lat,j} T^{n-1}_{HTF,j}}{h_{conv} A_{lat,j} - \frac{q_{ref}}{T_{ref} - T_{PCM,0}}} \tag{4.17}$$

Then, the heat exchanged at the wall $q^n_{wall,j}$ is calculated according to Eq. 4.16. The advective heat transfer coefficient h_{conv} is evaluated through the thermal conductivity of the HTF (k_{HTF}), the pipe inner diameter (d_i) and the Nusselt non-dimensional number (Eq. 4.18). This, in turn, is estimated either by means of the Dittus-Boelter correlation (Eq. 4.19) when the HTF flow is turbulent or by the correlation for laminar flows with an entry length (Eq. 4.20) [152].

$$h_{conv} = \frac{k_{HTF} Nu}{d_i} \tag{4.18}$$

$$Nu = 0.023 Re^{4/5} Pr^n \quad with\ n = 0.4(discahrge);\ 0.3(charge) \tag{4.19}$$

$$Nu = 3.66 + \frac{0.0668(d_i/z) RePr}{1 + 0.04(d_i/z) RePr)^{2/3}} \tag{4.20}$$

Consequently, the inner values of the right-end side vector (b^n_j) can be expressed through Eq. 4.21. As a result, the HTF temperature distribution at each time step ($T^n_{HTF,j}$) is obtained applying *Python*'s sparse linear algorithm [153] to Eq. 4.14.

$$b^n_j = T^{n-1}_{HTF,j} + \frac{\Delta t}{\rho_{HTF} c_{p,HTF} A_{lat,j} \Delta z} q^n_{wall,j} \tag{4.21}$$

Before exiting the loop, the output variables of interest are stored. These are:

- the **HTF outlet temperature** (i.e., the last value of $T^n_{HTF,j}$);
- the **total LHTS heat rate** (q^n_{LHTS}), which is calculated as: $q^n_{LHTS} = n_{pipes} \sum q^n_{wall,j}$;
- the **LHTS state of charge** (SOC^n), which is calculated as the average state of charge of all the PCM-HCM small volumes associated to each HTF domain discretized volume.

Moreover, several quantities are updated for the following iteration. These are: the total LHTS energy content, the LHTS state of charge and the HTF temperature distribution ($T^n_{HTF,j} - 1 = T^n_{HTF,j}$). If there is a change in the inlet boundary conditions (in terms of HTF temperature and/or mass flow rate), also the following quantities are updated: $T_{HTF,j=0}$, the inlet velocity u and h_{conv} (which depends on the new mass flow rate value). In this case, also the terms in the matrix A and right-end side vector b depending on $T_{HTF,j=0}$ and u are updated. The full script of the proposed model is available at the following online repository [154]. The following sections demonstrate the excellent performance that the proposed solution algorithm possesses both in terms of reduced computational times and results accuracy.

4.5 Model accuracy vs. computational time: benchmark with a 3D LHTS numerical model

The LHTS dynamic model presented in the previous sections is characterised by two main advantages. On the one hand, it only relies on thermo-physical parameters that can be easily retrieved from the specifications of the storage unit that one intends to model. On the other hand, it gives fast and accurate results, which is an essential requirement when simulating the storage unit at the system level. Concerning the latter aspect, the dynamic model output is compared with the results of a 3-dimensional shell-and-tube LHTS numerical model as a benchmark for the computational time. In the upcoming chapter, the dynamic model accuracy is also discussed in light of several experimental results (see Chapter 5).

4.5.1 3D numerical model for a LHTS heat exchanger with longitudinal fins

Only the shell-and-tube LHTS tank with longitudinal fins presented in chapter 3 is here considered. The features of its 3-dimensional model are here summarised. The physical problem involving the discharging phase of the storage under study is solved through the finite volume method implemented in the commercial code Ansys Fluent (2020 R2). The computational domain is presented in Fig. 4.8, which actually represents a reduced domain thanks to the thermal and geometrical symmetry of the assembly.

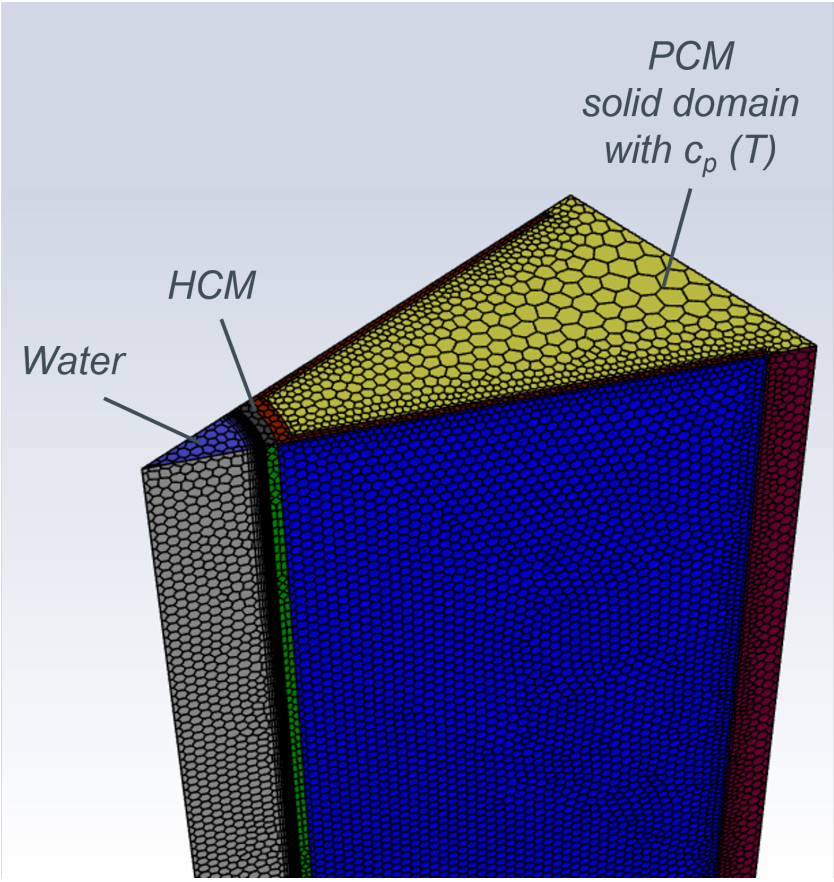

Fig. 4.8 Mesh of the LHTS 3-dimensional domain

Natural convection phenomena in the PCM are assumed to be negligible due to the LHTS compact design [104]. Hence, the continuity and momentum equations are only applicable to the HTF domain (Eq. 4.22 - 4.23). The water fluid-flow regime

is turbulent in all the analysed case studies. Thus, the $k-\omega$ turbulence model is here adopted [155]. On the contrary, the energy equation is applicable to the whole computational domain (Eq. 4.24). However, the solidification process of the PCM requires specific attention. Hence, the PCM domain is treated as a solid material whose heat capacity is expressed as a function of the temperature as shown in Fig. 4.9 (apparent heat capacity method). With this method the PCM latent heat content involved in the solidification process is accounted through the imposed large value of the PCM heat capacity in proximity of its solidification temperature.

$$\nabla \cdot \mathbf{u} = 0 \tag{4.22}$$

$$\rho \frac{\partial \mathbf{u}}{\partial t} + \rho \mathbf{u} \cdot \nabla \mathbf{u} = -\nabla p + \mu \nabla^2 \mathbf{u} \tag{4.23}$$

$$\frac{\partial (\rho H)}{\partial t} + \nabla \cdot (\rho \mathbf{u} H) = \nabla \cdot (k \nabla T) + S \tag{4.24}$$

Where the enthalpy H is calculated as:

$$H = H_{ref} + \int_{T_{ref}}^{T} c_p dT \tag{4.25}$$

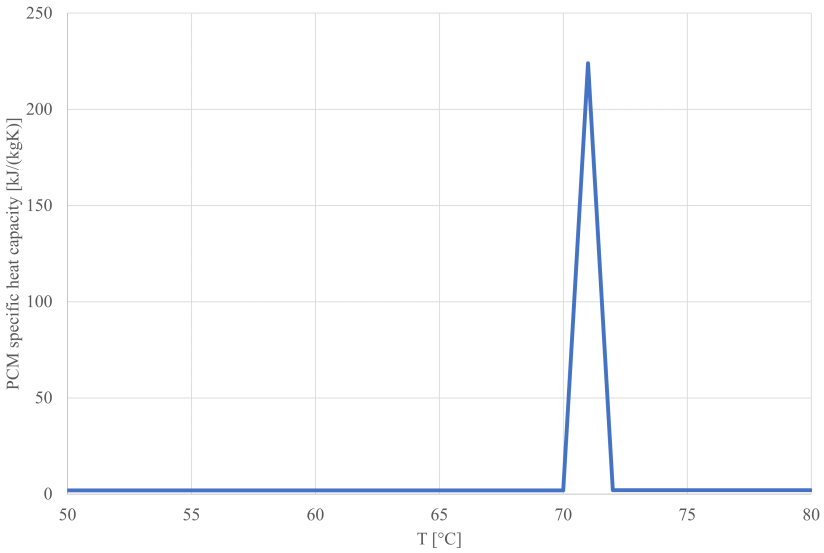

Fig. 4.9 Apparent heat capacity accounting for PCM latent heat

As far as the boundary conditions are concerned, adiabatic walls are considered on the top, bottom and external faces of the PCM-HCM assembly; symmetry is imposed on the lateral faces of all the subdomains; the entrance of the HTF is represented as a velocity inlet, while the fluid exit is modelled as a pressure outlet. The computational grid consists of a non-structured polygonal mesh. Particular attention was devoted to the identification of a suitable number of prism layers at the wall of the HTF domain through a preliminary study. As a matter of fact, the HTF domain constitutes only part of the total computational domain. However, the influence of the HTF domain mesh on the overall results is relevant. For this reason, a steady state simulation of the HTF pipe alone with a fixed wall temperature was first performed. The optimal mesh identified with this preliminary study was then used for the transient simulation where also the PCM and fins domains are present. More specifically, 20 prism layers at the contact wall between the HTF domain and the PCM-HCM assembly proved to be the best trade-off between accuracy and computational time. Furthermore, the estimated Nusselt number using the identified mesh falls within the range of the correlations proposed by Dittus-Boelter, Gnielinski and Sieder-Tate [152]. Overall, also the entire mesh for the total computational domain (see Fig. 4.8) proved to be sufficiently fine not to influence the results. In particular, four meshes with decreasing average cell side were tested for the PCM-HCM assembly coupled to the previously identified grid for the HTF domain. The spatial discretisation is performed with Second Order Upwind schemes except for the turbulent kinetic energy and the specific dissipation rate equations, which are discretised with a First Order Upwind scheme. The gradient calculation is computed with the Least Square Cell method. As far as the solution method is concerned, the SIMPLE algorithm is used for the pressure-velocity coupling. Convergence is assumed to be reached when the residuals are lower than 10^{-3}. Finally, the transient nature of the problem is approached with a First Order Implicit Euler method, with a time-step of 1 s. This value proved to be sufficiently fine not to influence the results.

4.5.2 Benchmark results

This section compares the results between the 1-dimensional dynamic model and the 3D LHTS numerical model previously introduced. The results here presented are intended as an initial benchmark for the 1D dynamic model. As a matter of fact, this analysis was developed while the experimental facility was still under construction

in an attempt to gain useful insights on the simplified model performance and anticipate possible drawbacks before the experimental campaign. Moreover, this section aims at highlighting the relevant gains in the overall computational time provided by the 1D dynamic model whenever system-level quantities (such as the water outlet temperature and the LHTS state of charge) constitute the scope of the modeller's analysis. Consequently, the time evolution of the above-mentioned LHTS quantities (i.e., $T_{HTF,out}$ and SOC) are here represented for both the models under the same initial and boundary conditions. The initial condition is constituted by a fully charged LHTS storage, implying that all the simulation domains are set at an initial temperature equal to 80 °C. Instead, the boundary conditions are represented by the inlet water temperature (always fixed at 50 °C) and variable values for the inlet water mass flow rate. Regarding the latter parameter, this is maintained constant within each test, but several flow conditions are tested. More specifically, these are three turbulent flow conditions (Re = 6700, Re = 16900 and Re = 28000) and one laminar flow condition (Re = 840). Obviously, the laminar case excludes the k-omega turbulence model for the HTF fluid flow.

As can be seen from Figs. 4.10 - 4.12, the 1D dynamic model appears pretty accurate when the time evolution of the HTF outlet temperature and the LHTS state of charge are monitored. In the turbulent cases, the 1D dynamic model overestimates the LHTS state of charge towards the end of the discharging process. This might be due to the diffusive behaviour of the 1D model, which smears out the final discharging time by its own nature. As a result, the overall discharging process appears slightly slower compared to the 3D model. However, this deviation is not particularly relevant considering that in practice most of the useful energy content of the LHTS has already been released when its state of charge drops below 15-20% (indeed, at this stage the HTF has a temperature increase lower than 1°C compared to its inlet value). As far as the laminar case is concerned (Fig. 4.13), the 1D model still appears to perform well compared to the 3D model. One of the most relevant differences concern the absence of a peak in the HTF outlet temperature at the very beginning of the discharging phase. This might be due to a faster advection process in the 1D model. However, this aspect is not deemed particularly interesting considering that the overall LHTS state charge compares well between the two models. Regarding this latter quantity, it should be noticed that the 1D model predicts a slightly faster discharge. This is probably due to the fact that when the

HTF fluid flow is laminar the thermal resistance of the HCM composing the pipe shell and the fins may not be completely negligible.

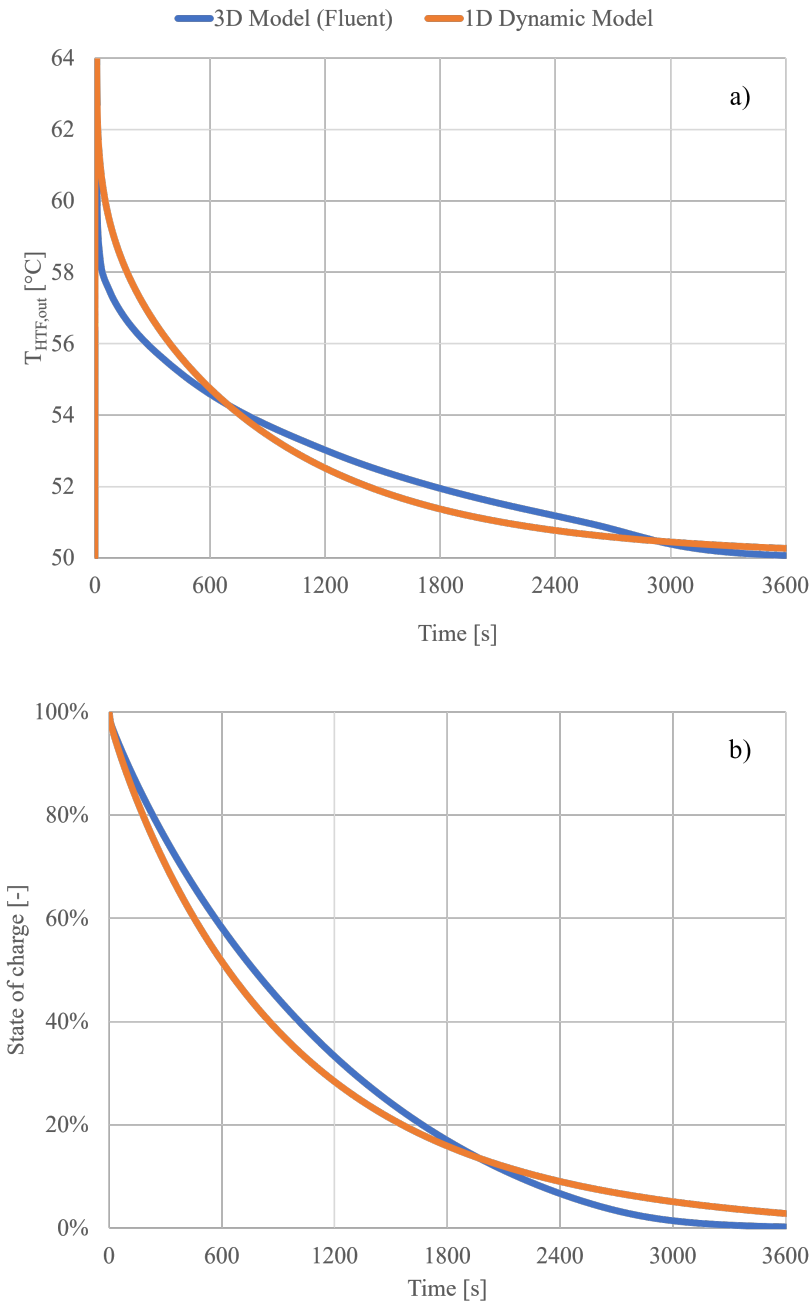

Fig. 4.10 Comparison between 3D and 1D model outputs (Re = 6700): (a) HTF outlet temperature; (b) LHTS state of charge

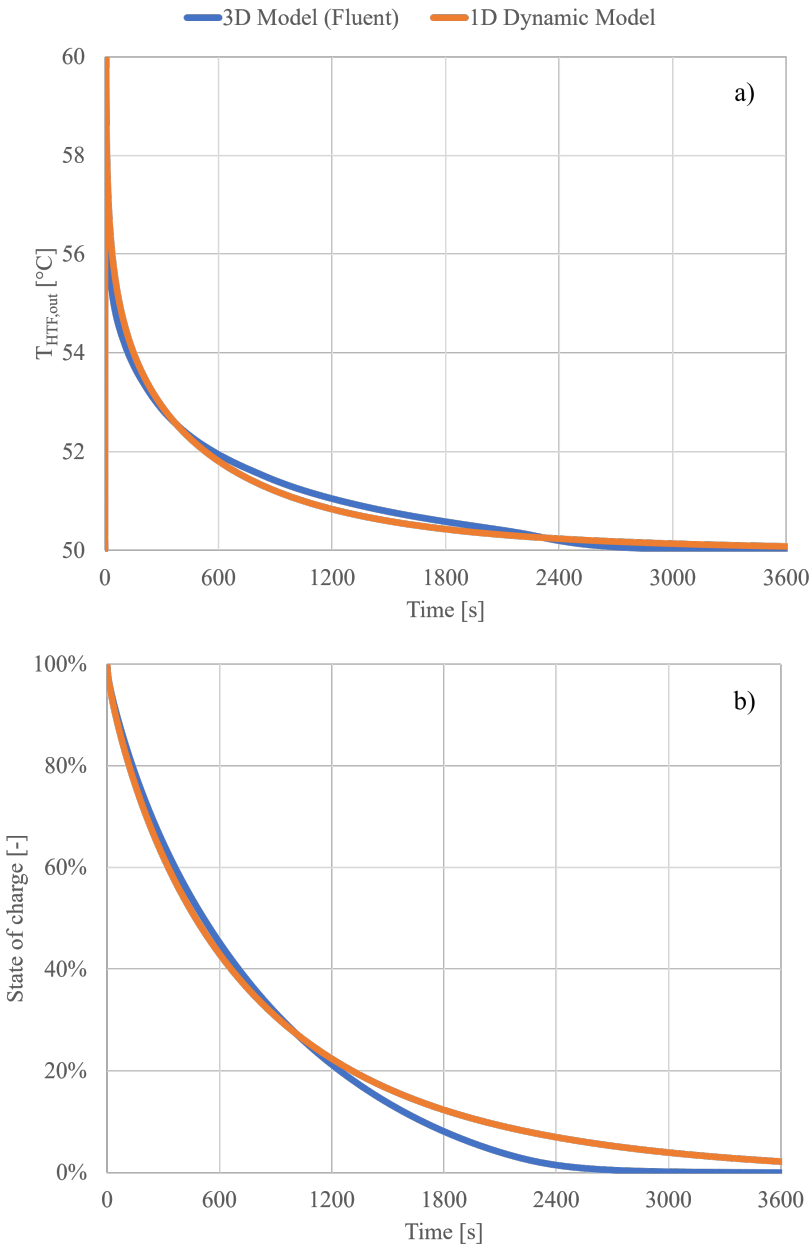

Fig. 4.11 Comparison between 3D and 1D model outputs (Re = 16900): (a) HTF outlet temperature; (b) LHTS state of charge

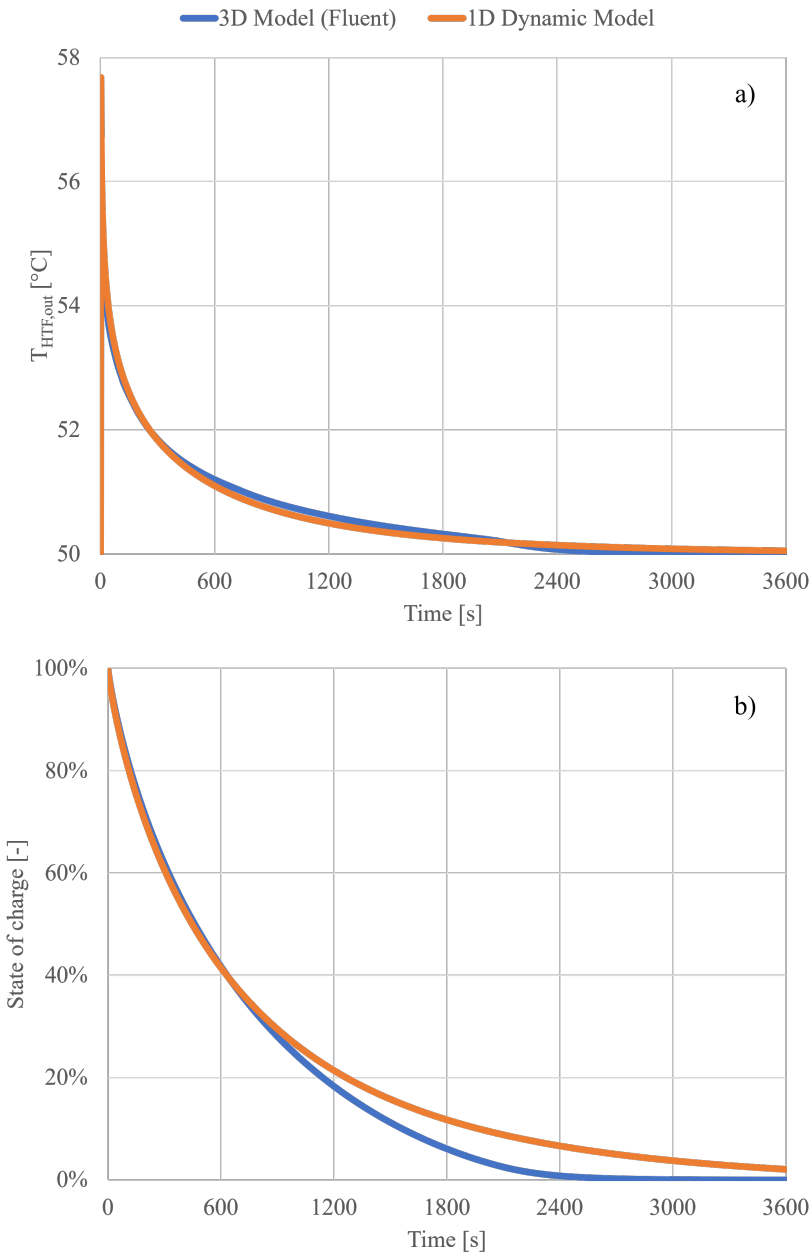

Fig. 4.12 Comparison between 3D and 1D model outputs (Re = 28000): (a) HTF outlet temperature; (b) LHTS state of charge

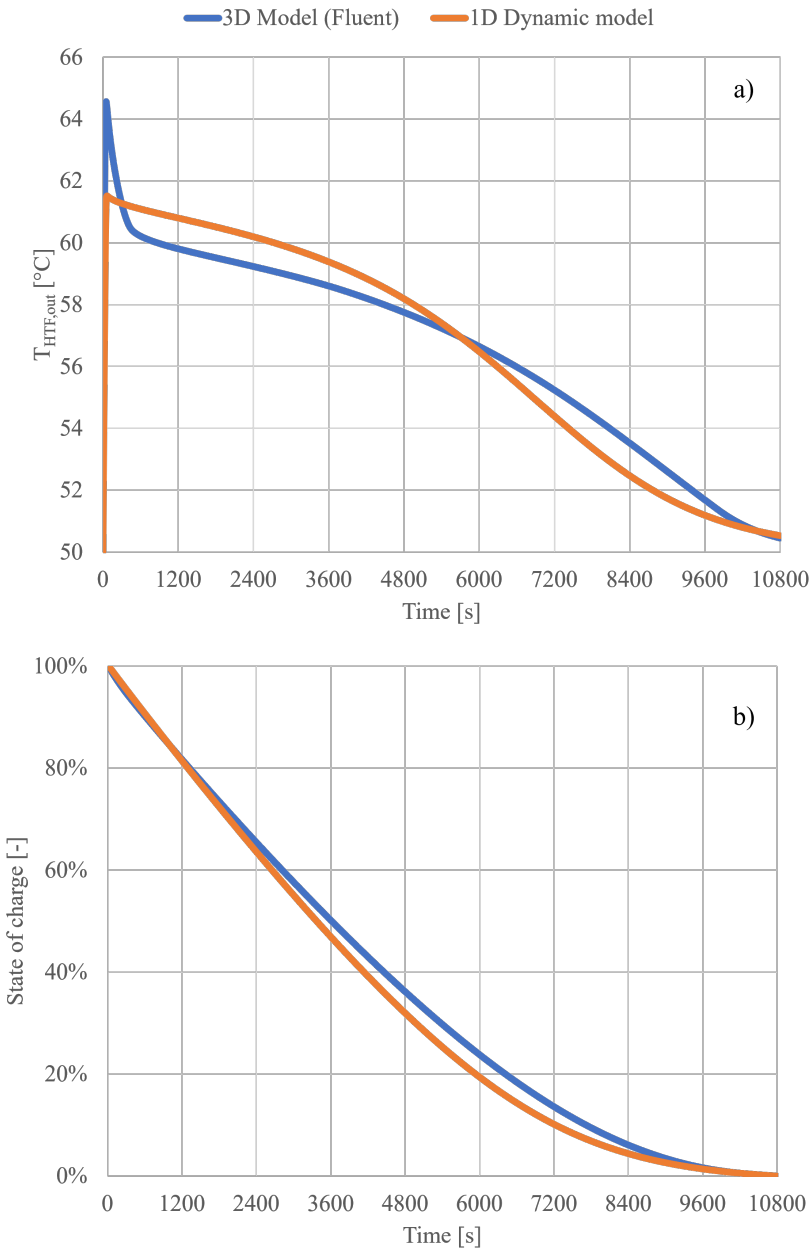

Fig. 4.13 Comparison between 3D and 1D model outputs (Re = 840): (a) HTF outlet temperature; (b) LHTS state of charge

Overall, Fig. 4.14 shows the average relative errors along the time simulation interval of the 1D dynamic model with respect to the 3D model concerning the water outlet temperature and the discharged energy. The relative error is calculated according to Eq. 4.26. At higher HTF inlet mass flow rates (i.e., $Re > 6700$) the 1D

dynamic model appears more accurate, even though the error of the dynamic model is pretty acceptable also when the HTF inlet mass flow rate is lower ($Re < 6700$). This is due to the fact that the time evolution of the heat transfer rate between the HTF and the PCM-HCM assembly is very well represented by the thermal power characteristic curves described in section 4.3 when the HTF inlet mass flow rate is intense. On the contrary, when the HTF inlet velocity is reduced, the heat transfer is slower and its time evolution curve presents a plateau due to the almost constant temperature of the PCM during its solidification process.

$$Rel.\ error = \frac{|y_{3D}(t) - y_{1D}(t)|}{y_{3D}(t)} \tag{4.26}$$

Where: $y_{3D}(t)$ is the quantity of interest at time t calculated with the 3D model, while $y_{1D}(t)$ is the quantity of interest at time t calculated with the 1D dynamic model.

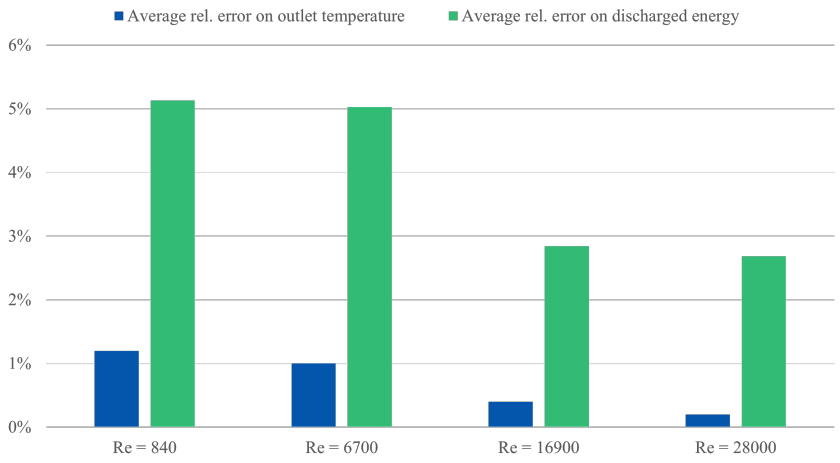

Fig. 4.14 Relative errors between 3D and 1D results on $T_{HTF,out}$ and discharged energy over different flow regimes

Concerning the computational time, the presented simulations were implemented in the commercial software Matlab® R2020a (for the 1D dynamic model) and Ansys Fluent 2020 R2 (for the 3D numerical model). These simulations were run on an 8-core CPU (Intel i7-9700 CPU @ 3.00 GHz, 16 GB RAM). The computational times for the presented cases are summarised in Table 4.1. As already anticipated, when the modeller's interest is computing the most relevant quantities from a system integration perspective, the 1D dynamic model proposed in this study has a remark-

able advantage over the 3D numerical modelling approach. Hence, the 1D dynamic model could be also used as a first step in the LHTS design process. Successively, the 3D numerical modelling approach could be integrated for a punctual design of the fins shape.

Table 4.1 Computational time: LHTS 3D numerical model vs. 1D dynamic model

	Re = 840	**Re = 6700**	**Re = 16900**	**Re = 28000**
3D numerical model	9h 25min	5h 40 min	5h 23min	5h 15min
1D dynamic model	1.6s	0.90s	0.87s	0.79s

4.6 Key findings of the present chapter

This chapter presented an original 1-dimensional dynamic model to simulate the behaviour of shell-and-tube LHTS units from a system perspective with a low computational effort. The strengths of the proposed model formulation can be summarised as follows:

1. The modelling approach is rather general and entirely based on a-priori known physical and geometrical parameters that do not require any experimental calibration (although this practice could still be implemented in the modelling approach in case some physical or geometrical parameters are not available);
2. The computational effort is extremely low compared to more complex 3D models;
3. The model results are reliable concerning the most relevant quantities from a heating system integration perspective (i.e., HTF outlet temperature and LHTS state of charge). This aspect is further proved in the next chapter.

The full script of the proposed model is available at the following online repository [154].

In few words, such a modelling approach has the potential to support the following activities:

- The determination of an LHTS optimal size tailored on the specific needs of the examined heating system (**design phase**);
- The simulation of LHTS control strategies and relative effects on residential heating systems (**operational phase**).

Chapter 5

Experimental analysis

This chapter thoroughly presents the experimental analysis related to the two LHTS units described in Chapter 3. The outcomes of the experimental campaign are used for two different purposes:

- The validation of the dynamic model presented in Chapter 4;
- The comparison of the two LHTS performance considering that they are characterised by a different internal heat exchanger design.

Section 5.1 provides an overview of the methodology adopted to validate the dynamic model presented in this thesis. The boundaries of the experimental campaign are here clarified.

Section 5.2 validates the LHTS dynamic model by comparing the simulated and measured outcomes under different input conditions. This section addresses the discharging phase of both the "Longitudinal" and "TopOpt" LHTS units.

Section 5.3 aims at proving the reliability of the modelling results by analysing several "Longitudinal" LHTS discharges performed in a restricted period of time and characterised by very similar input and environmental boundary conditions.

Section 5.4 compares the performance of the "Longitudinal" and "TopOpt" LHTS units under similar input conditions.

Eventually, section 5.5 summarises the key findings of this chapter.

5.1 Overview on the 1D dynamic model validation process

Several rounds of tests were carried out with the aim of validating the 1D dynamic model presented in the previous chapter. Since the LHTS performance mainly depends on the inlet HTF mass flow rate and the inlet HTF temperature, the experimental tests were categorized around these two inputs. As already presented in section 4.4, the 1D dynamic model is also conceived in such a way that the inlet HTF mass flow rate and temperature constitute a model input that can be updated at each timestep. Although the presented dynamic model could be theoretically used for the simulation of both the LHTS charging and discharging phases, this section validates only the model discharging mode. The reason for this restriction is twofold. On the one hand, the presented modelling approach was initially conceived targeting the discharging phase because of the higher application interest of this operational mode (for instance when considering the reduction of the morning energy peak in DH networks). On the other hand, during the experimental tests the LHTS units were mostly charged at a constant power rate via an electric resistance because the district heating substation dedicated to the laboratory could not be employed for maintenance. In such a case, the proposed modelling approach is meaningless because the charging power (and consequently the HTF temperature difference and LHTS state of charge) can be calculated a priori. On the contrary, it would have been interesting to analyze the model performance if a hot HTF stream with a fairly constant temperature (higher than the PCM phase change temperature) was available.

The discharge testing conditions were selected based on the following considerations. As far as the HTF mass flow rate is concerned, this parameter was regulated by means of the variable-speed pump installed in the experimental loop and the two manual flow controller valves disposed on each LHTS branch (see section 3.3). Three levels of HTF mass flow rates were reproduced (low, medium and high) roughly between 1400 l/h and 2500 l/h. These operational values were selected analyzing the mass flow rate adopted in the secondary side of the district heating network in Turin. When the user heated building volume is between 2000-3000 m^3 (for which a 40-kWh LHTS unit would be suitable), the HTF mass flow rate circulating in the heating system of the building is generally comprised between 1400 l/h and 2500 l/h. Hence, these two boundaries were taken as a reference. Instead, the HTF

temperature at the inlet of each LHTS unit was indirectly regulated through the fans speed of the dry cooler connected to the experimental loop. Indeed, the dry cooler motor has an inverter that allows to regulate the thermal power dissipated towards the external environment. Thus, apart from the heat losses in the piping connections, the HTF temperature at the inlet of the LHTS units coincides with the return temperature from the dry cooler (which in this case simulates the terminals of general a heating system). Again, three levels of HTF inlet temperatures were tested (low, medium, and high) ranging between 26°C and 54 °C for each inlet mass flow rate value. HTF inlet temperatures above 45°C are labelled as "high", values between 35°C and 45°C are labelled as "medium", while HTF inlet temperatures below 35°C are labelled as "low". More details are provided in section 5.2. It should be noticed that the dry cooling unit is placed in the outdoor environment due to spatial constraints, as already described in Chapter 3. Hence, the HTF return temperature (and consequently the HTF temperature at the inlet of the LHTS units) also depends on external air conditions. As a result, it was not possible to exactly replicate the LHTS inlet conditions throughout the tests.

Summarizing, each charge-discharge cycle was carried out following the procedures described hereafter. The prescribed HTF mass flow rate was regulated selecting the appropriate electric pump speed and adjusting the circuit hydraulic resistance with a manual flow control valve. Similarly, the heat load was controlled by setting the dry cooler fan speed. The electric heater allowed to charge the LHTS at a constant power rate. This process generally took around 5 hours. Unfortunately, the district heating substation could not be employed for this purpose due to maintenance reasons. The discharging phase was initiated when all the LHTS internal thermocouples displayed a temperature above 76°C (which is the point of complete PCM melting). First of all, the electric heater was switched off and the water flow was deviated towards the dry cooler by means of the dedicated group of valves (see Fig. 3.15). However, the LHTS was not immediately supplied with the cold water produced by the dry cooler in order to let the heating system achieve a new stationary condition (the LHTS can be easily by-passed with ad-hoc valves). This interval was set to 20 minutes. This choice was made since initial observations showed a highly unstable HTF inlet temperature when the operating mode was immediately switched from charge to discharge (probably due to the fact that the charging and the discharging loop share part of the piping system). Consequently, transient effects generated by the new water flow path (towards the dry cooler) were minimized.

Following this settlement interval, the tested LHTS unit was finally discharged under the abovementioned conditions.

5.2 LHTS dynamic model validation for discharging phase

An overview of the rationale behind the experimental tests used for the 1D dynamic model validation is presented in Table 5.1 and Table 5.2. The comparison between the simulation and the experimental results is performed for both the LHTS units described in Chapter 3. Due to time constraints, it was not possible to carry out the same number of tests for the two storage systems. As a result, a larger number of HTF inlet temperatures was tested for the LHTS with longitudinal fins, while only two levels of HTF inlet temperature (for each level of HTF mass flow rate) are available concerning the "TopOpt" LHTS unit. Nevertheless, the following sections provide interesting results regarding the comparison between the experimental and the simulation outcomes.

Table 5.1 Longitudinal LHTS: Test matrix for validating the 1D dynamic model discharging phase

HTF flow rate level	**HTF average flow rate**	**HTF average inlet temperature**
Low level (section 5.2.1)	1398 ±10 l/h	High (>45°C) Mid (35-45°C) Low (<35°C)
Medium level (section 5.2.3)	1898 ±9 l/h	High (>45°C) Mid (35-45°C) Low (<35°C)
High level (section 5.2.5)	2493 ±26 l/h	High (>45°C) Mid (35-45°C) Low (<35°C)

Table 5.2 TopOpt LHTS: Test matrix for validating the 1D dynamic model discharging phase

HTF flow rate level	**HTF average flow rate**	**HTF average inlet temperature**
Low level (section 5.2.2)	1398 ±14 l/h	Mid (35-45 °C)
Medium level (section 5.2.4)	1863 ±9 l/h	Mid (35-45 °C) Low (<35°C)
High level (section 5.2.6)	2478 ±4 l/h	Mid (35-45 °C) Low (<35°C)

As already anticipated in section 5.1, the tested HTF mass flow rates were adjusted manually. Nevertheless, their variability is contained, and three levels can be clearly identified:

- A low HTF mass flow rate value around 1400 l/h
- A medium HTF mass flow rate value around 1900 l/h
- A high HTF mass flow rate value around 2500 l/h

For the validation of the 1D dynamic model, the real HTF inlet mass flow rate and temperature values are fed as input for the model at each time instant. The model timestep is thus set at 30 seconds because the monitoring system provides data with a 30-seconds frequency. As described in section 3.2, all the geometrical and energy-related parameters are the same for both the LHTS units. The only exception is represented by the internal heat exchanger fins configuration. This is reflected into a different model input parameter regarding the PCM characteristic length l_c (see section 4.3.1). This parameter is estimated as follows. As far as the "Longitudinal" LHTS unit is concerned, the temperature gradients are predominantly radial around each HTF pipe. Consequently, the simple dimensional formula $l_c = V_{PCM}/A_{contact}$ is deemed appropriate. On the contrary, the main temperature gradients inside the "TopOpt" heat exchanger are expected to be perpendicular to each HCM rod. Hence, an equivalent average PCM radius around each rod is calculated. As a result, the

model input parameter concerning the characteristic length l_c is differentiated as follows:

- For the "Longitudinal" LHTS unit, l_c **= 7.6 mm**
- For the "TopOpt" LHTS unit, l_c **= 10.2 mm**

5.2.1 Tests with low HTF mass flow rate (around 1400 l/h): Longitudinal LHTS

Four tests were performed concerning the discharging phase of the "Longitudinal" LHTS at a low HTF mass flow rate (i.e., around 1400 l/h). The average HTF inlet temperature spans from 28.2 °C to 45.5 °C, as shown in Table 5.3. Hence, three levels of HTF inlet temperature can be identified: high (45.5 °C), medium (41.7°C and 37.8 °C) and low (28.2 °C). The outcomes of each experimental test are compared with the model simulation results in the following sections.

Table 5.3 Longitudinal LHTS: discharging tests with a low HTF mass flow rate

HTF mass flow rate [l/h]	HTF average inlet temperature [°C]
1388	45.5
1387	41.7
1403	37.8
1413	28.2

High level HTF inlet temperature (>45°C)

The comparison between the experimental and simulated HTF outlet temperature is presented in Fig. 5.1. Similarly, the time evolution of the "Longitudinal" LHTS thermal power and total energy release are shown respectively in Fig. 5.2 and Fig. 5.3. The HTF inlet temperature is quite stable throughout the discharging time, remaining always around 45 °C. This facilitates the model simulation, even though the initial HTF outlet temperature spike is well captured by the model. This is triggered by a very short initial transient in which the HTF inlet temperature drops down to 40°C. After 20 minutes, the HTF inlet temperature rapidly increases by around 2°C

following the thermal response of the dry cooler. The simulated outlet temperature agrees well with the experimental values, remaining within the experimental error bars for most of the discharging phase. Consequently, also the LHTS thermal power and released energy are very well represented by the model outcome, since these two quantities are derived from the HTF temperature difference and mass flow rate. Even though the initial thermal power peak is not exactly captured by the model, this has practically no influence on the LHTS behaviour from a heating system point of view. Indeed, this thermal power transient is negligible compared to both the system and the LHTS thermal inertia. Overall, the simulated evolution of the released energy is slightly underestimated throughout the process, although the model results appear extremely satisfactory.

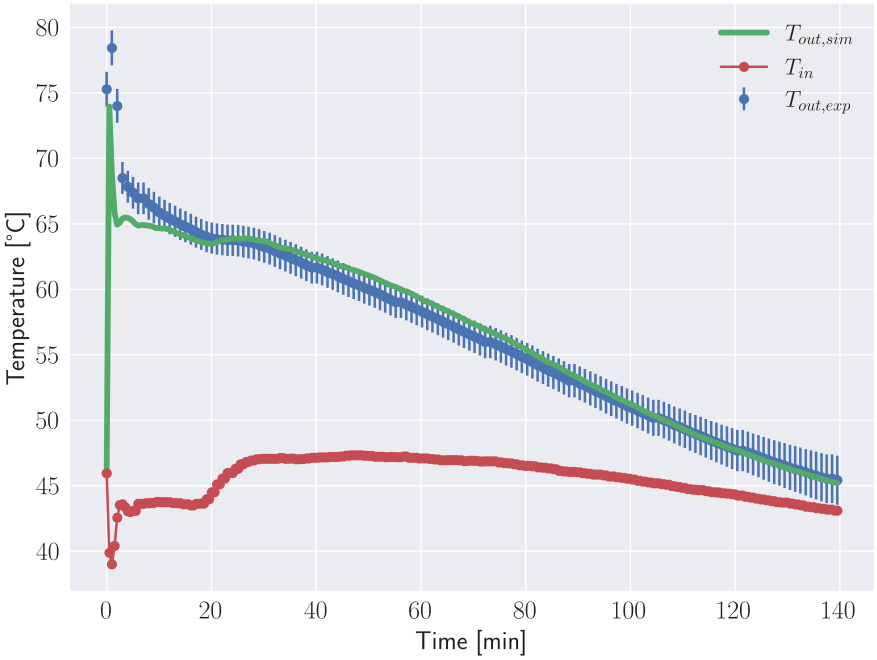

Fig. 5.1 Longitudinal LHTS: comparison between simulated and measured HTF outlet temperature ($G_{HTF,avg}$ = 1388 l/h, $T_{HTF,in,avg}$ = 45.5 °C)

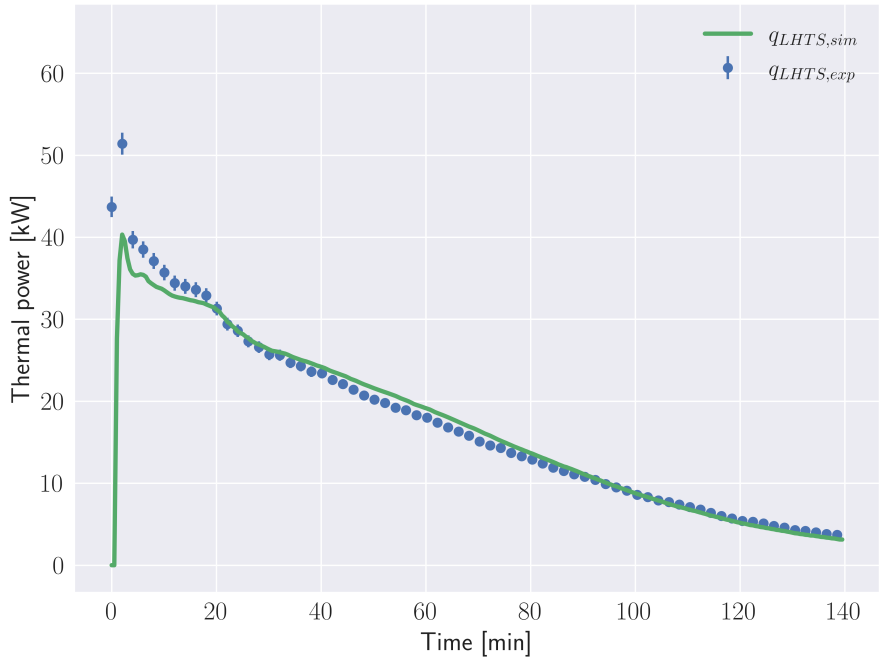

Fig. 5.2 Longitudinal LHTS: comparison between simulated and measured thermal power ($G_{HTF,avg}$ = 1388 l/h, $T_{HTF,in,avg}$ = 45.5 °C)

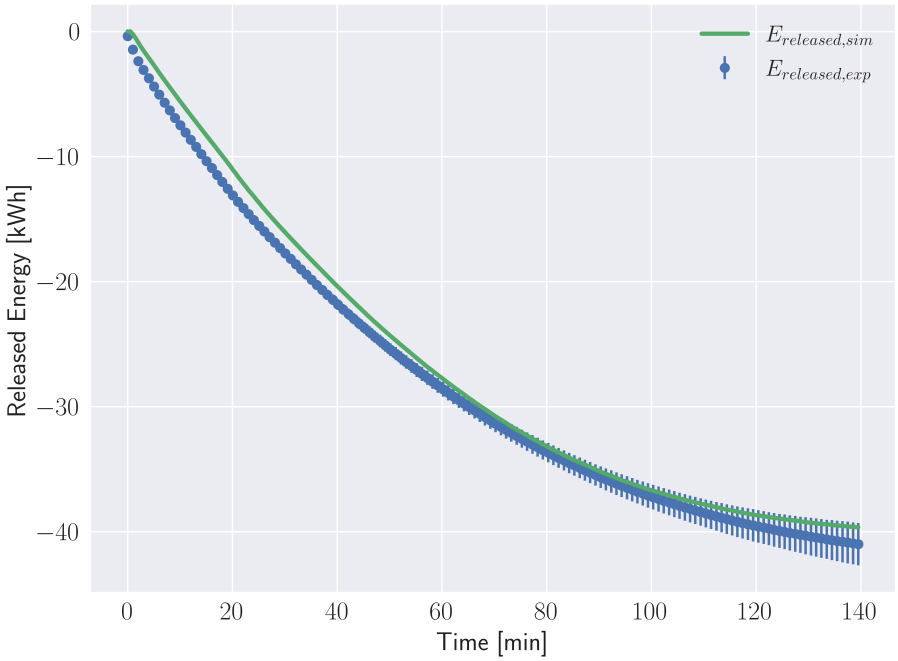

Fig. 5.3 Longitudinal LHTS: comparison between simulated and measured discharged energy history ($G_{HTF,avg}$ = 1388 l/h, $T_{HTF,in,avg}$ = 45.5 °C)

Medium level HTF inlet temperature (35°C – 45°C)

Two tests were concluded with a medium level average HTF inlet temperature. The former value of $T_{HTF,in,avg}$ is 41.7°C, while the latter is 37.8 °C. Concerning the former experimental test, the comparison between the experimental and simulated HTF outlet temperature is presented in Fig. 5.4. Similarly, the time evolution of the "Longitudinal" LHTS thermal power and total energy release are shown respectively in Fig. 5.5 and Fig. 5.6. The HTF inlet temperature is quite stable throughout the discharging time, remaining always around 42 °C. The LHTS behaviour is very similar to the previous case (with high HTF temperature level). As a matter of fact, the HTF inlet temperature evolution is basically displaced by -3°C. Hence all the considerations presented in section 5.2.1 are also valid here. The simulated outlet temperature agrees well with the experimental values, and it is generally contained within the experimental error bars for most of the discharging phase. As a result, also the LHTS thermal power and released energy are very well represented by the model outcome. Overall, also in this case the simulated evolution of the released energy is slightly underestimated throughout the process, but the model results appear extremely satisfactory.

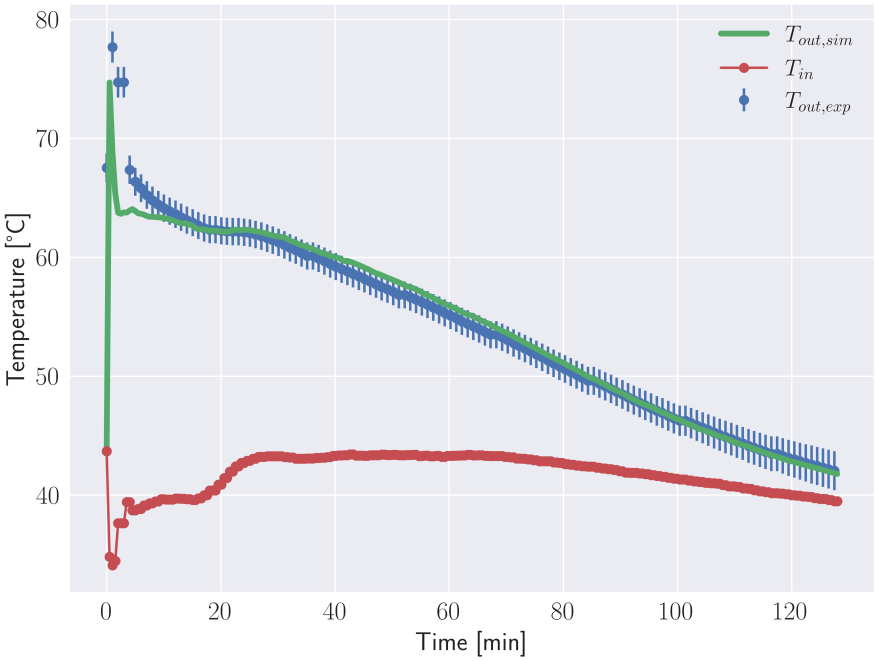

Fig. 5.4 Longitudinal LHTS: comparison between simulated and measured HTF outlet temperature ($G_{HTF,avg}$ = 1387 l/h, $T_{HTF,in,avg}$ = 41.7 °C)

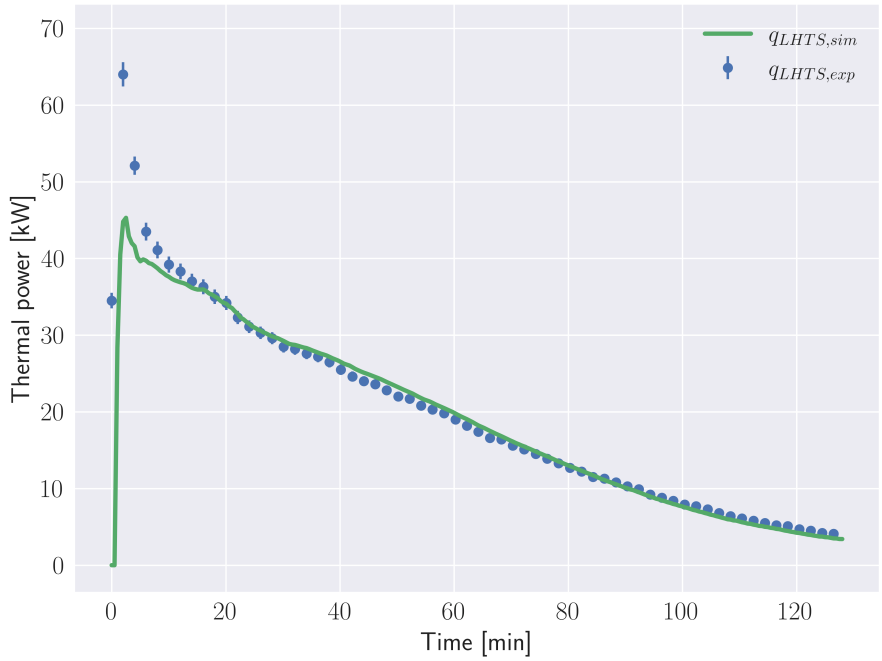

Fig. 5.5 Longitudinal LHTS: comparison between simulated and measured thermal power ($G_{HTF,avg}$ = 1387 l/h, $T_{HTF,in,avg}$ = 41.7 °C)

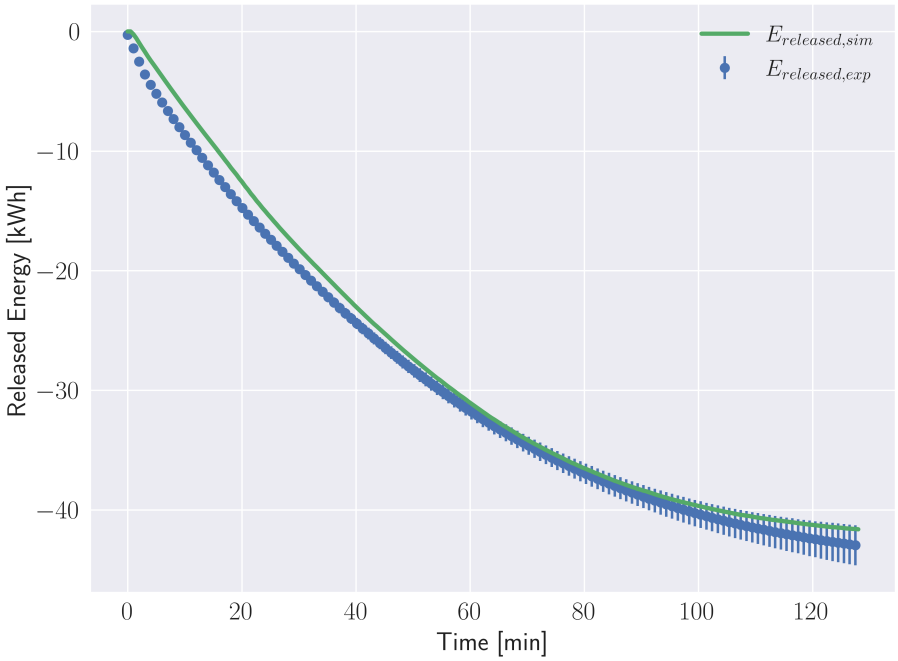

Fig. 5.6 Longitudinal LHTS: comparison between simulated and measured discharged energy history ($G_{HTF,avg}$ = 1387 l/h, $T_{HTF,in,avg}$ = 41.7 °C)

Concerning the latter experimental test (T_HTF,in,avg = 37.8 °C), the time evolution of the experimental and simulated HTF outlet temperature is presented in Fig. 5.7, while the "Longitudinal" LHTS thermal power and total energy release are shown respectively in Fig. 5.8 and Fig. 5.9. In this test, the HTF inlet temperature has an oscillatory behaviour during the first 40 minutes of discharge, probably due to the fact that hotter and colder water volumes were still present in the pipes of the experimental system. This effect might be ascribed to the absence of a water buffer increasing the system thermal inertial. As already discussed in Chapter 3, this is one of the drawbacks of the current system design. Nevertheless, the model outcomes follow with good accuracy the experimental values for all the three quantities of interest: $T_{HTF,out}$, q_{LHTS} and $E_{released}$. This proves that the model is well structured to sustain also variable inlet HTF inlet temperatures, thus answering positively to one of the modelling objectives. The larger value in the experimental error bars towards the end of the discharging phase is related to an increased uncertainty in temperature sensors when the temperature difference is minimal, as described in section 3.3.1. Overall, also in this case the simulation results are deemed satisfactory.

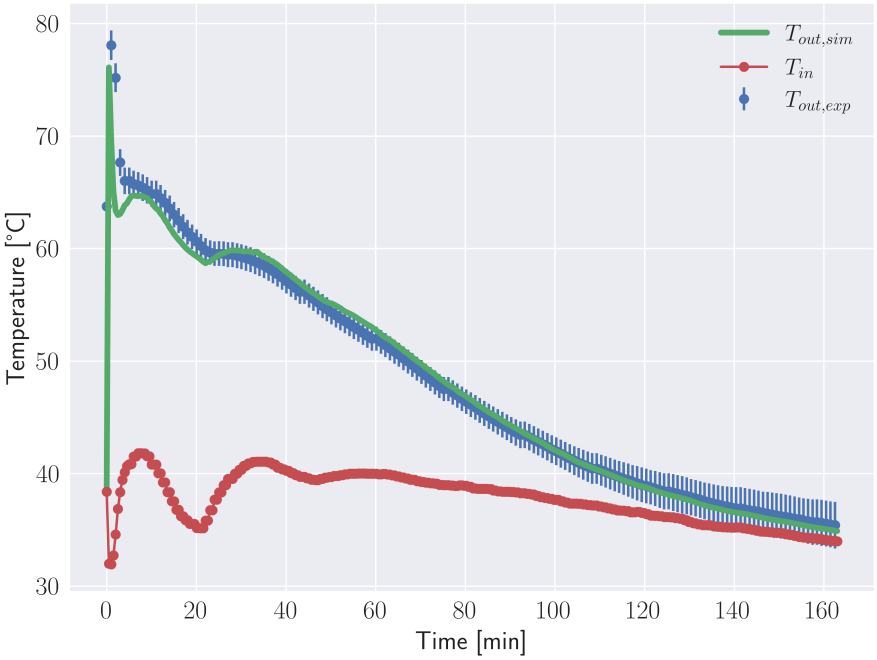

Fig. 5.7 Longitudinal LHTS: comparison between simulated and measured HTF outlet temperature ($G_{HTF,avg}$ = 1403 l/h, $T_{HTF,in,avg}$ = 37.8 °C)

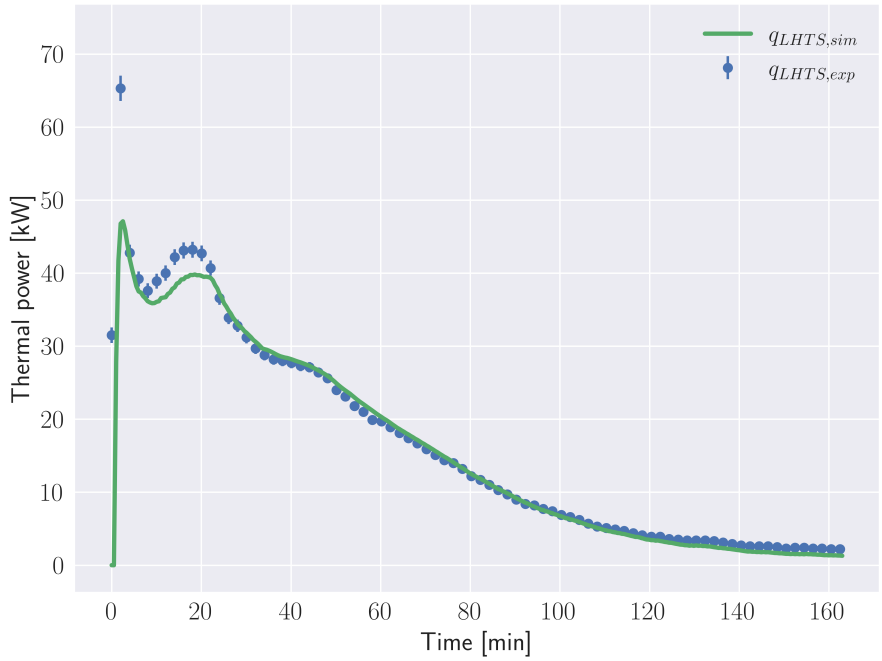

Fig. 5.8 Longitudinal LHTS: comparison between simulated and measured thermal power ($G_{HTF,avg}$ = 1403 l/h, $T_{HTF,in,avg}$ = 37.8 °C)

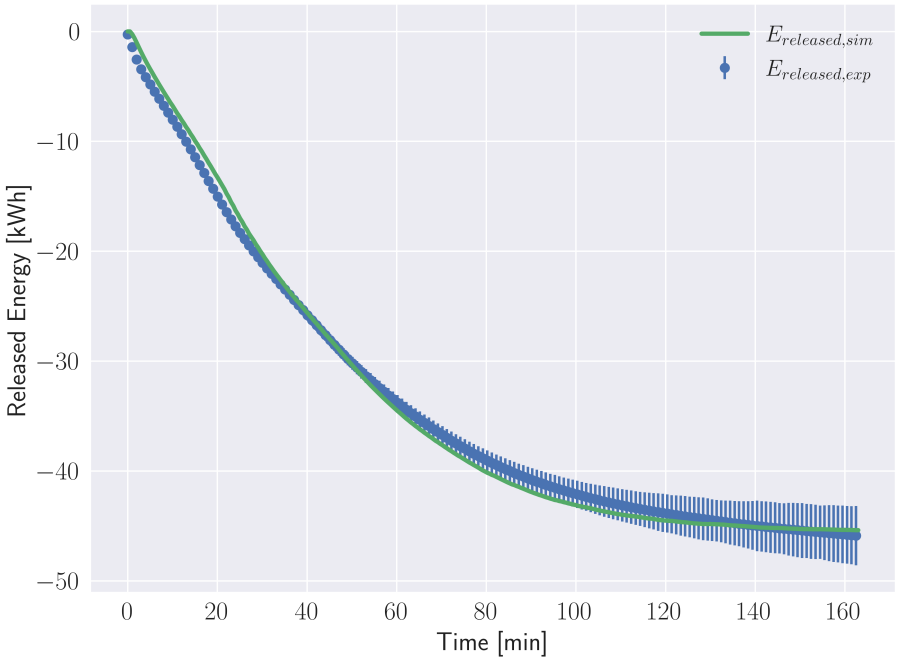

Fig. 5.9 Longitudinal LHTS: comparison between simulated and measured discharged energy history ($G_{HTF,avg}$ = 1403 l/h, $T_{HTF,in,avg}$ = 37.8 °C)

Low level HTF inlet temperature (<35°C)

This test compares the experimental and simulated HTF outlet temperature when the average inlet HTF temperature is 28.2 °C (Fig. 5.10). Similarly, the time evolution of the "Longitudinal" LHTS thermal power and total energy release are shown respectively in Fig. 5.11 and Fig. 5.12. Also in this case, the HTF inlet temperature is quite variable throughout the discharging process, although marked oscillations are not present. The HTF inlet temperature reaches a maximum value of around 33°C and drops to a minimum value of 21 °C at the end of the test. The reason of this system behaviour can be once more ascribed to the absence of a water buffer combined with the highly dynamic behaviour of the system thermal sink (i.e., the dry cooler). As a result, in this test the model outcomes are less accurate. As a matter of fact, the higher driving temperature difference (between the PCM phase change temperature and the HTF inlet temperature) enhances the model inaccuracies in the estimation of the LHTS state of charge. Consequently, the slower discharging rate estimated during the initial 20 minutes affects the following time intervals. Nevertheless, it should be remarked that the goal of this modelling approach is representing the LHTS behaviour from a system perspective. Hence, contained variations in the instantaneous HTF outlet temperature and LHTS released thermal power are generally absorbed by the heating system thermal inertia. Overall, the model performance from a systemic point of view is deemed satisfactory, as witnessed by the time evolution of the LHTS released energy (Fig. 5.12).

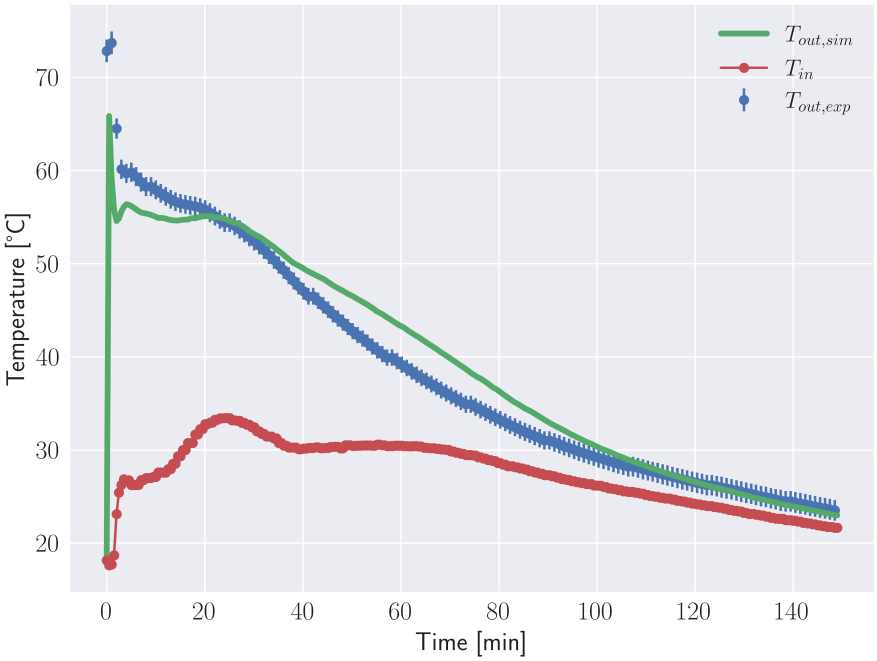

Fig. 5.10 Longitudinal LHTS: comparison between simulated and measured HTF outlet temperature ($G_{HTF,avg}$ = 1413 l/h, $T_{HTF,in,avg}$ = 28.2 °C)

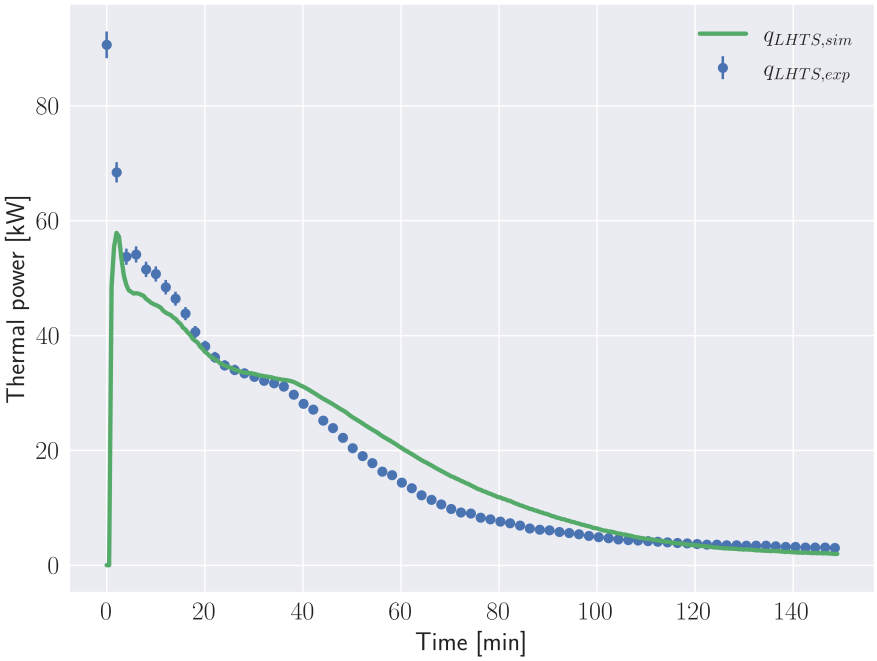

Fig. 5.11 Longitudinal LHTS: comparison between simulated and measured thermal power ($G_{HTF,avg}$ = 1413 l/h, $T_{HTF,in,avg}$ = 28.2 °C)

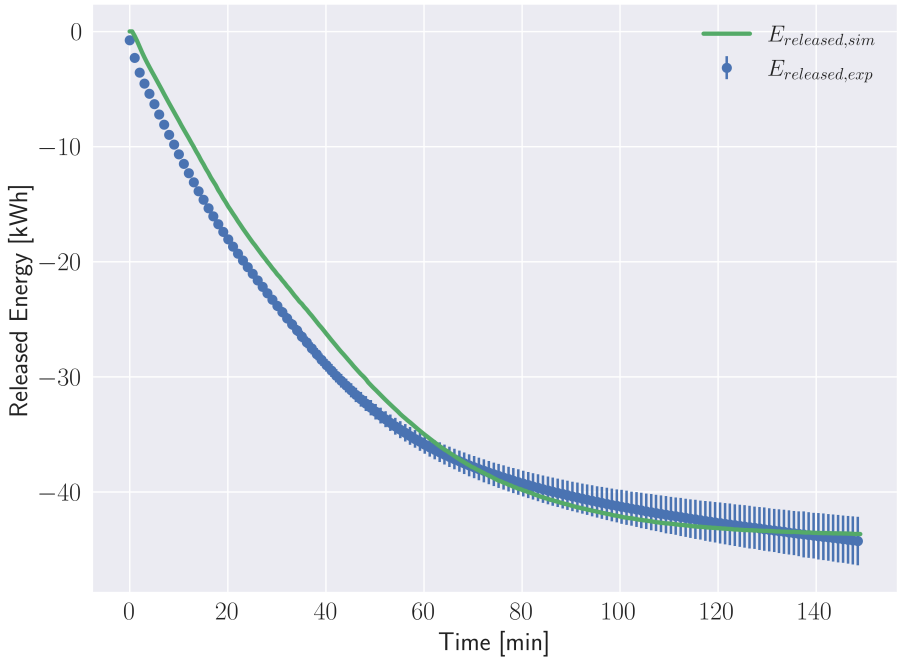

Fig. 5.12 Longitudinal LHTS: comparison between simulated and measured discharged energy history ($G_{HTF,avg}$ = 1413 l/h, $T_{HTF,in,avg}$ = 28.2 °C)

5.2.2 Tests with low HTF mass flow rate (around 1400 l/h): TopOpt LHTS

Concerning the discharging phase of the "TopOpt" LHTS at a low HTF mass flow rate (i.e., around 1400 l/h), only two tests were performed due to a lack of time. The calibration of the entire experimental system resulted in a time-consuming activity, thus the number of tests related to the "TopOpt" LHTS was affected. The two cases presented below are characterised by two levels of average HTF inlet temperature. However, these are both classified as "medium" temperature levels for consistency with the other analysed cases. The details are reported in Table 5.4.

Table 5.4 TopOpt LHTS: discharging tests with a low HTF mass flow rate

HTF mass flow rate [l/h]	HTF average inlet temperature [°C]
1384	42.9
1412	37.5

Medium level HTF inlet temperature (35°C – 45°C)

The two tests conducted in this category are characterised by an average HTF inlet temperature equal to 42.9°C and 37.5 °C. Concerning the former experimental test, the comparison between the experimental and simulated HTF outlet temperature is presented in Fig. 5.13. Similarly, the time evolution of the "TopOpt" LHTS thermal power and total energy release are shown respectively in Fig. 5.14 and Fig. 5.15. The HTF inlet temperature is quite stable throughout the discharging time, although a small step increase is evident after 20 minutes due to the dynamic behaviour of the dry cooler. As the time passes, the HTF temperature at the dry cooler inlet decreases as a consequence of the natural LHTS discharge. However, the dry cooler structure might still be hotter because of the previous higher temperatures. As a result, part of this heat might be reversed towards the flowing HTF instead of the external environment. Generally, the simulated outlet temperature is in good agreement with the experimental values, although it is underestimated during the initial discharging phase and overestimated in the remaining time. As a result, the model "TopOpt" LHTS thermal power and released energy are not as accurate as in the model for the "Longitudinal" LHTS. This difference is mainly caused by the different heat transfer mechanisms triggered by the diverse internal heat exchanger configuration. Nevertheless, considering the unconventional design of the "TopOpt" LHTS, the model results are deemed acceptable.

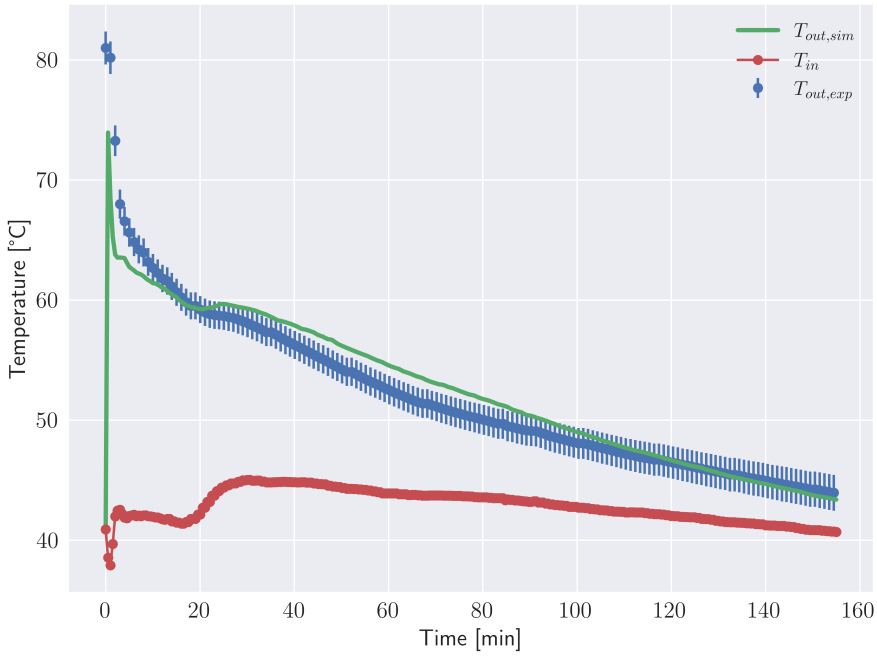

Fig. 5.13 TopOpt LHTS: comparison between simulated and measured HTF outlet temperature ($G_{HTF,avg}$ = 1384 l/h, $T_{HTF,in,avg}$ = 42.9 °C)

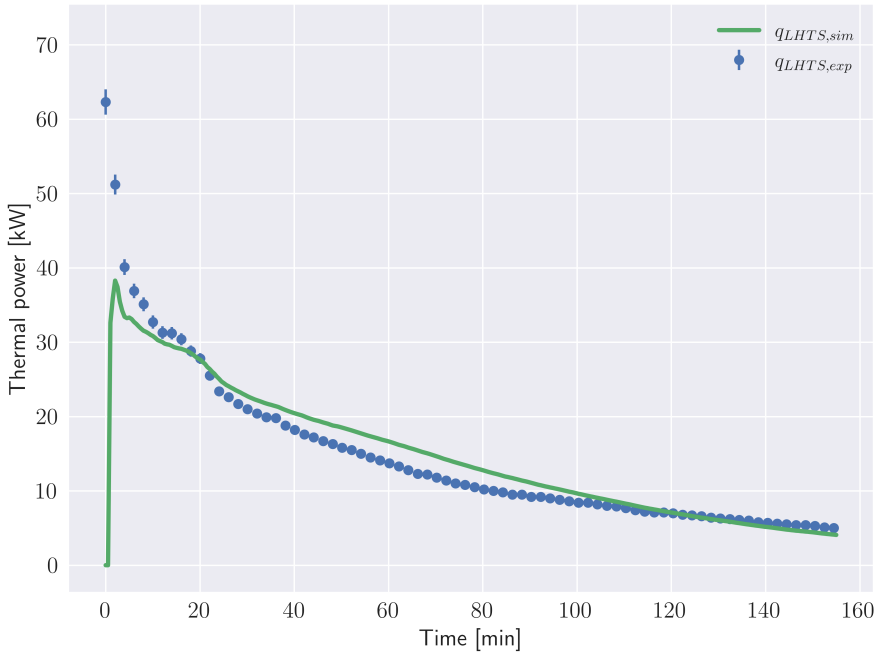

Fig. 5.14 TopOpt LHTS: comparison between simulated and measured thermal power ($G_{HTF,avg}$ = 1384 l/h, $T_{HTF,in,avg}$ = 42.9 °C)

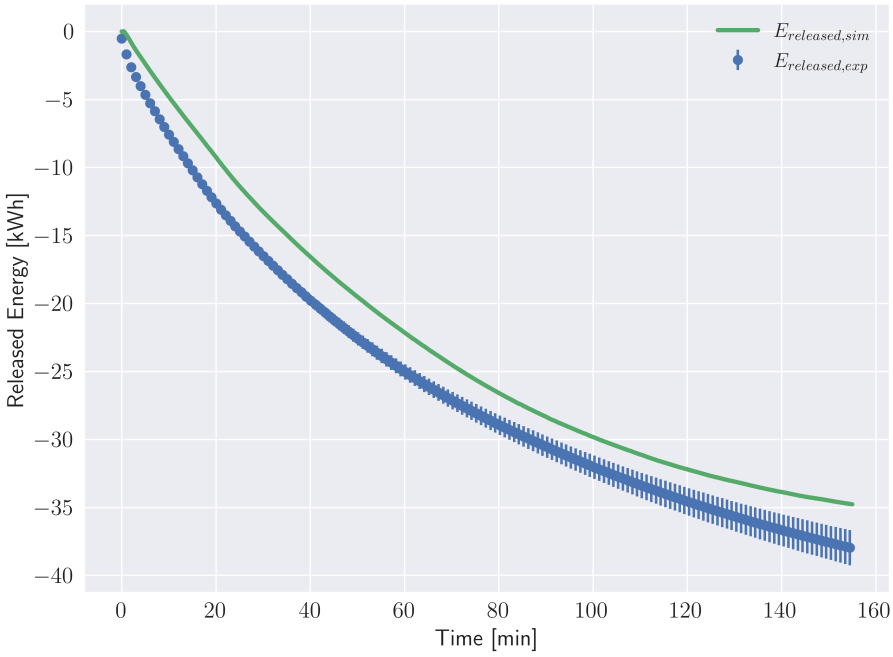

Fig. 5.15 TopOpt LHTS: comparison between simulated and measured discharged energy history ($G_{HTF,avg}$ = 1384 l/h, $T_{HTF,in,avg}$ = 42.9 °C)

Regarding the latter experimental test ($T_{HTF,in,avg}$ = 37.5 °C), the time evolution of the experimental and simulated HTF outlet temperature is presented in Fig. 5.16, while the "TopOpt" LHTS thermal power and total energy release are shown respectively in Fig. 5.17 and Fig. 5.18. In this test, the HTF inlet temperature is relatively stable, although it shows a decreasing trend. Again, the initial LHTS performance underestimation produced by the model affects the rest of the simulation. As already discussed, this is probably due to the heat transfer mechanism active in the "TopOpt" LHTS unit. When the PCM is entirely liquid at the beginning of the discharging phase, natural convection is assumed to be relevant with this heat exchanger configuration. On the contrary, the proposed model is purely diffusive. Thus, the difference that is generated at the beginning of the discharge between the experimental and the simulated energy release is mostly kept throughout the whole process. Nevertheless, remarking again the unconventional design of the "TopOpt" LHTS, the model results are deemed acceptable for simulating such a LHTS configuration from a system perspective.

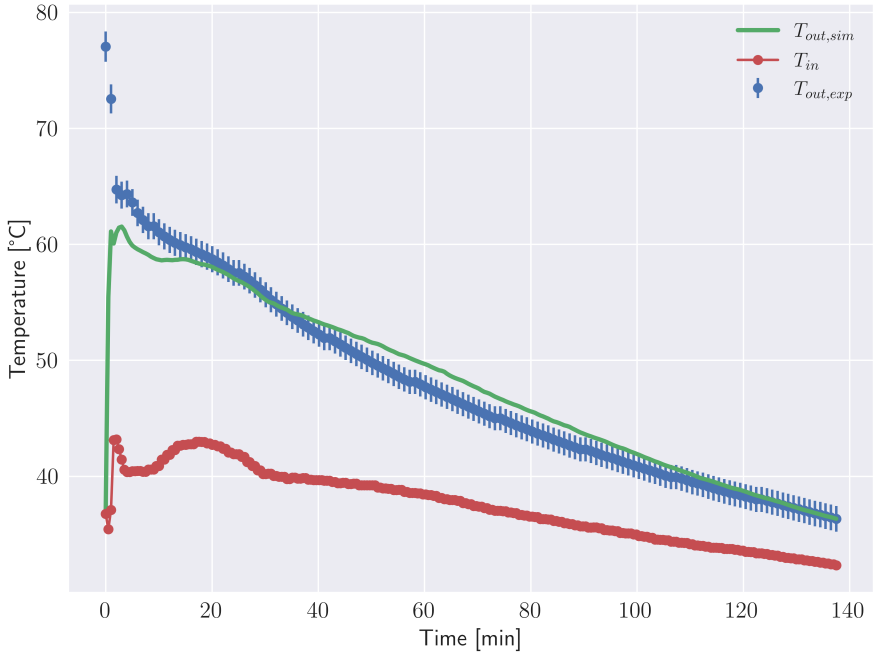

Fig. 5.16 TopOpt LHTS: comparison between simulated and measured HTF outlet temperature ($G_{HTF,avg}$ = 1412 l/h, $T_{HTF,in,avg}$ = 37.5 °C)

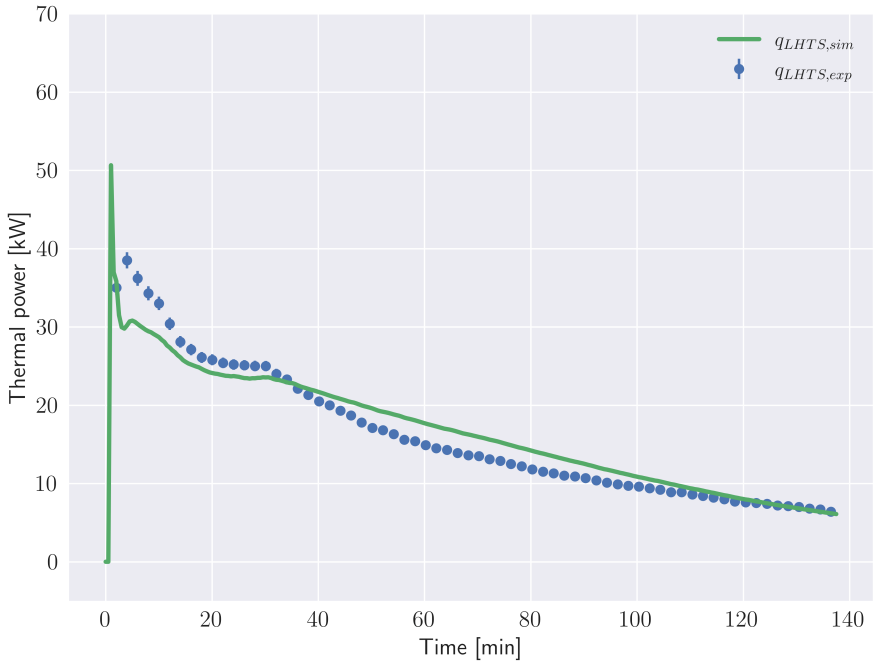

Fig. 5.17 TopOpt LHTS: comparison between simulated and measured thermal power ($G_{HTF,avg}$ = 1412 l/h, $T_{HTF,in,avg}$ = 37.5 °C)

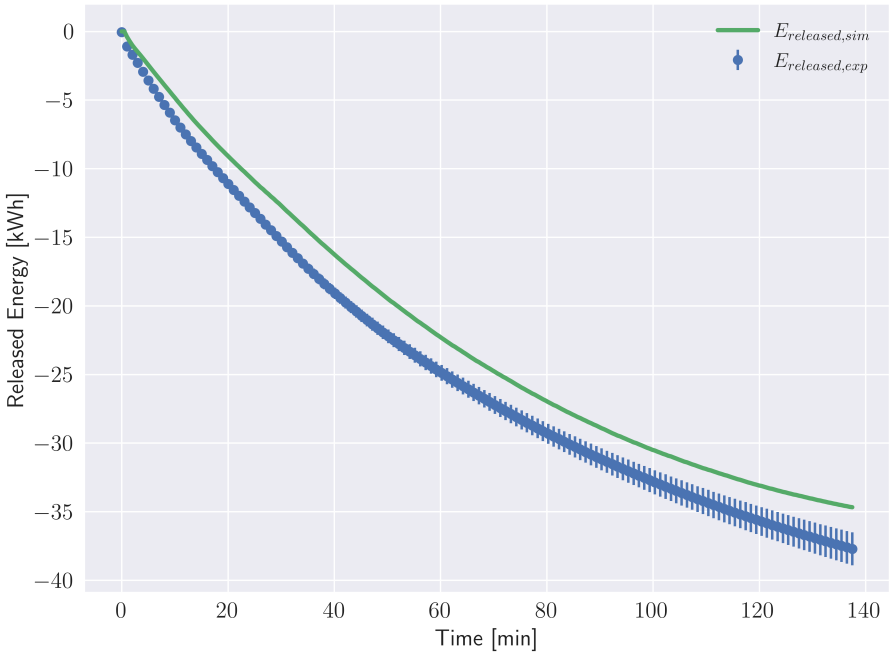

Fig. 5.18 TopOpt LHTS: comparison between simulated and measured discharged energy history ($G_{HTF,avg}$ = 1412 l/h, $T_{HTF,in,avg}$ = 37.5 °C)

5.2.3 Tests with medium HTF mass flow rate (around 1900 l/h): Longitudinal LHTS

Four tests are presented regarding the discharging phase of the "Longitudinal" LHTS at a medium HTF mass flow rate (i.e., around 1900 l/h). The average HTF inlet temperature spans from 29 °C to 53.7 °C, as detailed in Table 5.5. According to the proposed classification, three levels of HTF inlet temperature can be identified: high (53.7 °C and 44.9 °C), medium (41.3°C) and low (29 °C). It should be noticed that most of the input temperature levels are very similar to those analysed for the "Longitudinal" test campaign with an inlet mass flow rate equal to 1400 l/h. The outcomes of each experimental test are compared with the model simulation results in the following sections.

Table 5.5 Longitudinal LHTS: discharging tests with a medium HTF mass flow rate

HTF mass flow rate [l/h]	HTF average inlet temperature [°C]
1909	53.7
1905	44.9
1884	41.3
1895	29

High level HTF inlet temperature (>45°C)

Two tests were performed with a high-level average HTF inlet temperature. The former value of $T_{HTF,in,avg}$ is 53.7°C, while the latter is 44.9 °C. Concerning the former experimental test, the comparison between the experimental and simulated HTF outlet temperature is presented in Fig 5.19. Similarly, the time evolution of the "Longitudinal" LHTS thermal power and total energy release are shown respectively in Fig 5.20 and Fig 5.21. In this test, the HTF inlet temperature is rather unstable throughout the discharging time, also displaying an increasing trend. As already reflected in some of the previous cases, this effect is due to the dynamic behaviour of the dry cooler. Moreover, to obtain a higher HTF temperature level at the LHTS inlet, the dry cooler fan speed was set to zero. Hence, this component behaved as a passive unit subjected to external air conditions during the test. However, although the high variability in the inlet HTF temperature, the model outcomes are in good agreement with the experimental values. Obviously, the oscillations in the inlet HTF temperature affect the model accuracy, especially concerning the released energy. The initial high HTF temperature difference between inlet and outlet determines a fast energy discharge in the first 20 minutes which is not precisely captured by the model. Overall, considering all these limitations, the model results can be evaluated as acceptable.

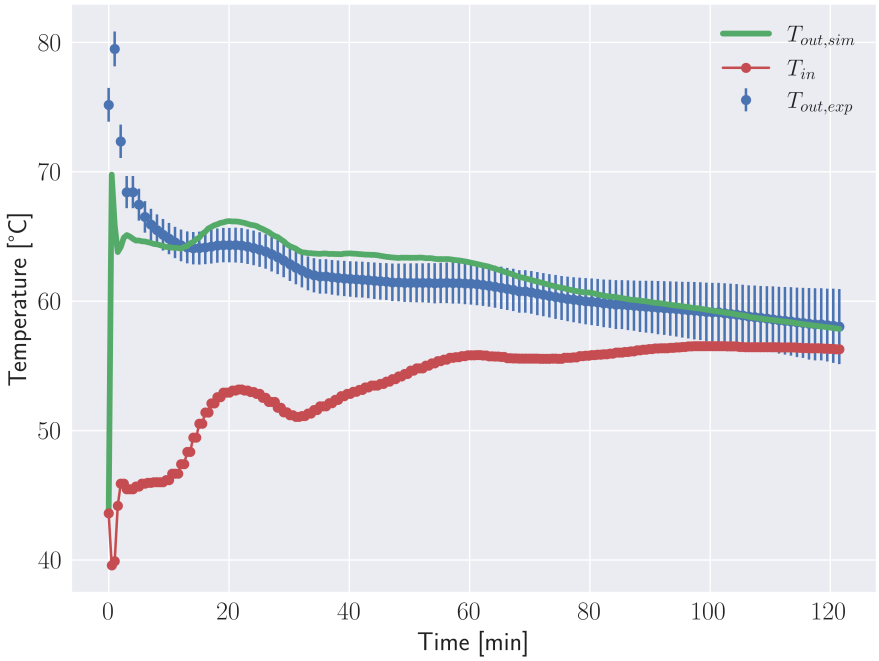

Fig. 5.19 Longitudinal LHTS: comparison between simulated and measured HTF outlet temperature ($G_{HTF,avg}$ = 1909 l/h, $T_{HTF,in,avg}$ = 53.7 °C)

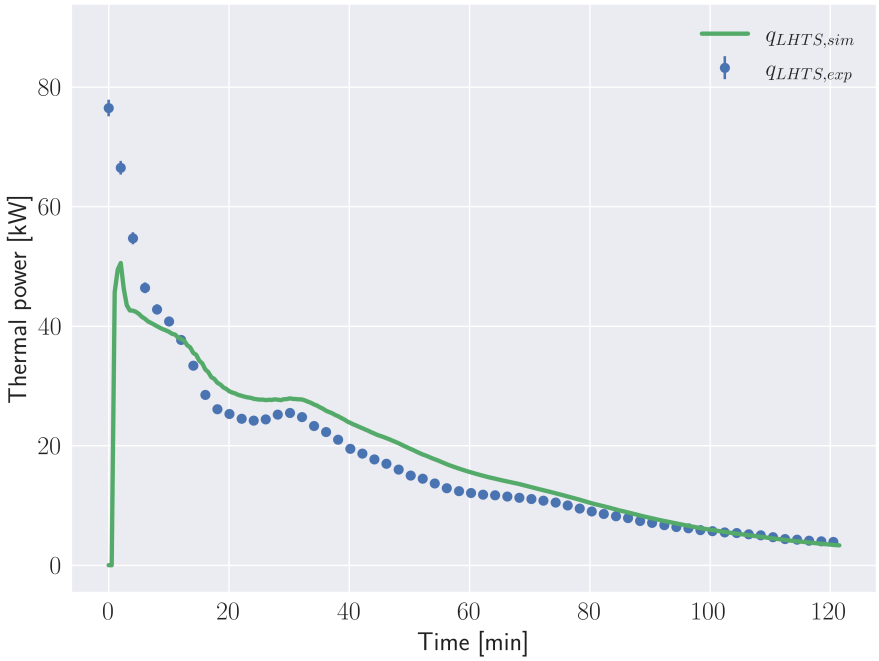

Fig. 5.20 Longitudinal LHTS: comparison between simulated and measured thermal power ($G_{HTF,avg}$ = 1909 l/h, $T_{HTF,in,avg}$ = 53.7 °C)

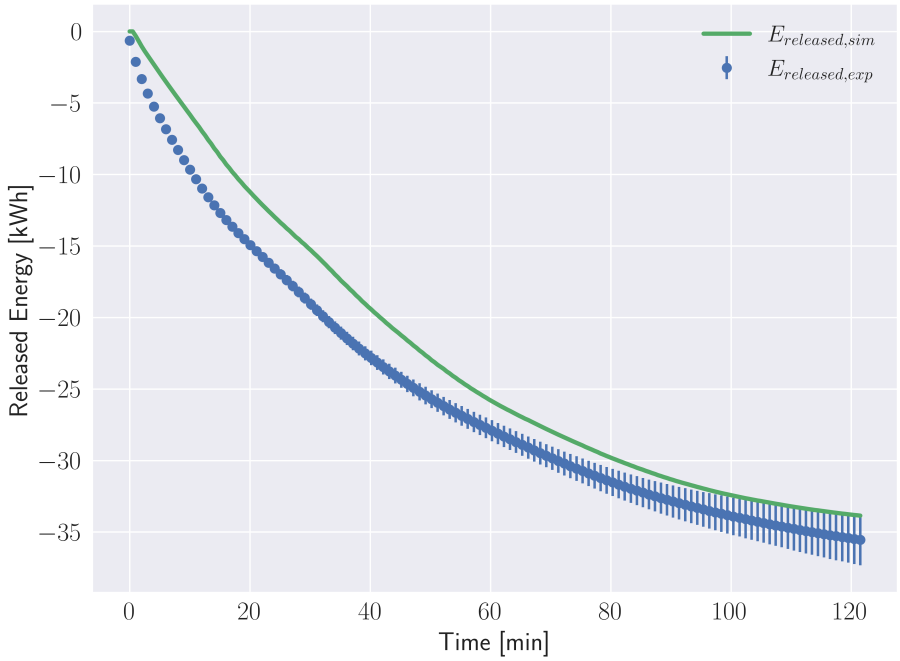

Fig. 5.21 Longitudinal LHTS: comparison between simulated and measured discharged energy history ($G_{HTF,avg}$ = 1909 l/h, $T_{HTF,in,avg}$ = 53.7 °C)

Concerning the latter experimental test ($T_{HTF,in,avg}$ = 44.9 °C), the time evolution of the experimental and simulated HTF outlet temperature is presented in Fig 5.22, while the "Longitudinal" LHTS thermal power and total energy release are shown respectively in Fig 5.23 and Fig 5.24. In this test, the HTF inlet temperature is more stable compared to the previous case, although a large spike is registered in the very first discharging instants. Even though $T_{HTF,in,avg}$ = 44.9 °C, it should be remarked that this test is classified within the "high level HTF temperature" because the HTF inlet temperature is largely above 45°C for the most relevant part of the discharging phase. As expected, since the driving HTF inlet temperature is more stable compared to the previous case, the simulated energy release is in good agreement with the relative measured values. Hence, also in this case the model results are considered extremely satisfactory.

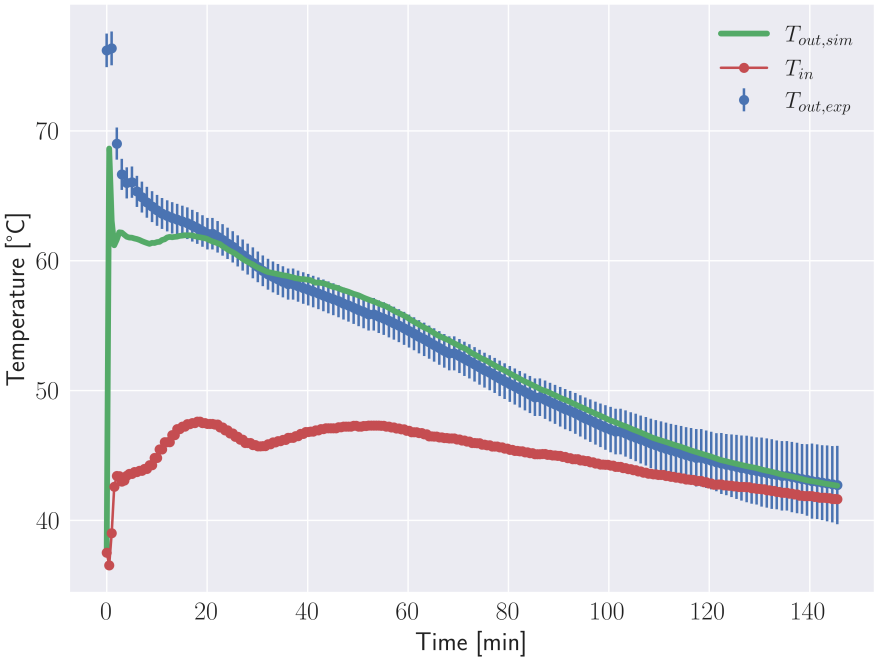

Fig. 5.22 Longitudinal LHTS: comparison between simulated and measured HTF outlet temperature ($G_{HTF,avg}$ = 1905 l/h, $T_{HTF,in,avg}$ = 44.9 °C)

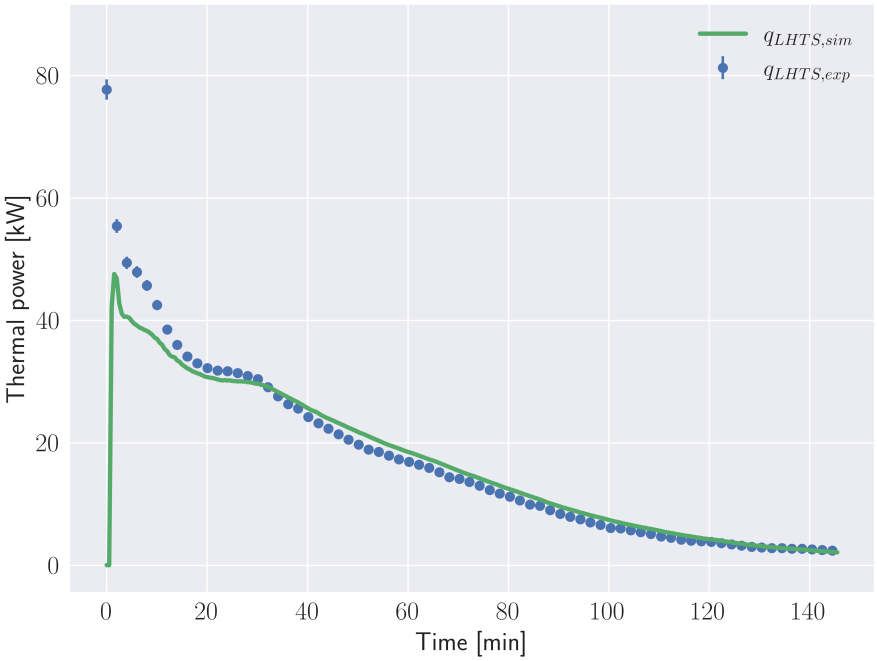

Fig. 5.23 Longitudinal LHTS: comparison between simulated and measured thermal power ($G_{HTF,avg}$ = 1905 l/h, $T_{HTF,in,avg}$ = 44.9 °C)

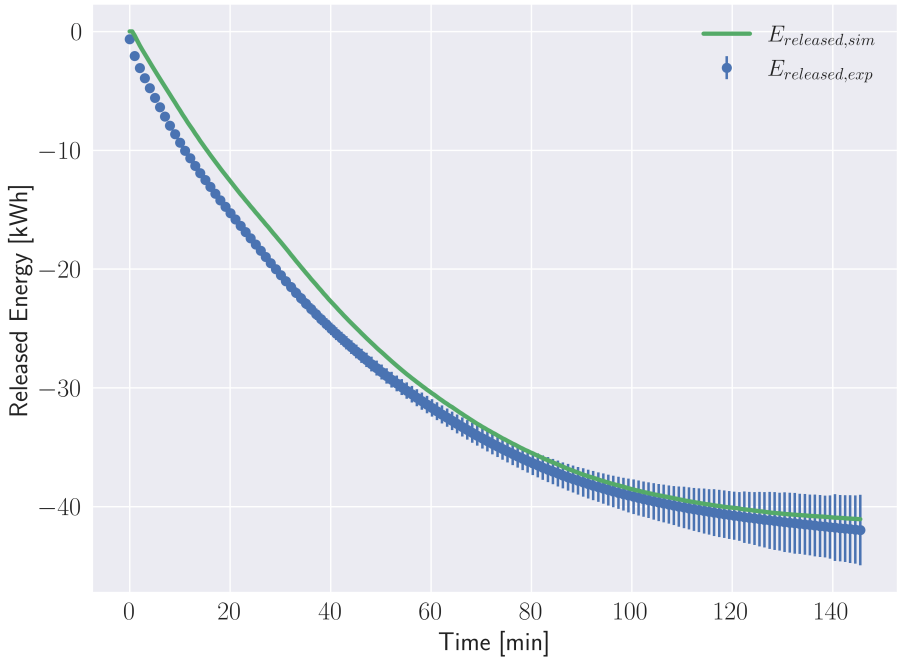

Fig. 5.24 Longitudinal LHTS: comparison between simulated and measured discharged energy history ($G_{HTF,avg}$ = 1905 l/h, $T_{HTF,in,avg}$ = 44.9 °C)

Medium level HTF inlet temperature (35°C – 45°C)

The comparison between the experimental and simulated HTF outlet temperature is presented in Fig 5.25, while the "Longitudinal" LHTS thermal power and total energy release are shown respectively in Fig 5.26 and Fig 5.27. The real and simulated LHTS performance in this case is very similar to the previous test (5.2.3) because the driving HTF inlet temperature has practically the same behaviour, even though its average value is shifted down by 3.6 °C. Hence, all the comments and considerations made in the previous section are also valid here. However, it should be noticed a marked underestimation in the simulated HTF outlet temperature during the first discharging instants. This is a common feature in this class of tests with a medium level HTF mass flow rate (1900 l/h), especially if compared with those performed at 1400 l/h. It is possible that the heat transfer coefficient allowing to estimate the heat rate between the HTF domain and the PCM-HCM assembly (see section 4.2) does not properly capture the initial turbulent flow behaviour.

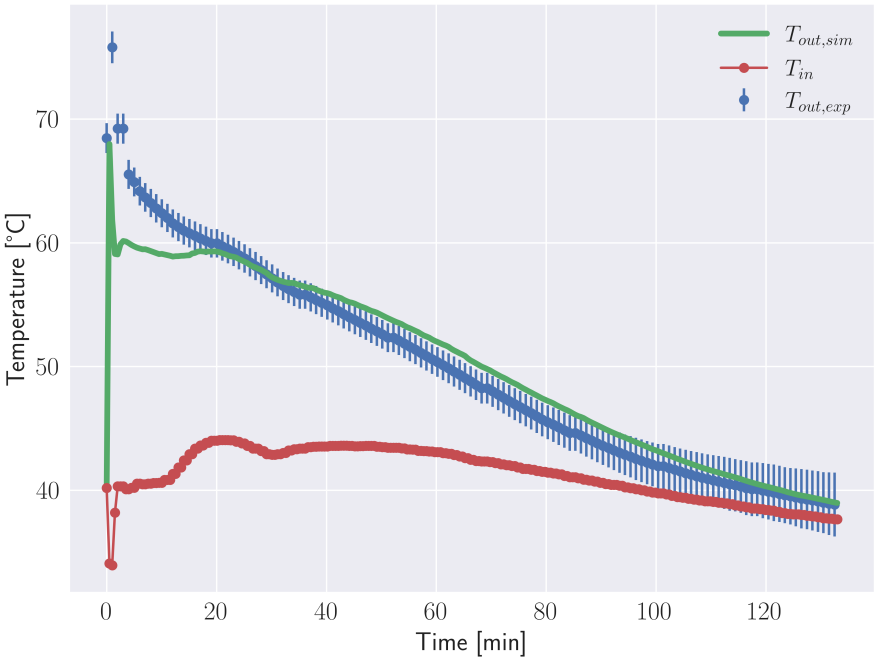

Fig. 5.25 Longitudinal LHTS: comparison between simulated and measured HTF outlet temperature ($G_{HTF,avg}$ = 1884 l/h, $T_{HTF,in,avg}$ = 41.3 °C)

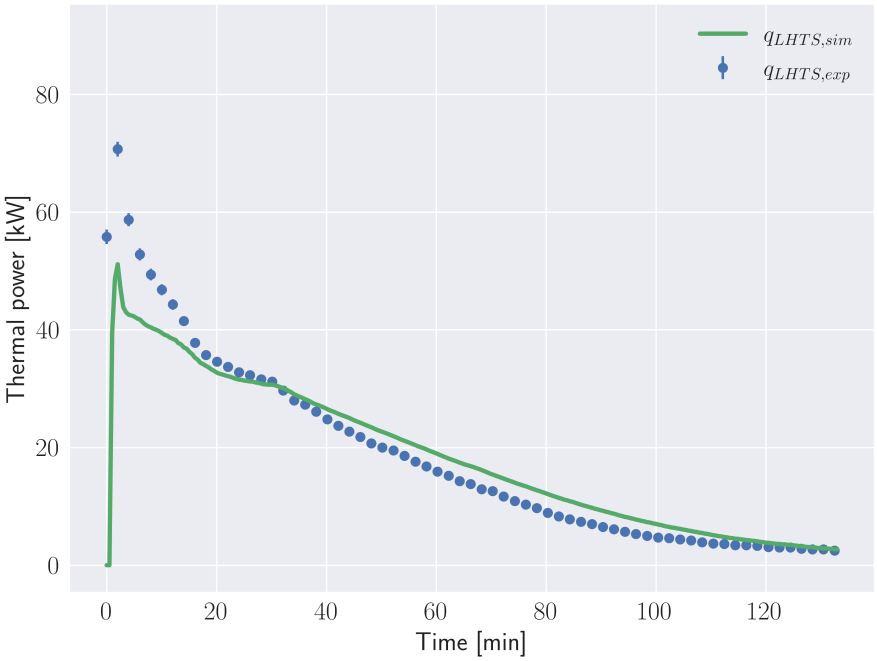

Fig. 5.26 Longitudinal LHTS: comparison between simulated and measured thermal power ($G_{HTF,avg}$ = 1884 l/h, $T_{HTF,in,avg}$ = 41.3 °C)

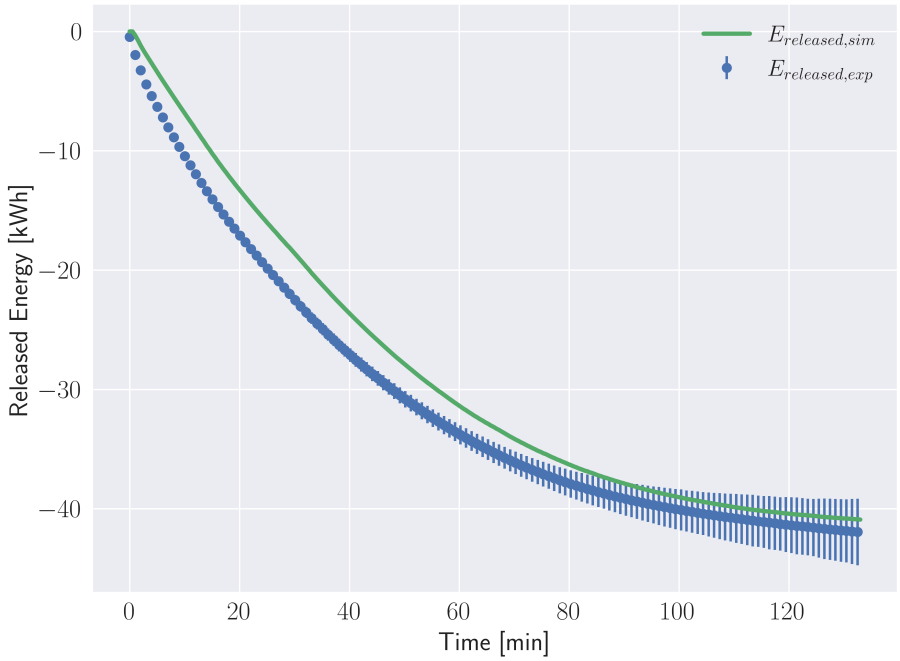

Fig. 5.27 Longitudinal LHTS: comparison between simulated and measured discharged energy history ($G_{HTF,avg}$ = 1884 l/h, $T_{HTF,in,avg}$ = 41.3 °C)

Low level HTF inlet temperature (<35°C)

The time evolution of the measured and simulated HTF outlet temperature is shown in Fig 5.28, while the "Longitudinal" LHTS thermal power and total energy release are presented respectively in Fig 5.29 and Fig 5.30. Again, the real and simulated LHTS performance in this case is very similar to the previous test (5.2.3) because the HTF inlet temperature displays a similar evolution in time, even though its average value is much lower. Consequently, the LHTS discharge is faster. Precisely, in this case the "Longitudinal" LHTS unit releases around 40.5 kWh after 80 minutes, while in the previous case the same amount of energy is released after 100 minutes. However, apart from this difference, all the other considerations are still valid here, including those related to the underestimation in the simulated HTF outlet temperature during the first discharging instants. This model inaccuracy yields to a slight underestimation in the energy evolution history (Fig 5.30).

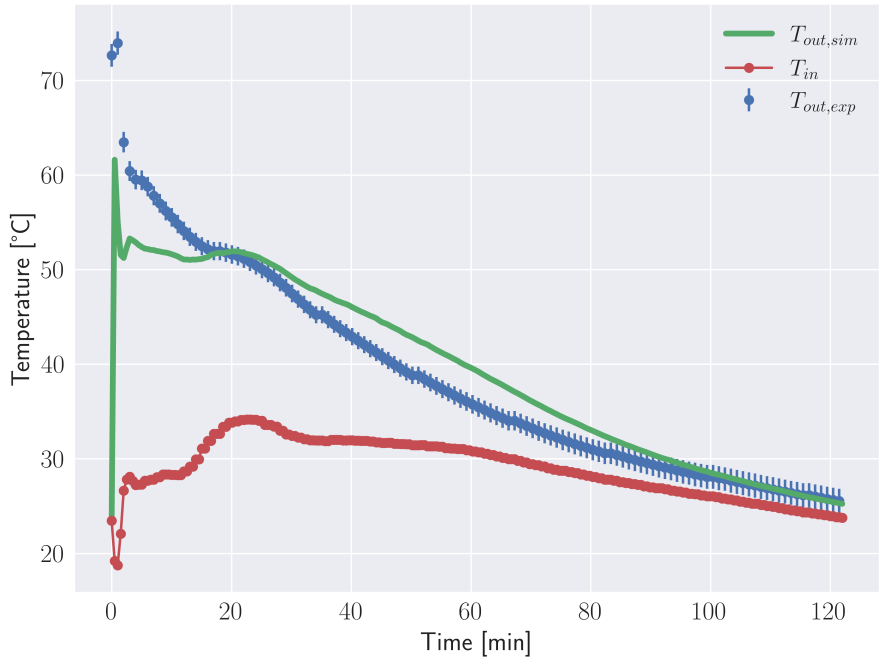

Fig. 5.28 Longitudinal LHTS: comparison between simulated and measured HTF outlet temperature ($G_{HTF,avg}$ = 1895 l/h, $T_{HTF,in,avg}$ = 29 °C)

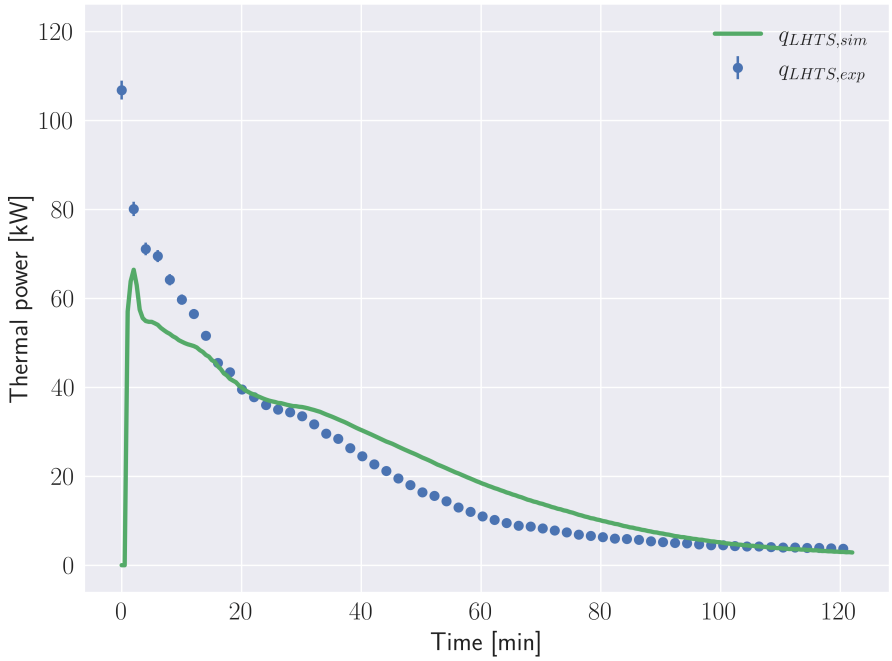

Fig. 5.29 Longitudinal LHTS: comparison between simulated and measured thermal power ($G_{HTF,avg}$ = 1895 l/h, $T_{HTF,in,avg}$ = 29 °C)

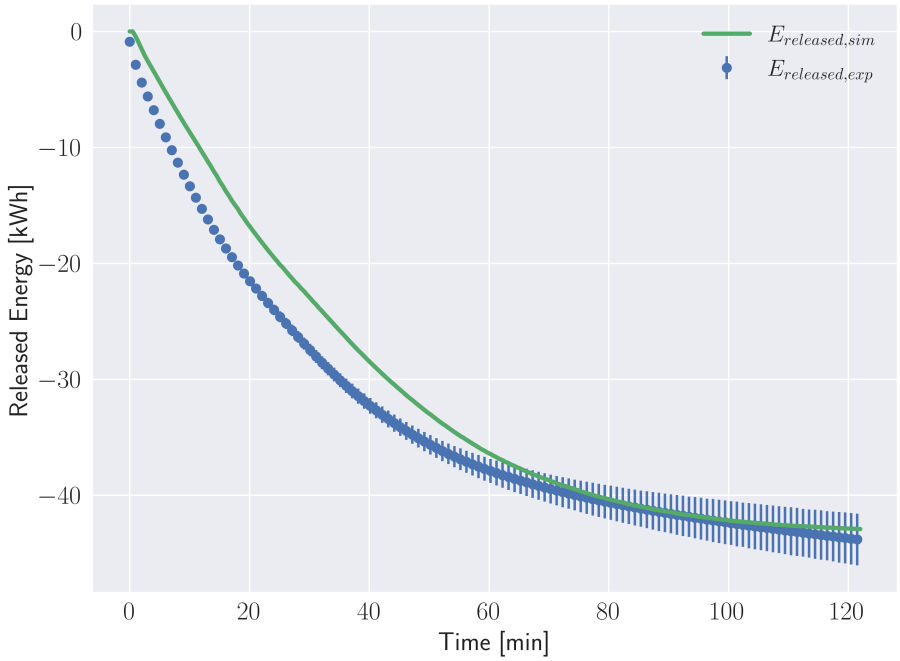

Fig. 5.30 Longitudinal LHTS: comparison between simulated and measured discharged energy history ($G_{HTF,avg}$ = 1895 l/h, $T_{HTF,in,avg}$ = 29 °C)

5.2.4 Tests with medium HTF mass flow rate (around 1900 l/h): TopOpt LHTS

Only two experimental tests are available concerning the discharging phase of the "TopOpt" LHTS at a medium HTF mass flow rate (i.e., around 1900 l/h) due to the same reasons already underlined in section 5.2.2. These two cases are characterised by two levels of the average HTF inlet temperature: a medium level (43.8 °C), and a low level (31 °C). Table 5.6 summarises the driving forces for these two tests.

Table 5.6 TopOpt LHTS: discharging tests with a medium HTF mass flow rate

HTF mass flow rate [l/h]	HTF average inlet temperature [°C]
1854	43.8
1871	31

Medium level HTF inlet temperature (35°C – 45°C)

The time evolution of the measured and simulated HTF outlet temperature is presented in Fig 5.31, while the "TopOpt" LHTS thermal power and total energy release are shown respectively in Fig 5.32 and Fig 5.33. There are no specific additional features to underline in this case, all the considerations made in the previous cases still hold here. The most evident difference between the simulated and experimental outcomes in the "TopOpt" LHTS is again the underestimation of the energy evolution history (Fig 5.33) due to the complex heat transfer mechanism with this type of heat exchanger. Nevertheless, the model results appear acceptable.

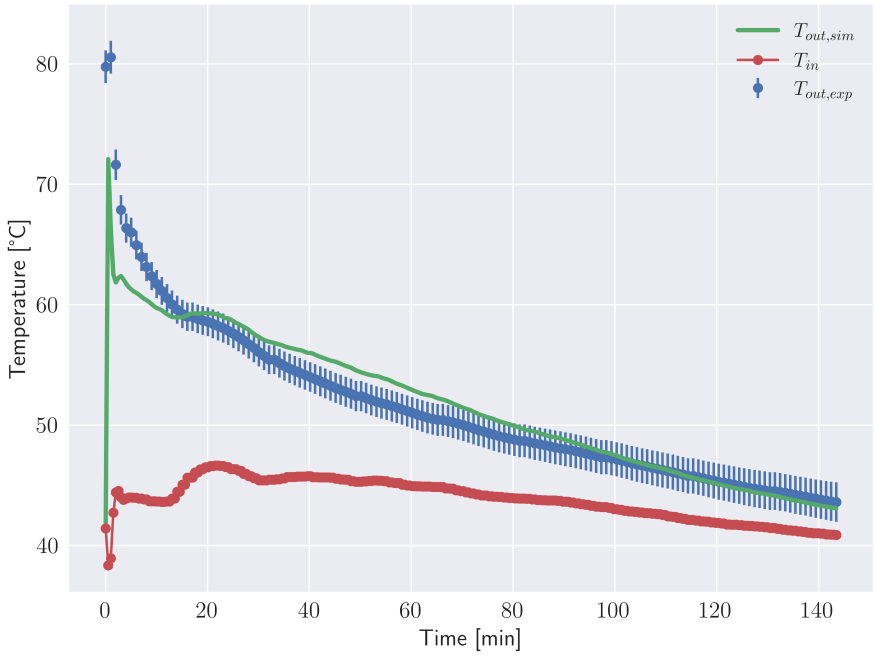

Fig. 5.31 TopOpt LHTS: comparison between simulated and measured HTF outlet temperature ($G_{HTF,avg}$ = 1854 l/h, $T_{HTF,in,avg}$ = 43.8 °C)

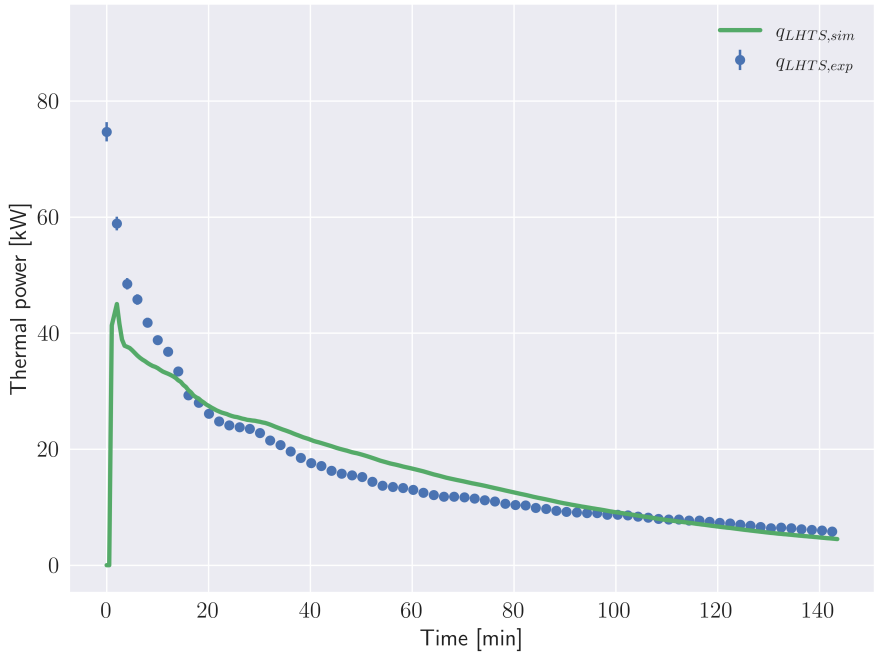

Fig. 5.32 TopOpt LHTS: comparison between simulated and measured thermal power ($G_{HTF,avg}$ = 1854 l/h, $T_{HTF,in,avg}$ = 43.8 °C)

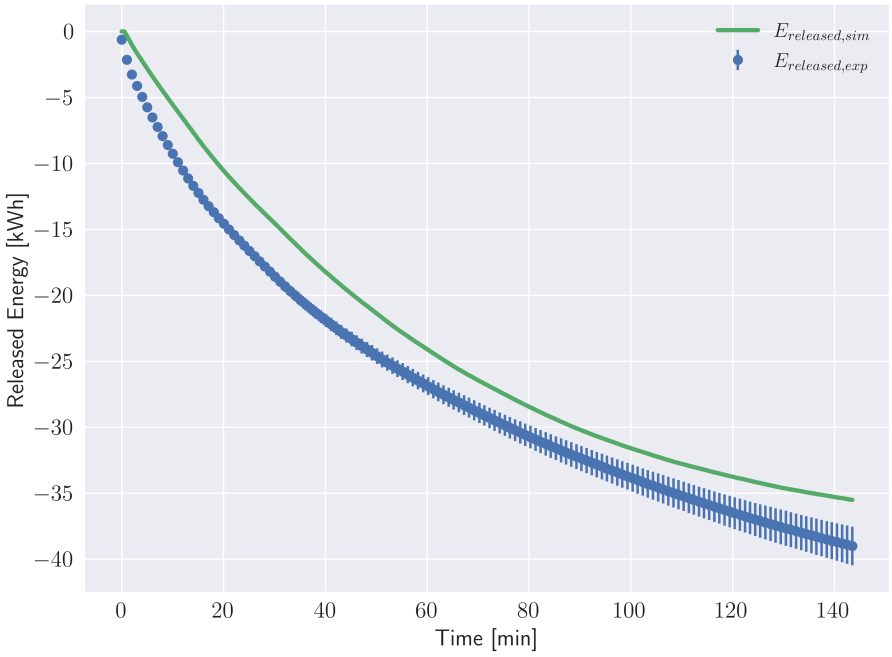

Fig. 5.33 TopOpt LHTS: comparison between simulated and measured discharged energy history ($G_{HTF,avg}$ = 1854 l/h, $T_{HTF,in,avg}$ = 43.8 °C)

Low level HTF inlet temperature (<35°C)

The comparison between the experimental and simulated HTF outlet temperature is available in Fig 5.34, while the "TopOpt" LHTS thermal power and total energy release are presented respectively in Fig 5.35 and Fig 5.36. Again, there are no additional comments with respect to the previous analyses. However, it should be noticed how a higher HTF temperature difference between inlet and outlet further exacerbates the model tendency to underestimate the "TopOpt" LHTS unit discharging rate, especially during the initial 15 minutes.

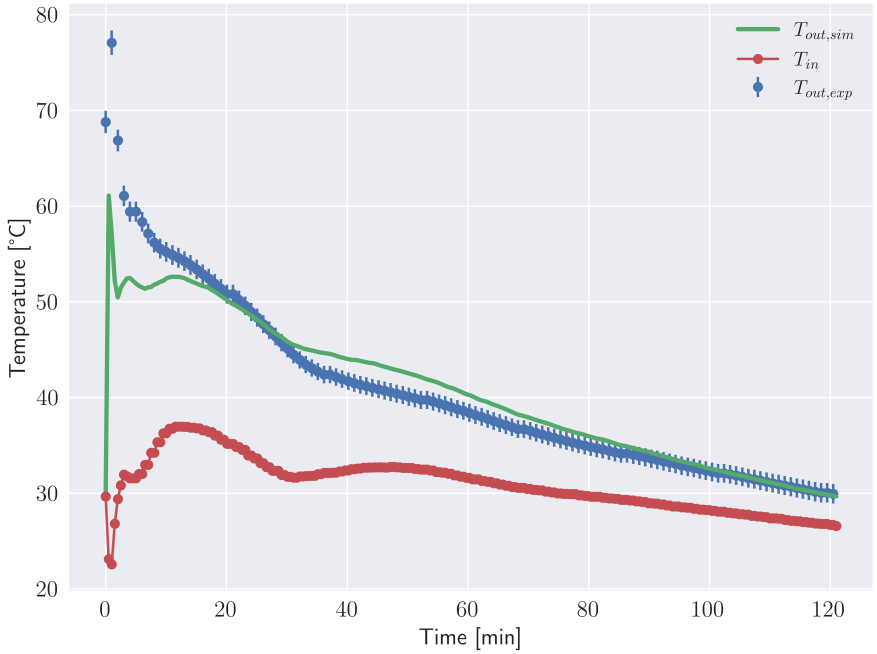

Fig. 5.34 TopOpt LHTS: comparison between simulated and measured HTF outlet temperature ($G_{HTF,avg}$ = 1871 l/h, $T_{HTF,in,avg}$ = 31 °C)

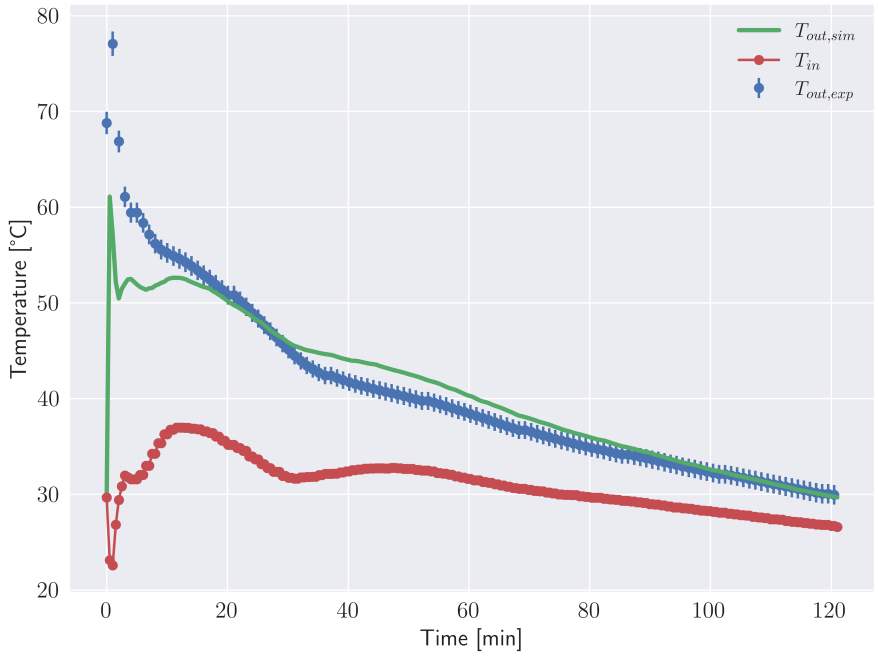

Fig. 5.35 TopOpt LHTS: comparison between simulated and measured thermal power ($G_{HTF,avg}$ = 1871 l/h, $T_{HTF,in,avg}$ = 31 °C)

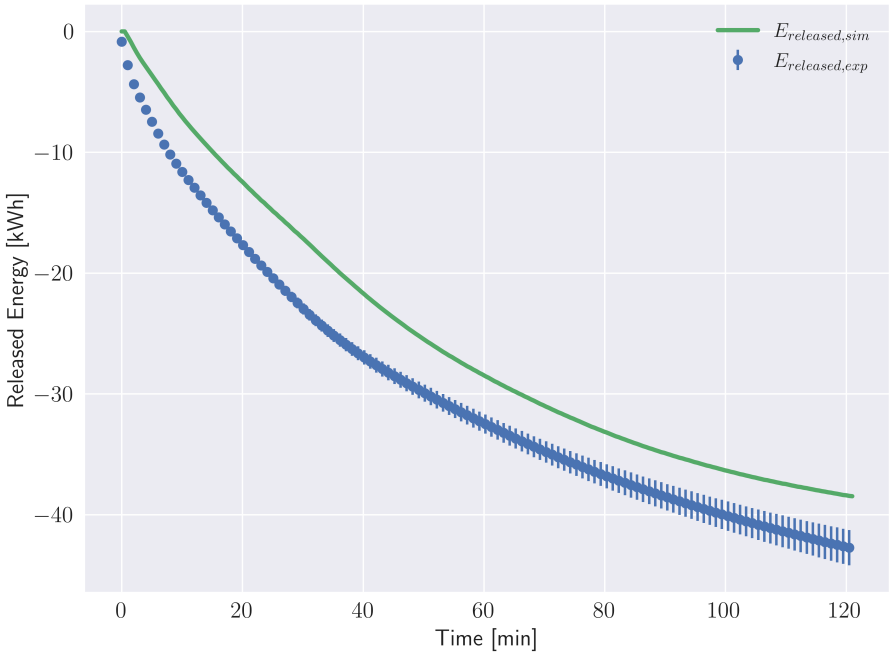

Fig. 5.36 TopOpt LHTS: comparison between simulated and measured discharged energy history ($G_{HTF,avg}$ = 1871 l/h, $T_{HTF,in,avg}$ = 31 °C)

5.2.5 Tests with high HTF mass flow rate (around 2500 l/h): Longitudinal LHTS

This section validates the "Longitudinal" LHTS model comparing the measured and simulated results over three tests at a high HTF mass flow rate (i.e., around 2500 l/h). The considered average HTF inlet temperatures span from 32.1 °C to 52.4 °C, as shown in Table 5.7. Unfortunately, the dependency of the experimental set up on the external weather conditions (because of the dry cooler) did not allow to obtain the exact same levels of temperature of the previous groups of tests in section 5.2.1 and 5.2.3.

Table 5.7 Longitudinal LHTS: discharging tests with a high HTF mass flow rate

HTF mass flow rate [l/h]	HTF average inlet temperature [°C]
2471	52.4
2532	36.9
2477	32.1

High level HTF inlet temperature (>45°C)

The measured and simulated HTF outlet temperature are compared in Fig. 5.37. Similarly, the time evolution of the "Longitudinal" LHTS thermal power and total energy release are shown respectively in Fig. 5.38 and Fig. 5.39. As in the previous test with a high HTF inlet temperature, $T_{HTF,in}$ is rather unstable throughout the discharging time with an increasing trend. For this reason, only a portion of the entire discharging process is presented in Fig. 5.39. As already explained, this particular effect is due to the dynamic behaviour of the dry cooler. Furthermore, this issue is enhanced by the higher turbulence in the experimental system pipes. Moreover, as the HTF inlet mass flow rate increases, the model tends to underestimate the LHTS performance during the initial minutes of the discharging process probably because the turbulence model in the HTF domain is not able to capture the high variability of this transient phase. As a result, the energy deficit in the model outcome is propagated until the end of the simulation.

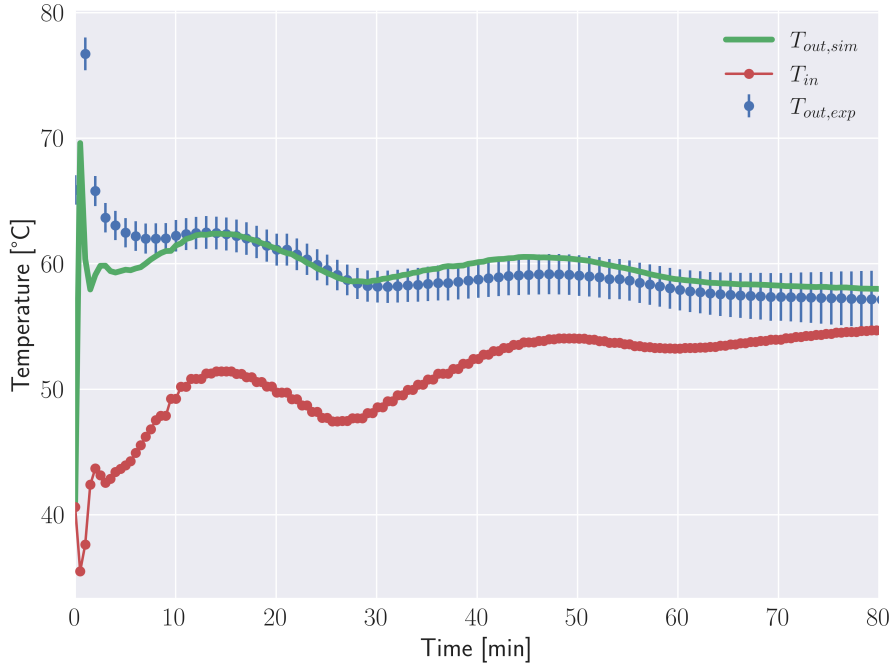

Fig. 5.37 Longitudinal LHTS: comparison between simulated and measured HTF outlet temperature ($G_{HTF,avg}$ = 2471 l/h, $T_{HTF,in,avg}$ = 52.4 °C)

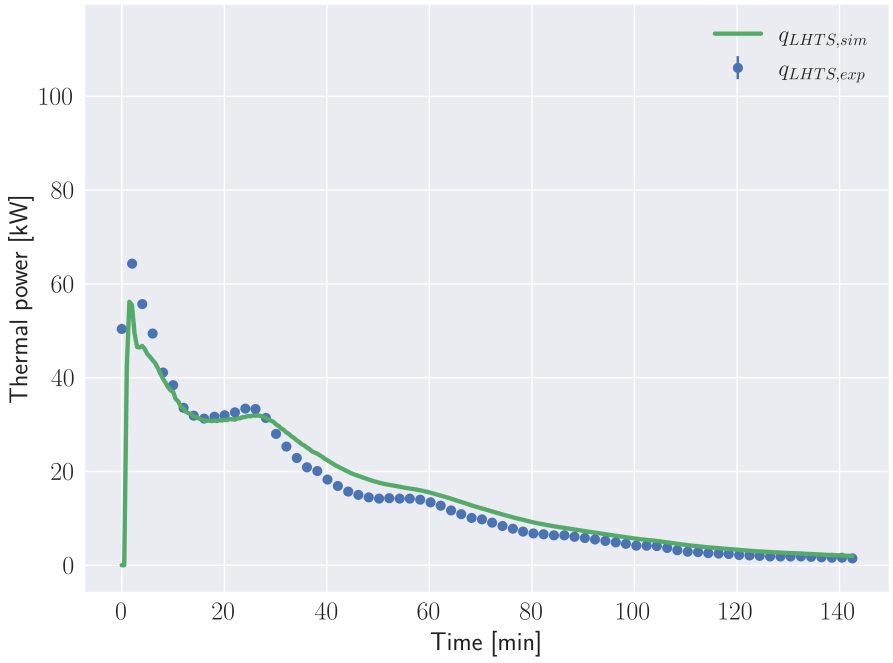

Fig. 5.38 Longitudinal LHTS: comparison between simulated and measured thermal power ($G_{HTF,avg}$ = 2471 l/h, $T_{HTF,in,avg}$ = 52.4 °C)

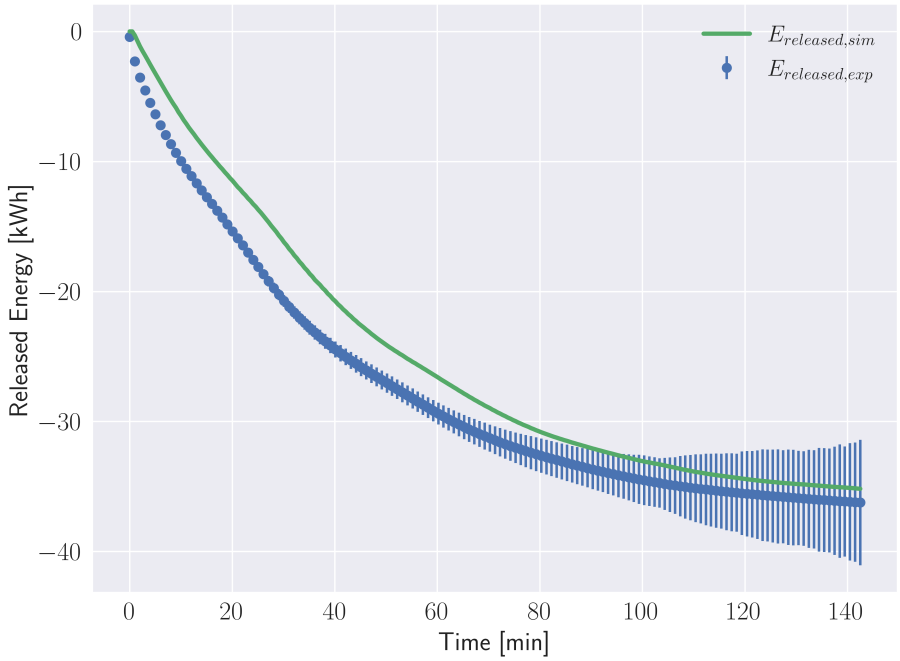

Fig. 5.39 Longitudinal LHTS: comparison between simulated and measured discharged energy history ($G_{HTF,avg}$ = 2471 l/h, $T_{HTF,in,avg}$ = 52.4 °C)

Medium level HTF inlet temperature (35°C – 45°C)

Fig. 5.40 presents the time evolution of the measured and simulated HTF outlet temperature, while Fig. 5.41 and Fig. 5.42 show the history of the "Longitudinal" LHTS thermal power and total energy release. Again, the inlet HTF temperature is fluctuating at the beginning of the discharging process for the abovementioned reasons. There are no further aspects to address compared to the previous cases. An overall overview of the model accuracy throughout the various tests is presented in section 5.2.7.

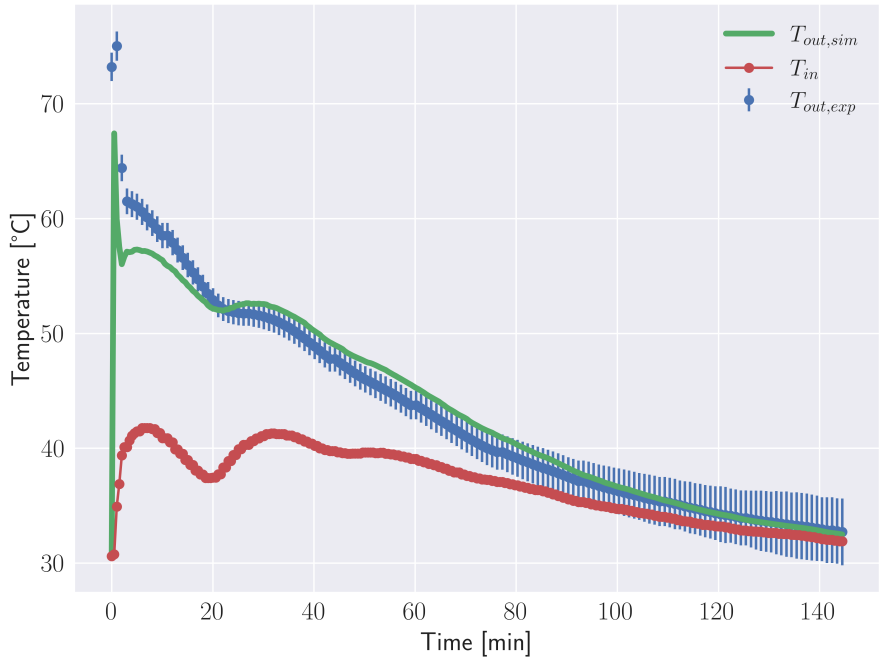

Fig. 5.40 Longitudinal LHTS: comparison between simulated and measured HTF outlet temperature ($G_{HTF,avg}$ = 2532 l/h, $T_{HTF,in,avg}$ = 36.9 °C)

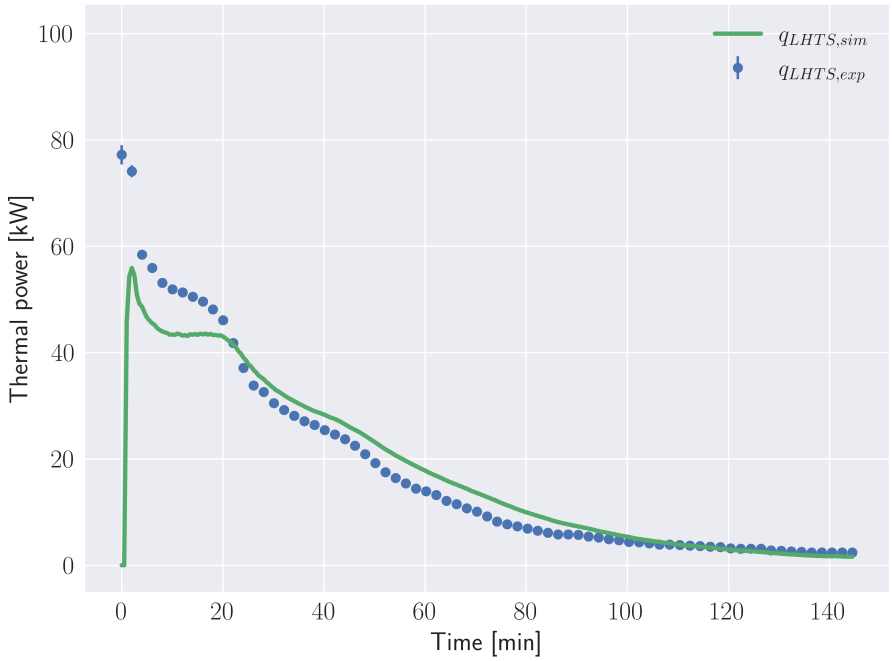

Fig. 5.41 Longitudinal LHTS: comparison between simulated and measured thermal power ($G_{HTF,avg}$ = 2532 l/h, $T_{HTF,in,avg}$ = 36.9 °C)

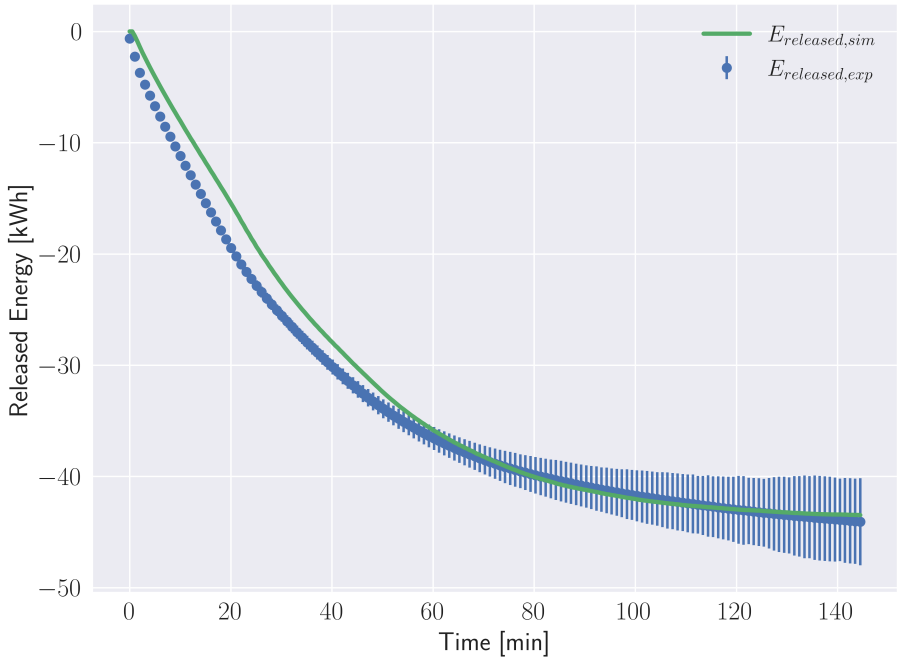

Fig. 5.42 Longitudinal LHTS: comparison between simulated and measured discharged energy history ($G_{HTF,avg}$ = 2532 l/h, $T_{HTF,in,avg}$ = 36.9 °C)

Low level HTF inlet temperature (<35°C)

The comparison between the experimental and simulated HTF outlet temperature is available in Fig. 5.43, while the "Longitudinal" LHTS thermal power and total energy release are presented respectively in Fig. 5.44 and Fig. 5.45. Again, the inlet HTF temperature is fluctuating at the beginning of the discharging process for the abovementioned reasons. This test clearly shows how an elevated HTF mass flow rate combined with a low HTF inlet temperature determines a fast-discharging rate (after 50 minutes the LHTS unit has already released 40 kWh). Apart from this aspect, there are no further features to address compared to the previous cases, considering that an overall overview of the model accuracy throughout the various tests is presented in section 5.2.7.

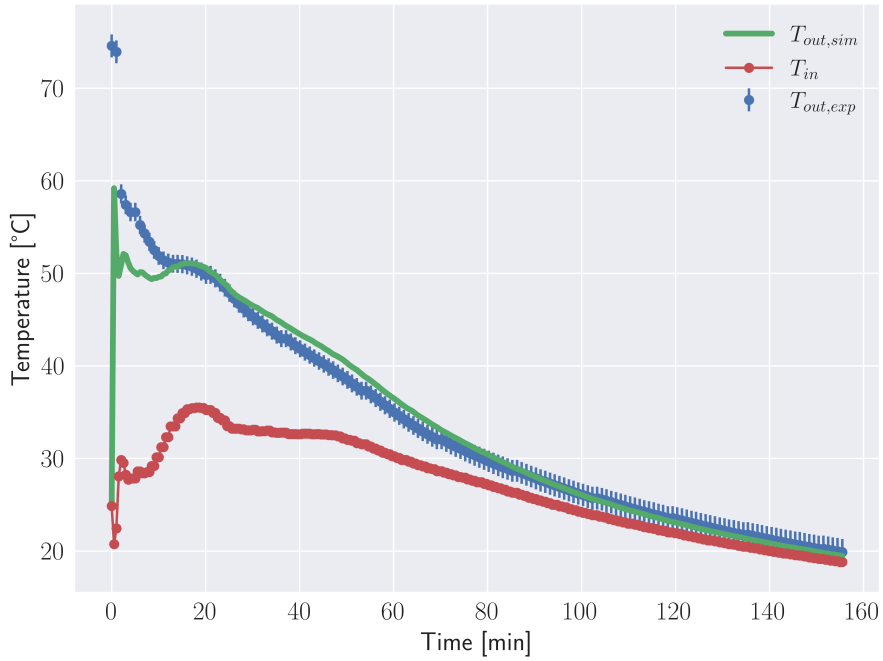

Fig. 5.43 Longitudinal LHTS: comparison between simulated and measured HTF outlet temperature ($G_{HTF,avg}$ = 2477 l/h, $T_{HTF,in,avg}$ = 32.1 °C)

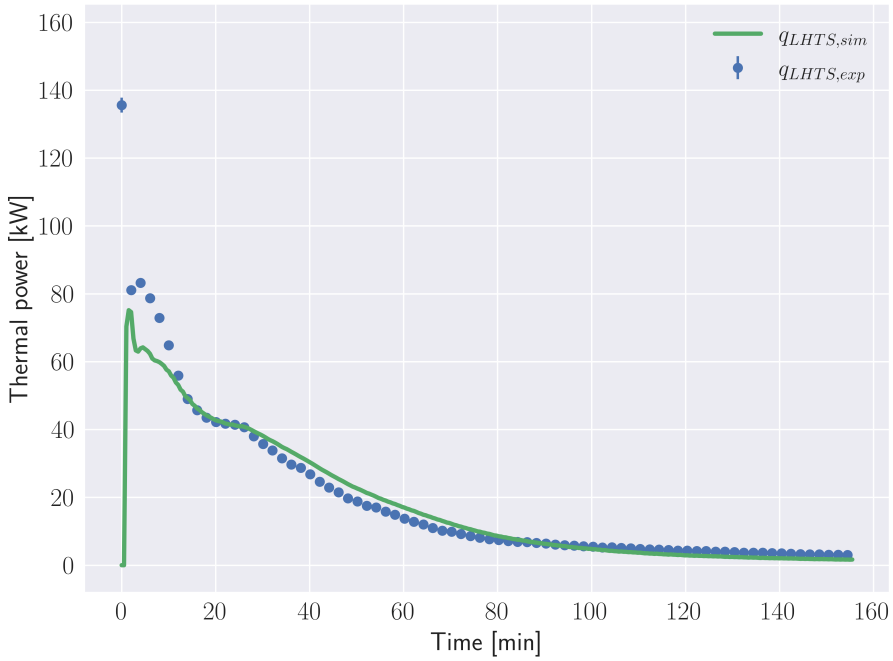

Fig. 5.44 Longitudinal LHTS: comparison between simulated and measured thermal power ($G_{HTF,avg}$ = 2477 l/h, $T_{HTF,in,avg}$ = 32.1 °C)

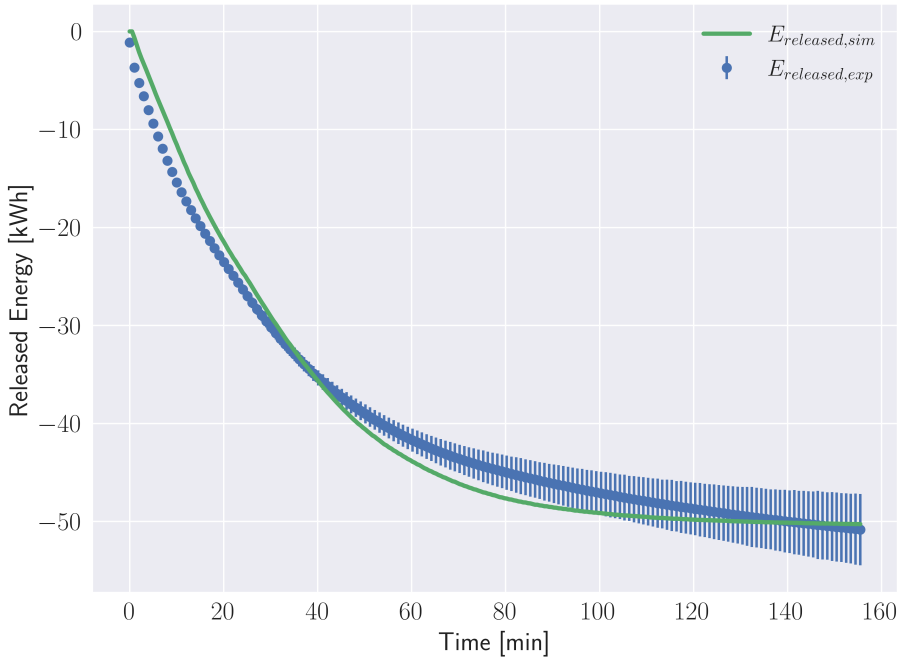

Fig. 5.45 Longitudinal LHTS: comparison between simulated and measured discharged energy history ($G_{HTF,avg}$ = 2477 l/h, $T_{HTF,in,avg}$ = 32.1 °C)

5.2.6 Tests with high HTF mass flow rate (around 2500 l/h): TopOpt LHTS

As in the previous sections related to the "TopOpt" LHTS discharging tests, only two cases are available at a high HTF mass flow rate (i.e., around 2500 l/h) due to the same reasons already underlined in section 5.2.2. These two cases are characterised by a medium (37.4 °C) and a low (26 °C). Table 5.8 summarises the driving parameters for these two experimental tests.

Table 5.8 TopOpt LHTS: discharging tests with a high HTF mass flow rate

HTF mass flow rate [l/h]	HTF average inlet temperature [°C]
2482	37.4
2474	26

Medium level HTF inlet temperature (35°C – 45°C)

The measured and simulated HTF outlet temperature are compared in Fig. 5.46. Similarly, the time evolution of the "TopOpt" LHTS thermal power and total energy release are presented respectively in Fig. 5.47 and Fig. 5.48. Again, the HTF inlet temperature displays a marked oscillatory behaviour due to the combination of the dry cooler effect and the turbulent flow. As in the other cases that concern the "TopOpt" LHTS unit, the dynamic model presented in this thesis is less accurate compared to the model for "Longitudinal" LHTS, especially when an oscillating HTF inlet temperature is supplied to the storage unit for the reasons already exposed in the previous sections. In this particular case, the initial underestimation of the outlet HTF temperature calculated by the model determines a large energy deficit that is kept until the end of the simulation (Fig. 5.48). A further contextualisation of the model performance is available in section 5.2.7.

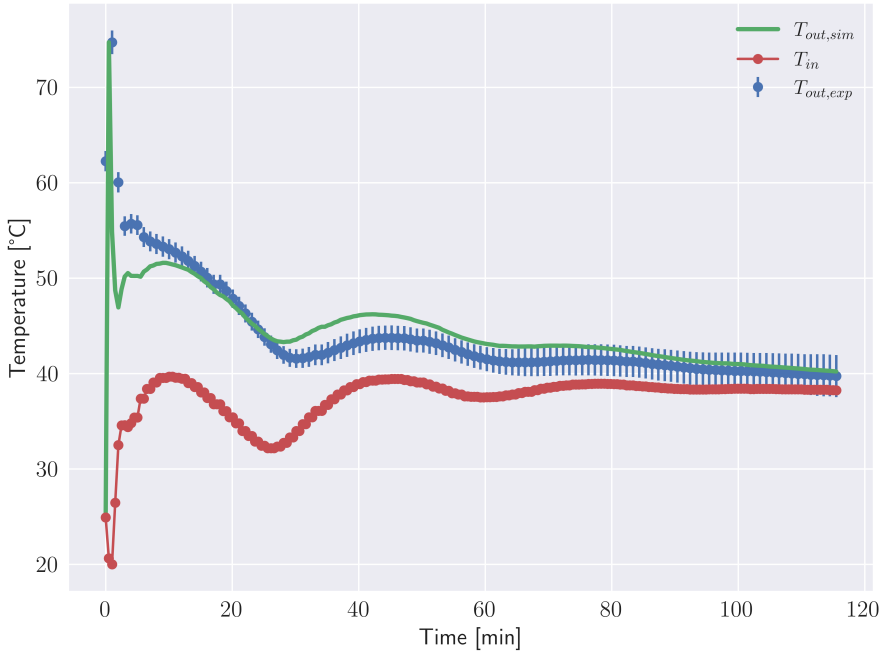

Fig. 5.46 TopOpt LHTS: comparison between simulated and measured HTF outlet temperature ($G_{HTF,avg}$ = 2482 l/h, $T_{HTF,in,avg}$ = 37.4 °C)

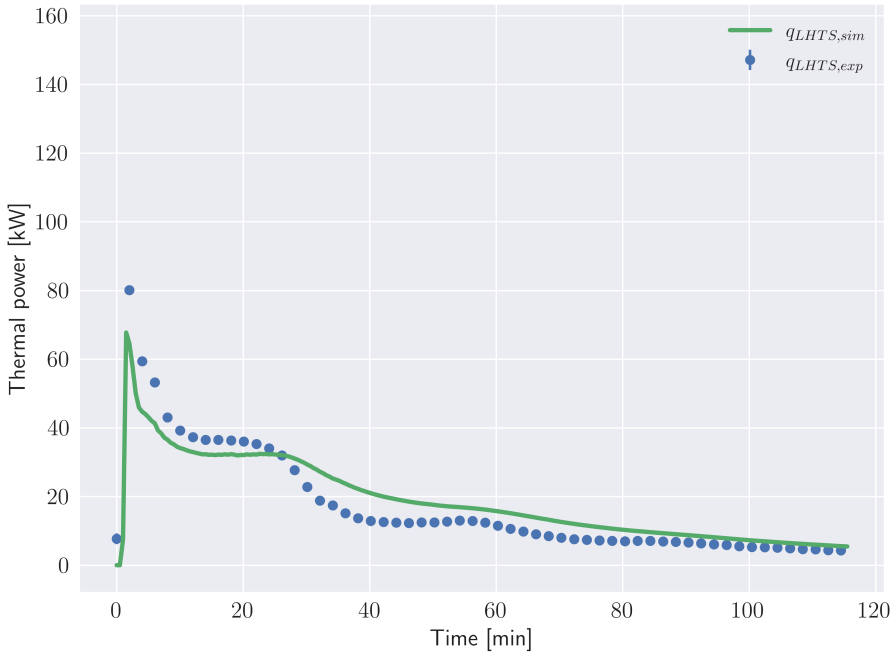

Fig. 5.47 TopOpt LHTS: comparison between simulated and measured thermal power ($G_{HTF,avg}$ = 2482 l/h, $T_{HTF,in,avg}$ = 37.4 °C)

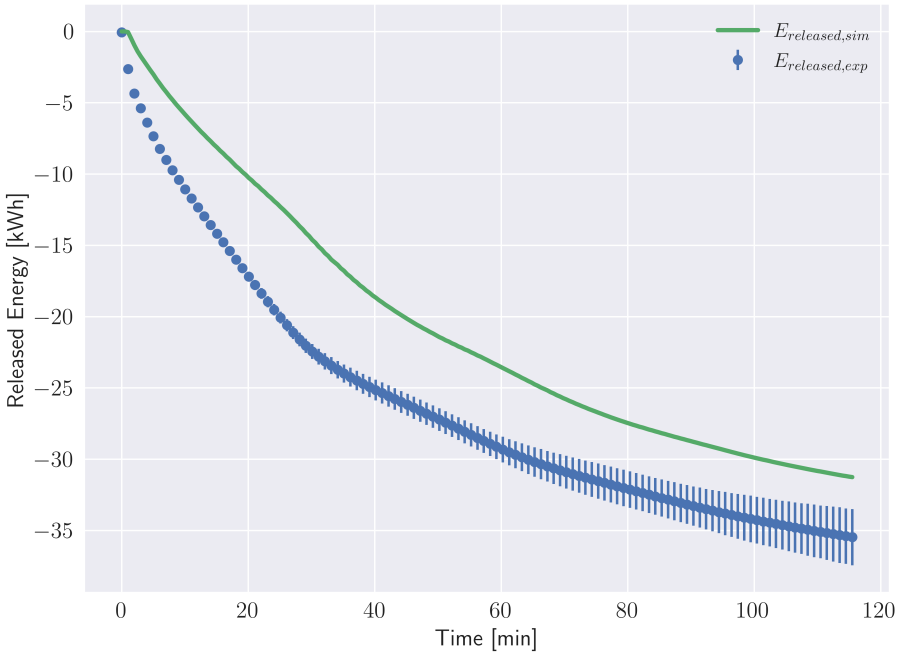

Fig. 5.48 TopOpt LHTS: comparison between simulated and measured discharged energy history ($G_{HTF,avg}$ = 2482 l/h, $T_{HTF,in,avg}$ = 37.4 °C)

Low level HTF inlet temperature (<35°C)

This section contains the last test concerning the model validation of the LHTS discharging phase. As in the previous sections, Fig. 5.49 compares the measured and simulated HTF outlet temperature, while the "TopOpt" LHTS thermal power and total energy release are shown respectively in Fig. 5.50 and Fig. 5.51. As expected, also in this test the model underestimates the LHTS discharging rate and the initial error is propagated throughout the simulation. There are no further features to address compared to the cases that have already been analysed, considering that an overall overview of the model accuracy throughout the various tests is presented in section 5.2.7.

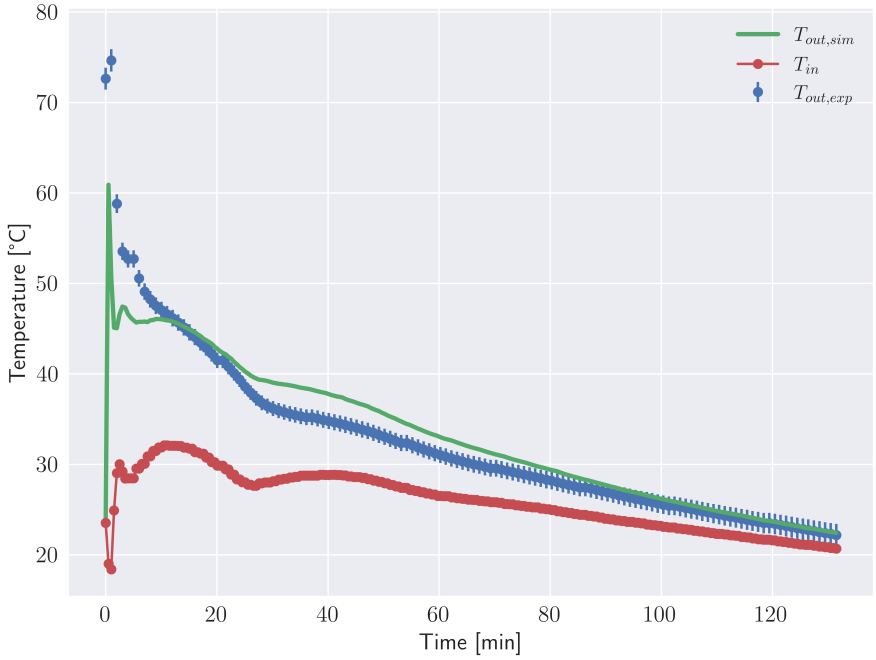

Fig. 5.49 TopOpt LHTS: comparison between simulated and measured HTF outlet temperature ($G_{HTF,avg}$ = 2474 l/h, $T_{HTF,in,avg}$ = 26 °C)

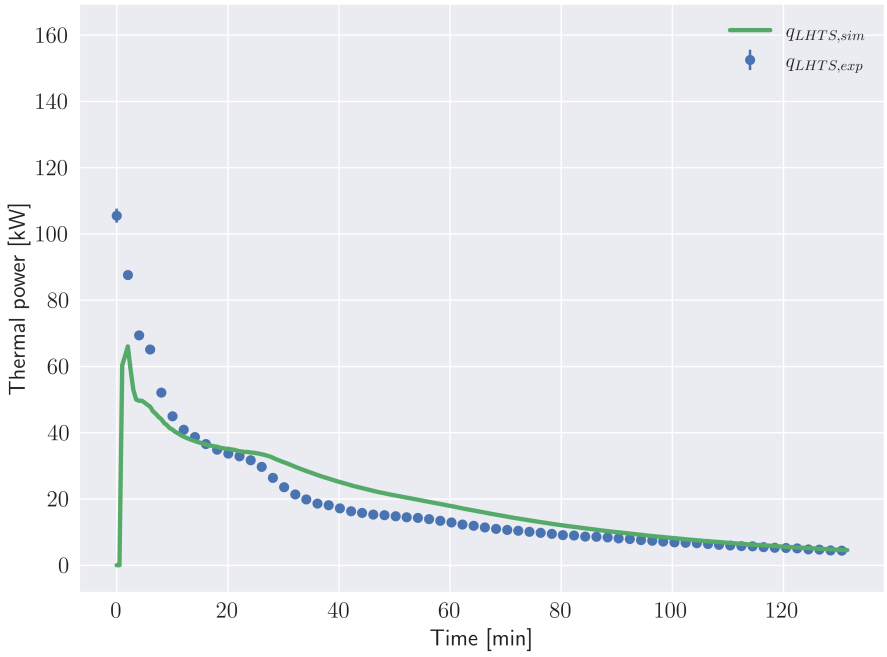

Fig. 5.50 TopOpt LHTS: comparison between simulated and measured thermal power ($G_{HTF,avg}$ = 2474 l/h, $T_{HTF,in,avg}$ = 26 °C)

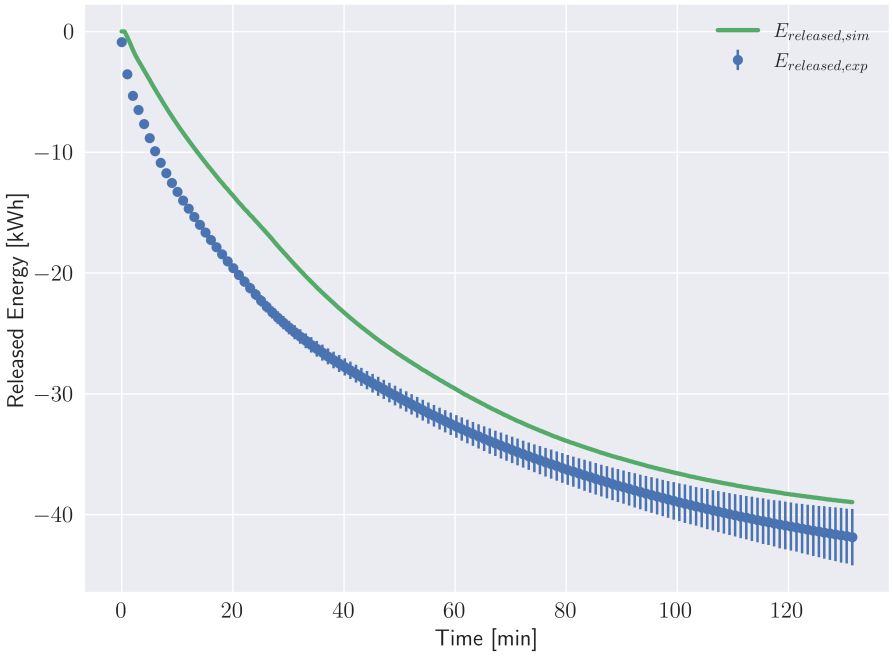

Fig. 5.51 TopOpt LHTS: comparison between simulated and measured discharged energy history ($G_{HTF,avg}$ = 2474 l/h, $T_{HTF,in,avg}$ = 26 °C)

5.2.7 Dynamic model validation during the LHTS discharging phase: summary

This section summarises the performance of the LHTS dynamic model proposed in this thesis through a comparative analysis of all the discharging tests presented above. To evaluate the model accuracy, the root mean square error (*RMSE*) between the simulated and the measured results is evaluated for three main quantities of interest: the HTF outlet temperature ($T_{HTF,out}$), the thermal power released by the LHTS unit (q_{LHTS}) and the LHTS state of charge (*SOC*). The latter parameter is estimated considering the energy released at the end of the discharging test. The formula used to calculate the root means square error is shown in Eq. 5.1.

$$RMSE = \sqrt{\frac{\sum(x_{sim} - x_{exp})^2}{N}} \tag{5.1}$$

Where x_{sim} are the simulated values at each time instant; x_{exp} are the measured values; N is the total number of measurements. Results are reported in Table 5.9 for the "Longitudinal" LHTS unit and in Table 5.10 for the "TopOpt" LHTS unit.

Table 5.9 Longitudinal LHTS: Root Mean Square Errors on discharging tests

$G_{HTF,avg}$ **[l/h]**	$T_{HTF,in,avg}$ **[°C]**	*RMSE* **on** $T_{HTF,out}$ **[°C]**	*RMSE* **on** q_{LHTS} **[kW]**	*RMSE* **on** *SOC* **[%]**
1388	45.5	2.21	5.50	2.89
1387	41.7	2.23	6.11	2.95
1403	37.8	1.96	5.29	1.90
1413	28.2	4.19	8.77	3.74
1909	53.7	2.87	8.93	7.36
1905	44.9	2.80	7.68	3.82
1884	41.3	2.89	8.62	5.89
1895	29.0	4.61	12.5	6.26
2471	52.4	2.25	9.02	7.24
2532	36.9	3.14	9.23	3.96
2477	32.1	3.64	13.2	3.83

Table 5.10 TopOpt LHTS: Root Mean Square Errors on discharging tests

$G_{HTF,avg}$ **[l/h]**	$T_{HTF,in,avg}$ **[°C]**	*RMSE* **on** $T_{HTF,out}$ **[°C]**	*RMSE* **on** q_{LHTS} **[kW]**	*RMSE* **on** *SOC* **[%]**
1384	42.9	2.92	6.32	7.15
1412	37.5	3.20	11.8	8.66
1854	43.8	3.09	8.44	7.77
1871	31.0	4.10	12.1	10.1
2482	37.4	3.66	15.4	15.6
2474	26.0	4.35	14.9	9.10

Overall, the model accuracy appears extremely satisfactory for the LHTS units analysed. With the aim of creating a model able to simulate the behaviour of a general shell-and-tube LHTS unit from a system perspective, the most relevant error to monitor is arguably the one on the LHTS state of charge. As a matter of fact, discrepancies in the instantaneous values of the other two monitored quantities ($T_{HTF,out}$ and q_{LHTS}) are not as influent as those on the released energy (or, equivalently the state of charge) because of heating systems thermal inertia. Such a consideration is valid especially if the timespan of the LHTS discharging process is considered, which rarely exceeds 2h. In this restricted interval of time the entire heating system thermal inertia smoothens any thermal power peak through the heating terminals that supply useful heat to the final users. The results of the model validation show that the RMSE on the LHTS state of charge is mostly below 10%, with the only exception of one test of the "TopOpt" LHTS unit (which is however characterised by a highly unstable inlet HTF temperature). As a general trend, the model accuracy concerning the instantaneous values of $T_{HTF,out}$ and q_{LHTS} decreases as the driving discharging forces (i.e. $\Delta T_{PCM-HTF}$ and the HTF mass flow rate) increase. However, LHTS units are generally designed to work with a reduced temperature gap between the PCM phase change and the HTF temperature. Moreover, the best simulation results are achieved when the inlet HTF temperature is stable in time, which is expected to be a normal condition in most of the residential heating systems. Unfortunately, as already explained, the experimental system used for these tests did not allow such a temperature regulation concerning the heat transfer fluid. When comparing the two types of LHTS units, it is evident that the dynamic model proposed in this thesis is more accurate if the behaviour of the "Longitudinal" LHTS is simulated. This is due

to the fact that in the "Longitudinal" LHTS unit the largest thermal gradients are radial (from the centre of the HTF pipe towards the PCM-HCM assembly), while in the "TopOpt" LHTS unit the HCM rods modify this pattern. Moreover, the extremely compact design of the "Longitudinal" LHTS unit favours a diffusive heat transfer mechanism, while in the "TopOpt" LHTS unit natural convection is largely present when the PCM is liquid. As a matter of fact, these two distinctive features of the "Longitudinal" LHTS unit are more in line with the dynamic model hypotheses. Notwithstanding these differences, the simulated outcomes for the "TopOpt" LHTS unit are quite satisfactory. It should be remarked that the only difference between the model for the "Longitudinal" LHTS and the model for the "TopOpt" LHTS resides in the calculation of the characteristic length l_c, which is a lumped parameter estimated a priori based on the LHTS inner heat exchanger geometrical features (see section 5.2). It is expected that the model accuracy for the "TopOpt" LHTS unit could be further improved if the parameter l_c is calibrated on the experimental tests instead of estimating an a-priori value. In general, it is assumed that such a procedure should be valid for all those storage units that are not dominated only by radial thermal gradients. However, this aspect is out of the scope of this thesis because the proposed model aims at providing acceptable simulation results without any experimental calibration of the modelling parameters.

5.3 LHTS dynamic model validation: repeated similar discharging tests

Before the definition of the experimental test matrix reported in Table 5.1, a series of repetitive discharging tests were performed with the "Longitudinal" LHTS unit over a couple of weeks. These tests are characterised by very similar HTF input conditions. Moreover, also the environmental conditions affecting the dry cooler performance were very similar thanks to the restricted testing period. Thus, this group of experimental results constitute a good resource to verify if the proposed dynamic model provides stable and reliable outcomes. The HTF input conditions are reported as follows:

- Test 1: Average HTF flow rate: 2577 l/h; average HTF inlet temperature: 36.7°C

- Test 2: Average HTF flow rate: 2557 l/h; average HTF inlet temperature: 34.7°C
- Test 3: Average HTF flow rate: 2522 l/h; average HTF inlet temperature: 35.0°C
- Test 4: Average HTF flow rate: 2455 l/h; average HTF inlet temperature: 35.2°C

To verify the stability of the model results, Fig. 5.52 shows which is the evolution of the temperature difference between the measured and simulated HTF outlet temperature. Apart from a high initial discrepancy in the very first instants of the LHTS discharging phase, the model reproduces well the real HTF outlet temperature after 10 minutes of discharge. Moreover, after 20 minutes the variability is always contained within 2.5 °C. The initial difference between the measured and simulated outcome witnesses again the limit of the model in capturing all the heat transfer mechanisms at the beginning of the discharging phase. As already pointed out in section 5.2, the start of the discharging process is very complex and natural convection phenomena in the liquid PCM generally have an enhancing effect. Nevertheless, this picture proves that under similar input conditions the model yields stable results.

A further proof, is presented in Fig. 5.53. Here, this represents how the absolute difference between the measured and simulated energy release evolves in time. In line with the previous considerations, the initial phase of the discharging process is characterised by an underestimation of the energy release. As a matter of fact, after around 20 minutes a peak is reached in the difference between the measured and simulated energy release. However, in the following time instants the model recovers this gap, and the error is reduced below 2 kWh after 60 minutes. To better contextualize this value, it should be remembered that the LHTS discharges more than 40 kWh during its cycle. Hence, the abovementioned gap constitutes only the 5% of the whole discharged energy. In conclusion, also this picture proves that the dynamic model outcomes are very consistent across similar input conditions.

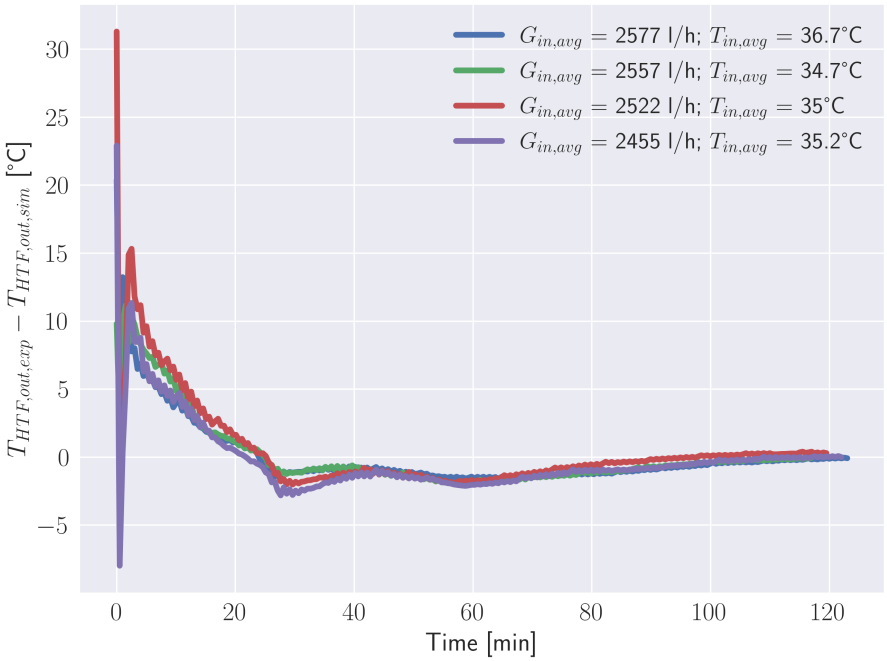

Fig. 5.52 Longitudinal LHTS: temperature difference between simulated and measured HTF outlet temperature in repeated similar discharging tests

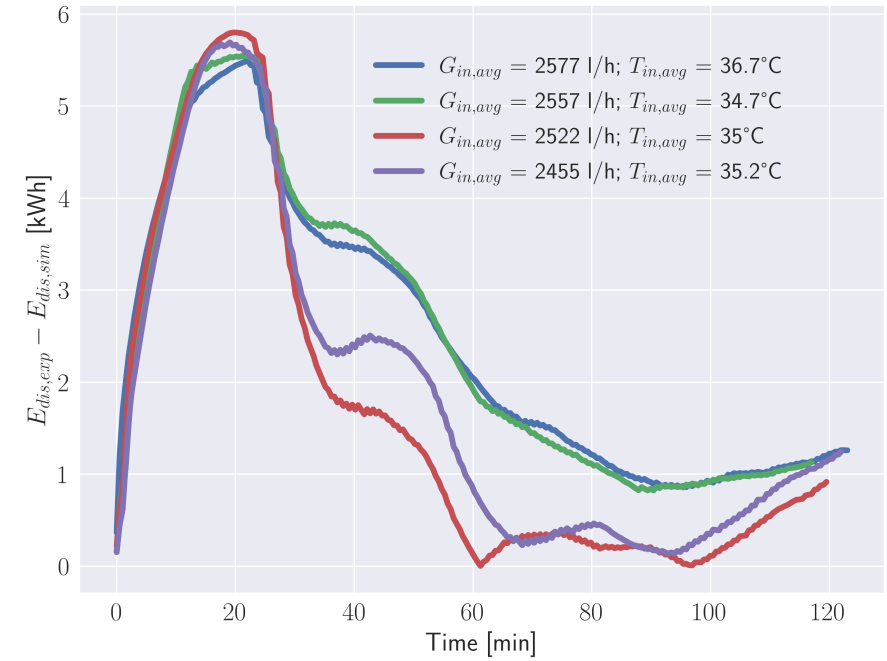

Fig. 5.53 Longitudinal LHTS: difference between simulated and measured released energy history in repeated similar discharging tests

5.4 Comparative analysis of the "Longitudinal" and “TopOpt” LHTS

As detailed in Chapter 3, the two LHTS units realised for this study are characterised by a different design concerning the inner heat exchanger. Although the quantity of high conducting material for the fins around the HTF pipes is the same for both the configurations, these two types of fins interact differently with the surrounding PCM. Hence, this section aims at exploring the performance of the “Longitudinal” and the “TopOpt” LHTS units when similar boundary conditions are applied. Consequently, four cases are presented hereafter. Among these, three are dedicated to the analysis of the storage discharging phase considering different levels of inlet HTF mass flow rates. On the contrary, the remaining two cases compare the LHTS units during the charging phase both with the electrical resistance and with the DH supply.

5.4.1 Comparative analysis during the discharging phase

Table 5.11 summarises the inlet boundary conditions of the experimental tests selected to compare the discharging performance of the “Longitudinal” and “TopOpt” LHTS units.

Table 5.11 Test matrix for the comparative analysis of "Longitudinal" and "TopOpt" LHTS during discharge

HTF flow rate level	Longitudinal LHTS	TopOpt LHTS
Low	$G_{HTF,avg}$=1403 l/h; $T_{HTF,in,avg}$=37.8 °C	$G_{HTF,avg}$=1412 l/h; $T_{HTF,in,avg}$=37.5 °C
Medium	$G_{HTF,avg}$=1905 l/h; $T_{HTF,in,avg}$=44.9 °C	$G_{HTF,avg}$=1854 l/h; $T_{HTF,in,avg}$=43.8 °C
High	$G_{HTF,avg}$=2532 l/h; $T_{HTF,in,avg}$=36.9 °C	$G_{HTF,avg}$=2482 l/h; $T_{HTF,in,avg}$=37.4 °C

As far as the first test is concerned, Fig. 5.54 reports the temperature increase of the HTF between inlet and outlet. The choice to represent the HTF temperature

increase instead of presenting separately the HTF inlet and outlet temperature for both the storage units is due to the fact that the time evolution of the HTF inlet temperature is not exactly coincident in these two cases. Instead, the HTF temperature increase is a good parameter to compare the performance of the two LHTS units because it is practically independent on the HTF inlet temperature value. However, it should be noticed that this consideration holds when the driving discharge conditions (i.e., the HTF inlet mass flow rate and temperature) are comparable. As a matter of fact, in this test the average HTF inlet mass flow rate values are 1403 l/h and 1412 l/h, while the average HTF inlet temperatures are 37.8 °C and 37.5 °C, respectively for the "Longitudinal" LHTS and the "TopOpt" LHTS. As a result, the "Longitudinal" LHTS appears more effective than the "TopOpt" LHTS in transferring the stored energy content towards the HTF. Consequently, at the end of the discharging process the "Longitudinal" LHTS can release 20% more energy than the "TopOpt" LHTS (45 kWh vs. 37 kWh), as depicted in Fig. 5.55. For a better contextualization of these results, it should be mentioned that average PCM temperature ($T_{PCM,initial}$) at the beginning of the discharging test is slightly different for the two examined storage units. This quantity is calculated as the average of the values measured by the 16 thermocouples placed inside the PCM. More specifically, for the "Longitudinal" LHTS $T_{PCM,initial}$ = 80.2°C, while for the "TopOpt" LHTS its value is 76.2 °C. However, this difference in the initial conditions is not particularly influential because both these values are above the PCM phase change temperature (69°C when cooling down). Moreover, the additional sensible energy content of the "Longitudinal" LHTS generated by this temperature difference amounts to 1.1 kWh considering the PCM total mass and specific heat capacity. This constitutes only the 2% of the overall energy released by the "Longitudinal" LHTS.

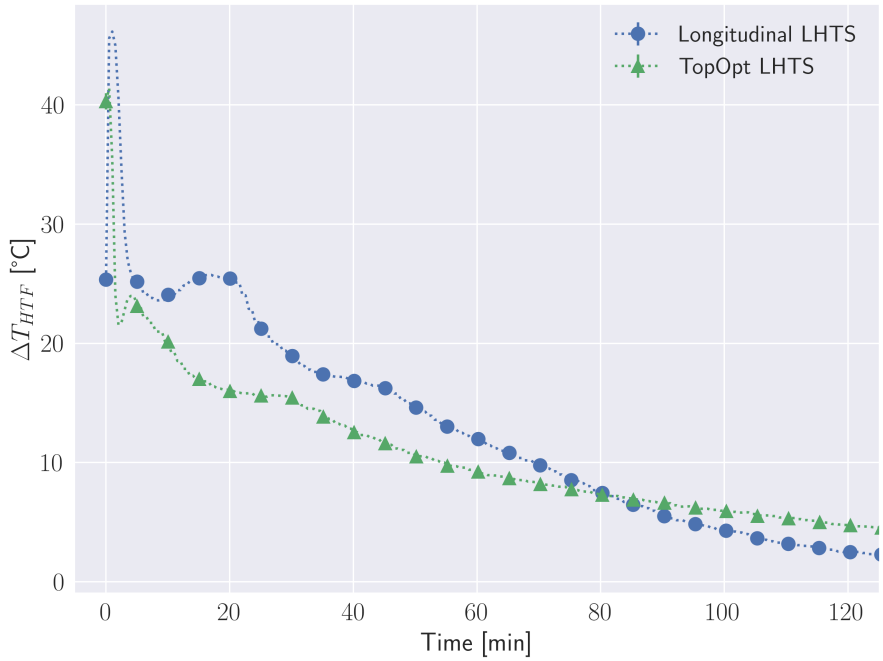

Fig. 5.54 Comparative analysis between HTF temperature increase across the "Longitudinal" and "TopOpt" LHTS (low HTF flow rate)

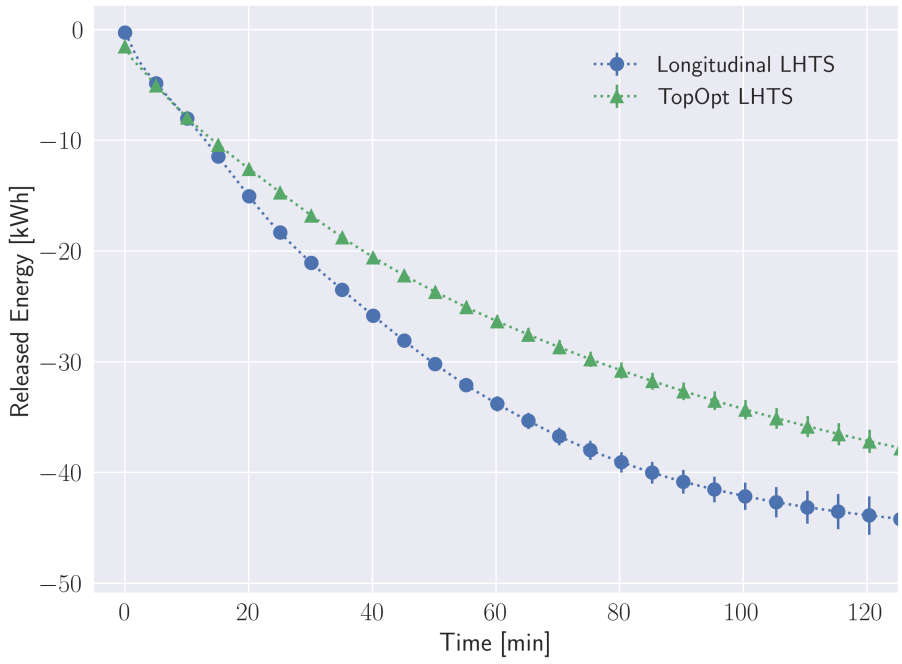

Fig. 5.55 Comparative analysis between the energy histories of the "Longitudinal" and "TopOpt" LHTS (low HTF flow rate)

As far as the test with a medium level HTF inlet mass flow rate is concerned (around 1900 l/h), Fig. 5.56 reports the temperature increase of the HTF between inlet and outlet. The increased HTF mass flow rate with respect to the previous case induces a more similar behaviour of the two LHTS units because the increased turbulence favours the heat transfer from the PCM to the HTF. Nevertheless, the inner heat exchanger of the "Longitudinal" LHTS has again a better performance compared to the "TopOpt" LHTS. Indeed, the "Longitudinal" LHTS releases 8% more energy than the "TopOpt" LHTS after 2h of discharge (see Fig. 5.57). In this case, the average PCM temperature at the beginning of the discharging process is slightly in favour of the "TopOpt" LHTS (81.7 °C). The "Longitudinal" LHTS is instead characterised by $T_{PCM,initial}$ = 78.4 °C, meaning an energy content deficit equal to 0.9 kWh.

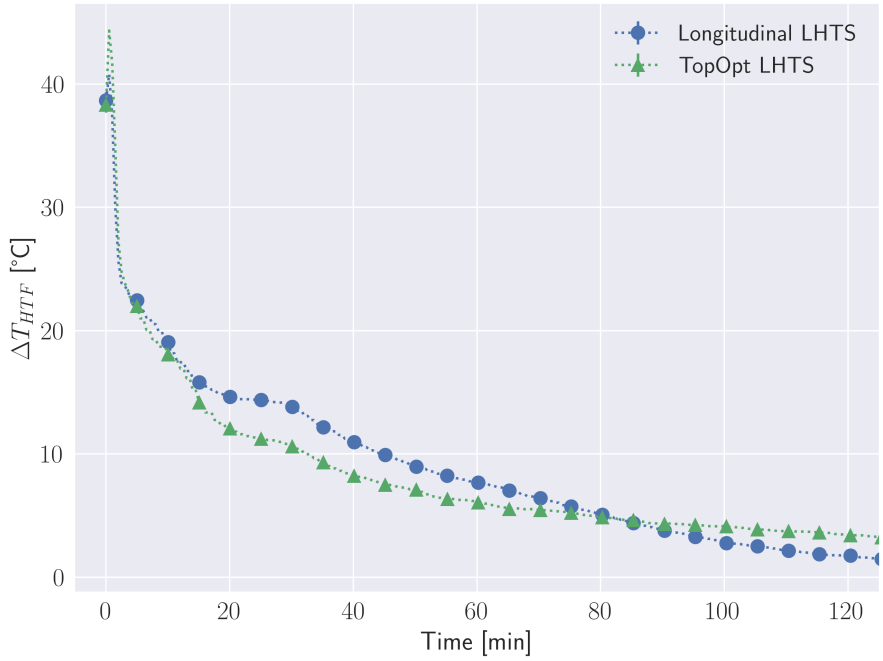

Fig. 5.56 Comparative analysis between HTF temperature increase across the "Longitudinal" and "TopOpt" LHTS (medium HTF flow rate)

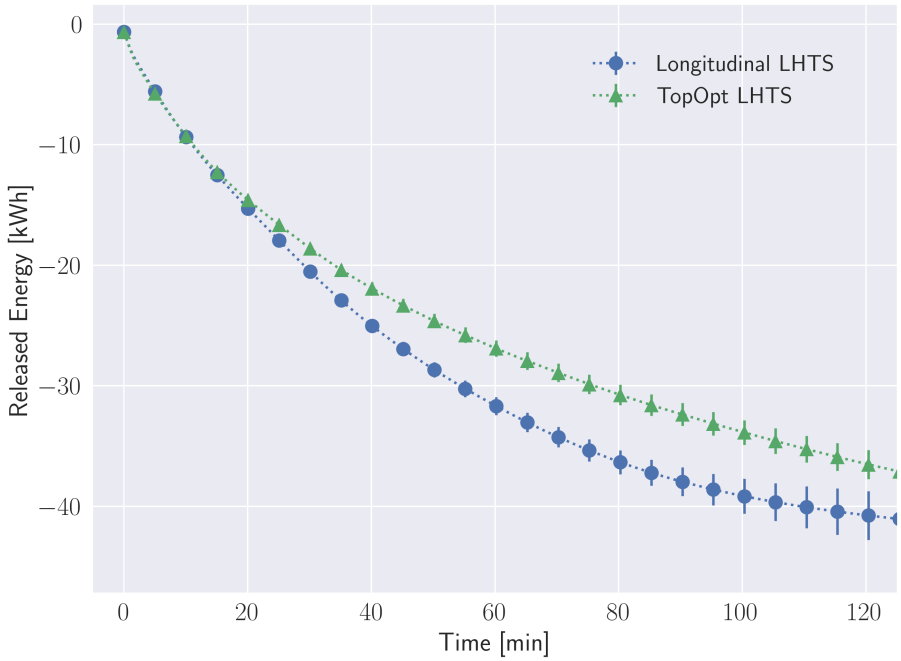

Fig. 5.57 Comparative analysis between the energy histories of the "Longitudinal" and "TopOpt" LHTS (medium HTF flow rate)

The third test features a high level of HTF inlet mass flow (around 2500 l/h). Fig. 5.58 reports the temperature increase of the HTF between inlet and outlet across the two examined storage units, while Fig. 5.59 presents the respective energy histories. Overall, the increased HTF mass flow rate determines a faster discharging process for both the LHTS systems. If compared with the test at around 1400 l/h (which is also characterised by similar average HTF inlet temperatures), both the storage units release 10% more energy after 60 minutes. Notwithstanding the HTF inlet temperature oscillations in this test, the heat transfer from the PCM to the HTF is faster in the “Longitudinal” LHTS. Overall, at the time when the energy discharge is stopped for the “TopOpt” LHTS (< 2h), the “Longitudinal” LHTS has released 19% more energy. Again, the initial conditions of the two storage systems are slightly different: for the “Longitudinal” LHTS $T_{PCM,initial}$ = 77°C, while for the “TopOpt” LHTS this value reaches 74.7 °C (meaning an energy content deficit equal to 0.6 kWh).

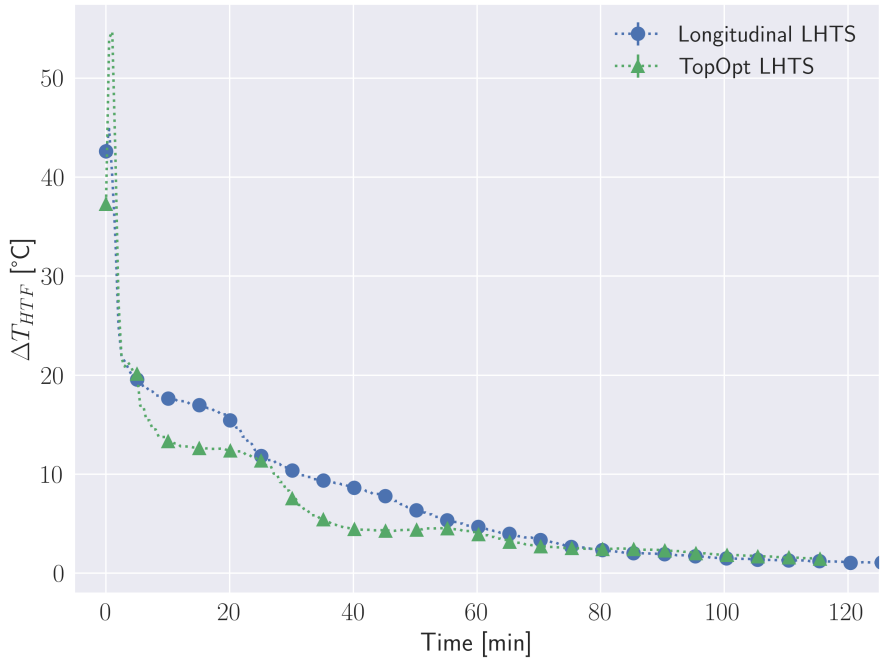

Fig. 5.58 Comparative analysis between HTF temperature increase across the "Longitudinal" and "TopOpt" LHTS (high HTF flow rate)

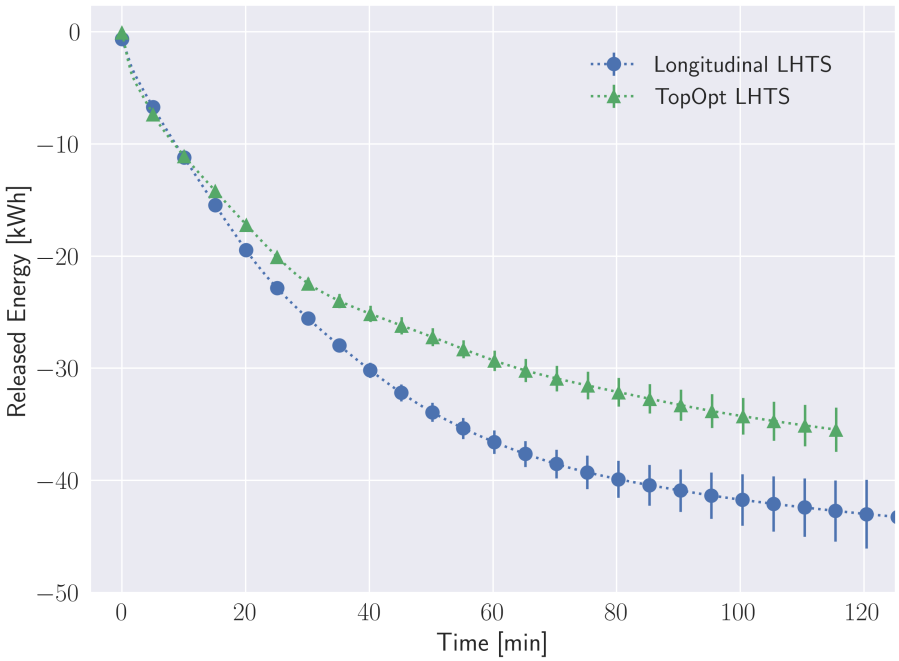

Fig. 5.59 Comparative analysis between the energy histories of the "Longitudinal" and "TopOpt" LHTS (high HTF flow rate)

Summarising, the “Longitudinal” LHTS unit showed a higher performance compared to the “TopOpt” LHTS in terms of speed of discharge. The former heat exchanger is more efficient in transferring the stored heat from the PCM to the HTF when similar boundary and initial conditions are applied to these two types of storage units. Considering that the only substantial difference between the two configurations resides in the way in which the high conducting material (HCM) is arranged around the pipes, the performance gap can be ascribed to the fins design. More specifically, the longitudinal fins create a very compact heat exchanger design and reduce the average PCM thickness around each pipe. Thus, the average diffusion distance is shorter in the “Longitudinal” LHTS unit creating a great advantage since the discharging process is largely dominated by diffusion [151, 106]. On the contrary, the HCM rods in the “TopOpt” LHTS tend to favour natural convection phenomena [146]. Moreover, the total contact surface resulting from the longitudinal fins design is 3.5 times higher than in the “TopOpt” configuration. Unfortunately, this is due to a limitation that was encountered during the realization of the “TopOpt” fins, which could not be made thinner than 5 mm (as already explained in section 3.2). Hence, it is expected that the “TopOpt” LHTS performance could be largely improved if the overall contact surface is increased (still maintaining the same amount of HCM in the storage design).

5.4.2 Comparative analysis during the charging phase

To compare the performance of the two LHTS units during the charging phase, two cases are analysed. The difference between these two tests resides in the charging mode. The former is characterised by the use of the electrical resistance, while in the latter case the two storage units are charged by means of the DH supply. It should be reminded that for the entire experimental campaign both the LHTS units were charged only through the electrical resistance because the DH substation located in the building was under maintenance. Nevertheless, the DH supply was briefly available at the time when the whole experimental test rig was set up. Hence, in this section the only available charging test through the DH supply is also analysed and presented.

Concerning the charging mode with the electrical resistance, Fig. 5.60 reports the absolute HTF temperature difference between inlet and outlet. Contrary to the discharging phase, the HTF temperature is decreased when passing through the

LHTS units. Moreover, considering that the electrical resistance supplies a constant thermal power rate to the heating fluid, the HTF temperature difference is extremely stable throughout the charging phase. As a matter of fact, the outlet section of the LHTS units coincides with the inlet section of the electrical resistance (neglecting the temperature losses of the piping system). Hence, the electrical resistance maintains almost the same HTF temperature difference at every time instant. Interestingly, the HTF temperature difference starts increasing after around 60 minutes and finds a plateau at a higher level for both the storage units. This effect can be ascribed to the absorption of energy in the form of latent heat. Regarding the other relevant input parameter, i.e. the average HTF mass flow rate, this is equal to 1387 l/h for the "Longitudinal" LHTS and 1384 l/h for the "TopOpt" LHTS. Again, two cases with similar driving parameters were chosen to compare the performance of these two units. Indeed, like the discharging tests previously presented, also in this case the two storage units are charged separately because the power of the electrical resistance is too small for a simultaneous charge. The results show that the "Longitudinal" LHTS is slightly more efficient than the "TopOpt" LHTS in absorbing the energy released by the HTF, since the HTF temperature difference is generally higher in the former LHTS unit. Consequently, the "TopOpt" LHTS reaches the same energy content of the "Longitudinal" LHTS (52.7 kWh) 26 minutes later (+9.5% in charging time), as shown in Fig. 5.61. From this figure it is also evident the constant power rate supplied by the electrical resistance since the energy history of the two LHTS units is very close to a straight line. It should be noticed that this outcome is not affected by the initial state of the charge of the LHTS units because the average PCM temperature at the beginning of the charging test is very similar (35.2°C for the "Longitudinal" LHTS and 32.5°C for the "TopOpt" LHTS).

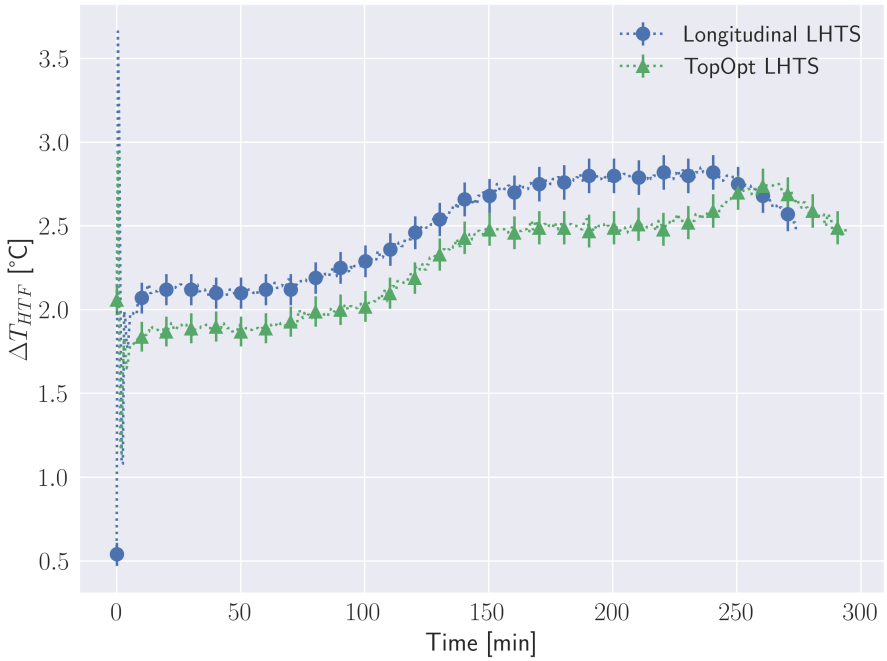

Fig. 5.60 Comparative analysis between HTF absolute temperature decrease across the "Longitudinal" and "TopOpt" LHTS (Charge with electric heater)

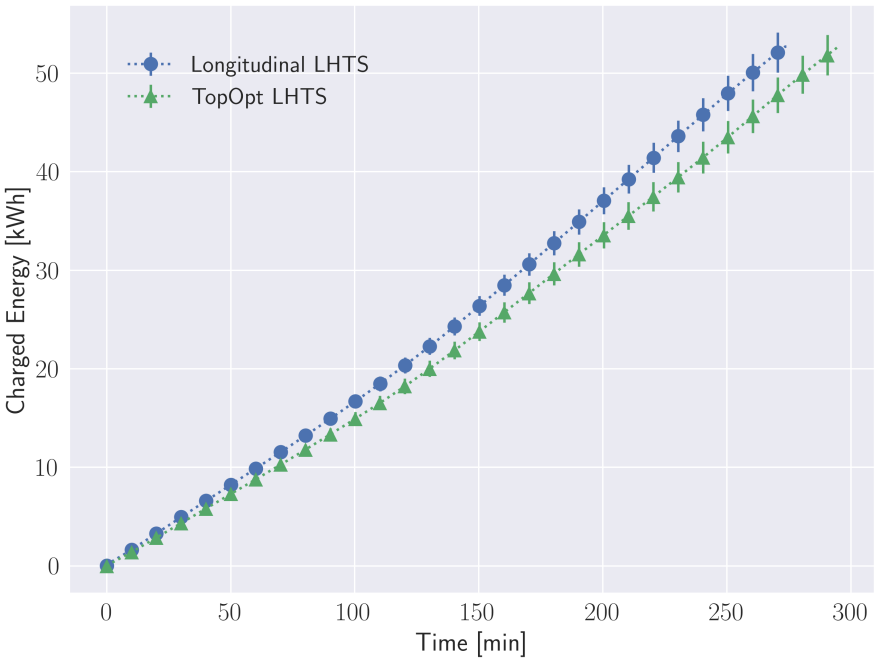

Fig. 5.61 Comparative analysis between the energy histories of the "Longitudinal" and "TopOpt" LHTS (Charge with electric heater)

Concerning the charging mode with the DH substation, Fig. 5.62 reports the absolute HTF temperature difference between inlet and outlet. Although a constant HTF inlet temperature above 80°C should be provided by the secondary side of the DH substation located in the building, the initial 50 minutes of the charging process are characterised by an extreme variability in the HTF inlet temperature, which obviously affects also the HTF outlet temperature. Nevertheless, the HTF inlet stream is the same for the LHTS units because in this test they were charged simultaneously. As a matter of fact, the average HTF inlet temperature is equal to 77.5 °C both for the "Longitudinal" and the "TopOpt" LHTS. Instead, the average HTF mass flow rate is slightly different for the two storage units because of a diverse hydrodynamic resistance in the pipes and valves (4666 l/h for the "Longitudinal" LHTS and 4787 for the "TopOpt" LHTS). The experimental results show that the "Longitudinal" LHTS appears again more effective than the "TopOpt" LHTS in absorbing the energy derived from a hot HTF stream, since the HTF temperature difference is generally higher in the former LHTS unit. Consequently, after 3.5 hours of charge, the "Longitudinal" LHTS stored 21.8% more energy than the "TopOpt" LHTS (59.8 kWh vs. 49.1 kWh), as shown in Fig. 5.63. From this figure it is also evident how the energy history of the two LHTS units has a completely different behaviour if compared to the case with the electrical resistance. Indeed, in this test the heat is supplied by a constant hot HTF stream that guides the LHTS energy content towards a saturation point. On the contrary, when the electrical resistance is used the final charging state is continuously moved forward. Again, it should be mentioned that the test outcome is not affected by the initial state of the charge of the LHTS units because the average PCM temperature at the beginning of the charging test is very similar (27.3°C for the "Longitudinal" LHTS and 26.5°C for the "TopOpt" LHTS).

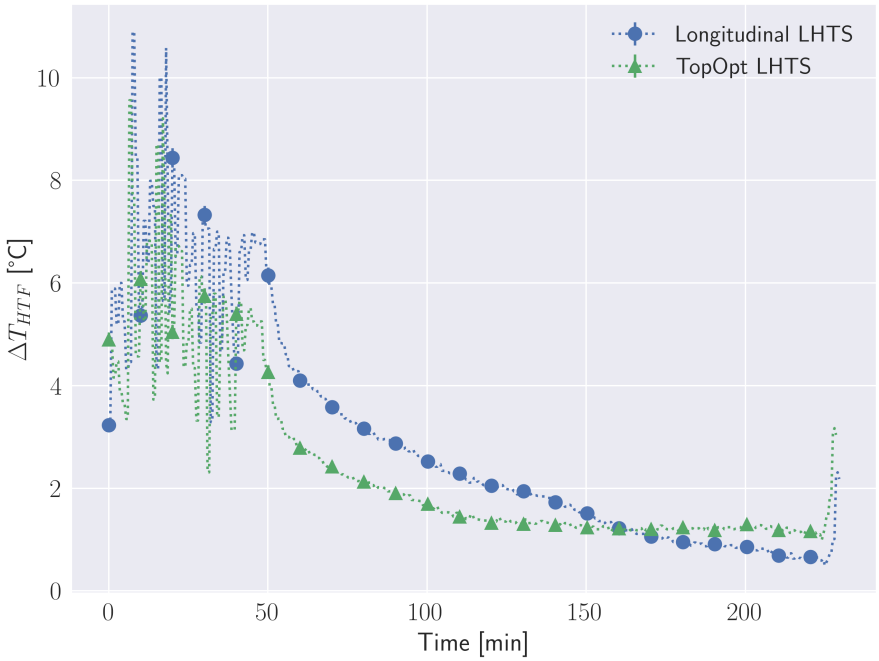

Fig. 5.62 Comparative analysis between HTF absolute temperature decrease across the "Longitudinal" and "TopOpt" LHTS (Charge with DH supply)

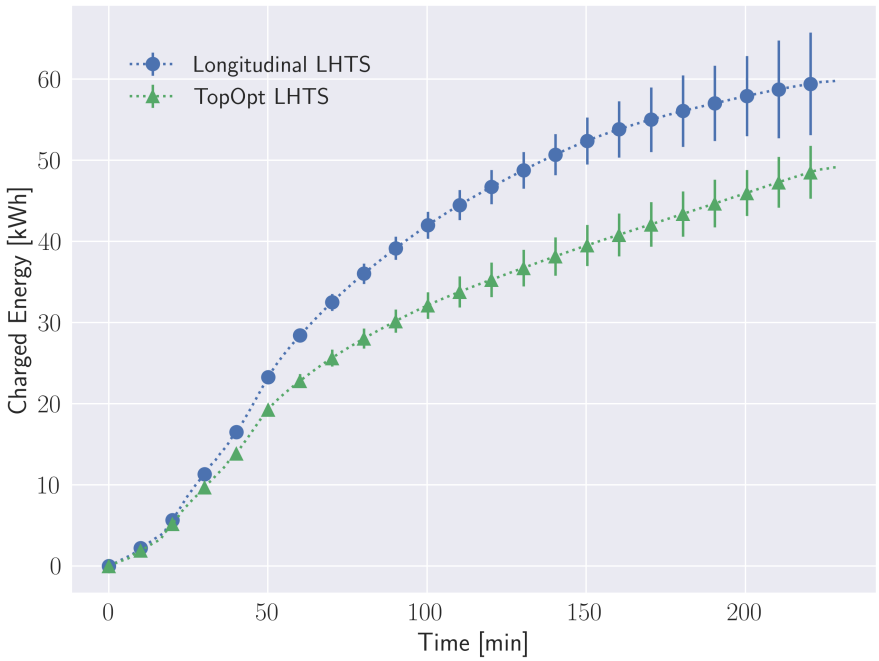

Fig. 5.63 Comparative analysis between the energy histories of the "Longitudinal" and "TopOpt" LHTS (Charge with DH supply)

Summarising, the "Longitudinal" LHTS unit showed a higher performance compared to the "TopOpt" LHTS unit also in terms of speed of charge. The former heat exchanger is more efficient in absorbing the heat released by the HTF when similar boundary and initial conditions are applied to these two types of storage units. As expected, the performance gap between the "Longitudinal" and "TopOpt" LHTS is much more evident when the heat is supplied through a hot HTF stream rather than through a constant thermal power rate. As a matter of fact, when a constant thermal power rate is supplied, the HTF temperature difference between inlet and outlet mainly depends on the heating source rather than on the design of the LHTS heat exchanger. On the contrary, when the supply conditions are constituted by a HTF stream characterised by a relatively constant (hot or cold) temperature, the internal LHTS heat exchanger is able to show its potential in transferring the heat from the HTF to the PCM and vice versa. In conclusion, the smaller overall contact surface between the high conducting material and the PCM in the "TopOpt" fins configuration constitutes again a limiting factor in the LHTS charging performance compared to the "Longitudinal" configuration.

5.5 Key findings of the present chapter

This chapter presented a thorough experimental analysis related to the two LHTS units realised for this study, which are generally referred throughout this thesis as the "Longitudinal" and the "TopOpt" configurations. The outcomes of such an extensive experimental campaign were employed for two distinct purposes:

- The validation of the LHTS 1D dynamic model presented in Chapter 4;
- The performance evaluation of the two LHTS heat exchangers by comparing the results of those experimental tests characterised by similar boundary and initial conditions.

Regarding the former goal, the model accuracy proved to be extremely satisfactory. With the aim of creating a model able to simulate the behaviour of a general shell-and-tube LHTS unit from a system perspective, the most relevant error to monitor is arguably the one on the LHTS state of charge. Such an error was mostly below 10% with respect to the experimental value of the storages state of charge, with the

only exception of one test concerning the "TopOpt" LHTS unit (which was however characterised by a highly unstable inlet HTF temperature, an uncommon situation in residential heating systems). Moreover, the proposed dynamic model proved to be more accurate when the behaviour of the "Longitudinal" LHTS is simulated. Regrading the latter objective, the "Longitudinal" LHTS showed a better performance both in terms of speed of charge and discharge compared to the "TopOpt" LHTS. In the analysed experimental tests, the "Longitudinal" LHTS stored or released between 8% and 22% more energy than the "TopOpt" LHTS considering the same amount of time.

Chapter 6

The RE-cognition EU Project and the LHTS prototypes

This chapter aims at describing an application for the two LHTS prototypes presented in Chapter 3. A consistent part of the PhD activities presented in this thesis were developed within the European project RE-cognition (grant number: 815301). More specifically, my tasks included the development of the aforementioned LHTS prototypes and their integration in one of the project pilot sites (i.e., the Energy Center, a building own by Politecnico di Torino). The following sections are organised as follows.

Section 6.1 provides an overview of the RE-cognition project. Its concept, scope and consortium are here presented.

Section 6.2 deals with the information and communication technology (ICT) framework that was conceived and realised during the project duration. As a matter of fact, the RE-cognition project strongly relies on two ICT components (an engine based on artificial intelligence and an ad-hoc gateway) to optimize the integration of several on-field energy technologies.

Section 6.3 describes all the energy technologies that were developed by some of the project partners.

Section 6.4 presents all the project pilot sites selected for the validation of the ICT framework and the energy technologies. Particular attention is dedicated to

description of the Energy Center, which is the pilot site where the LHTS units are installed.

Section 6.5 shows the results that were achieved by integrating together the ICT components, the LHTS units and the Energy Center pilot site.

Eventually, section 6.6 summarises the key findings of this chapter.

Some portions of this chapter were presented at the following conference: *35th International Conference on Efficiency, Cost, Optimization, Simulation and Environmental Impact of Energy Systems (ECOS 2022)*, held in Copenhagen from 3rd to 7th July 2022. Moreover, part of the following work has already been published as project report. The full list of the published documents can be accessed on the RE-cognition project website [156].

6.1 Overview on the RE-cognition project

The "Clean Energy Package for all Europeans" [157] has made the European Union (EU) a leading country in environmental policies and sustainable transition. This policy is designed to rapidly install Renewable Energy Sources (RES) and increase clean electricity production in the grid. The EU has set ambitious targets to face climate change and related environmental issues, including a 32% share of RES in final consumption and a 40% reduction in CO2 emissions by 2030. The ultimate goal is to achieve carbon neutrality by 2050. These targets were revised following the COVID-19 pandemic, and the new green transition plan called "fit for 55" [158] proposes reducing CO2 emissions by 55% by 2030. In parallel, the EU promotes events, proposes projects, and writes new policies and regulations to accelerate the transition to a more sustainable society. In this context, the "RE-cognition" project was financed by the Horizon 2020 research framework, which is one of the most renowned EU research programs. The project acronym stands for “**RE**newable **COG**eneration and storage tech**N**ologies **I**ntegra**TI**on for energy aut**ON**omous buildings” [156]. This project, which started in April 2019 and was concluded in September 2022, has a twofold objective: on the one hand it aims at implementing cutting-edge renewable sources at the building level, on the other hand it aims at producing optimal management strategies through ad-hoc information and communication technologies.

As a matter of fact, in terms of renewable energy production and efficiency two main approaches can be pursued to reach the EU targets: a centralised one versus a decentralised one. The former involves the diffusion of large renewable power plants (such as PV at utility scale or wind farms). The latter, instead, determines the creation of small renewable energy hubs. The centralised approach is more focused on strategic investments and visions at national or regional levels, while the decentralised system is more complex as it involves more actors, such as local authorities, grid operators, and prosumers. The decentralised system is also closely linked to the building sector because some renewable energy technologies are designed to be installed in buildings. A large portion of the EU building stock is more than 50 years old, has very little or no installed renewable energy generation systems, and is not designed for the installation of renewable energy systems and advanced control and management tools. To address this challenge, important research is being conducted to effectively integrate renewable energy architecture into existing buildings. The RE-cognition project is part of this effort, which aims to create a solid mix of software and hardware components to facilitate and promote the integration of multiple renewable energy sources into buildings and improve RES energy use for heating/cooling technologies.

In few words, the RE-cognition methodology consists in developing an integration framework able to incorporate and manage existing energy technologies along with newly developed RES and storage components. At the core of the proposed integrated solution there is an agent-based distributed intelligence that manages the on-site energy production and demand. A general overview of the envisioned solution is shown in Fig. 6.1.

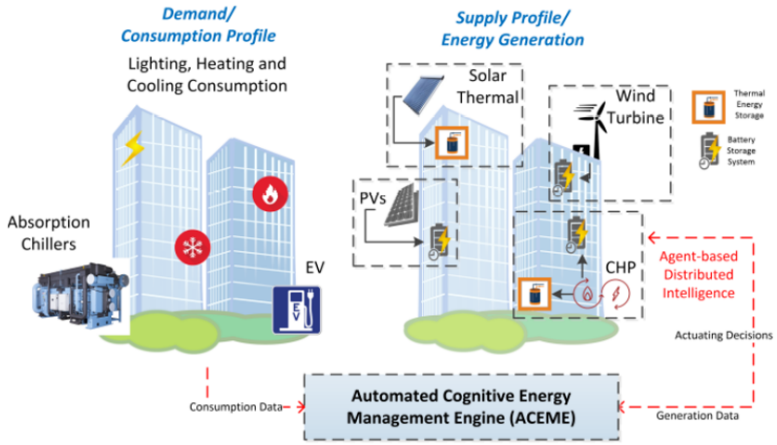

Fig. 6.1 Overview on the RE-cognition integrated solution

6.1.1 RE-cognition consortium and work packages

The RE-cognition consortium is made of 15 partners with a various background. More specifically, there are: 3 universities, 2 research institutes, 7 private enterprises, 2 industrial partners and 1 non-profit organization. The role of each partner is detailed in Table 6.1.

For a complete overview on the project structure, Fig. 6.2 reports the 7 work packages in which the project was divided. For further information, the interested reader is referred to the project official website [156]. Most of the activities presented in this thesis were carried out within the WP2 and the WP5. These dealt with the LHTS prototypes design, modelling, installation and testing in parallel with the POLITO pilot site realization.

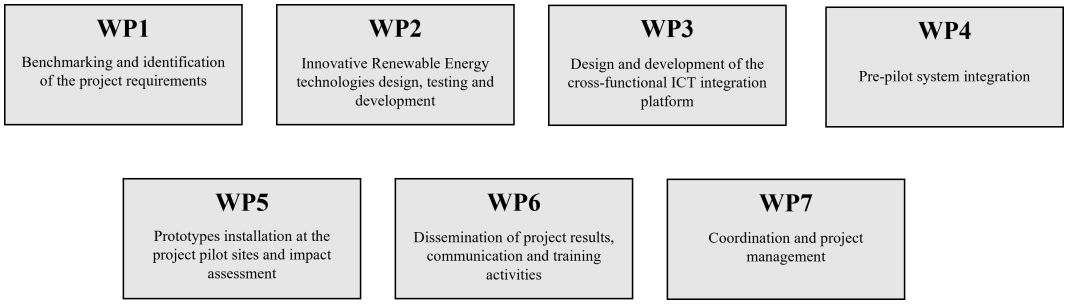

Fig. 6.2 Overview on the RE-cognition Work Packages (WPs)

Table 6.1 RE-cognition project partners

Partner	Country	Acronym
Politecnico di Torino	Italy	POLITO
Centre for Research and Technology Hellas	Greece	CERTH
Energy@Work (company)	Italy	E@W
Intracom sa Defense Electronic Systems	Greece	IDE
ZH S.r.l. (company)	Italy	ZH
Ecole Polytechnique Federale de Lausanne	Switzerland	EPFL
Centre Suisse d'Electronique et de Microelectronique	Switzerland	CSEM
Windcity (company)	Italy	WINDCITY
Micro Turbine Technology BV (company)	Netherlands	MTT
Hellenic Petroleum (company)	Greece	HELPE
Servelect (company)	Romania	SVT
University of Bristol	UK	UoB
Electric Corby Community Interest Company	UK	EC
Etrel (company)	Slovenia	ETREL
Technical University of Cluj-Napoca	Romania	TUCN

6.2 RE-cognition ICT framework

The RE-cognition project's ICT infrastructure comprises two primary components: a gateway (called i-Gateway) for communication with on-site equipment and an agent-based distributed intelligence. The latter is called Automated Cognitive Energy Management Engine (ACEME) and constitutes the backbone of the proposed integrated solution. ACEME is composed by several agents able to determine the optimal operation of the available energy technologies based on the flow of information exchanged with the i-Gateway. As a result, ACEME suggests a day-ahead optimized schedule that minimizes one of the following three variables:

- The building energy-related operational cost;
- The building imported energy cost (from the electrical grid or the district heating system);
- The building self-sufficiency.

The optimization problem is formulated as a Mixed Integer Linear Programming (MILP) problem. Its formulation stems from CERTH's extensive scientific research on Micro-grid Energy Management Systems. More details on the MILP problem are provided in section 6.5. ACEME's agents can operate autonomously, provided that they receive decision rules from a centralized control mechanism. These rules derive from forecasted data and simulations of the building energy flows. More specifically, ACEME receives measurements from the on-site sensors and predicts patterns for the aggregated load of the building. Moreover, through the acquisition of weather information from local station units or online weather services, ACEME is able to predict RES generation within various time intervals. The most general version of this computational engine is composed of the following agents:

- The **optimal dispatch agent**, which determines the day-ahead schedule of the available energy resources;
- The **centralized balancing agent**, which translates the strategy selected by the optimal planning into actions that can be executed by on-field devices in a close to real-time scale;
- The **auxiliary services agent**, which is responsible for data retrieval from external services (e.g. energy prices or meteorological data);
- The **forecasting agent**, which predicts the future building energy demand and the RES generation profiles through machine learning algorithms;
- The **asset agents**, which are a virtual representation of the energy technologies deployed on-site and are responsible for the exchange of information with the gateway.

All the generated information (models, raw data, control actions, etc.) are stored in a common repository. As a result, both static (e.g. building characteristics) as well as dynamic information can be accessed by ACEME's agents through this database. An overview of this ICT framework is presented in Fig. 6.3. It should be noticed that this figure depicts the most general configuration of the proposed ICT framework. Some of the listed agents and relative technologies are actually not deployed at the Energy Center in Turin (such as the battery storage and the EV charger), as detailed in section 6.4.1.

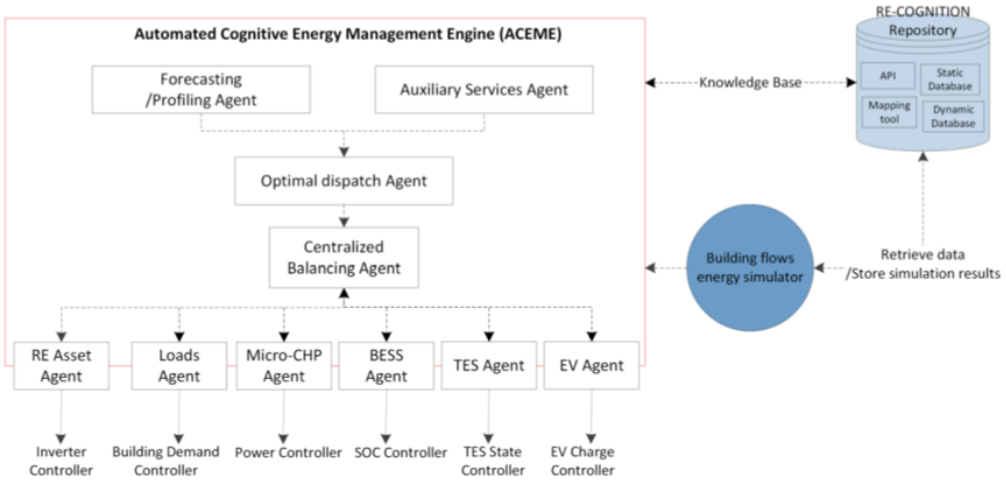

Fig. 6.3 Overview on the RE-cognition ICT framework

As far as the communication layer is concerned, the i-Gateway represents the pivotal element between the on-field Renewable Energy Technologies (RETs) and ACEME. All these three elements together constitute the information chain that is applied to each pilot site. Since the i-Gateway collects and sends data in both directions, a further crucial set of components is represented by the field sensors expressing the real-time status of each technology. A high-level sketch of such an information flow is presented in Fig. 6.4. Here, the LHTS is taken as a reference, but the same considerations apply to the other RETs and even to the building itself (although the quantities monitored by the sensors are different). The iGateway sends a request to the technology sensors and retrieves the real-time data. After that, the iGateway publishes these pieces of information via MQTT protocol so that ACEME's broker is able to collect the desired data and make the correct decision (Fig. 6.4a). Following the optimization procedure, ACEME sends back to the i-Gateway the actuation instructions (Fig. 6.4b).

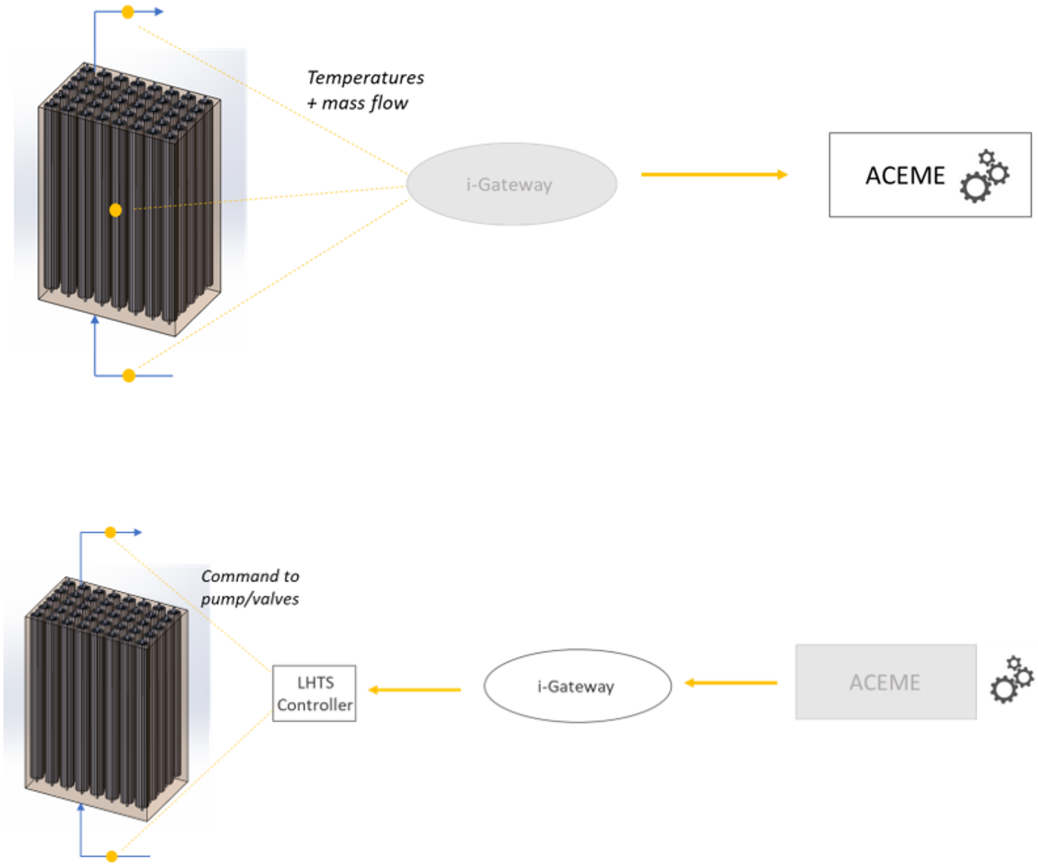

Fig. 6.4 High level sketch of the RE-cognition information flow: (a) decision layer; (b) actuation layer

Furthermore, Fig. 6.5 shows the deployed i-Gateway at the Energy Center. Thanks to the fact that all the relevant quantities (i.e., the pilot site energy consumption and the RETs status variables) are exchanged through the local LAN network, the i-Gateway was simply connected to an ethernet port in the Energy Center laboratory after the MQTT protocol was properly configured.

Fig. 6.5 Detail of the i-Gateway installed at the Energy Center pilot site

6.3 RE-cognition technologies

A secondary outcome of the RE-cognition project is the development of various innovative renewable energy and storage technologies which are currently characterized by a mid-low Technology Readiness Level. These are:

- A micro combined heat and power (micro-CHP) possibly running with biogas;
- A vertical axis wind turbine (VAWT) with variable geometry;

- Building Integrated Photovoltaic (BIPV) panels;
- A Latent Heat Thermal Storage (LHTS);
- A Hybrid Solar Cooling (HSC) unit.

The micro-CHP (Fig. 6.6) provides 3.2 kW of electrical power and 15.6 kW of thermal power for heating and hot water production at full load. An ad-hoc design allows the gas turbine to maintain a stable combustion even when low-caloric gases (such as biogas) are burnt. Specifically, a new combustor was developed by MTT able to achieve a stable combustion during cold start, hot restart, full load and partial load, meeting at the same time European emission requirements for NOx and CO. Moreover, particular attention was devoted to the materials of the gas turbine because the biogas combustion residuals usually contain aggressive components.

Fig. 6.6 Detail of the micro-CHP installed at the Energy Center pilot site

The VAWT prototype (Fig. 6.7) is developed by Windcity and displays an optimised design for good performance also at low wind speeds (nominal power: 1.2 kW). This is obtained through a patented passive variable geometry (PVG) turbine, which can automatically adapt to wind conditions in real time. More specifically,

the PVG maximizes the energy production by adjusting the 3 degrees of freedom that are present during the movement of any blade: rotation, pitch, and diameter. Furthermore, Windcity also developed an ad-hoc power converter with a Maximum Power Point Tracking (MPPT) logic that is based on the turbine power curve and real-time electrical measurements.

Fig. 6.7 Detail of the Vertical Axis Wind Turbine installed at the Corby pilot site [156]

The BIPV modules (Fig. 6.8) are developed by EPFL and CSEM. These are lightweight PV modules based on composite materials and polymer films with the aim to replace the standard glass-glass configuration for the back and the front sheets respectively. To achieve the target of aesthetical appealing lightweight BIPV modules that can be effectively integrated in building facades, two different processes for coloring polymeric film (adhesive or non-adhesive) were developed. Both these processes generate colored lightweight BIPV modules which still maintain good stability and electrical performance.

Fig. 6.8 Detail of the BIPV modules installed at TUCN pilot site [156]

The LHTS units tested in the RE-cognition project are those described in Chapter 3. As previously documented, these are two shell-and-tube units able to store thermal energy in the form of latent heat of an organic Phase Change Material (PCM) with an optimized fins design. Overall, each storage unit has a capacity of roughly 40 kWh (depending on the operational conditions). Finally, the Hybrid Solar Cooling (HSC) prototype was also developed by one of POLITO's research teams. This unit (Fig. 6.9) aims at supporting traditional cooling systems based on chillers through a solar dehumidification process. This technology relies on the sorption properties of silica (or, equivalently, a micro porous material) which can absorb the vapor content in the process air until saturation. As a result, the coupled traditional chiller can operate at a higher supply temperature (implying better efficiency), since the dehumidification of the process air is no longer based on vapor condensation at atmospheric pressure. The adsorption material is then cyclically regenerated by low-temperature heat provided by solar thermal collectors. Hence the definition of Hybrid Solar Cooling system.

Fig. 6.9 Detail of the Hybrid Solar Cooling prototype

6.4 RE-cognition pilot sites

The project consortium selected different pilot sites to test the project outcomes under different local conditions, such as: varying meteorological conditions, electricity prices, regulations on RES integration, building characteristics, and types of users. More specifically, pilot tests targeted two main objectives:

1. The performance of the ICT integration platform (i.e., ACEME and iGateway) in different buildings characterised by several supply, demand, and storage assets (either novel or already existing);
2. The on-site performance of the newly developed RE-cognition technologies.

Overall, 5 pilot sites spread all over Europe were selected:

- The Corby Enterprise Center (UK)
- Four buildings in the Technical University of Cluj-Napoca (TUCN) campus (Romania)

- The townhall of the city of Lizzanello (Italy)
- The Hellenic Petroleum (HELPE) headquarters (Greece)
- The Energy Center of POLITO (Italy)

Since the LHTS technology was installed at the Energy Center, only this case study is presented hereafter.

6.4.1 The Energy Center case study

The Energy Center is a building owned and managed by Politecnico di Torino which hosts firms, academic staff and public administration who jointly conduct research activities. This facility is developed on four floors with a total net surface of 5441 m^2. The Energy Center is equipped with several technologies for the satisfaction of the building energy demand. These are:

- Monocrystalline photovoltaic (PV) panels both on the rooftop and on the hall glass façade;
- A ground-source heat pump (GSHP) that provides both heating and cooling (even simultaneously);
- Two District Heating (DH) substations for space heating and domestic hot water (DHW) production.

The existing grid-connected PV system is distributed in different zones of the building, as shown in Fig. 6.10. There are two free-standing plants on the rooftop and a series of PV cells integrated in the hall façade. The total gross PV surface is 261 m^2 with a nominal overall capacity of 47 kW. The GSHP, located in the basement, is an open-loop groundwater heat pump. This machine uses R134a as working fluid and it is able to supply at the same time heat and cooling thanks to two independent circuits. The GSHP is mainly used for cooling during summer and for supporting the production of domestic hot water. Indeed, this type of heat pump has a recovery mode allowing to produce heat for DHW during the cooling season. During winter, instead, the heating demand of the building is supplied by the local district heating provider. The nominal capacity of this substation is 350 kW.

Fig. 6.10 Detail of the Energy Center pilot site (POLITO)

A widespread net of sensors allows to monitor the most relevant physical quantities necessary to manage and control the energy assets of the building. Hence, the agent-based distributed intelligence (ACEME) developed in this project can be added as a further virtual control layer. A thorough collection of energy data with a sampling time of 15 minutes is available on-site. The average yearly energy consumption of the whole building resulting from the data collection between 2018 and 2021 is detailed as follows (see also Fig. 6.11):

- Electricity: 423 MWh/year
- Heating demand: 373 MWh/year
- Cooling demand: 161 MWh/year

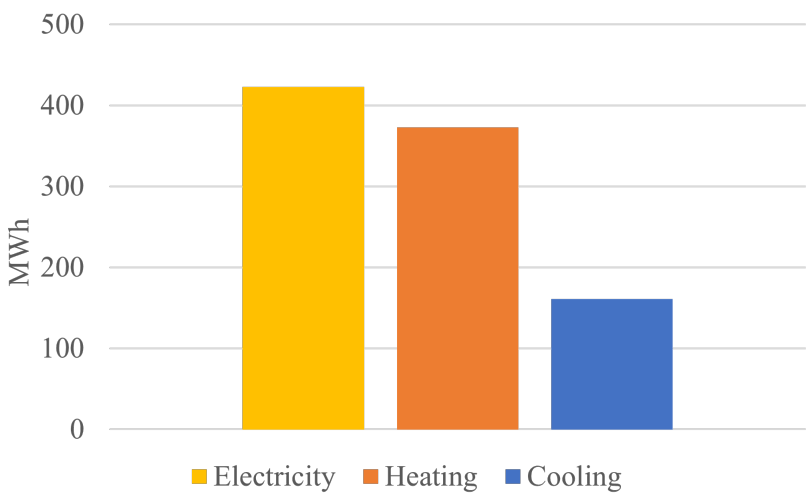

Fig. 6.11 Average electricity, heating and cooling annual demand of the Energy Center pilot site

Among these types of energy demand, the electricity is the one showing the highest variability throughout the year. This is due to the fact that during the cooling season (i.e., between June and August) the building cooling demand is satisfied through the GSHP, which consumes electricity to produce chilled water. As a result, in this period, the daily electricity consumption pattern is strongly affected. The seasonal effects on the daily electricity demand are clearly visible when comparing Fig. 6.12 and Fig. 6.13, representing two characteristic days (one in June 2021 and one in December 2021). In Fig. 6.12, the overall electricity demand is largely affected by the operation of the GSHP in cooling mode. This represents almost 40% of the total daily demand. The remainder can be attributed to the large number of appliances and devices belonging to the offices and the building centralized systems. Indeed, a significant amount of stand-by energy consumption is visible even when the facility is closed (between 22.00 pm and 7.00 am).

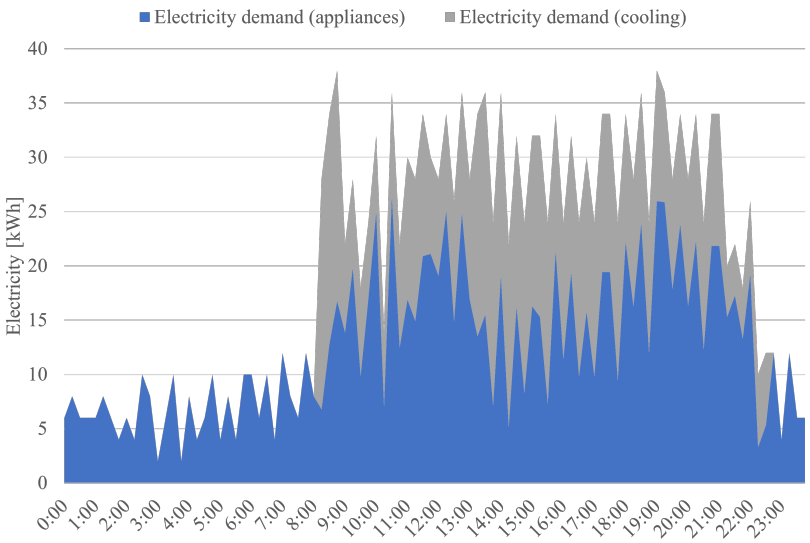

Fig. 6.12 Energy Center daily electricity demand in a typical summer day

During the winter season (Fig. 6.13), the daily electricity consumption is lower compared to summer days. The energy consumption due to stand-by is approximately the same, however a higher electricity demand due to lighting appliances is evident in the middle of the day. Nevertheless, throughout the heating season (from 15th October to 15th April) the GSHP is turned off in favor of the DH supply, hence the peak electricity demand is drastically reduced (-25% with respect to summer).

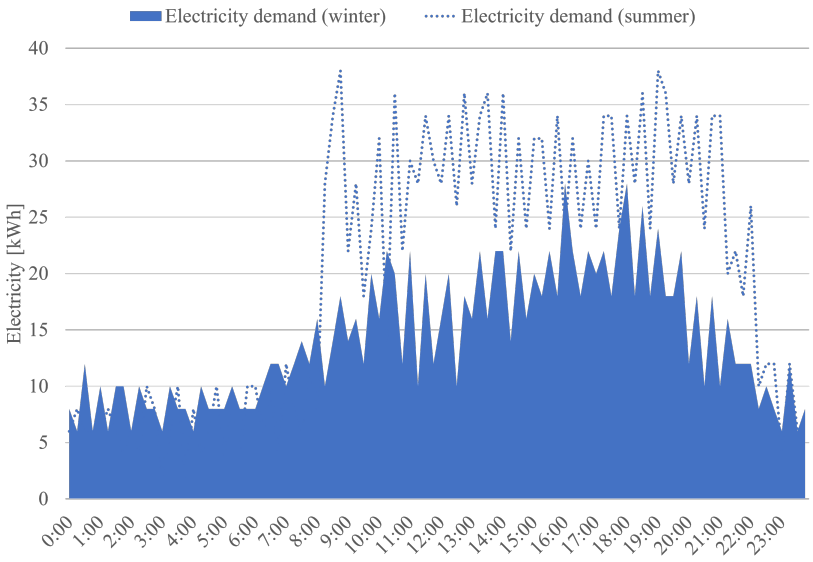

Fig. 6.13 Energy Center daily electricity demand in a typical winter day

Concerning the heating demand, instead, the most important variability is displayed throughout each day of the heating season, as showed by a representative day in December 2021 (Fig. 6.14). This is due to the fact that the DH substation is generally switched on between 6.00 am and 22.00 pm, while it is kept idle during the night. As a result, a noticeable peak energy demand is often experienced at the start. During the heating season, this peak is around 2 times larger than the average daily heat demand. Moreover, the colder is the outdoor air temperature, the higher is the morning peak. On the contrary, when the outdoor climate is mild, the morning peak is flattened. However, the choice to keep the heating system idle for the whole night still causes an abrupt increase in the heating demand at the start.

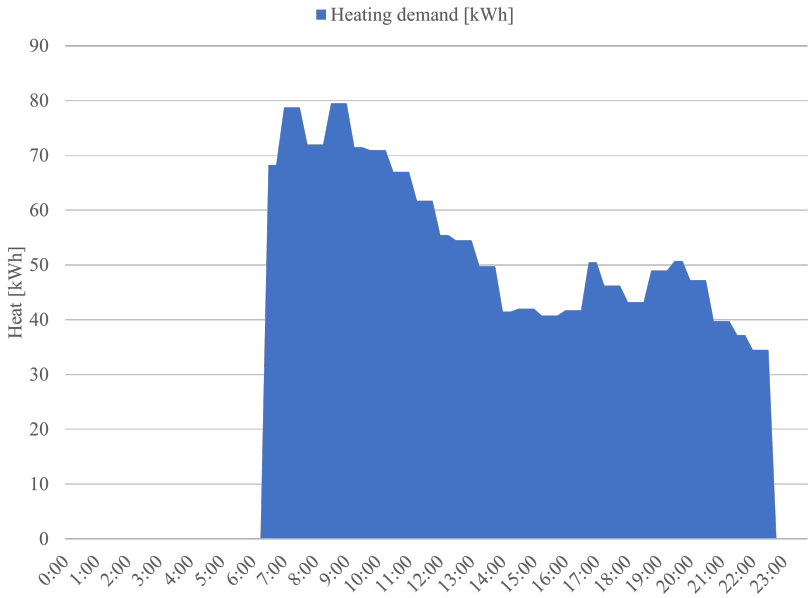

Fig. 6.14 Energy Center daily heat demand in a typical winter day

Alongside the existing energy assets, some of the energy technologies specifically developed in the RE-cognition project were installed in the building premises. These are the micro-CHP and the LHTS. Moreover, the HSC technology was also installed in one of the university premises close to the Energy Center. Considering that the all the university buildings are connected to the same local network, this allows ACEME to communicate with the HSC even if it is located in another building. The impact of these technologies on the building energy consumption is presented in section 6.5. It should be mentioned that the micro-CHP was fed with the natural gas available from the local grid due to the difficulty of finding a continuous biogas

supply in such an urban context during the project timeframe. Moreover, it was not possible to install the remaining newly developed RE-cognition technologies (VAWT and BIPV) due to legal restrictions on the Energy Center rooftop and façade. Nevertheless, the existing PV panels integrated in the hall windows offer a good example of how this technology might respond in the present context. A further consideration regards the size of the two LHTS units installed at the Energy Center (around 40 kWh each). This can cover only a small fraction of the average daily pilot site thermal energy demand. However, this is justified by the prototypal concept behind this installation. Furthermore, the RE-cognition project firstly aims at proving the integration of several field technologies through an agent-based ICT platform rather than satisfying the entire energy demand of such a large building.

6.5 RE-cognition results and the role of the LHTS

As already anticipated in section 6.2, ACEME's optimal dispatch agent determines the optimal power balance schedule (through a MILP problem) considering the available building energy assets and the pilot site energy consumption forecast. This thesis contributed on both these aspects. On the one hand, a thorough collection of historical energy consumption and weather data of the Energy Center pilot site was provided to CERTH. This dataset was loaded by CERTH into pre-trained Machine Learning models (one for each pilot site) in order to generate the required day-ahead forecasts. As an example, the Energy Center predicted and actual heating and cooling demands in two distinct days are presented in Fig. 6.15. In this case, the Load Demand Forecasting Accuracy (LDFA) is equal to 76.1% for the heating demand and 97.2% for the cooling demand. Similarly, Fig. 6.16 compares the forecasted and the real building electricity demand in another sample day. In this case, the LDFA is equal to 98.7%.

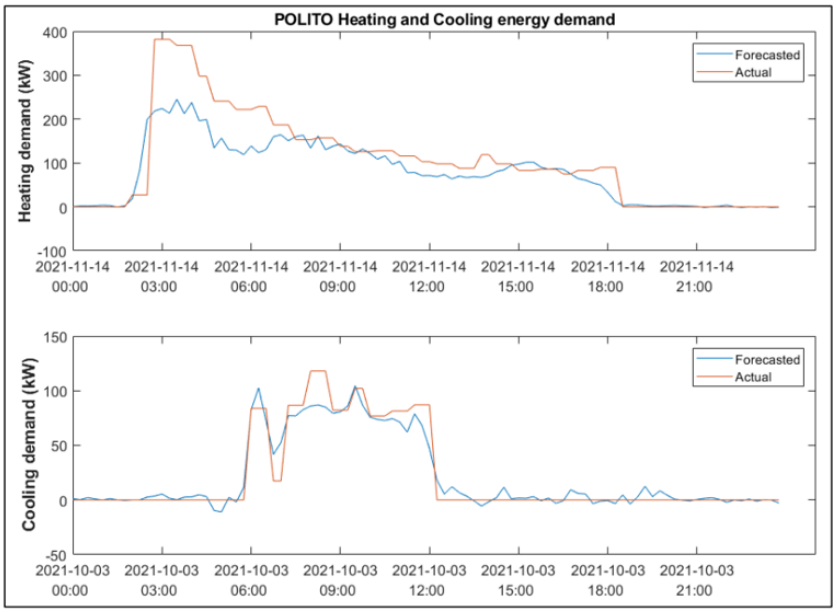

Fig. 6.15 Comparison between forecasted and actual heating and cooling demand of the Energy Center pilot site (concession of CERTH)

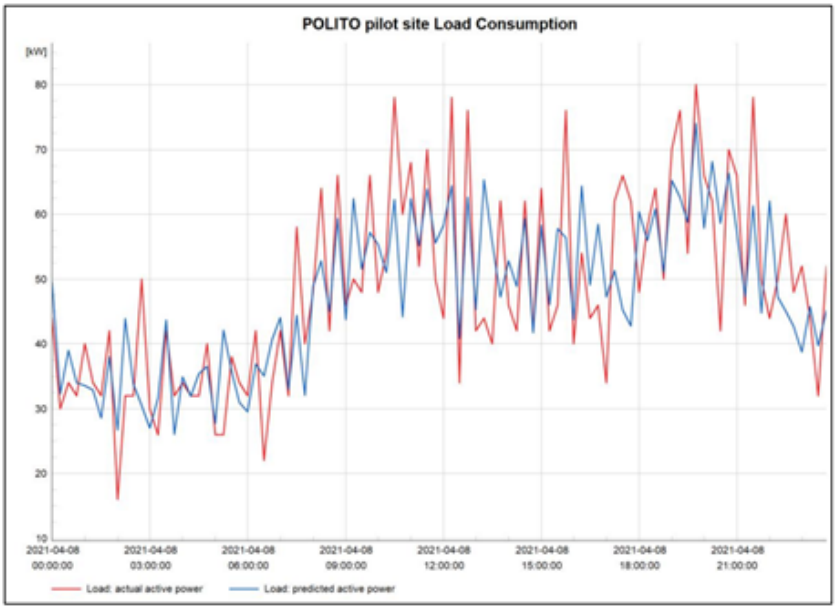

Fig. 6.16 Comparison between forecasted and actual electricity demand of the Energy Center pilot site (concession of CERTH)

The most important contribution of this thesis to the development of ACEME's MILP problem was the translation of the LHTS behaviour into a set of mathematical

constraints related to the operational parameters of this technology. For a better contextualization of this contribution, the objective function of the MILP problem developed by CERTH is presented in Eq. 6.1.

$$min \;\; OC = \sum_{t=1}^{H} \left[\sum_{a \in B} (E_t^a \cdot EEC^a) + E_t^{grid} \cdot ToUT_t^{grid} \right] + \sum_{t=1}^{H} \left[\sum_{a \in T} (Q_t^a \cdot TEC^a) + Q_t^{aux} \cdot TEC_t^{aux} \right] \tag{6.1}$$

Each resulting problem is studied for a time horizon that consists of H time intervals. These are usually 96 intervals for the day-ahead schedule optimization (i.e., 15 minutes intervals for 24 hours), but they can also be lower in case of the intra-day rescheduling. The optimization variables are the energy generation or consumption of the electrical assets (subset B) and thermal assets (subset T) during each time interval. Moreover, any electrical power mismatch is compensated by the electrical grid. Similarly, an auxiliary thermal energy source is considered to model an additional power input in case of imbalanced heating/cooling demand (such as district heating network and HVAC system). The building's total cost function (Eq. 6.1) is obtained multiplying these energy variables by their respective unit cost, which is either the Electrical Energy Cost (EEC) or the Thermal Energy Cost (TEC). Regarding the connection to the electrical grid, a net-metering scheme is considered. This scheme entails a Time-of-Use Tariff (ToUT) which is the same for the imported and exported energy quantities. ToUT schemes can be categorized in three forms, namely static, dynamic and a combination of the two [159]. The optimization problem includes 17 restrictive constraints, which either regard several assets or are asset specific. These constraints regard:

- The energy balance between the building demand, the local energy production and the energy import or export from/to the grid;
- The bidirectional assets (such as the grid or the storage technologies) that can either supply or absorb energy through a binary optimization variable [0;1];
- The operational limits, such as minimum and maximum power rate for each asset and minimum/maximum amount of energy that can be stored or released by storage technologies.

Among these constraints, those regarding the LHTS technology were specifically developed adopting the thermal power characteristic curves approach described in section 4.3. As already documented in the previous chapters, LHTS units are not able to release or absorb a

constant thermal power rate during the discharging or charging phase. Moreover, the power rate also depends on the state of charge of the LHTS. However, introducing the mathematical description of the thermal power characteristic curves would not have been tolerable in the MILP problem formulation. For this reason, a simplified piece-wise constant version of the LHTS thermal power characteristic curves was provided to CERTH. As a further simplification, the HTF working temperatures of the heating system are assumed fixed. Thus, the only two parameters on which the LHTS thermal power depends are the LHTS state of charge (SOC) and the HTF mass flow rate. The former is selected as independent variable, while the latter is used as a parametric factor to scale the LHTS thermal power magnitude. A graphical representation of this approach is also provided in Fig. 6.17.

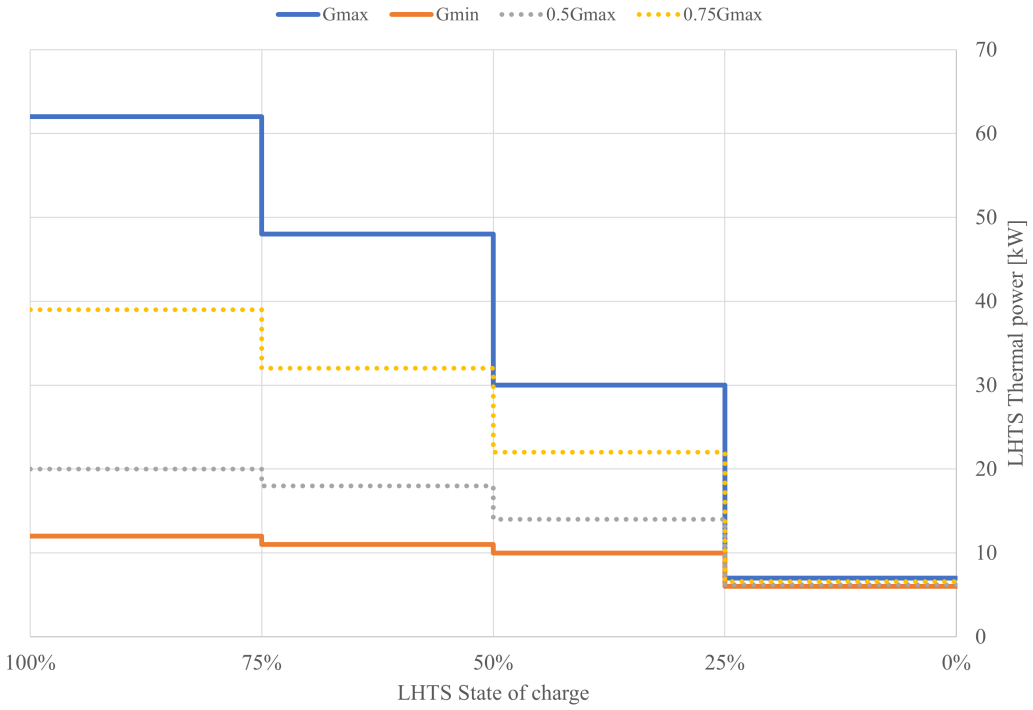

Fig. 6.17 Linearization of the LHTS thermal power characteristic curve for MILP problem formulation

Similar considerations are valid for the charging phase. As a first approximation, the same maximum and minimum thermal power values were suggested also for the charging phase, even though the values of the LHTS state of charge were obviously inverted from 0 to 1. To demonstrate the potential of integrating different renewable energy technologies orchestrated by an intelligent automated algorithm, three cases are presented in the following subsections based on the available energy consumption data of the Energy Center pilot site. First, the actual facility energy demand and local production is evaluated in two reference

days (*case 0*). This represents a benchmark for the successive cases. The same evaluation is thus repeated with the ideal addition of the RE-cognition prototypes available at the Energy Center (*case 1*). Finally, the impact of an upscaled version of these renewable technologies is also assessed (*case 2*). With the aim of highlighting the different performance between the summer and winter seasons, two representative days are selected among those monitored in 2021 (one in June and the other in December). The choice of displaying the results for a single day instead of the whole season is due to the fact that ACEME proposes a day ahead optimisation schedule.

6.5.1 Case 0: pilot site energy performance with current technologies

As already anticipated in section 6.4.1, the existing energy technologies at the Energy Center pilot site are the PV panels, the GSHP and the DH system. The daily electricity demand and local production including these technologies in the selected representative summer day is shown in Fig. 6.18. The overall electricity demand is largely affected by the operation of the GSHP in cooling mode. This represents almost 40% of the total. The remainder is attributable to the large number of appliances and the devices belonging to the offices and the building centralised systems. Indeed, a significant amount of stand-by energy consumption is visible even when the facility is closed (between 22.00 pm and 7.00 am). On the contrary, the contribution of the existing PV system appears to be marginal even in sunny days. As a matter of fact, also the electricity produced throughout the year is entirely consumed locally and the total PV share is lower than 10%. During the winter season, the daily electricity consumption is lower compared to summer days. The energy consumption due to stand-by is approximately the same, however a higher electricity demand due to lighting appliances is evident in the middle of the day (Fig. 6.19). Nevertheless, throughout the heating season (from 15th October to 15th April) the GSHP is turned off in favour of the DH supply, hence the peak electricity demand is drastically reduced (-25% with respect to summer). The DH substation is generally switched on between 6.00 am and 22.00 pm, while it is idle during the night.

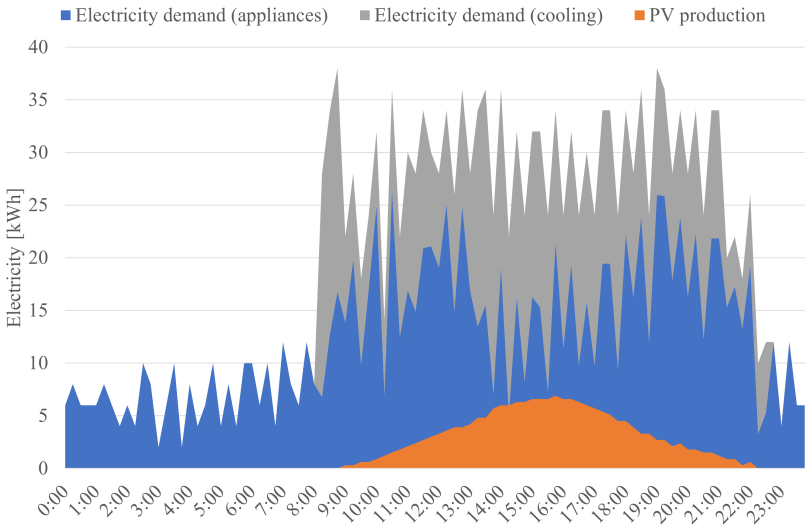

Fig. 6.18 Energy Center typical daily electricity demand and renewable energy production in summer (*case 0*)

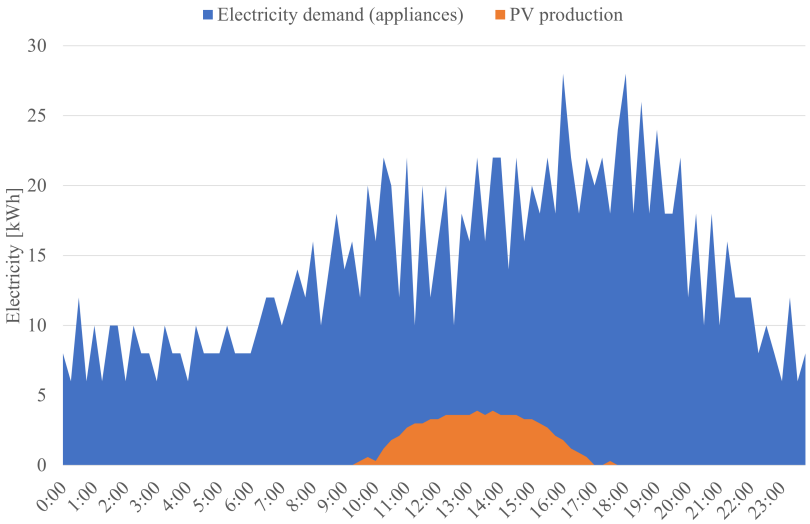

Fig. 6.19 Energy Center typical daily electricity demand and renewable energy production in winter (*case 0*)

6.5.2 Case 1: pilot site energy performance with RE-cognition prototypal technologies

This section analyses the impact that some of the renewable energy technologies developed in the project might have on the same summer and winter reference days. Although the

size of these prototypal technologies is small compared to the energy demand in the pilot site, it is important to reflect on their effect considering the goals of the RE-cognition project. As previously mentioned, the additional RE-cognition technologies considered in this case are the micro-CHP, the Hybrid Solar Cooling (HSC) and the Latent Heat Thermal Storage (LHTS). The micro-CHP is operated both in summer (mainly useful for electricity production) and winter (both for electricity and heat). On the contrary, the HSC is only available in summer, while the LHTS is mostly needed in winter. As shown in (Fig. 6.20), the micro-CHP would ideally produce a baseload that sums up to the electricity generated by the existing PV system in both seasons. At the same time, the presence of the HSC in summer would slightly reduce the electricity consumption for cooling purposes (-3% with respect to *case 0*), although this is not appreciable in the graph as the GSHP would still be largely employed (Fig. 6.20a). As expected, the proposed prototypal size of the HSC is rather small for the Energy Center cooling demand. Overall, the daily electricity withdrawn from the grid would be reduced by roughly 6% with respect to *case 0* in both seasons mainly thanks to the deployment of the m-CHP. As a result, this would still imply an appreciable cost reduction over the facility electricity bill.

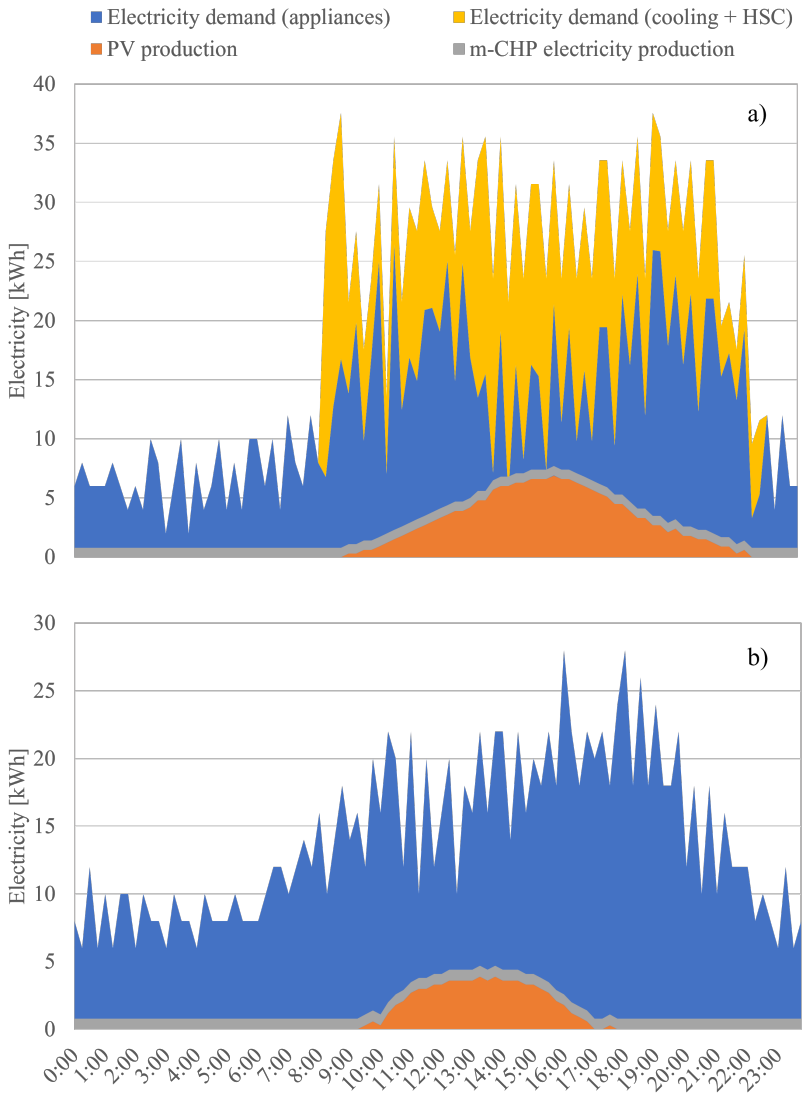

Fig. 6.20 Energy Center typical daily electricity demand and renewable energy production (*case 1*): (a) summer, (b) winter

The heat generated by the micro-CHP is suitable for coupling with the LHTS, especially in winter when space heating is required. As depicted in Fig. 6.21, these two technologies combined together would determine a slight reduction in the energy requested to the local DH network. More specifically, the LHTS would be charged by the micro-CHP a few hours before the DH morning start and discharged during the peak energy demand. This would decrease the instant peak energy request by more than 10% with respect to *case 0*, thus generating positive feedback for the local DH provider and, consequently, an economic advantage.

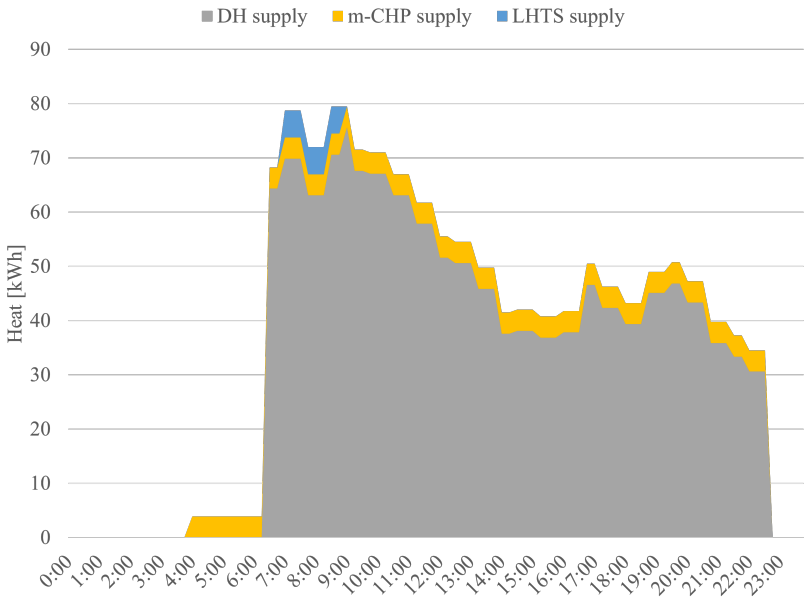

Fig. 6.21 Energy Center typical daily heating demand and local energy production in winter (*case 1*)

6.5.3 Case 2: pilot site energy performance with RE-cognition upscaled technologies

Following the results presented in the previous section, the potential impact of upscaled renewable energy technologies is here evaluated. It is estimated that the existing PV system capacity could be increased by 5 times exploiting part of the surface that is still available on the building rooftop. Hence, the electricity production of the local PV system is ideally multiplied by this factor. Similarly, it is assumed that four additional micro-CHP units could be simultaneously managed on site. Then, considering the good pairing between the micro-CHP and the LHTS, also the thermal storage size is increased by a factor 5. Finally, the HSC technology has a great upscaling potential. It is estimated that the prototypal version requires around 13 m^2 of solar collectors for the silica regeneration phase. Hence, considering the rooftop surface that remains available after increasing the number of PV panels and the ground surface with good solar exposure, it is estimated that the HSC could be confidently upscaled by a factor 10 without interfering with the other technologies. As a result, the ideal electricity consumption and production daily profiles are presented in Fig. 6.22 (for summer) and Fig. 6.23 (for winter). The micro-CHP would still be suitable for an electricity baseload during most of the day. However, during the central hours of the day, its power production should be curtailed in favour of the photovoltaic production

(especially in summer). With the aforementioned hypotheses, it is estimated that almost 7% of the PV electricity production exceeds the electricity demand. This amount of energy could be further locally reused if a suitable pack of batteries were installed. Furthermore, the HSC capacity increment effectively reduces the electricity consumption for cooling (-35% with respect to *case 0*). This is due to the fact that most of the latent heat load is removed by the pack of silica, thus the heat pump working in cooling mode is more efficient.

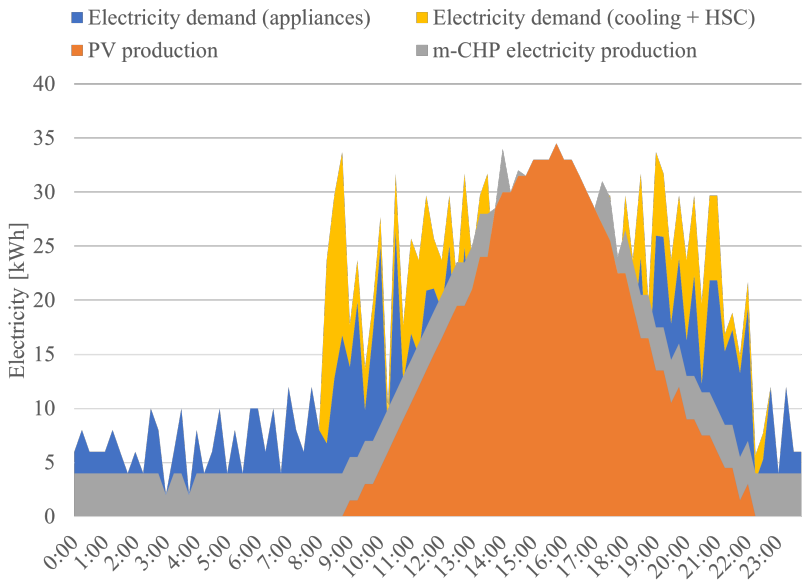

Fig. 6.22 Energy Center typical daily electricity demand and renewable energy production in summer (*case 2*)

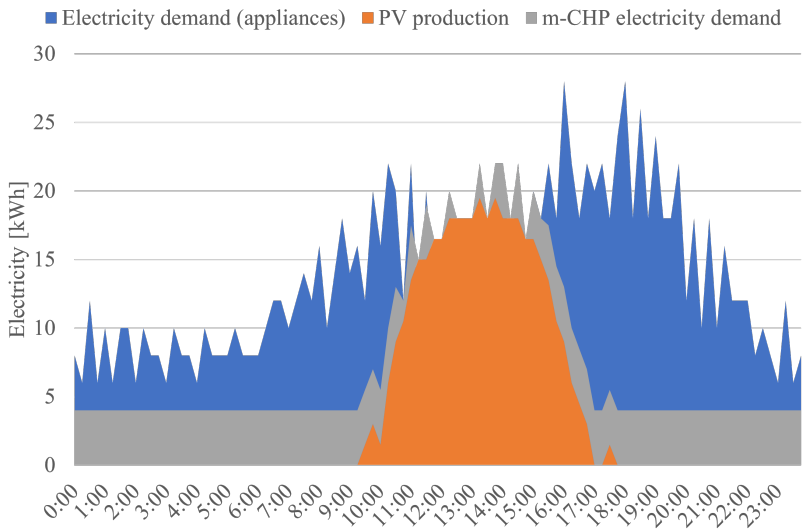

Fig. 6.23 Energy Center typical daily electricity demand and renewable energy production in winter (*case 2*)

When considering a typical winter day, the heat produced by the micro-CHP is employed in the same way as *case 1*. However, due to the electricity curtailment in the central hours of the day, it is more convenient to discharge the LHTS in those hours to compensate the lower heat production of the micro-CHP (Fig. 6.24).

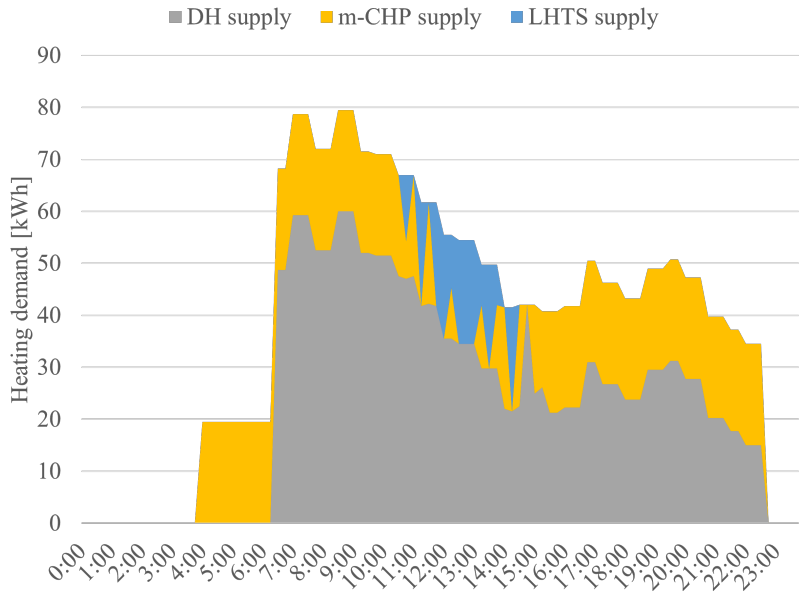

Fig. 6.24 Energy Center typical daily heating demand and local energy production in winter (*case 2*)

6.5.4 Evaluation of Key Performance Indicators

The presented case studies are here analysed in light of different Key Performance Indicators (KPIs). These cover the three main fields of interest for this project: energy, environmental and economic aspects. Concerning the pilot site energy performance, the selected KPIs are self-consumption and self-sufficiency. The former quantifies how much local energy production is consumed on-site, while the latter expresses the relevance of the local energy production over the total building demand. Regarding the environmental performance, the elected KPI is the amount of CO_2 emissions. This is obtained through the emission factors of the Italian electrical grid (276 gCO_2/kWh, from [160]) and the local DH network (161 gCO_2/kWh, from [161]). Finally, the economic performance is evaluated in terms of daily operating energy cost, which coincides with one of the objective functions of ACEME's algorithm. Table 6.2 and Table 2s summarise the results respectively for the reference summer and winter days.

Table 6.2 KPIs for a typical summer day

KPI	***case 0***	***case 1***	***case 2***
RES self-consumption [-]	100%	100%	96%
Self-sufficiency [-]	10%	14%	72%
CO_2 emissions [kg/day]	478	450	131
Normalized operating cost [-]	1	0.94	0.27

Table 6.3 KPIs for a typical winter day

KPI	***case 0***	***case 1***	***case 2***
Electricity: RES self-consumption [-]	100%	100%	96%
Electricity: Self-sufficiency [-]	6%	11%	52%
Heat: RES self-consumption [-]	-	100%	100%
Electricity: Self-sufficiency [-]	-	8%	35%
CO_2 emissions [kg/day]	918	871	639
Normalized operating cost [-]	1	0.95	0.70

As expected, the size of the prototypal technologies cannot provide a significant contribution to the building self-sufficiency. However, the hypothetical scaled versions (*case 2*)

appear to be beneficial from an energy, environmental and economic perspective. Nevertheless, the KPIs on CO_2 emissions and self-sufficiency indirectly show that it would still be difficult to strongly reduce the dependency on fossil fuels with this set of technologies. Thus, further efforts towards a decarbonized energy supply should be considered to increase the effectiveness of the project's outcomes. Moreover, it should be remarked that a constant biogas supply might be hard to obtain in an urban context, although this aspect was not addressed in the presented simulations.

6.6 Concluding remarks

This chapter presented the scope and outcomes of the European project RE-cognition. Most of the PhD activities reported in this thesis were actually performed within the framework of this project. The key results obtained during the project duration can be summarised as follows:

- An intelligent ICT system was successfully developed and installed in several pilot sites (including the Energy Center pilot site);
- Several renewable energy technologies prototypes were developed and installed around the selected European pilot sites;
- The Energy Center showed great potential for becoming a near Zero Energy Building even during its day-to-day operation;
- The LHTS could be extremely beneficial from a system perspective, especially if coupled with an intelligent controller that optimises its operation in view of the building needs.

Chapter 7

Conclusions and future perspectives

7.1 Research contributions

This chapter summarises the outcomes presented in this thesis, highlighting the main research contributions, identifying the limitations and proposing future perspectives. The research contributions of this dissertation are essentially represented by:

1. A **fast, accurate and experimentally validated dynamic model** for system-level simulations of latent heat storage units;
2. The documentation of the realization process and the experimental measurements of **two 40-kWh shell-and-tube LHTS prototypes** characterised by a different inner heat exchanger design.

The former contribution pertains to the sphere of method-oriented advances, while the latter mostly concerns application-related advances. The research objectives of this thesis were formulated in Chapter 1 and expressed through four research questions. The answers to these questions emerging from the work presented in the previous chapters are here summarised.

Q1: ***Is it possible to develop a dynamic LHTS model that is fast, accurate and experimentally validated for system level simulations?***

The dynamic modelling approach proposed in Chapter 4 proved to be extremely fast, acceptably accurate and, most importantly, experimentally validated. The model computational effort is remarkably low: roughly speaking a 2-hours LHTS discharging process can

be simulated in less than 1 second. This constitutes a great advantage when the modeller's interest is simply directed to system-level quantities such as the storage state of charge, the overall heat rate and the inlet/outlet heat transfer fluid temperatures. As a matter of fact, a full 3-dimensional LHTS model would require more than 5 hours for the same simulation to produce comparable system-level results on an average computer. The presented modelling approach proved to be also accurate enough when compared both with a complex numerical model and, most importantly, with experimental measurements. Although the proposed dynamic model was applied to two diverse shell-and-tube LHTS concepts, the LHTS state of charge was generally underestimated by less than 10% with respect to the measured value. Among the numerous tests performed, only one exception concerning the "TopOpt" LHTS unit was reported (however, this test was characterised by a highly unstable inlet HTF temperature, an uncommon situation in residential heating systems). Moreover, the model results proved to be more accurate when a more standard configuration (i.e., the "Longitudinal" LHTS) was simulated.

Q2: ***Can the parameters of such a model be independent on experimental calibration?***

The one-dimensional dynamic model presented in this dissertation is entirely based on a-priori known physical and geometrical parameters that do not require any experimental calibration. In the author's view this aspect constitutes the crucial advantage of this approach. As a matter of fact, there are similar dynamic models proposed in literature, but these all require an experimental calibration for some parameters. Nevertheless, also the presented dynamic model could implement an experimental calibration if desired. Hence, the modeller can choose whether to calibrate the two model parameters (i.e. the shape and time factors) for a better accuracy or to be satisfied with the resulting precision without recurring to on-field measurements. Furthermore, a third possibility could be considered. This concerns the inclusion of a correction factor useful to adjust the state of charge in the initial operational phases. However, although this parameter would improve the model accuracy, the experimental results proved that such a parameter would depend on the LHTS operational boundary conditions, as the initial model inaccuracy is not constant throughout the analysed cases. Hence, a reasonable determination of such a parameter would probably require some additional experimental calibration. As a result, considering the purpose of producing a simple and fairly accurate dynamic model, a correction factor was not included in the proposed modelling approach. In few words, the proposed modelling approach allows a trade-off between accuracy and experimental calibration depending on the user's goals and expectations.

Q3: ***How can the inner heat exchanger design affect the performance of shell-and-tube LHTS units?***

The design of the inner heat exchanger in shell-and-tube LHTS units is notably known as a crucial factor affecting the LHTS performance in terms of speed of charge/discharge and efficiency. In this thesis two fins configurations were tested: classical longitudinal fins around each pipe and HCM rods connecting all the pipes (resulting in a sort of HCM matrix). The latter concept actually constitutes the practical realization of the design guidelines derived from a preceding topological optimization study. For a thorough comparison, both the LHTS prototypes are characterised by the same amount of storage material (PCM) and high conducting material (HCM). The only difference resides in the way in which the HCM is arranged around the heat exchanger tubes. Moreover, the comparative analysis was performed considering similar boundary conditions (i.e., similar HTF flow rate values and inlet temperatures) both during charging and discharging phases. As a result, the "Longitudinal" LHTS showed a better performance both in terms of speed of charge and discharge compared to the "TopOpt" LHTS. In the analysed experimental tests, the "Longitudinal" LHTS stored or released between 8% and 22% more energy than the "TopOpt" LHTS considering the same amount of time. However, these results are certainly affected by the different contact surface that characterises the two prototypes. The "Longitudinal" LHTS has indeed a contact surface between the PCM and the HCM that is 3.5 times higher compared to that of the "TopOpt" prototype. This is due to the practical limitations that were encountered when translating the guidelines suggested by the topological optimization study into real-world HCM fins. Nevertheless, despite this relevant difference between the two LHTS prototypes, the performance gap between the two units is lower than expected. Hence, the design of LHTS units through a topological optimization approach has the potential to improve the performance of such storage units provided that a finer manufacturing process could be implemented.

Q4: ***How shell-and-tube LHTS units interact with a real heating system in terms of the most relevant operational parameters (i.e. heat rate, state of charge and heating system temperatures)?***

The experimental campaign performed on the two storage units confirmed that the LHTS thermal power is constantly decreasing in time when a LHTS device is discharged through the supply of a fairly constant HTF flow rate and inlet temperature. This aspect might reduce the actual useful energy that the storage is able to provide to the heating system users. As a matter of fact, all the experimental tests showed that the outlet HTF has an initial spike at the beginning of the discharging process, but then this value is drastically reduced when more than half of the storage energy content has yet to be delivered. Although the initial peak in the discharged power might be absorbed by the system thermal inertia (pipes, terminals and building envelope), the low thermal power values in the second half of

the discharging process might constitute a barrier for using these devices in a stand-alone mode. Hence, the adoption of a management system appears to be essential. In this regard, the intelligent ICT system developed within the EU research project RE-cognition aims at overcoming this barrier. The project results showed great potential concerning the integration of a LHTS technology in a multi-energy system context, especially when an intelligent controller suggests an optimal schedule for the building energy operations.

Overall, the objective of this research is to favour a larger penetration of thermal storage units in the building sector by presenting a fast, accurate and experimentally validated LHTS dynamic model and by analysing the real performance of two prototype units. In the author's view, the former contribution might facilitate the LHTS sizing process for an optimal match of the user needs and might support optimal LHTS control strategies. On the other hand, the latter contribution is supposed to advance the knowledge on the real-world behaviour of such storage units. Hence, the combination of these two results might have a relevant impact on the diffusion of these technologies and, ultimately, on the building sector's energy demand. Indeed, as already stated in the introduction, thermal storage units are an essential element for decarbonizing the building sector's heat consumption. For example, LHTS units could be used in combination with heat pumps and renewable energy sources to decouple the heating demand from the intermittent renewable energy production. Moreover, a larger diffusion of LHTS units could be beneficial in district heating networks because they might enable Demand Side Management (DSM) strategies and a more efficient network operation.

7.2 Limitations and future perspectives

According to the author's point of view, a few limitations of this study can be identified concerning the experimental analysis. Despite the initial intention of inspecting the LHTS behaviour in a real heating system, the available testing rig did not allow a full emulation of a standard residential hydronic system. This is due to the fact that the heat sink of the realized experimental facility is constituted by a dry cooler located outdoor. As a result, the thermal inertia of such a system is much lower compared to a real domestic heating system. This effect was indeed demonstrated by the frequent fluctuations in the HTF temperatures. A further reflection concerns the practical realization of the topological optimization guidelines for the second LHTS tank. The application and extension of such theoretical guidelines to an extremely practical problem (i.e., the manufacturing of a heat exchanger) led, in the author's view, to a sub-optimal design. As a matter of fact, the "TopOpt" LHTS showed lower performance compared to the "Longitudinal" LHTS mainly due to the smaller contact surface between the PCM and HCM (keeping the HCM quantity constant). Finally, the outcomes

of the RE-cognition project may not be judged completely satisfactory because the pilot testing was hampered by several bureaucratic barriers related to the building management operations.

Nevertheless, from the author's point of view, this study opens numerous future perspectives. First, the proposed modelling approach has the potential to support both LHTS optimal sizing and LHTS system level performance investigations. The former aspect would allow to tailor the LHTS size on specific user needs (design phase); the latter aspect, instead, would enable the inspection of effective LHTS control strategies (operational phase). Hence, different optimization problems that include the user dynamic behaviour and integrate the model proposed in this study could be developed depending on the modeller's goal (optimal sizing or optimal operational phase). Moreover, such a dynamic model would be suitable also for long-term simulations in well-known commercial software packages (e.g. *TRNSYS* and *Simulink*). This could open up opportunities in the study of how LHTS units dynamically interact with other energy technologies in different systems. To this extent, the model performance should be verified also for the LHTS charging phase. Hence, a new experimental campaign focused on the LHTS charging phase should be set up in order to validate and extend the model results. Furthermore, additional shell-and-tube LHTS internal geometries could be tested against the model outcomes to confirm the model general application. Finally, also additional LHTS operational conditions could be examined within the experimental facility, such as partial charge or discharge, repeated cycles or even charge/discharge through different loops and simultaneous charge/discharge. As a matter of fact, the piping connections that were realized for the experimental testing rig allow to separate the tubes dedicated to the charging process from the tubes dedicated to the discharging process. In conclusion, this study not only provides valuable insights into the simulation and experimental fields but also paves the way for interesting future research possibilities in both domains.

References

[1] International Energy Agency (IEA). Key world energy statistics 2021. Technical report, 2021.

[2] International Energy Agency (IEA). Buildings, <https://www.iea.org/energy-system/buildings>, accessed on April 2023.

[3] International Energy Agency (IEA). Heating, <https://www.iea.org/energy-system/buildings/heating>, accessed on April 2023.

[4] International Renewable Energy Agency (IRENA). Innovation outlook: Thermal energy storage. Technical report, 2020.

[5] H. Zhang, J. Baeyens, G. Cáceres, J. Degrève, and Y. Lv. Thermal energy storage: Recent developments and practical aspects. *Progress in Energy and Combustion Science*, 53:1–40, March 2016.

[6] D. Fernandes, F. Pitié, G. Cáceres, and J. Baeyens. Thermal energy storage: "How previous findings determine current research priorities". *Energy*, 39(1):246–257, March 2012.

[7] A. Hauer, S. Gschwander, B. Fumey, D. Lager, A. Lazaro, C. Rathgeber, A. Ristic, and W. van Helden. Material and Component Development for Thermal Energy Storage. Technical report, 2020.

[8] E. Guelpa and V. Verda. Demand response and other demand side management techniques for district heating: A review. *Energy*, 219:119440, March 2021.

[9] A.G. Olabi, C. Onumaegbu, T. Wilberforce, M. Ramadan, M. A. Abdelkareem, and A. H. Al – Alami. Critical review of energy storage systems. *Energy*, 214:118987, 2021.

[10] E. Hossain, H. M. R. Faruque, Md. S. H. Sunny, N. Mohammad, and N. Nawar. A comprehensive review on energy storage systems: Types, comparison, current scenario, applications, barriers, and potential solutions, policies, and future prospects. *Energies*, 13(14), 2020.

[11] V. Etacheri, R. Marom, R. Elazari, G. Salitra, and D. Aurbach. Challenges in the development of advanced li-ion batteries: a review. *Energy Environ. Sci.*, 4:3243–3262, 2011.

[12] A. Z. Weber, M. M. Mench, J. P. Meyers, P. N. Ross, J. T. Gostick, and Q. Liu. Redox flow batteries: a review. *Journal of Applied Electrochemistry*, 41:1137–1164, 2011.

[13] A. Sharma, V.V. Tyagi, C.R. Chen, and D. Buddhi. Review on thermal energy storage with phase change materials and applications. *Renewable and Sustainable Energy Reviews*, 13(2):318–345, February 2009.

[14] J. Lizana, R. Chacartegui, A. Barrios-Padura, and J. M. Valverde. Advances in thermal energy storage materials and their applications towards zero energy buildings: A critical review. *Applied Energy*, 203:219–239, October 2017.

[15] H. Mehling and L. F. Cabeza. *Heat and cold storage with PCM: An up to date introduction into basics and applications*. Heat and Mass Transfer. Springer-Verlag, Berlin Heidelberg, 2008.

[16] M. J. Huang, P. C. Eames, and N. J. Hewitt. The application of a validated numerical model to predict the energy conservation potential of using phase change materials in the fabric of a building. *Solar Energy Materials and Solar Cells*, 90(13):1951–1960, August 2006.

[17] E. Osterman, V. V. Tyagi, V. Butala, N. A. Rahim, and U. Stritih. Review of PCM based cooling technologies for buildings. *Energy and Buildings*, 49:37–49, June 2012.

[18] S. E. Kalnæs and B. P. Jelle. Phase change materials and products for building applications: A state-of-the-art review and future research opportunities. *Energy and Buildings*, 94:150–176, May 2015.

[19] F. Souayfane, F. Fardoun, and P. Biwole. Phase change materials (PCM) for cooling applications in buildings: A review. *Energy and Buildings*, 129:396–431, October 2016.

[20] V. V. Tyagi and D. Buddhi. PCM thermal storage in buildings: A state of art. *Renewable and Sustainable Energy Reviews*, 11(6):1146–1166, August 2007.

[21] K. Menoufi, A. Castell, M. M. Farid, D. Boer, and L. F. Cabeza. Life Cycle Assessment of experimental cubicles including PCM manufactured from natural resources (esters): A theoretical study. *Renewable Energy*, 51:398–403, March 2013.

[22] A. de Gracia, L. Rincón, A. Castell, M. Jiménez, D. Boer, M. Medrano, and L. F. Cabeza. Life Cycle Assessment of the inclusion of phase change materials (PCM) in experimental buildings. *Energy and Buildings*, 42(9):1517–1523, September 2010.

[23] C. Carbonaro, Y. Cascone, S. Fantucci, V. Serra, M. Perino, and M. Dutto. Energy Assessment of A Pcm–Embedded Plaster: Embodied Energy Versus Operational Energy. *Energy Procedia*, 78:3210–3215, November 2015.

[24] Y. Cascone, A. Capozzoli, and M. Perino. Optimisation analysis of PCM-enhanced opaque building envelope components for the energy retrofitting of office buildings in Mediterranean climates. *Applied Energy*, 211:929–953, February 2018.

[25] X. Sun, Q. Zhang, M. A. Medina, and K. O. Lee. Energy and economic analysis of a building enclosure outfitted with a phase change material board (PCMB). *Energy Conversion and Management*, 83:73–78, July 2014.

[26] M. Saffari, A. de Gracia, S. Ushak, and L. F. Cabeza. Economic impact of integrating PCM as passive system in buildings using Fanger comfort model. *Energy and Buildings*, 112:159–172, January 2016.

[27] L. Yantong, Z. Quan, S. Xiaoqin, D. Yaxing, and L. Shuguang. Optimization on Performance of the Latent Heat Storage Unit (LHSU) in Telecommunications Base Stations (TBSs) in China. *Energy Procedia*, 75:2119–2124, August 2015.

[28] S. Lu, Y. Chen, S. Liu, and X. Kong. Experimental research on a novel energy efficiency roof coupled with PCM and cool materials. *Energy and Buildings*, 127:159–169, September 2016.

[29] J. Lei, K. Kumarasamy, K. T. Zingre, J. Yang, M. P. Wan, and E. Yang. Cool colored coating and phase change materials as complementary cooling strategies for building cooling load reduction in tropics. *Applied Energy*, 190:57–63, March 2017.

[30] F. Kuznik, D. David, K. Johannes, and J. Roux. A review on phase change materials integrated in building walls. *Renewable and Sustainable Energy Reviews*, 15(1):379–391, January 2011.

[31] R. Baetens, B. P. Jelle, and A. Gustavsen. Phase change materials for building applications: A state-of-the-art review. *Energy and Buildings*, 42(9):1361–1368, September 2010.

[32] D. Zhou, C. Y. Zhao, and Y. Tian. Review on thermal energy storage with phase change materials (PCMs) in building applications. *Applied Energy*, 92:593–605, April 2012.

[33] H. Akeiber, P. Nejat, M. Z. A. Majid, M. A. Wahid, F. Jomehzadeh, I. Zeynali Famileh, J. K. Calautit, B. R. Hughes, and S. A. Zaki. A review on phase change material (PCM) for sustainable passive cooling in building envelopes. *Renewable and Sustainable Energy Reviews*, 60:1470–1497, July 2016.

[34] B. Zalba, J. Marin, L. F. Cabeza, and H. Mehling. Review on thermal energy storage with phase change: materials, heat transfer analysis and applications. *Applied Thermal Engineering*, 23(3):251–283, February 2003.

[35] P. Zhang, X. Xiao, and Z. W. Ma. A review of the composite phase change materials: Fabrication, characterization, mathematical modeling and application to performance enhancement. *Applied Energy*, 165:472–510, March 2016.

[36] A. Pizzolato. *Topology Optimization for Energy Problems*. PhD Thesis, Politecnico di Torino, 2018.

[37] Y. Yuan, N. Zhang, W. Tao, X. Cao, and Y. He. Fatty acids as phase change materials: A review. *Renewable and Sustainable Energy Reviews*, 29:482–498, January 2014.

[38] A. Sarı, H. Sarı, and A. Önal. Thermal properties and thermal reliability of eutectic mixtures of some fatty acids as latent heat storage materials. *Energy Conversion and Management*, 45(3):365–376, February 2004.

[39] A. Sarı. Eutectic mixtures of some fatty acids for low temperature solar heating applications: Thermal properties and thermal reliability. *Applied Thermal Engineering*, 25(14):2100–2107, October 2005.

[40] A. Sarı, A. Biçer, and A. Karaipekli. Synthesis, characterization, thermal properties of a series of stearic acid esters as novel solid–liquid phase change materials. *Materials Letters*, 63(13):1213–1216, May 2009.

[41] K. Pielichowska and K. Pielichowski. Phase change materials for thermal energy storage. *Progress in Materials Science*, 65:67–123, August 2014.

[42] R. K. Sharma, P. Ganesan, V. V. Tyagi, and T. M. I. Mahlia. Accelerated thermal cycle and chemical stability testing of polyethylene glycol (PEG) 6000 for solar thermal energy storage. *Solar Energy Materials and Solar Cells*, 147:235–239, April 2016.

[43] G. Alva, L. Liu, X. Huang, and G. Fang. Thermal energy storage materials and systems for solar energy applications. *Renewable and Sustainable Energy Reviews*, 68:693–706, February 2017.

[44] A. Solé, H. Neumann, S. Niedermaier, L. F. Cabeza, and E. Palomo. Thermal Stability Test of Sugar Alcohols as Phase Change Materials for Medium Temperature Energy Storage Application. *Energy Procedia*, 48:436–439, January 2014.

[45] L.F. Cabeza, J. Roca, M. Nogués, H. Mehling, and S. Hiebler. Immersion corrosion tests on metal-salt hydrate pairs used for latent heat storage in the 48 to 58°C temperature range. *Materials and Corrosion*, 53(12):902–907, 2002. _eprint: https://onlinelibrary.wiley.com/doi/pdf/10.1002/maco.200290004.

[46] K. Nagano, K. Ogawa, T. Mochida, K. Hayashi, and H. Ogoshi. Performance of heat charge/discharge of magnesium nitrate hexahydrate and magnesium chloride hexahydrate mixture to a single vertical tube for a latent heat storage system. *Applied Thermal Engineering*, 24(2):209–220, February 2004.

[47] M. Liu, W. Saman, and F. Bruno. Review on storage materials and thermal performance enhancement techniques for high temperature phase change thermal storage systems. *Renewable and Sustainable Energy Reviews*, 16(4):2118–2132, May 2012.

[48] B. C. Shin, S. D. Kim, and W. Park. Ternary carbonate eutectic (lithium, sodium and potassium carbonates) for latent heat storage medium. *Solar Energy Materials*, 21(1):81–90, November 1990.

[49] B. Cárdenas and N. León. High temperature latent heat thermal energy storage: Phase change materials, design considerations and performance enhancement techniques. *Renewable and Sustainable Energy Reviews*, 27:724–737, November 2013.

[50] F. Agyenim and N. Hewitt. Experimental investigation and improvement in heat transfer of paraffin PCM RT58 storage system to take advantage of low peak tariff rates for heat pump applications. *International Journal of Low-Carbon Technologies*, 8(4):260–270, December 2013.

[51] C. Rathgeber, H. Schmit, P. Hennemann, and S. Hiebler. Investigation of pinacone hexahydrate as phase change material for thermal energy storage around 45°C. *Applied Energy*, 136:7–13, December 2014.

[52] B. C. Zhao and R. Z. Wang. Perspectives for short-term thermal energy storage using salt hydrates for building heating. *Energy*, 189:116139, December 2019.

[53] J. P. da Cunha and P. Eames. Compact latent heat storage decarbonisation potential for domestic hot water and space heating applications in the UK. *Applied Thermal Engineering*, 134:396–406, April 2018.

[54] P. B. Salunkhe and D. Jaya Krishna. Investigations on latent heat storage materials for solar water and space heating applications. *Journal of Energy Storage*, 12:243–260, August 2017.

[55] H. Huang, Y. Xiao, J. Lin, T. Zhou, Y. Liu, and Q. Zhao. Improvement of the efficiency of solar thermal energy storage systems by cascading a PCM unit with a water tank. *Journal of Cleaner Production*, 245:118864, February 2020.

[56] F. Agyenim, N. Hewitt, P. Eames, and M. Smyth. A review of materials, heat transfer and phase change problem formulation for latent heat thermal energy storage systems (LHTESS). *Renewable and Sustainable Energy Reviews*, 14(2):615–628, February 2010.

[57] F. Colella, A. Sciacovelli, and V. Verda. Numerical analysis of a medium scale latent energy storage unit for district heating systems. *Energy*, 45(1):397–406, September 2012.

[58] T. Xu. *Integrating Latent Heat Storage into Residential Heating Systems*. PhD thesis, KTH Royal Institute of Technology, 2021.

[59] C. Finck, R. Li, R. Kramer, and W. Zeiler. Quantifying demand flexibility of power-to-heat and thermal energy storage in the control of building heating systems. *Applied Energy*, 209:409–425, January 2018.

[60] R. Hirmiz, H. M. Teamah, M. F. Lightstone, and J. S. Cotton. Performance of heat pump integrated phase change material thermal storage for electric load shifting in building demand side management. *Energy and Buildings*, 190:103–118, May 2019.

[61] C. P. Underwood, T. Shepherd, S. J. Bull, and S. Joyce. Hybrid thermal storage using coil-encapsulated phase change materials. *Energy and Buildings*, 159:357–369, January 2018.

[62] F. J. Batlles, B. Gil, S. Ushak, J. Kasperski, M. Luján, D. Maldonado, M. Nemś, A. Nemś, A. M. Puertas, M. S. Romero-Cano, S. Rosiek, and M. Grageda. Development and Results from Application of PCM-Based Storage Tanks in a Solar Thermal Comfort System of an Institutional Building—A Case Study. *Energies*, 13(15):3877, January 2020. Number: 15 Publisher: Multidisciplinary Digital Publishing Institute.

[63] Z. Wang, F. Wang, Z. Ma, W. Lin, and H. Ren. Investigation on the feasibility and performance of transcritical CO2 heat pump integrated with thermal energy storage for space heating. *Renewable Energy*, 134:496–508, April 2019.

[64] N. J. Kelly, P. G. Tuohy, and A. D. Hawkes. Performance assessment of tariff-based air source heat pump load shifting in a UK detached dwelling featuring phase change-enhanced buffering. *Applied Thermal Engineering*, 71(2):809–820, October 2014.

[65] J. Lizana, D. Friedrich, R. Renaldi, and R. Chacartegui. Energy flexible building through smart demand-side management and latent heat storage. *Applied Energy*, 230:471–485, November 2018.

[66] Y. Hamada and J. Fukai. Latent heat thermal energy storage tanks for space heating of buildings: Comparison between calculations and experiments. *Energy Conversion and Management*, 46(20):3221–3235, December 2005.

[67] J. Zhao, Y. Ji, Y. Yuan, Z. Zhang, and J. Lu. Energy-Saving Analysis of Solar Heating System with PCM Storage Tank. *Energies*, 11(1):237, January 2018. Number: 1 Publisher: Multidisciplinary Digital Publishing Institute.

[68] Y. Wang, X. Yang, T. Xiong, W. Li, and K. W. Shah. Performance evaluation approach for solar heat storage systems using phase change material. *Energy and Buildings*, 155:115–127, November 2017.

[69] Y. Li, G. Huang, T. Xu, X. Liu, and H. Wu. Optimal design of PCM thermal storage tank and its application for winter available open-air swimming pool. *Applied Energy*, 209:224–235, January 2018.

[70] Y. Li, Z. Ding, and Y. Du. Techno-economic optimization of open-air swimming pool heating system with PCM storage tank for winter applications. *Renewable Energy*, 150:878–890, May 2020.

[71] M. M. Prieto, I. Suárez, and B. González. Analysis of the thermal performance of flat plate PCM heat exchangers for heating systems. *Applied Thermal Engineering*, 116:11–23, April 2017.

[72] F. Bentivoglio, S. Rouge, O. Soriano, and A. Tempass de Sousa. Design and operation of a 180 kWh PCM heat storage at the Flaubert substation of the Grenoble urban heating network. *Applied Thermal Engineering*, 185:116402, February 2021.

[73] M. Jurkowska and I. Szczygieł. Review on properties of microencapsulated phase change materials slurries (mPCMS). *Applied Thermal Engineering*, 98:365–373, April 2016.

[74] M. Delgado, A. Lázaro, J. Mazo, and B. Zalba. Review on phase change material emulsions and microencapsulated phase change material slurries: Materials, heat transfer studies and applications. *Renewable and Sustainable Energy Reviews*, 16(1):253–273, January 2012.

[75] Z. Qiu, X. Ma, P. Li, X. Zhao, and A. Wright. Micro-encapsulated phase change material (MPCM) slurries: Characterization and building applications. *Renewable and Sustainable Energy Reviews*, 77:246–262, September 2017.

[76] S. Niedermaier, M. Biedenbach, and S. Gschwander. Characterisation and Enhancement of Phase Change Slurries. *Energy Procedia*, 99:64–71, November 2016.

[77] P. Zhang, Z. W. Ma, Z. Y. Bai, and J. Ye. Rheological and energy transport characteristics of a phase change material slurry. *Energy*, 106:63–72, July 2016.

[78] A. Shrivastava and P. R. Chakraborty. Shell-and-Tube Latent Heat Thermal Energy Storage (ST-LHTES). In Himanshu Tyagi, Avinash Kumar Agarwal, Prodyut R. Chakraborty, and Satvasheel Powar, editors, *Advances in Solar Energy Research*, Energy, Environment, and Sustainability, pages 395–441. Springer, Singapore, 2019.

[79] A. Agarwal and R. M. Sarviya. An experimental investigation of shell and tube latent heat storage for solar dryer using paraffin wax as heat storage material. *Engineering Science and Technology, an International Journal*, 19(1):619–631, March 2016.

[80] M. Longeon, A. Soupart, J. Fourmigué, A. Bruch, and P. Marty. Experimental and numerical study of annular PCM storage in the presence of natural convection. *Applied Energy*, 112:175–184, December 2013.

[81] A. S. Fleischer. *Thermal Energy Storage Using Phase Change Materials: Fundamentals and Applications*. Springer, June 2015.

[82] M. Liu, S. Riahi, R. Jacob, M. Belusko, and F. Bruno. A new methodology for designing and assessing latent heat thermal energy storage systems. *AIP Conference Proceedings*, 2303(1):190023, December 2020. Publisher: American Institute of Physics.

[83] L. Yang, H. Xu, F. Cola, B. Akhmetov, A. Gil, L. F. Cabeza, and A. Romagnoli. Shell-and-Tube Latent Heat Thermal Energy Storage Design Methodology with Material Selection, Storage Performance Evaluation, and Cost Minimization. *Applied Sciences*, 11(9):4180, January 2021. Number: 9 Publisher: Multidisciplinary Digital Publishing Institute.

[84] A. M. Abdulateef, S. Mat, J. Abdulateef, K. Sopian, and A. A. Al-Abidi. Geometric and design parameters of fins employed for enhancing thermal energy storage systems: a review. *Renewable and Sustainable Energy Reviews*, 82:1620–1635, February 2018.

[85] Z. Khan, Z. Khan, and A. Ghafoor. A review of performance enhancement of PCM based latent heat storage system within the context of materials, thermal stability and compatibility. *Energy Conversion and Management*, 115:132–158, May 2016.

[86] G. R. Solomon and R. Velraj. Analysis of the heat transfer mechanisms during energy storage in a Phase Change Material filled vertical finned cylindrical unit for free cooling application. *Energy Conversion and Management*, 75:466–473, November 2013.

[87] A. A. Rabienataj Darzi, M. Jourabian, and M. Farhadi. Melting and solidification of PCM enhanced by radial conductive fins and nanoparticles in cylindrical annulus. *Energy Conversion and Management*, 118:253–263, June 2016.

[88] A. Beck, M. Koller, H. Walter, and M. Hameter. Transient Numerical Analysis of Different Finned Tube Designs for Use in Latent Heat Thermal Energy Storage Devices. American Society of Mechanical Engineers Digital Collection, October 2015.

[89] Y. Yuan, X. Cao, B. Xiang, and Y. Du. Effect of installation angle of fins on melting characteristics of annular unit for latent heat thermal energy storage. *Solar Energy*, 136:365–378, October 2016.

[90] M. Kazemi, M. J. Hosseini, A. A. Ranjbar, and R. Bahrampoury. Improvement of longitudinal fins configuration in latent heat storage systems. *Renewable Energy*, 116:447–457, February 2018.

[91] C. Liu and D. Groulx. Experimental study of the phase change heat transfer inside a horizontal cylindrical latent heat energy storage system. *International Journal of Thermal Sciences*, 82:100–110, August 2014.

[92] S. Paria, S. Baradaran, A. Amiri, A. A. D. Sarhan, and S. N. Kazi. Performance evaluation of latent heat energy storage in horizontal shell-and-finned tube for solar application. *Journal of Thermal Analysis and Calorimetry*, 123(2):1371–1381, February 2016.

[93] W. Wang, L. Wang, and Y. He. Parameter effect of a phase change thermal energy storage unit with one shell and one finned tube on its energy efficiency ratio and heat storage rate. *Applied Thermal Engineering*, 93:50–60, January 2016.

[94] X. Yang, Z. Lu, Q. Bai, Q. Zhang, L. Jin, and J. Yan. Thermal performance of a shell-and-tube latent heat thermal energy storage unit: Role of annular fins. *Applied Energy*, 202:558–570, September 2017.

[95] I. Jmal and M. Baccar. Numerical study of PCM solidification in a finned tube thermal storage including natural convection. *Applied Thermal Engineering*, 84:320–330, June 2015.

[96] S. Kuboth, A. König-Haagen, and D. Brüggemann. Numerical Analysis of Shell-and-Tube Type Latent Thermal Energy Storage Performance with Different Arrangements of Circular Fins. *Energies*, 10(3):274, March 2017. Number: 3 Publisher: Multidisciplinary Digital Publishing Institute.

[97] N. H. S. Tay, F. Bruno, and M. Belusko. Comparison of pinned and finned tubes in a phase change thermal energy storage system using CFD. *Applied Energy*, 104:79–86, April 2013.

[98] N. Beemkumar, A. Karthikeyan, D. Yuvarajan, and S. Lakshmi Sankar. Experimental Investigation on Improving the Heat Transfer of Cascaded Thermal Storage System Using Different Fins. *Arabian Journal for Science and Engineering*, 42(5):2055–2065, May 2017.

[99] A. Sciacovelli, F. Gagliardi, and V. Verda. Maximization of performance of a PCM latent heat storage system with innovative fins. *Applied Energy*, 137:707–715, January 2015.

[100] A. Sciacovelli and V. Verda. Second-law design of a latent heat thermal energy storage with branched fins. *International Journal of Numerical Methods for Heat & Fluid Flow*, 26(2):489–503, 2016.

[101] S. Lohrasbi, M. Gorji-Bandpy, and D. D. Ganji. Thermal penetration depth enhancement in latent heat thermal energy storage system in the presence of heat pipe based on both charging and discharging processes. *Energy Conversion and Management*, 148:646–667, September 2017.

[102] M. Sheikholeslami, S. Lohrasbi, and D. D. Ganji. Response surface method optimization of innovative fin structure for expediting discharging process in latent heat thermal energy storage system containing nano-enhanced phase change material. *Journal of the Taiwan Institute of Chemical Engineers*, 67:115–125, October 2016.

[103] D. Laing, T. Bauer, N. Breidenbach, B. Hachmann, and M. Johnson. Development of high temperature phase-change-material storages. *Applied Energy*, 109:497–504, September 2013.

[104] J. Vogel and M. Johnson. Natural convection during melting in vertical finned tube latent thermal energy storage systems. *Applied Energy*, 246:38–52, July 2019.

[105] A. Rozenfeld, Y. Kozak, T. Rozenfeld, and G. Ziskind. Experimental demonstration, modeling and analysis of a novel latent-heat thermal energy storage unit with a helical fin. *International Journal of Heat and Mass Transfer*, 110:692–709, July 2017.

[106] A. Pizzolato, A. Sharma, K. Maute, A. Sciacovelli, and V. Verda. Design of effective fins for fast PCM melting and solidification in shell-and-tube latent heat thermal energy storage through topology optimization. *Applied Energy*, 208:210–227, December 2017.

[107] A. Pizzolato, A. Sharma, K. Maute, A. Sciacovelli, and V. Verda. Topology optimization for heat transfer enhancement in Latent Heat Thermal Energy Storage. *International Journal of Heat and Mass Transfer*, 113:875–888, October 2017.

[108] V. R. Voller. An overview of numerical methods for solving phase change problems. *Advances in Numerical Heat Transfer*, 1997.

[109] H. Hu and S. A. Argyropoulos. Mathematical modelling of solidification and melting: a review. *Modelling and Simulation in Materials Science and Engineering*, 4(4):371, July 1996.

[110] T. R. Goodman and J. J. Shea. The Melting of Finite Slabs. *Journal of Applied Mechanics*, 27(1):16–24, March 1960.

[111] R. S. Gupta and D. Kumar. A modified variable time step method for the one-dimensional stefan problem. *Computer Methods in Applied Mechanics and Engineering*, 23(1):101–109, July 1980.

[112] R. Bonnerot and P. Jamet. Numerical computation of the free boundary for the two-dimensional Stefan problem by space-time finite elements. *Journal of Computational Physics*, 25(2):163–181, October 1977.

[113] D. R. Lynch and K. O'Neill. Continuously deforming finite elements for the solution of parabolic problems, with and without phase change. *International Journal for Numerical Methods in Engineering*, 17(1):81–96, 1981. _eprint: https://onlinelibrary.wiley.com/doi/pdf/10.1002/nme.1620170107.

[114] M. R. Albert and K. O'Neill. Moving boundary-moving mesh analysis of phase change using finite elements with transfinite mappings. *International Journal for Numerical Methods in Engineering*, 23(4):591–607, 1986. _eprint: https://onlinelibrary.wiley.com/doi/pdf/10.1002/nme.1620230406.

[115] N. Zabaras and Y. Ruan. Moving and deforming finite-element simulation of two-dimensional Stefan problems. *Communications in Applied Numerical Methods*, 6(7):495–506, 1990. _eprint: https://onlinelibrary.wiley.com/doi/pdf/10.1002/cnm.1630060702.

[116] Q. T. Pham. Comparison of General-Purpose Finite-Element Methods for the Stefan Problem. *Numerical Heat Transfer, Part B: Fundamentals*, 27(4):417–435, June 1995. Publisher: Taylor & Francis _eprint: https://doi.org/10.1080/10407799508914965.

[117] V. R. Voller, C. R. Swaminathan, and B. G. Thomas. Fixed grid techniques for phase change problems: A review. *International Journal for Numerical Methods in Engineering*, 30(4):875–898, 1990. _eprint: https://onlinelibrary.wiley.com/doi/pdf/10.1002/nme.1620300419.

[118] S. N. Al-Saadi and Z. Zhai. Modeling phase change materials embedded in building enclosure: A review. *Renewable and Sustainable Energy Reviews*, 21:659–673, May 2013.

[119] V. R. Voller and C. R. Swaminathan. Eral Source-Based Method for Solidification Phase Change. *Numerical Heat Transfer, Part B: Fundamentals*, 19(2):175–189, January 1991. Publisher: Taylor & Francis _eprint: https://doi.org/10.1080/10407799108944962.

[120] A. de Gracia and L. F. Cabeza. Numerical simulation of a PCM packed bed system: A review. *Renewable and Sustainable Energy Reviews*, 69:1055–1063, March 2017.

[121] A. A. Al-Abidi, S. Bin Mat, K. Sopian, M. Y. Sulaiman, and A. T. Mohammed. CFD applications for latent heat thermal energy storage: a review. *Renewable and Sustainable Energy Reviews*, 20:353–363, April 2013.

[122] H. Niyas, S. Prasad, and P. Muthukumar. Performance investigation of a lab–scale latent heat storage prototype – Numerical results. *Energy Conversion and Management*, 135:188–199, March 2017.

[123] H. Niyas, C. R. C. Rao, and P. Muthukumar. Performance investigation of a lab-scale latent heat storage prototype – Experimental results. *Solar Energy*, 155:971–984, October 2017.

[124] M. Esapour, M.J. Hosseini, A.A. Ranjbar, Y. Pahamli, and R. Bahrampoury. Phase change in multi-tube heat exchangers. *Renewable Energy*, 85:1017–1025, January 2016.

[125] M. Esapour, M. J. Hosseini, A. A. Ranjbar, and R. Bahrampoury. Numerical study on geometrical specifications and operational parameters of multi-tube heat storage systems. *Applied Thermal Engineering*, 109:351–363, October 2016.

[126] S. Seddegh, X. Wang, and A. D. Henderson. A comparative study of thermal behaviour of a horizontal and vertical shell-and-tube energy storage using phase change materials. *Applied Thermal Engineering*, 93:348–358, January 2016.

[127] A. Sciacovelli, V. Verda, and F. Colella. Numerical Investigation on the Thermal Performance Enhancement in a Latent Heat Thermal Storage Unit. In *Volume 2: Applied Fluid Mechanics; Electromechanical Systems and Mechatronics; Advanced Energy Systems; Thermal Engineering; Human Factors and Cognitive Engineering*, pages 543–551, Nantes, France, July 2012. American Society of Mechanical Engineers.

[128] A. Sciacovelli, F. Colella, and V. Verda. Melting of PCM in a thermal energy storage unit: Numerical investigation and effect of nanoparticle enhancement: Melting of PCM in a thermal energy storage unit. *International Journal of Energy Research*, 37(13):1610–1623, October 2013.

[129] Y. Dutil, D. R. Rousse, N. B. Salah, S. Lassue, and L. Zalewski. A review on phase-change materials: Mathematical modeling and simulations. *Renewable and Sustainable Energy Reviews*, 15(1):112–130, January 2011.

[130] A. Raul, M. Jain, S. Gaikwad, and S. K. Saha. Modelling and experimental study of latent heat thermal energy storage with encapsulated PCMs for solar thermal applications. *Applied Thermal Engineering*, 143:415–428, October 2018.

[131] K. A. R. Ismail and R. Stuginsky Jr. A parametric study on possible fixed bed models for pcm and sensible heat storage. *Applied Thermal Engineering*, 19(7):757–788, July 1999.

[132] S. Karthikeyan and R. Velraj. Numerical investigation of packed bed storage unit filled with PCM encapsulated spherical containers – A comparison between various mathematical models. *International Journal of Thermal Sciences*, 60:153–160, October 2012.

[133] A. J. Parry, P. C. Eames, and F. B. Agyenim. Modeling of Thermal Energy Storage Shell-and-Tube Heat Exchanger. *Heat Transfer Engineering*, 35(1):1–14, January 2014. Publisher: Taylor & Francis _eprint: https://doi.org/10.1080/01457632.2013.810057.

[134] H. Neumann, V. Palomba, A. Frazzica, D. Seiler, U. Wittstadt, S. Gschwander, and G. Restuccia. A simplified approach for modelling latent heat storages: Application and validation on two different fin-and-tubes heat exchangers. *Applied Thermal Engineering*, 125:41–52, October 2017.

[135] N. H. S. Tay, M. Belusko, A. Castell, L. F. Cabeza, and F. Bruno. An effectiveness-NTU technique for characterising a finned tubes PCM system using a CFD model. *Applied Energy*, 131:377–385, October 2014.

[136] M. Johnson, J. Vogel, M. Hempel, B. Hachmann, and A. Dengel. Design of high temperature thermal energy storage for high power levels. *Sustainable Cities and Society*, 35:758–763, November 2017.

[137] R. Waser, F. Ghani, S. Maranda, T. S. O'Donovan, P. Schuetz, M. Zaglio, and J. Worlitschek. Fast and experimentally validated model of a latent thermal energy storage device for system level simulations. *Applied Energy*, 231:116–126, December 2018.

[138] Y. Li, N. Zhang, and Z. Ding. Investigation on the energy performance of using air-source heat pump to charge PCM storage tank. *Journal of Energy Storage*, 28:101270, April 2020.

[139] European Association for Storage of Energy. EASE-EERA Energy Storage Technology Development Roadmap 2017. Technical report, 2017.

[140] B. C. Zhao, T. X. Li, J. C. Gao, and R. Z. Wang. Latent heat thermal storage using salt hydrates for distributed building heating: A multi-level scale-up research. *Renewable and Sustainable Energy Reviews*, 121:109712, April 2020.

[141] D. Laing, T. Bauer, N. Breidenbach, B. Hachmann, and M. Johnson. Development of high temperature phase-change-material storages. *Applied Energy*, 109:497–504, September 2013.

[142] T. Xu, E. N. Humire, S. Trevisan, M. Ignatowicz, S. Sawalha, and J. N. Chiu. Experimental and numerical investigation of a latent heat thermal energy storage unit with ellipsoidal macro-encapsulation. *Energy*, 238:121828, January 2022.

[143] T. Xu, E. N. Humire, J. N. Chiu, and S. Sawalha. Latent heat storage integration into heat pump based heating systems for energy-efficient load shifting. *Energy Conversion and Management*, 236:114042, May 2021.

[144] CRODA. Data sheet crodatherm 74, <https://www.crodaenergytechnologies.com>, accessed on March 2023.

[145] J. Vogel, J. Felbinger, and M. Johnson. Natural convection in high temperature flat plate latent heat thermal energy storage systems. *Applied Energy*, 184:184–196, December 2016.

[146] A. Pizzolato, A. Sharma, R. Ge, K. Maute, V. Verda, and A. Sciacovelli. Maximization of performance in multi-tube latent heat storage – Optimization of fins topology, effect of materials selection and flow arrangements. *Energy*, February 2019.

[147] Kamstrup. Documentation for MULTICAL® 403.

[148] M. J. Hosseini, M. Rahimi, and R. Bahrampoury. Experimental and computational evolution of a shell and tube heat exchanger as a PCM thermal storage system. *International Communications in Heat and Mass Transfer*, 50:128–136, January 2014.

[149] K. A. R. Ismail and M. M. Gonçalves. Thermal performance of a pcm storage unit. *Energy Conversion and Management*, 40(2):115–138, January 1999.

[150] S. Seddegh, X. Wang, M. M. Joybari, and F. Haghighat. Investigation of the effect of geometric and operating parameters on thermal behavior of vertical shell-and-tube latent heat energy storage systems. *Energy*, 137:69–82, October 2017.

[151] A. Sciacovelli, V. Verda, and F. Colella. Numerical Model for Storage Systems Based on Phase-Change Materials. In *Volume 4: Energy Systems Analysis, Thermodynamics and Sustainability; Combustion Science and Engineering; Nanoengineering for Energy, Parts A and B*, pages 237–245, Denver, Colorado, USA, January 2011. ASMEDC.

[152] F. P. Incropera, D. P. DeWitt, T. L. Bergman, and A. S. Lavine, editors. *Fundamentals of heat and mass transfer*. Wiley, Hoboken, NJ, 6. ed edition, 2007. OCLC: 266080940.

[153] Python library. Sparse linear algebra (scipy.sparse.linalg) — SciPy v1.10.1 Manual, <https://docs.scipy.org/doc/scipy/reference/sparse.linalg.html>, accessed on April 2023.

[154] A. Colangelo. Github latent heat thermal storage dynamic model repository, <https://github.com/alesco20/LHTS-dynamic-model>, September 2023.

[155] ANSYS. Ansys Fluent Theory Guide, 2020.

[156] Re-Cognition - Renewable Energy Integration Framework, <https://re-cognition-project.eu/>, accessed on April 2023.

[157] European Commission. Clean energy for all Europeans package, <https://energy.ec.europa.eu/topics/energy-strategy/clean-energy-all-europeans-package>, accessed on April 2023.

[158] European Commission. Fit for 55, <https://www.consilium.europa.eu/en/policies/green-deal/fit-for-55-the-eu-plan-for-a-green-transition/>, accessed on April 2023.

[159] International Renewable Energy Agency (IRENA). Time-of-use tariffs – Innovation Landscape Brief. Technical report, 2019.

[160] ISPRA. Fattori di emissione atmosferica di gas a effetto serra nel settore elettrico nazionale e nei principali Paesi Europei. Technical report, March 2020.

[161] IREN Energia. Comunicazione dei fattori di conversione in energia primaria dell'energia termica fornita ai punti di consegna della rete di teleriscaldamento della rete di Torino. Technical report, November 2020.